Intensity Mapping: Science and Instrumentation Across the Electromagnetic Spectrum

by

Trevor M. Oxholm

A dissertation submitted in partial fulfillment of

the requirements for the degree of

Doctor of Philosophy

(Physics)

at the

UNIVERSITY OF WISCONSIN–MADISON

2022

Date of final oral examination: 04/29/2022

The dissertation is approved by the following members of the Final Oral Committee:

Peter Timbie, Professor, Physics
Keith Bechtol, Assistant Professor, Physics
Moritz Münchmeyer, Assistant Professor, Physics
Amy Barger, Professor, Astronomy
Eric Switzer, Research Astrophysicist, NASA-Goddard Space Flight Center

For my grandparents, who provided the crucial foundation for all the work that went into this thesis, and all that is yet to come.

ACKNOWLEDGMENTS

Success consists of going from failure to failure without loss of enthusiasm.

— Winston Churchill

No great adventure involves simply pointing a compass and proceeding straight to the final destination. The real path is riddled with obstacles, failures, and hardships, each providing an opportunity to overcome. My route to Ph.D. is certainly no exception — throughout, I have benefited immensely from mentors, friends, and family who have helped me navigate through these obstacles and failures without loss of enthusiasm, and I am honored and humbled by the journey. This measure of success of failing again and again while maintaining enthusiasm, along with the great adventure of the process, is far greater than any three-letter accolade can provide.

Without question, the biggest thanks go to my advisor, Professor Peter Timbie. Peter has a special talent as a leader to bring out the best in his students, while still remaining an enormously kind mentor. I have benefitted greatly from his leadership and mentorship, and will certainly use him as an example as I gain leadership throughout my career. In addition to being an excellent advisor, I also consider him a friend.

Next, I'd like to express immense gratitude to my NASA mentor and 'second advisor', Dr. Eric Switzer, whose collaboration with me is the result of my proudest failure. We first connected while I was writing a proposal for a prestigious NASA fellowship, for which proposed work in support of the EXCLAIM mission. Despite the uncertainty of funding, I pushed forward because EXCLAIM was a mission I was passionate about, and an area of science and technology I wanted to contribute to. Throughout, Eric mentored me as closely as a primary advisor would, and his mentorship has been essential to my holistic understanding of science and instrumentation.

This legacy of mentorship traces back to high school physics classes. At Portsmouth High School, Mr. Moss and Mr. Duncan helped to spark my love for physics through coursework and through independent projects. In one of these projects, I worked with Mike Baier, a former student of Mr. Duncan, who provided the initial seed for my career in research. At Northeastern University, this seed grew into my first research experiences with Professor Nian Sun and Professor Satoru Emori (then a postdoc, now faculty at Virginia Tech). I recall being in awe of Nian's command over materials science and engineering, as he seemingly had an answer to everything. Later, I had the opportunity to work at the University of Washington working with Professor Jerry Miller and Dr. Tim Hobbs (now at Fermilab). Before graduate school, Professors Jim Halverson and Brent Nelson further sparked my interest in physics, broadening it to cosmology and particle physics. It was Professor Nelson who helped to inspire me to switch fields to physics, and Professor Halverson who stated that I should "definitely apply to UW-Madison", not only for the high-quality researchers but for the collaborative culture aided by cheese curds and Newglaurus products.

Outside of my primary mentors throughout graduate school, I have benefitted from additional mentorship and collaboration at UW-Madison, Fermilab, and NASA-Goddard. I was fortunate to work with many students and researchers in Peter's group, including Dr. Santanu Das, Calvin Osinga, Haotian Cao, David Kwak, Lily Robinthol, Yanlin Wu, Anh Phan, John Podczerwinski, Faizah Siddique, and especially Gage Siebert. I have also enjoyed a close-knit group of students and postdocs from other cosmology groups, including Jimena Gonzalez, Yurii Kvasiuk, Michael Martinez, Mitch McNanna, Megan Tabbutt, Dr. Peter Ferguson, Dr. Yjan Gordon, and Dr. Robert Morgan[1]. Beyond these students, I have learned a great deal from Professors Keith Bechtol and Moritz Munchmeyer, along with Professor Daniel Chung, through

[1]If the Churchill quote holds for chess games, I've been enormously successful.

cosmology journal club. I'd also like to think Professors Bechtol, Munchmeyer, and Barger for joining my committee alongside Professor Timbie and Dr. Switzer.

One of my favorite things about the EXCLAIM group at NASA-Goddard is the diversity of backgrounds, including a range of scientists and engineers. I have greatly enjoyed learning from Dr. Tom Essinger-Hileman on optics and general instrumentation. Likewise, Dr. Emily Barrentine (my academic older sister!), Dr. Thomas Stevenson, Dr. Jim Hays-Wehle, Dr. Maryam Rahmani, and Carrie Volpert have been close mentors and collaborators on detector modeling and development. Additionally, I have greatly enjoyed learning from the engineers' perspectives through Dr. Giuseppe Cataldo and Tatsat Parekh, and from other scientists including Dr. Chris Anderson (another academic older sibling!), Dr. Patrick Breysse, Dr. Jason Glenn, and Prof. Anthony Pullen. Through previous studies on Tianlai data, I further benefitted by learning from Dr. Albert Stebbins and Dr. John Marriner.

My friends and family have helped me to maintain my status as one of the happiest graduate students people meet, keeping me grounded and helping remind me that there is more to life than work. Dr. Gregory Holdman, Brad Kumm, Dr. Rob Morgan, Abby Bishop, Juan Bohorquez, Zach Huemann, Cody Poole, and many others have been constant staples throughout graduate school, and have somehow tolerated me for upwards of 5 years. Meanwhile, my sisters Jacquelyn and Johanna, as well as Tim Englert and Tom Young, have continued to be staples in my life, and they are now just as much friends as they are family.

My parents have also been a constant support for my choice to pursue graduate school and a career in research. They continue to be my most trusted advisors and my greatest teachers, and no words can adequately describe my gratitude to them.

Finally, I end these acknowledgments with a dedication to my grandparents, who provided the foundation for my parents and me. While I never had the opportunity

to meet my grandfather, John Oxholm, his impact on my father is clear, and laid the foundation for my family's principles of integrity and a strong work ethic, and the importance of balancing it out through fun with friends and family. From my grandmother, Emilie "Milly" Lamson, I learned the value and strength of a relentlessly positive disposition; not only did that help enable her fulfilling life, but she spread nothing but positivity with those around her. From my grandmother, Thelma "Kitty" Oxholm, I have learned the value of community and public service; these themes, also taught by my late aunt Kristina Oxholm, are inspirations for my career choice following graduate school. Lastly, my grandfather, Rev. Dr. Robert Lamson has constantly challenged me to think outside of my comfort zone, reminding me that there are some things even science can't explain. He also taught me to appreciate the value of all perspectives and to question the central narrative - both crucial characteristics in a good scientist and analytical thinker.

LIST OF TABLES

1.1 Incomplete summary of LIM experiments. 28

5.1 EXCLAIM instrument model separated into three redshift bins. Here, $n_{\rm ch}$ describes the number of frequency channels in the bin, $\Delta\nu$ is the bandwidth of the bin, the σ_n^2 is the instrument noise per voxel, and the following four columns describe the redshift of the [CII] and CO measurements for $J = 6, 5, 4$, respectively. Finally, $\Delta\Theta$ describes the $1/e$ angular resolution of the beam. 106

5.2 Survey region parameters. For the n and σ_z columns, the four entries correspond to [CII] / CO(6-5) / CO(5-4) / and CO(4-3), and for the z range column, the two entries correspond to [CII] and the aggregate CO. 106

5.3 Distance, volume, and noise for each line and redshift bin for the BOSS-S82 survey. $\Delta L_{||}$, $\Delta L_{\perp}$, and $V_{\rm surv}$ correspond to the dimensions and total volume of the redshift bin bin consisting of 100 frequency channels, while $dL_{||}$, $dL_{\perp}$, and dV correspond to single voxels. Distances are in units of Mpc/h, volumes in Mpc$^3/h^3$, and instrument noise in kJy^2/sr^2 Mpc$^3/h^3$. 108

6.1 Nominal EXCLAIM MKID design parameters. 124

7.1 MKID design reference parameters for the EXCLAIM detector array. . . 160

8.1 Simulation parameters for POPPY simulation using the `Fresnel Optical System` setting. The aperture at the lens is simulated as a Gaussian with FWHM provided above. The mirrors are simulated through POPPY as lenses with focal lengths denoted by f. The baffles and the Cold Stop are simulated as pupils with radii given by r. Note that we consider 9 optics tube baffles, each with the same radius of truncation, and we do not consider the finite sizes of the lenses/mirrors because they contribute negligibly. 171

8.2 Positions of the beam waist/focus, using time-reversed propagation (i.e. from the lens to the primary). The first column describes the optical element that was most recently propagated through, where e.g. the first row describes the optical rays between the lens and the secondary mirror. The three columns describe the positions of the focus via ray-tracing, beam waist via analytic Gaussian optics, and beam waist via POPPY. Zero distance corresponds to the position of the lens. 174

LIST OF FIGURES

1.1 Density components vs time. Individual components to Ω are shown in the dashed curves, while the total energy density relative to today is shown in solid black. The left vertical gray curve shows the epoch of matter-radiation equality, while the right one shows the epoch of dark energy-matter equality. 4

1.2 Matter power spectrum from redshift 0-4, calculated using `Colossus` software [48]. Note the BAO wiggles visible between $k = 0.01$ and $0.1h/\,\mathrm{Mpc}$. 7

1.3 Dark matter density profile in k space at $z = 0$. Vertical dashed lines correspond to the virial radius for each halo mass. 9

1.4 'Madau Plot' [96] showing the cosmic star formation rate as a function of redshift. Here, ψ represents the cosmic star formation rate density. IR data are shown in shades of red, orange, and brown [130, 150, 97, 98, 66] and UV data are shown in shades of blue, green, magenta, and black [163, 133, 129, 38, 39, 126, 19, 132] 15

1.5 CII luminosity function from Padmanabhan [116], shown in Equation 1.21, and associated observables. 19

1.6 (Modified) Schechter Function corresponding to [CII] at $z = 1$. 21

1.7 Overview of LIM as a technique for tomagraphically mapping the universe. Image provided from the NASA LAMBDA archive. 24

2.1 [CII] intensity parameters corresponding to Equations 2.6 and 2.7. The four panels show the [CII] luminosity function, the HMF, the integrand of the line intensity, and the integrand of the [CII] intensity, and the integrand of the [CII] shot power, respectively. The integrals of the latter two are given by the first and second moments of the luminosity function. 45

2.2 Pictorial representation of central and satellite galaxies. Central galaxy correlations are described by the 2-halo power spectrum $P_{\rm 2h}$ while correlations between satellites are represented by $P_{\rm 1h}$. 48

2.3 [CII] Autopower components using the Padmanabhan [116] model at $z = 1$. 51

2.4 Calculations for the galaxy number density components of Equation 2.27. The top panel shows the eBOSS QSO galaxy HOD, the middle panel shows the HMF, and the bottom panel shows the integrand of the galaxy number density calculation. 59

2.5 [CII] crosspower for based on the Padmanabhan [116] [CII] model and an arbitary galaxy redshift survey, at $z = 1$. 61

3.1 Overdensities over 2 deg. corresponding to the (top) matter, (middle) intensity, and (bottom) galaxy fields, where the latter two include arbitrary levels of Gaussian noise. 68

3.2 Illustration of cosmic variance evasion technique for a single mode in the cross-power spectra given by Equation 3.24 with noise parameters arbitrarily chosen as $(W_I, W_\times, W_g) = (0.01, 0, 0.01)$. The red ellipse shows the case where $r_\times = 0$, i.e. the maps are uncorrelated, resulting in a variance-limited measurement in $[Ib]$. Here, measurements of $Ib/(Ib)_0$ and P_m/P_{m0} are degenerate in P_I, resulting in coupling between errors in the P_m and $[Ib]$. The blue ellipse shows the $r_\times = 1$ case, where we are able to flatten the covariance ellipse in the $Ib/(Ib)_0 - P_m/P_{m0}$ plane, allowing us to marginalize the P_m errors with minimal residual errors. 76

3.3 Power spectra corresponding to the wide survey model in 3.2: (top) intensity mapping auto-power spectrum, (upper middle) cross-power spectrum, (lower middle) galaxy auto-power spectrum, and (bottom) map-space cross-correlation coefficient. 81

3.4 Fractional variance per mode in $[Ib]$. We model errors in the intensity map autocorrelation, and cross-correlation marginalized over $P_{\rm shot}^{\times}$, specified by Equations 3.14 and 3.17, respectively. The instrument design is specified in Section 3.2. 82

3.5 Fractional variance per mode in $[Ib]$ varying the survey area from 10 to 40000 deg^2 (full-sky) at fixed survey time. 83

4.1 EXCLAIM instrument overview. Taken from Switzer et al. [149]. 88

4.2 To-scale diagram of the EXCLAIM spectrometer. Taken from Switzer et al. [149]. 88

4.3 Anticipated EXCLAIM background loading assuming cooled and ambient optics. Taken from Switzer et al. [149]. 90

4.4 EXCLAIM focal plane, describing (left, center) the packaging for the six spectrometers and (right) baffles between the lenslet and lens. Taken from Switzer et al. [149]. 91

4.5 EXCLAIM spectrometer layers. Taken from Switzer et al. [149]. (Drawing is not to scale.) 91

4.6 Demonstration of the various background levels of the EXCLAIM signal, including the space background signal (labeled Background). 92

4.7 Azimuth pointing for various Hyper Suprime-Cam (HSC), BOSS-S82, and HETDEX fields. 94

4.8 EXCLAIM Raster scan. The upper panel shows the angular position and angular velocity of the azimuth, while the bottom panel shows the declination, both as a function of time. 96

4.9 Raster scan image on the sky, after 50 seconds of observation. The top and bottom panels show the same curves, but the bottom plot is zoomed in to reflect the size of the beam relative to the scan coverage. The circles represent the FWHM of the beam. 98

4.10 Stripe-82 coverage with precession due to a center-of-mass offset. The three columns correspond to a sinusoidal throw in azimuth with peak-to-peak amplitudes of $6, 12, 24$ arcmin, from left to right. The bottom row shows the same scan as the top, zoomed in to see the increased pointing modulation associated with the higher-throw cases. 99

4.11 EXCLAIM Key Performance Parameters. Taken from Switzer et al. [149]. 102

5.1 EXCLAIM-tracer auto and cross power spectra with [CII]-quasar on the left and CO(4-3)-galaxy on the right using Stripe 82. The top, middle, and bottom panels show the intensity auto, intensity-tracer cross, and tracer auto-power, respectively. All power spectra are spherically averaged in k-space. The dashed (dotted) curves show the clustering (shot) power spectra, the solid curves show the total power spectra, and the dash-dotted curve shows instrument noise. The quasar power spectrum (bottom left) is dominated by shot noise, while the CO(4-3) auto-power (top right) is dominated by instrument noise. 107

5.2 Number of modes per $k_{||}$, $k_{\perp}$ bin for [CII] at $2.83 < z < 3.16$. Each axis features 20 bins equally spaced logarithmically from $k_{||}h^{-1} = 0.0052\,\mathrm{Mpc}^{-1}$ to $0.62\,\mathrm{Mpc}^{-1}$, and from $k_{\perp}h^{-1} = 0.015\,\mathrm{Mpc}^{-1}$ to $2.00\,\mathrm{Mpc}^{-1}$. White regions contain no modes. 109

5.3 Spherically averaged signal-to-noise per k for [CII] cross-correlated with BOSS-S82, for three redshift bins. The solid, dashed, and dotted curves correspond to including all modes, excluding the lowest nonzero $k_{||}$ mode, and excluding the two lowest nonzero $k_{||}$ modes, respectively, suggesting the effect of foreground removal. 112

5.4 Triangle plots for [CII] forecasts, jointly fitting Ib and $I_{\times\mathrm{shot}}$. 113

5.5 Triangle plots for CO forecasts, jointly fitting Ib and $I_{\times\mathrm{shot}}$. 114

5.6 Forecasts for the modified Padmanabhan [116] [CII] model, comparing Gaussian priors to Gaussian priors with the $P(k)$ analysis. 117

5.7 Comparison between CII (left) and CO (right) models near the EXCLAIM band. The [CII] models are from [62], [137], [167], [122], [116], and [165]; while the CO models are from [123], [89], [122], [115], [87]/[77], and [165]. 118

6.1 Illustration of MKID operation (taken from Day et al. [42]). 121

6.2 Fesponsivities of the quasiparticle-induced quality factor Q_{qp} and the fractional frequency shift x. 127

6.3 S21 curve for six background loads from 2 aW to 200 fW. 129

6.4 Magnitude of the S_{21} curve corresponding to Figure 6.3. 130

6.5 Summary of efficiencies (χ_g, χ_c, χ_a), readpowers (absorbed, feedline), and dip-depth, each as a function of optical load. 131

6.6 Quasiparticle generation efficiency. The blue and orange dotted curves show the optical and readout quasiparticle generation efficiencies, respectively. The solid curve describes the total quasiparticle generation efficiency, while the two dashed curves show the total generation efficiency if the readpower is doubled (upper) or halved (lower). Note that the readout generation efficiency drops at higher optical because χ_a decreases, as is shown in Figure 6.5 135

6.7 Quasiparticle number as a function of optical load. The upper and lower dashed curves represent the cases where the feedline readpower is an order of magnitude above and below that of Table 6.1, respectively. 141

6.8 NEP components for three fixed feedline readpowers: (top) 10 fW, (middle) 100 fW, (bottom) 1000 fW. Note that the rest of the plots in this section correspond to the middle plot, unless specified otherwise. 142

6.9 Top: Photon, generation, TLS, and amplifier NEP per channel for the MKID model specified by Table 6.1 given the background model of Section 4.2, with a fixed feedline readpower. Bottom: total NEP per channel (solid curve) and the effective NEP (dashed horizontal). 148

6.10 From top to bottom: Q_i/Q_c, $\mathrm{NEP_{tot}}/(\mathrm{W/Hz^{1/2}})$, $\mathrm{NEP_{tot}}/(\mathrm{W/Hz^{1/2}})$ (colorbar saturated at 10^{-17} to emphasize behavior at faint loads), $\mathrm{NEP_{gen}}/(\mathrm{W/Hz^{1/2}})$, and $\mathrm{NEP_{amp}}/(\mathrm{W/Hz^{1/2}})$, each as a function of frequency and Q_c, assuming the EXCLAIM background load and the MKID model. 154

6.11 Effective NEP vs. Q_c. Can be thought of as the weighted mean of the total NEP in the second panel of Figure 6.10 over the range of frequencies. 155

7.1 Simulated comparison between the three operational regimes. Left: instantaneous dynamic range, defined as the ratio of the optical power to the total NEP, akin to the signal-to-noise for one second of integration time. Right: magnitude of transmission S_{21} for a selection of incident optical power across the EXCLAIM band. 163

7.2 Simulated NEP curves for three cases: (left) fixed readpower without tone-tracking, (center) fixed readpower with tone-tracking, and (right) optimized readpower with tone-tracking. The shaded orange region represents the range of anticipated incident optical power for the EXCLAIM mission. In the left two plots, the readpower is fixed to minimize NEP at $P_{\mathrm{opt}} = 0.15\,\mathrm{fW}$, whereas the right plot optimizes at all input optical powers. In the left plot, the lack of tone-tracking causes a frequency mismatch, thereby increasing amplifier noise at high input optical power. 164

8.1 EXCLAIM optics overview. The features relevant to this section include the primary and secondary mirrors, folding flat, baffling, and lens. 173

8.2 Gaussian beamwidth as a function of propagation distance from the lenslet through POPPY simulation. The plot starts from the cold stop and lens. 174

8.3 Illumination on the secondary mirror. We consider four different cases corresponding to the inclusion/exclusion of the optics tube (OT) baffles the inclusion/exclusion of the intermediate focus (IF) baffle. *Left*: logarithmic scale with vertical dotted lines corresponding to the effective beam edges 38 cm from the beam center, and the horizontal dotted line corresponding to the −40 dB level. Note that the two "OT included" curves are nearly indistinguishable on this plot. *Right*: linear scale highlighting diffraction effects on the main lobe. Here, the two 'IF included' curves are nearly indistinguishable. 175

8.4 Illumination on the primary mirror. We consider four different cases corresponding to the inclusion/exclusion of the optics tube (OT) baffles the inclusion/exclusion of the intermediate focus (IF) baffle. *Left*: logarithmic scale with vertical dotted lines corresponding to the effective beam edges 38 cm from the beam center, and the horizontal dotted line corresponding to the −40 dB level. Note that the two "OT included" curves are nearly indistinguishable on this plot. *Right*: linear scale highlighting diffraction effects on the main lobe. Here, the two 'IF included' curves are nearly indistinguishable. 175

8.5 Far-field beam. *Left*: Radial cut through the beam center with a linear scale. The three pairs of vertical lines correspond to the three different $\Theta_{\mathrm{FWHM}}^{\mathrm{far-field}}$ cases: (i) (blue) full POPPY simulation (shown); (ii) (orange) estimate based on the primary FWHM $\Theta_{\mathrm{FWHM}}^{\mathrm{primary}}$; (iii) (red) estimate based the primary edge taper T_E(dB) *Right*: Radial cut through the beam center with a log scale. The vertical lines corresponds to Case (i). 176

8.6 Farfield beam based on the fast Fourier transform of the POPPY-modeled beams at the output of the primary mirror. 178

C.1 Conversion from intensity to noise-equivalent intensity 192

C.2 Background-limited NEP for incoherent (solid) and coherent (dotted) receivers over four decades in frequency, roughly spanning the microwave ($\sim 0.3 - 300\,\mathrm{GHz}$) to far-infrared band ($\sim 0.3 - 20\,\mathrm{THz}$). The two top panels represent fixed incident powers per channel $P = 1\,\mathrm{pW}$ and $1\,\mathrm{fW}$, while the bottom three represent fixed intensities $I = 1\,\mathrm{GJy}$, $1\,\mathrm{MJy}$, and $1\,\mathrm{kJy}$. The five curves in each panel correspond to frequency resolution $R = 10^1$ through 10^5. 201

C.3 Background-limited instantaneous dynamic range (P / NEP) for incoherent (solid) and coherent (dotted) receivers over four decades in frequency, roughly spanning the microwave ($\sim 0.3 - 300\,\mathrm{GHz}$) to far-infrared band ($\sim 0.3 - 20\,\mathrm{THz}$). The two top panels represent fixed incident powers per channel $P = 1\,\mathrm{pW}$ and $1\,\mathrm{fW}$, while the bottom three represent fixed intensities $I = 1\,\mathrm{GJy}$, $1\,\mathrm{MJy}$, and $1\,\mathrm{kJy}$. The five curves in each panel correspond to frequency resolution $R = 10^1$ through 10^5. 202

ABSTRACT

Line intensity mapping is a growing technique for obtaining tomographic maps of the universe. Line intensity maps capture the integrated emission of a target spectral line from all galaxies within a voxel, making it an unbiased tracer of galaxy emission and a powerful tool for galaxy evolution studies. Furthermore, line intensity mapping surveys may probe unprecedented volumes of the universe with modest time requirements, allowing for leading sensitivities of cosmological parameters.

In this thesis, I describe modeling efforts for measurements of the intensity mapping signal and for instrumentation developed for the Experiment for Cryogenic Large-aperture Intensity Mapping (EXCLAIM!). EXCLAIM is a pathfinding balloon-borne intensity mapping instrument aiming to map ionized carbon ([CII]) and carbon monoxide (CO) at redshifts $2.5 < z < 3.5$ and $z < 0.64$, respectively. I characterize the key observables in the survey and describe methods for forecasting the performance of the instrument. I apply these forecasting tools to the EXCLAIM survey and to a hypothetical space-based survey, which may be free from the limitations of cosmic variance.

The EXCLAIM detectors and optical systems are also described in detail, and with a parallel focus on system-level requirements. EXCLAIM features nascent superconducting spectrometer and detector technologies, which must be carefully characterized and modeled before the flight. I describe an operational procedure that may be used to optimize the detectors for an evolving signal, providing a critical advantage for EXCLAIM's detectors over competing technologies. Finally, the optical system is modeled and shown to comply with system-level mission goals.

CONTENTS

List of Tables **vi**

List of Figures **viii**

Abstract **xvii**

Contents **xviii**

1 How did we get here? **1**

1.1 Cosmic origins 2

1.2 Techniques and Observatories 22

1.3 Line intensity mapping 24

1.4 A tale of two surveys 28

1.5 How this thesis contributes to the development of line intensity mapping. 33

1.6 Thesis structure and publication overview 37

2 LIM: introduction to line intensity mapping **41**

2.1 Tracing the matter overdensity 42

2.2 Cross-correlation with a galaxy redshift survey 56

2.3 Instrument effects 62

3 LIM science: forecasts & cosmic variance evasion **65**

3.1 Dimensionless noise parameters and cosmic variance evasion 66

3.2 Designing an intensity mapping survey without cosmic variance . . . 78

3.3 Conclusion 84

4 EXCLAIM: mission overview and systems analysis **86**

4.1 Introduction to EXCLAIM 87
4.2 Background signal 90
4.3 Survey strategy 93
4.4 System constraints and Key Performance Parameters 100

5 EXCLAIM science: LIM forecasts 104
5.1 Instrument and survey models 105
5.2 Mode-counting 108
5.3 Covariance forecasts 109
5.4 Science interpretation 115

6 EXCLAIM detectors: MKID model 119
6.1 MKIDs: illustrative toy model 120
6.2 From quasiparticles to resonances 124
6.3 Quasiparticle model 134
6.4 MKID noise model 140
6.5 MKID model: numerical implementation and laboratory testing . . . 146
6.6 The impact of the MKID model on the EXCLAIM detector array . . 149

7 EXCLAIM detectors: operational optimization to maximize dynamic range in EXCLAIM microwave kinetic inductance detectors 156
7.1 Introduction 157
7.2 MKID sensitivity to a widely-varying background 159
7.3 Readout tone-tracking and readpower optimization 163
7.4 Discussion 167

8 EXCLAIM optics: modeling 169
8.1 EXCLAIM optical design 170

8.2 EXCLAIM Gaussian beam analysis 173

9 Conclusion and the future of intensity mapping 179

A 1-halo power spectrum 182

A.1 1-halo power spectrum limits - derivation 183

B Gaussian error estimation in cosmology 186

B.1 Gaussian error estimation 187

C EXCLAIM detectors: relating sky intensity to detector power for coherent and direct detectors 191

C.1 The sensitivities of coherent and incoherent detectors 193

D Optics: diffraction analysis 203

D.1 Optical modeling 204

Bibliography 209

1 HOW DID WE GET HERE?

This introductory chapter provides a background on large-scale structure cosmology and galaxy evolution. I provide an incomplete, quantitative introduction to both fields, focusing on areas relevant to line intensity mapping (LIM). I then provide a qualitative introduction to LIM and a discussion on the Tianlai Pathfinder Dish Array and the Experiment for Cryogenic Large-aperture Intensity Mapping (EXCLAIM!), the two surveys I have contributed to. Finally, I provide a personal account for my contributions to the LIM community and specifically to Tianlai and EXCLAIM, along with a discussion on the organization of the document. Sit back and enjoy the show!

1.1 Cosmic origins

(Mostly) flat, expanding universe

In the past century, cosmology has evolved from a purely theoretical field to a precision physical science. We have found that the Universe had a beginning known as the 'big bang' around 13.8 billion years ago. The universe has since expanded and structures have grown to form stars, galaxies, and galaxy clusters. Yet many questions remain in this historical account of the universe.

The cosmic microwave background provides the earliest observable light in the universe, representing the epoch of last scattering. Prior to this epoch, the matter in the universe formed a dense plasma where light could not travel appreciably without being absorbed by an electron. Over time, however, the universe has expanded and this density has decreased, and today, light can travel for billions of years without interacting with matter. Since the epoch of last scattering, the universe has expanded by a factor of ~ 1100.

As the universe expands, the wavelength of light expands with it. This phenomenon,

known as cosmological redshift, provides a basis for measurement; if we know the initial wavelength of a particular emission line, we can compare it to the measured wavelength and infer the scale of the Universe at the time of emission compared to today. For this reason, the redshift can be directly mapped to the cosmological redshift z as

$$1 + z \equiv \frac{\lambda_{\text{obs}}}{\lambda_{\text{rest}}} = \frac{1}{a}, \tag{1.1}$$

where λ_{obs} and λ_{rest} are the observed and rest-framed wavelength, respectively. a is the scale factor describing the scale of the Universe, where the present day is corresponding to $a = 1$ and $z = 0$.

Objects with a larger redshift, or smaller scale factor, recede from us with a velocity v proportional to the cosmological distance d. Today, this phenomenon is demonstrated by Hubble's Law [73, 139, 95],

$$v = H_0 d, \tag{1.2}$$

where $H_0 = 67.37 \pm 0.54\,\text{km/s/Mpc}$ is the Hubble constant [3].

Generally, the Hubble parameter H relates to the contents of the Universe through (assuming a flat curvature)

$$\frac{\dot{a}}{a} \equiv H(a) = H_0 \sqrt{\Omega_m(a) + \Omega_r(a) + \Omega_\Lambda(a)}, \tag{1.3}$$

where Ω_m, Ω_r, and Ω_Λ are the cosmological densities of matter, radiation, and dark energy, respectively. These densities are defined in relation to the critical density $\rho_{\text{cr}} = 3H_0^2/8\pi G_N$, the density that gives an asymptotically flat universe. Over time, these components evolve as $\Omega(a) = \Omega(a_0)a^{-3(1+w)}$, where $w \equiv P/\rho$ is the equation of

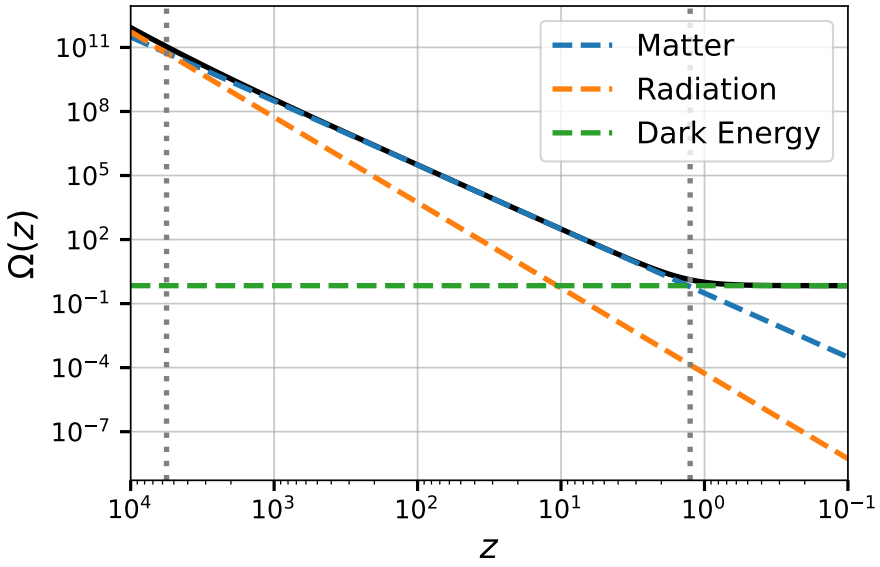

Figure 1.1: Density components vs time. Individual components to Ω are shown in the dashed curves, while the total energy density relative to today is shown in solid black. The left vertical gray curve shows the epoch of matter-radiation equality, while the right one shows the epoch of dark energy-matter equality.

state describing the ratio of the pressure P to the density ρ of a given constituent, assuming a perfect fluid given by a stress-energy tensor $T^{\mu}_{\nu} = \mathrm{diag}(\rho, -P, -P, -P)$, written in natural units. Here, $w = 0, 1/3, -1$ for matter, radiation, and dark energy, respectively. Therefore, $\Omega_m(a) \sim a^{-3}$, $\Omega_r(a) \sim a^{-4}$, and $\Omega_\Lambda(a) \sim 1$. Thus, the radiation density falls the fastest, followed by the matter density, while the dark energy density remains constant.

Figure 1.1 characterizes this expansion history. Initially, the universe was radiation dominated (RD). About 50 kyr after the big bang ($z \sim 3400$), the universe became matter dominated (MD). Finally, from about 9.4 Gyr after the big bang ($z \sim 1.1$) to now, dark energy dominates the universe's energy budget.

The Hubble parameter given by Equation 1.3 is used to calculate the comoving distance (i.e. the distance measure that remains constant as a function of the scale

factor) as

$$d_{\rm co}(z) = c\int_a^1 \frac{dt}{da'}\frac{da'}{a'} = c\int_a^1 \frac{da'}{H(a')a'^2} = c\int_0^z \frac{dz'}{H(z')}. \tag{1.4}$$

The comoving angular diameter diameter and luminosity distances are also useful in cosmological measurements, and are given by [71]

$$d_A(z) = \frac{d_{\rm co}(z)}{1+z} \tag{1.5}$$

$$d_L(z) = (1+z)d_{\rm co}(z). \tag{1.6}$$

Here, the angular diameter and luminosity distances are the comoving distances corresponding to a fixed angle on the sky, and a fixed luminosity, respectively. An angular resolution $\delta\Omega$ and redshift resolution δz, provide a comoving volume element

$$\delta V_{\rm co}(z) = A_\perp \frac{d\chi_{\rm co}}{dz}\delta z = \frac{d_A^2 c}{H(z)}\delta\Omega\delta z, \tag{1.7}$$

where $A_\perp = d_A^2 d\Omega$ and $d\chi_{\rm co}/dz = c/H_0$. Here, I have defined $\chi_{\rm co} \equiv d_{\rm co}$ to reduce confusion with the symbol d in the derivative.

Density fluctuations - deviations from flatness

While the universe is homogeneous and flat to one part in $\sim 10^5$, it features overdense and underdense regions relative to the mean, which were sourced by quantum fluctuations in the primordial universe. The statistical analysis of these fluctuations provides the basis for large-scale structure cosmology. These overdensities can be described in

Fourier space at redshift z through

$$\begin{aligned}\delta(\mathbf{k},z)=\frac{\rho(\mathbf{k},z)-\bar{\rho}(z)}{\bar{\rho}(z)} &= G(z)T(\mathbf{k})\delta(\mathbf{k}=\mathbf{0},z=z_0)\\ &= \int \delta(\mathbf{r},z)e^{i\mathbf{k}\cdot\mathbf{r}}d^3\mathbf{r}. \end{aligned} \tag{1.8}$$

Here, $\delta(\mathbf{k}{=}\mathbf{0}, z = z_0)$ is the overdensity on large scales at a reference redshift z_0. Here, $\rho(\mathbf{k}, z$ is the density of a given Fourier mode $\mathbf{k}$, while $\bar{\rho}(z)$ is the mean density at a redshift z. The growth factor $G(z)$ describes redshift evolution and the matter transfer function $T(\mathbf{k})$ describes the evolution as a function of $\mathbf{k}$.

Statistically, the matter overdensities are described by the matter power spectrum $P(k)$ as

$$\langle\delta(\mathbf{k},z)\delta^*(\mathbf{k'},z)\rangle = (2\pi)^3P(k,z)\delta^3(\mathbf{k}-\mathbf{k'}), \tag{1.9}$$

where the scalar $k = |\mathbf{k}|$ appears in the power spectrum because the power spectrum should be spatially independent in physical space.

Figure 1.2 shows the matter power spectrum from present day ($z = 0$) to $z = 4$. Here, lower k corresponds to large scales, and the leading measurements on the matter power spectrum at very low k is from CMB observation. Smaller scales ($k0.1h$/Mpc) tend to be dominated by shot noise and nonlinear structure within single dark matter halos, making their measurement difficult.

Dark matter

Dark matter comprises the primary component of the matter overdensity δ. As the universe evolves, overdense regions become increasingly dense, eventually collapsing in on themselves. Here, dark matter halos are formed, described by approximately spherical regions of self-gravitating dark matter. Baryonic matter also collapses in

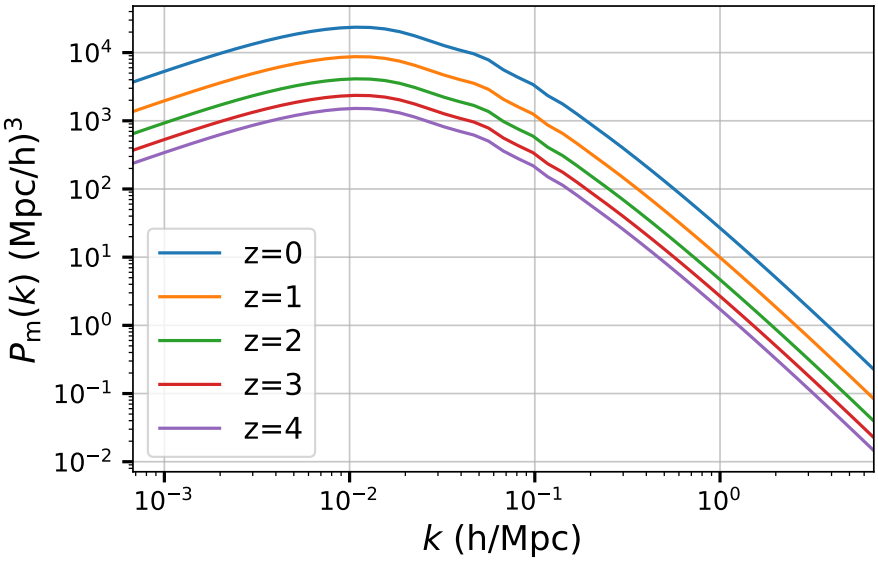

Figure 1.2: Matter power spectrum from redshift 0-4, calculated using `Colossus` software [48]. Note the BAO wiggles visible between $k = 0.01$ and $0.1h/$ Mpc.

this region, causing a dense and hot region at the halo center, providing the seeds for galaxy formation. Much of the subsequent evolution of galaxies is governed by the dynamics and cooling processes of this baryonic matter [105].

We can describe a dark matter halo overdensity δ_h through

$$\delta_h(M, \mathbf{k}, z) = b_h(M, z)\delta(\mathbf{k}, z), \tag{1.10}$$

where M is the dark matter halo mass and b_h is a halo bias, accounting for the fact that the dark matter halo distribution is an imperfect tracer of the matter overdensity.

Cosmological models predict the number density of halos n as a function of halo mass M, as a function of redshift. Here, taking logarithmic mass bins, we have the *halo mass function (HMF)* used to obtain the differential number count of dark matter

halos per mass bin. Here,

$$\frac{dn}{d\log M}(z) = \frac{\rho_M(z)}{M} f_{\rm PS}\left(\frac{\delta_c}{\sigma(M,z)}\right)\left|\frac{d\log\sigma}{d\log M}\right|, \tag{1.11}$$

where .... Here,

$$f_{\rm PS}(x) = \sqrt{\frac{2}{\pi}} x e^{-x^2/2}. \tag{1.12}$$

The halo bias is related to $f_{\rm PS}$ through

$$b_h(M,z) = -\frac{1}{\sigma(M,z)} \frac{d\log f_{\rm PS}(x)}{dx}\bigg|_{x=\delta_c/\sigma(M,z)}. \tag{1.13}$$

On scales much larger than individual halos ($\gtrsim 1Mpc$), the halo power spectrum is well-described by 2-halo statistics, in which halos are treated as point particles. On smaller scales, however, the distribution of matter within individual halos becomes important. These scales are governed by 1-halo statistics.

The spatial distribution of matter within an individual halo is still an active area of study, but the Novarro-Frank-White (NFW) profile [107] is a commonly-used model. Here, the matter density ρ is given as a function of radial distance from the halo center r and halo mass as

$$\rho(r,M,z) = \frac{\rho_0}{(r/r_s)^\alpha\,(1+r/r_s)^\beta}, \tag{1.14}$$

with implided M, z-dependence in ρ_0 and r_s. Here, ρ_0 is a constant of proportionality, and r_s, α, and β are phenomenological factors that may be found through N-body simulations or analytical profiles. Throughout this thesis, I will assume an NFW profile [107] which assumes $\alpha = 1$ and $\beta = 2$, while r_s and ρ_0 are mass- and redshift-dependent, and are provided through COLOSSUS software [48].

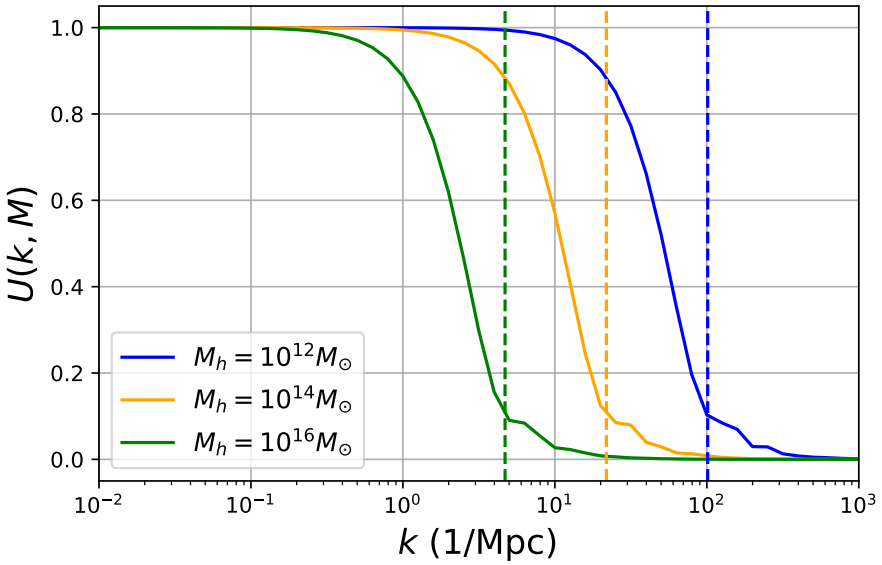

Figure 1.3: Dark matter density profile in k space at $z = 0$. Vertical dashed lines correspond to the virial radius for each halo mass.

The Fourier conjugate to ρ gives the halo profile in u, the Fourier conjugate to $\rho(r)/\rho_0$, as

$$u(\mathbf{k}, M) = \frac{\int \rho(\mathbf{r}, M) e^{i\mathbf{k}\cdot\mathbf{r}} d^3\mathbf{r}}{M}. \tag{1.15}$$

Here, $u \to 1$ on scales larger than the halo, i.e. where $k \ll 1/R_{\rm vir}$.

Equation 1.15 is displayed in Figure 1.3. Here, the integral was truncated at $R_{\rm vir}$, and the Bessel function solution was used to solve the integral. This Bessel function solution is responsible for the 'bumpiness' at high-k in each curve, and is a numerical artifact from finite r resolution. Colossus software [48] was used for the dark matter density profile calculation using a concentration $c = 4$. The vertical curves show the wavenumber corresponding to $R_{\rm vir}$ for each halo mass. Here, $U(k, M) \to 0$ as $k \gg 2\pi/R_{\rm vir}$ and $U(k, M) \to 1$ as $k \ll 2\pi/R_{\rm vir}$.

Open questions in cosmology

Beyond the connection between galaxy astrophysics and large-scale structure cosmology, numerous questions exist in our understanding of cosmology. Some of the most sought-after challenges include inflation, dark energy, and dark matter.

Inflation: Inflation simultaneously solves three open questions in the hot big bang model: the horizon problem, flatness problem, and magnetic monopole problem. The horizon problem states that the universe should not be as homogeneous as it is observed to be, because it would require correlations on distances larger than the causal horizon. The flatness problem arises because the universe's total density is very close to the critical density $\rho_{\rm cr}$; this would seem to require extreme fine-tuning, which is not desirable in a cosmological theory. Finally, the magnetic monopole problem comes from the non-observation of magnetic monopoles in nature, despite the fact that most high energy theories relevant to the very early (pre-recombination) universe predict them in non-negligible densities.

Inflation simultaneously solves all three of these problems, and is a natural consequence of many theories that unify the fundamental forces of nature. Despite the fact that the inflationary era precedes the earliest observable light in the CMB, it features several imprints on large-scale structure. First, inflationary theories predict a tilt in the primordial power spectrum. Here, the power spectrum is related the primordial power spectrum $P_{\rm prim}$ as

$$P(k,z) = G^2(z)T^2(k)P_{\rm prim}(k,z), \tag{1.16}$$

where again $G(z)$ is the growth factor and $T(k)$ is the transfer function. The primordial power spectrum can be characterized by $P_{\rm prim}(k) \sim k^{n_s-1}$, where n_s is known as the scalar index. A scale invariant primordial power spectrum is generically predicted

by general relativity without inflation, where $n_s = 1$. Inflation, however, predicts a small correlation on smaller spatial scales, i.e. $n_s < 1$. The Planck 2018 data release provides the most precise measurement of n_s to date [3] measure $n_s = 0.9665 \pm 0.0038$, providing a hint but not a smoking gun for inflation.

Primordial non-Gaussianity (PNG) would provide a smoking gun signature for inflation. Generally, this characterizes fluctuations that are non-Gaussian in the primordial power spectrum. This can be measured through scale-dependent bias, or through non-Gaussian statistics like the cosmological bispectrum, i.e. the Fourier conjugate to the three-point correlation function[1]. The PNG can be inferred through various non-Gaussian statistical parameters known as $f_{\rm NL}$. A detailed discussion on these parameters is beyond the scope of this thesis, but the relation between $f_{\rm NL}$ and the bias is well summarized in Dalal et al. [40] and its relation with inflationary theories is described in Alvarez et al. [7].

Dark energy: The nature of dark energy presents another mystery in the cosmological standard model. The negative pressure associated with dark energy causes accelerated expansion in the universe, as was discovered in the late 1990s by Riess et al. [127] and Perlmutter et al. [120]. The dark energy equation of state is very nearly $w_{DE} = -1$, consistent with a cosmological constant generally defined as Λ, associated with a vacuum energy.

Currently, there is no generally accepted solution to the mystery of dark energy. One of the chief goals of late-time ($z \lesssim 2$) large-scale structure surveys is to measure deviations from $w_{DE} = 1$. Generally, the goal is to find higher-order terms in a Taylor series expansion of w_{DE} around 1; for example, we may describe $w_{DE}(a) = w_0 + w_a(1-a) = w_0 + w_a z/(1+z)$. However, many other parametrizations exist in the literature, with different assumptions about the dark matter field, as reviewed in

[1] AKA 'triangles in the sky'.

Huterer and Shafer [74].

The primary techniques for measuring the dark energy equation of state are type 1a supernovae (SN1a), baryon acoustic oscillations (BAO), and the CMB. SN1a are used as standard candles; because supernovae feature known luminosities, if we can characterize the observed intensity we can find the distance via the luminosity distance measure 1.6. This can then be used to calculate $H(z)$ and its contribution from dark energy. BAO provide standard rulers, providing a known distance measurement that can again be related to $H(z)$ and therefore w_{DE} and Ω_{DE}. The BAO are relics in the matter power spectrum from acoustic waves in the early-universe matter and radiation fluctuations. The BAO peaks occur on distance scales corresponding to peaks in these oscillations, at the time where a given mode entered the causal horizon. The first, strongest mode occurs at a scale of $d \simeq 140\,\mathrm{Mpc}/h$ or $k \simeq 0.045\,h/\mathrm{Mpc}$, faintly visible in Figure 1.2.

Dark matter: The nature of dark matter is another longstanding mystery in cosmology. To date, dark matter has only been inferred through its gravitational effects on galaxy scales and above, and no direct or indirect particle interactions have been observed. LIM may potentially be used to improve existing large-scale structure inferences of dark matter, or to measure products of dark matter annihilation?.

Existing cosmological measurements can be improved by increasing the number of observable modes, which requires maps of extremely large volumes of the universe. Because LIM can economically measure extremely large volumes with exquisite redshift resolution, it may produce leading measurements of large-scale structure in the coming decades. This would improve measurements of the sum of the neutrino masses, the matter density, the cosmological growth factor, etc.

Bernal et al. [17] showed that the radiative decays of QCD axion-mass dark matter ($\sim 1 - 10\,\mathrm{eV}$) may produce spectral lines that appear in LIM observations as

interloping lines. These signatures would provide insight into the mass of the dark matter particle, based on the frequency of photons produced through the annihilation. Furthermore, ultralight axion (ULA) dark matter may be probed with LIM surveys, as discussed in Bauer et al. [13]. Here, ULAs are light enough to be treated as effectively massless like neutrinos in early-universe thermodynamic analyses, accounting for the potential excess in effective number of particle degrees of freedom in the early universe. Ultralight axions would suppress dark matter halo formation in low-mass halos. Because LIM surveys may trace the faint galaxies that are not detectable individually, it may be responsible for this suppression in halo formation, thereby pointing toward the existence of ULAs.

The interplay between galaxy formation and dark matter can also be inferred through LIM. Here, correlations on small scales will depend on $u(k, M)$ in Equation 1.15, which tends to be damped on scales smaller than $\sim 0.010\,\mathrm{Mpc}$, resulting in a measurement of the so-called *one-halo power spectrum* [160]. This small-scale measurement would effectively measure the line emission as a function of radial distance from the halo center. This may be used to better infer the radial structure of dark matter, as well as the line luminosity as a function of galaxy position due to heating and cooling throughout the galaxy evolution process.

Galaxy formation & evolution

In addition to the cosmological distribution of dark matter, a coherent picture of galaxy evolution and cosmic star formation history is emerging following decades of observation. The cosmic web of dark matter provides the seed for galaxy formation; dense regions of dark matter collapse into self-gravitating halos, trapping baryonic gas. This infalling gas undergoes shocks, resulting in significant heating. Eventually, the

gas cools enough for molecular clouds to form, where dense regions of cold molecular gas collapse and produce stars and planetary systems. Meanwhile, a supermassive black hole forms in the center of galaxies, actively heating the star-forming gas within the host galaxy. The large-scale distribution of galaxies is dictated by the clustering of dark matter, setting the environment for galaxy formation and forming a key connection between luminous and dark matter.

There are numerous holes in understanding this picture of galaxy formation and evolution. The interplay between dark and luminous matter remains mysterious even in local galaxies, owing to the complex dynamics of stars and interstellar gas and our inability to observe the structure of dark matter halos directly. Furthermore, the efficiency of star formation from cold, star-forming gas (H_2) is much lower than we would naively expect, as evidenced by smaller-than-expected ratios of stellar mass to halo mass [15, 56]. Compounding this mystery, the cosmic star formation rate has decreased by a factor of ~ 20 since $z \sim 2$ (10 Gya), despite the continued growth of structure, in a paradigm known as the 'cosmic noon' [159]. This paradigm is shown in the famous 'Madau Plot' [96] displayed in Figure 1.4.

Luminosity functions

Various feedback mechanisms may explain the suppression of star formation, including heating and winds from active galactic nuclei (AGN) and heating from star formation (SF) itself [136]. The interplay between these dynamics remains poorly understood, owing to the immense challenge of modeling all relevant scales, spanning 10-pc scales associated with star-forming molecular clouds to Mpc-scales associated with the galaxy cluster environment [142]. To resolve these monumental challenges, we must employ increasingly sensitive measurements, analytic modeling, and computational modeling

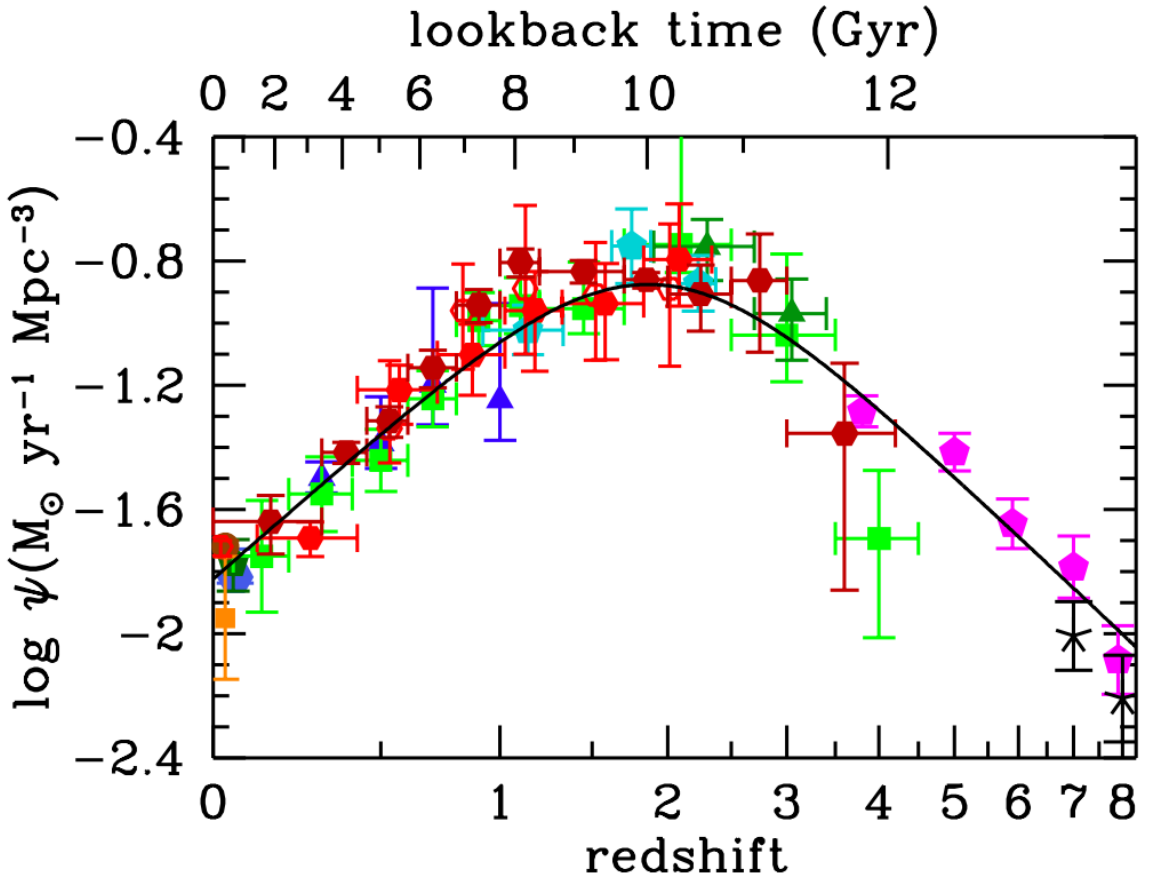

Figure 1.4: 'Madau Plot' [96] showing the cosmic star formation rate as a function of redshift. Here, ψ represents the cosmic star formation rate density. IR data are shown in shades of red, orange, and brown [130, 150, 97, 98, 66] and UV data are shown in shades of blue, green, magenta, and black [163, 133, 129, 38, 39, 126, 19, 132]

spanning this huge range of scales.

The cosmic star formation rate can be inferred through infrared and ultraviolet *luminosity functions*, defined as the differential number density of galaxies n per luminosity L, represented by $\Phi(L) \equiv dn/dL$. These luminosity functions can pertain to specific lines (e.g. ionized carbon or carbon monoxide lines), or bolometric frequency bands (e.g. $L_{\rm IR}$, defined as the luminosity integral over wavelengths from $8-1000\,\mu m$). The *Schechter function* is a commonly-used model for bolometric and line luminosity functions alike, and is given by

$$\Phi(L) \equiv \frac{dn}{dL} = \frac{\Phi_*}{L_*}\left(\frac{L}{L_*}\right)^{\alpha} e^{-L/L_*}. \tag{1.17}$$

Here, Φ_* is a uniform scaling factor, α is the faint-end slope, and L_* is the luminosity knee, above which $\Phi(L)$ is suppressed. The luminosity function can be used to infer a number of quantities including the average galaxy number density $\langle n \rangle$, mean luminosity $\langle L \rangle$, and mean squared-luminosity $\langle L^2 \rangle$ [105]:

$$\langle n \rangle_L = \int \Phi(L) dL = \Phi_* \Gamma(\alpha + 1) \tag{1.18}$$

$$\langle L \rangle_L = \int L\Phi(L) dL = \Phi_* L_* \Gamma(\alpha + 2) \tag{1.19}$$

$$\langle L^2 \rangle_L = \int L^2\Phi(L) dL = \Phi_* L_*^2 \Gamma(\alpha + 3). \tag{1.20}$$

Here, Γ is the Gamma function. While these convenient forms are valuable for obtaining intuition for the effects of various luminosity functions, the Schechter function is generally an imperfect representation of galaxy data.

When connecting to large-scale structure, it is also useful to represent the luminosity function as a function of halo mass. Here, we define a *mass-luminosity function*, with an example form corresponding to Equation 1.17,

$$L(M) = A(z)\left(\frac{M}{N_1}\right)^{\beta} e^{-N_1/M}, \tag{1.21}$$

where again M is the halo mass. This general form was used in Pullen et al. [125], reparametrized from Padmanabhan [116]. The halo model approach is used, where the distribution of galaxy luminosities is assumed to depend on the distribution of halos. Here, a population of halos is assumed from cosmology, and each halo features a characteristic luminosity[2] is included. Local ($z = 0$) measurements are extrapolated

[2]In precise models, scatter between M and L, and a duty cycle defining the fraction of halos

to the high-redshift [CII] measurement of Pullen et al. [124], assuming the luminosity function scales as a power of the cosmic star formation rate density. Here,

$$A(z) = \left(\frac{N_1}{M_1}\right)^{\beta} \mathrm{SFR}^{\alpha}, \tag{1.22}$$

with

$$\begin{aligned} M_1 &= (2.39 \pm 1.86) \times 10^{-5} \\ N_1 &= (4.19 \pm 3.27) \times 10^{11} \\ \alpha &= 1.79 \pm 0.30 \\ \beta &= 0.49 \pm 0.38 \\ \mathrm{SFR} &= \frac{(1+z)^{2.7}}{1 + [(1+z)/2.9]^{5.6}}. \end{aligned}$$

Here, the halo mass-weighted quantities corresponding to Equations 1.18, 1.19,1.20 are given by[34].

that feature line-emitting gas are included, as discussed in the next chapter.

[3]The halo mass approach can be connected to the luminosity function approach through a *conditional luminosity function* (CLF) $\phi(L|M)$ in, e.g., Schaan and White [131]. In the case of a single line, as I assume throughout this thesis, $dM \rightarrow \phi(L|M)dL$. In the case where multiple lines are present, a multi-line CLF can relate a single halo mass to multiple luminosities as $\phi(L_1, ..., L_n|M)dL_1...dL_n$ for n different lines. This is well beyond the scope of this thesis, but may be relevant in the future generations of surveys that will precisely map multiple lines and/or spectral line energy distributions.

[4]Beyond this simplified form, Yang et al. [165] use a semi-analytic model to show that a halo mass-dependent duty cycle factor $f_{\mathrm{duty}}(M)$, which suppresses galaxy/star formation in high-mass halos, is necessary to obtain the correct integrated quantities for far-infrared line luminosities. They fit f_{duty} to a power law that suppresses the line luminosity in high-mass halos for $z < 4$. We can implement f_{duty} into my calculations by replacing $dM \rightarrow f_{\mathrm{duty}}(M)dM$ in Equations 1.23, 1.24, and 1.25.

$$\langle n \rangle_M = \int \frac{dn}{dM} dM \tag{1.23}$$

$$\langle L \rangle_M = \int L(M) \frac{dn}{dM} dM \tag{1.24}$$

$$\langle L^2 \rangle_M = \int L^2(M) \frac{dn}{dM} dM. \tag{1.25}$$

Figure 1.5 shows Equation 1.21 and the integrands of Equations 1.23-1.25. While each individual measurement does not provide strong model constraining power on $L(M)$[5] without the use of prior information, the the joint measurements of at least two of these quantities will provide much stronger constraints.

Relation to the star formation rate

There are various ways to connect the luminosity function to the cosmic star formation rate $\rho_*(z)$ (Note the different notation compared to Figure 1.4.). The 'Kennicut relation' [79] relates the infrared luminosity function to the star formation rate density as

$$\rho_*(z) = \delta_{\rm MF} \times 10^{-10} L_{\rm IR}, \tag{1.26}$$

where generally $0.8 \lesssim \delta_{\rm MF} \lesssim 2.0$ [87] and is generally on the order of 1.

The infrared luminosity function is often related to infrared intensities through a power law. For example, Spinoglio et al. [143] use the form,

$$\begin{aligned} \log L_{\rm line} &= (A + \sigma_A) \log L_{\rm IR} - (B + \sigma_B) \\ &= (A + \sigma_A) (\log \rho_* - \log \delta_{\rm MF} + 10) - (B + \sigma_B), \end{aligned} \tag{1.27}$$

[5]Generally, $L(M)$ is not as well-constrained as dn/dM, which features constraints from simulation and measurement. Thus, in this thesis I will errors in these quantities are completely dominated by those of $L(M)$.

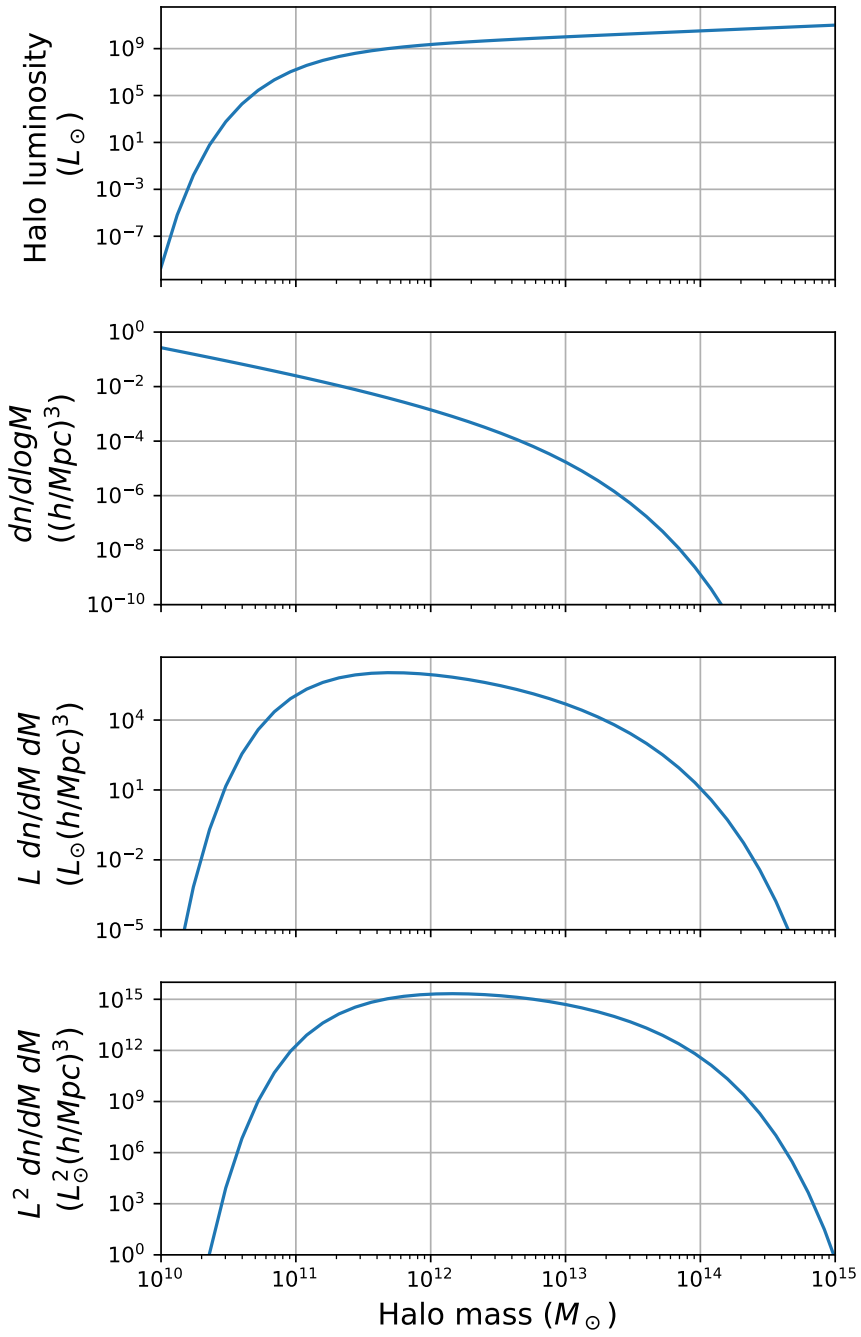

Figure 1.5: CII luminosity function from Padmanabhan [116], shown in Equation 1.21, and associated observables.

where all the logs are base-10. In the second line, we assume Equation 1.26 holds, relating $L_{\rm IR}$ to ρ_*.

If we assume a Schechter function for the bolometric infrared luminosity function and the form of the first line in Equation 1.27 for the [CII] luminosity, we find that

$$\left.\frac{dn}{dL}\right|_{\rm CII} = B\Phi_* \left(\frac{L_{\rm CII}^B}{A^B L_*^{\rm IR}}\right)^{\alpha+1} \exp\left[-\frac{L_{\rm CII}^B}{A^B L_*^{\rm IR}}\right], \tag{1.28}$$

taking a similar form to Equation 1.17, where

$$\begin{aligned} \Phi_* &\rightarrow \Phi_* B L_*^{\rm IR} \\ \alpha &\rightarrow \alpha + 1 \\ \frac{L}{L_*} &\rightarrow \frac{L_{\rm CII}^B}{L_*^{\rm IR} A^B}, \end{aligned} \tag{1.29}$$

with all the parameters except $L_{\rm CII}$ corresponding to the infrared luminosity function. Equation 1.29 does not exactly follow a Schechter function form because of the power law factor $L_{\rm CII}^B$ in the exponential. Note the residual dimension of luminosity in L_* in the replacement for Φ_*. This comes from the assumption that luminosities are given in specific units in Equation 1.27, and Φ_* should have the dimension of inverse volume.

Figure 1.6 shows a CII luminosity function model calculated using a (modified) Schechter function, related to [CII] luminosities through Equation 1.27.

I find that

$$\langle n_{\rm CII}\rangle_L = \Phi_* L_*^2 A^{2B} \Gamma(\alpha+4) \tag{1.30}$$

$$\langle L_{\rm CII}\rangle_L = \Phi_* L_*^{2-B} A^{B(2-B)} \Gamma(\alpha+4-B) \tag{1.31}$$

$$\langle L_{\rm CII}^2\rangle_L = \Phi_* L_*^{2-2B} A^{B(2-2B)} \Gamma(\alpha+4-2B). \tag{1.32}$$

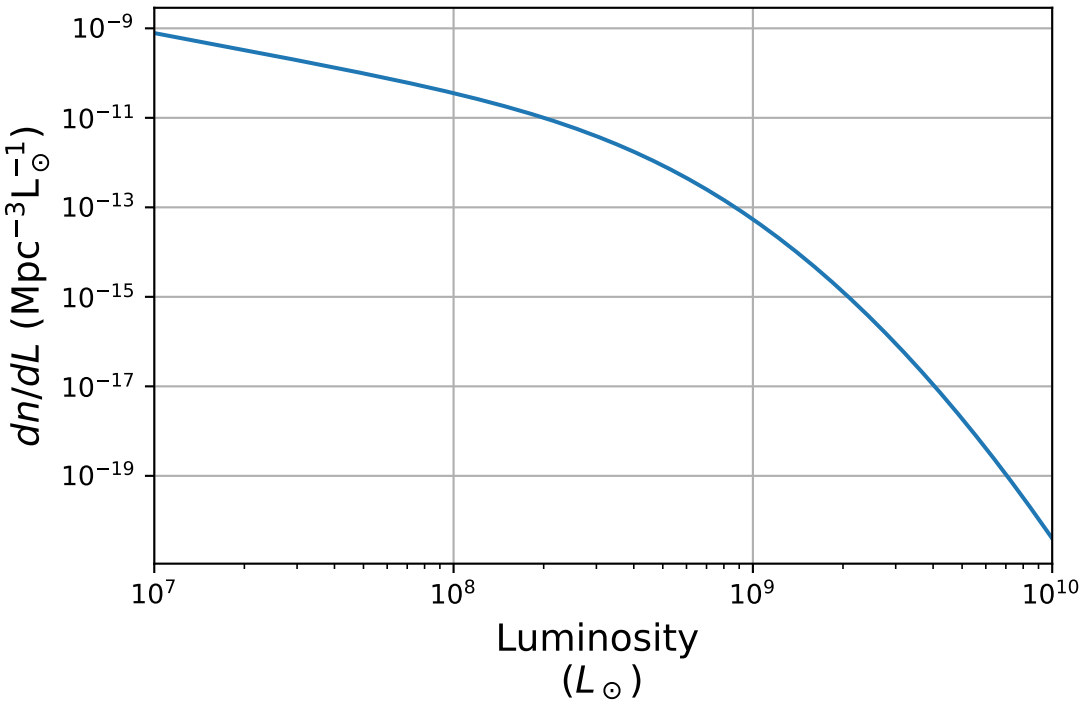

Figure 1.6: (Modified) Schechter Function corresponding to [CII] at $z = 1$.

I stress that many models exist for the [CII] lumininosity, infrared luminosity, and star formation rate. The calculations here should therefore be taken with a grain of salt for intuitive and pedagogical purposes, as the parametric dependencies and scaling factors of [CII] luminosity models vary drastically, resulting in orders of magnitude of variation between model predictions for the intensities of CII and other lines. One of the chief goals of the techniques described in this thesis is to refine this space of models by obtaining initial detections of line intensities over a wide range of redshift.

While the star formation rate is one of the main physical parameters related to the luminosity function, other properties like metallicity and AGN fraction can be inferred through the luminosity functions of [CII] and other lines. Much of this remains theoretical, however, as line luminosity functions are generally still poorly constrained. As measurements and models grow more sophisticated, we will gain

a better understanding of what physical processes can be probed through the line luminosity functions and their relation to galaxy evolution and the star formation history.

1.2 Techniques and Observatories

Most surveys of galaxy evolution and late-time cosmology[6] involve cataloging individual galaxies, in what I will refer to as *direct-detection surveys*. Here, the positions and redshifts of upwards of millions of galaxies are catalogued and used to determine statistics pertaining to galaxy evolution and large-scale structure cosmology.

In this thesis, I specifically focus on galaxy luminosity functions. In traditional direct-detection surveys, these luminosity functions are obtained by plotting the flux as a function of wavelength in many galaxies. A histogram of these galaxy luminosities (inferred from the flux) may be used to infer the luminosity, e.g. by inferring $\Phi(L)\delta L = N_g(L)/V_{\rm surv}$, where δL is the luminosity bin width, $N_g(L)$ is the number of galaxies observed in the bin, and $V_{\rm surv}$ is the survey volume. This may then be used to infer the parameters in e.g. the Schechter Function shown in Equation 1.17.

However, there are many limitations to this direct-detection method [7]. The detection of faint galaxies is limited by instrument noise and source confusion. Instrument noise may be ameliorated by increasing the integration time per pixel, though this limits the number of observable galaxies and the survey volume. Source confusion occurs when galaxies fainter than the detection threshold contribute Poisson noise

[6] Here I define late-time as post-reionization, or $z \lesssim 6$.

[7] Throughout, I will assume a blind survey. Here, the entire survey region is sampled with a constant time per pixel. On the other hand, targeted surveys require less time, because specific galaxies with known locations are sampled. However, targeted surveys are inherently biased by whatever catalog is being used to target galaxies, and may particularly miss out on the faint population.

to the survey, and is particularly problematic for instruments with low spatial and frequency resolution. The number of bright galaxies, which tend to be rarer than faint ones, is limited by survey volume.

The next generations of infrared space telescopes will be gamechanging in their ability to obtain galaxy luminosity statistics. They will be nearly background-limited owing to advances in detector technology, allowing them to sample the faint population with unprecedented efficiency. Furthermore, they will be equipped with state-of-the-art spectrometers, allowing for unprecedented frequency precision. These technological advancements are being developed for e.g. the Probe Far-Infrared Mission for Astrophysics (PRIMA) [58], Far-Infrared Spectroscopy Space Telescope (FIRSST) [34], and the Space Infrared Interferometric Telescope (SPIRIT) [85].

Direct-detection surveys are also used for large-scale structure measurement. Here, the positions and redshifts of millions to billions of galaxies are catalogued, and their positions are used to infer the matter power spectrum. Current imaging technology allows precise angular position measurements, while redshifts are less precisely known; in photometric surveys, redshift errors can be upwards of $\Delta z = 0.1$, while spectroscopic errors tend to be orders of magnitude smaller. However, spectroscopy is costly in observational time and computational resources, limiting the obtainable volume and number of galaxies in the survey. Furthermore, these galaxies cannot be observed prior to the reionization era [8]. Generally, photometric surveys can measure larger volumes and numbers of galaxies compared to spectroscopic ones, at the cost of redshift precision.

Some leading contemporary and recent surveys include SDSS [166], DES [1], KiDS [44], BOSS [41], and Hyper Suprime-Cam [5], while the coming generation includes

[8] and very few during the reionization era; if we're lucky, the James Webb Space Telescope will find some!

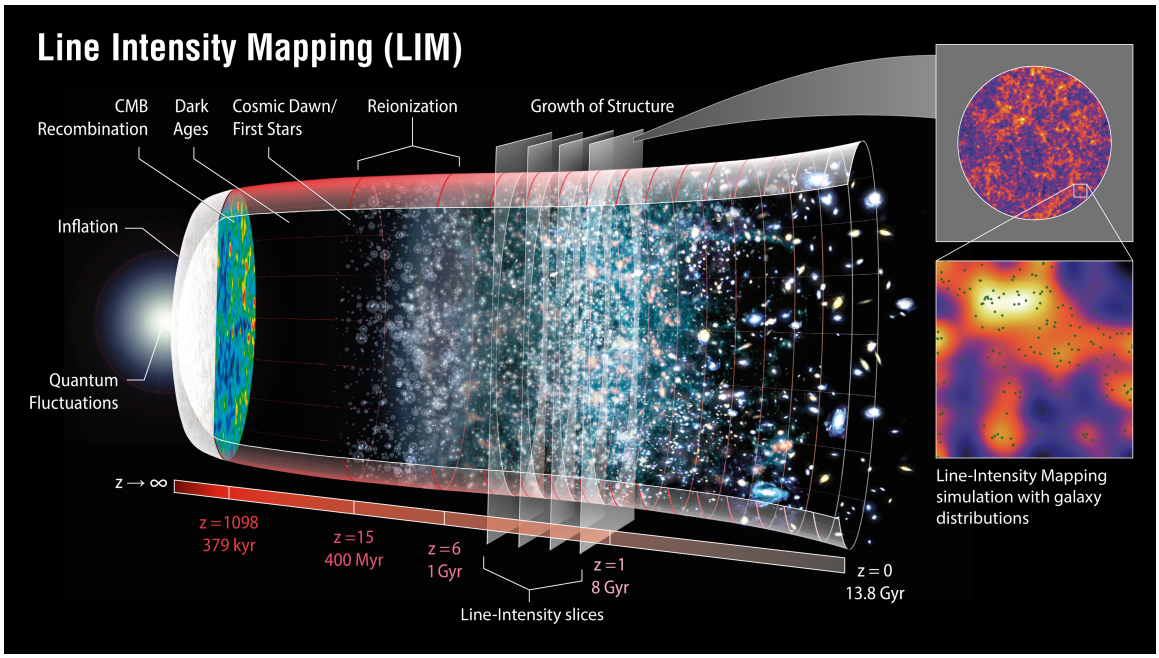

Figure 1.7: Overview of LIM as a technique for tomagraphically mapping the universe. Image provided from the NASA LAMBDA archive.

DESI [32], Rubin/LSST [155], and the Roman Space Telescope (formerly WFIRST) [65]. Decades in the future, various ambitious surveys are being proposed including MEGAMAPPER [134].

1.3 Line intensity mapping

Line intensity mapping is an emerging technique in large-scale structure cosmology and the physics of galaxy evolution. A line intensity map traces the cumulative emission of a given emission line from all galaxies in a target region. The target galaxies trace the matter overdensity, allowing for an unambiguous inference of the large-scale structure of dark matter. The target intensity (or rather, its overdensity) is therefore a biased tracer of the matter overdensity, with a multiplicative bias proportional to the mean intensity of the target line. Furthermore, by comparing the observed frequency to

the rest-frame frequency of the target line, we are able to obtain precise redshift information through the relation $z = \nu_{\rm rest}/\nu_{\rm obs} - 1$. This allows for high precision in the redshift of sample galaxies, while also determining the mean intensity from all galaxies emitting at the observed redshift. By providing tomographic data cubes, line intensity maps are a treasure trove for cosmological and astrophysical studies.

From a cosmological context, intensity mapping surveys may access much of the same information as traditional galaxy redshift surveys such as SDSS [166], DES [1], BOSS [41], etc. This information includes structure growth through the measurement of large-scale redshift-space distortions and the power spectrum itself. Intensity mapping surveys may also be used to measure baryon acoustic oscillations, allowing for inference of the dark energy equation of state and cosmological parameters. Furthermore, they may also be used to measure primordial non-Gaussianity, the sum of the neutrino masses, and even dark matter interactions.

Intensity mapping surveys are sensitive to the bulk gas content in a given line, including gas outside of galaxies. This property enables a truly novel capability: using HI, we can probe the early stages of the cosmic dawn and even into the cosmic dark ages. This would allow us to measure large-scale structure over the entire history of the observable universe. This would enable the most precise measurements of cosmological parameters possible with large-scale structure surveys.

Intensity mapping surveys may also be used to unlock mysteries of galaxy formation and evolution, as well as the mean star formation history. Target emission lines, such as neutral hydrogen (HI), singly-ionized carbon ([CII]), and carbon monoxide lines (CO) trace different properties of galaxies. HI and [CII] trace the signatures of star formation, and the latter is an effective proxy for the total infrared galaxy luminosities. Furthermore, the lower transition levels of CO trace cold gas, the fuel for star formation [18]. Numerous other lines trace other galaxy properties including metallicity and

AGN content.

Direct detection techniques for measuring target emission lines, which involve measuring spectra of individually-resolved galaxies, are subject to selection effects including confusion and instrument noise. Confusion occurs when undetected galaxies introduce noise to the signal, particularly affecting telescopes with small aperture sizes or poor frequency resolution. Instrument noise prevents astronomers from detecting galaxies much fainter than the levels of signal fluctuations in the instrument without unlimited integration time per pixel. Furthermore, time-intensive spectroscopy limits many surveys to smaller volumes, therefore undersampling the rarer, brighter objects. As a result, direct-detection surveys only detect a subset of the total galaxy population. More nefariously, this may lead to biases in the inference of properties of galaxy evolution. This includes, for example, a bias of measurable bright high-redshift galaxies ($z \gtrsim 2$) toward toward those hosting an AGN.

Intensity mapping may complement these studies by performing a measurement of the mean line intensity at a given redshift. Here, the large-scale clustering power spectrum is proportional to the first moment of the luminosity function $\langle L \rangle$, whereas the shot noise power spectrum is proportional to the second moment $\langle L^2 \rangle$. I stress that both of these statistics include the entire galaxy population, including the faint-end not detected by direct-detection surveys. These first- and second-moment statistics complement direct-detection surveys by sampling the entire population, and featuring unique parameter degeneracies in the line luminosity function.

A number of challenges remain in our ability to construct intensity maps. Light from the solar system and the Milky Way provide a bright foreground signal, which may be many orders of magnitude larger than the target intensity. Fortunately, however, most of these foreground signals vary smoothly with frequency, while the target intensity varies sharply due to matter fluctuations along the line of sight. Given

sufficient stability of the instrument passband response and knowledge of the telescope beam, the smooth modes can be effectively removed from the map, negating nearly the entire foreground population. Another challenge is contamination from interloping lines, though this may be more straightforwardly addressed through appropriate masking, modeling, or cross-correlation studies.

Line intensity mapping is a young, but rapidly-growing field. The first HI intensity mapping measurements were obtained through cross-correlations between radio telescopes and existing galaxy redshift surveys [28, 100, 147, 10, 161]. Following these measurements, the global HI intensity mapping signal during the EoR has tentatively been measured by [20]. Astrophysicists quickly began similar studies with other lines, and preliminary detections and constraints have been made for [CII] [124, 164, 9], CO [77, 78], and Lyα [37]. These first-generation detections have inspired confidence in our ability to overcome challenging systematics, while also providing novel information constraining galaxy evolution models.

Numerous instruments are being built with the goal of line intensity mapping. Table 1.1 summarizes many of these surveys. Here, most instruments are ground-based. HI experiments, which aim to probe the BAO at low redshift and EoR at high redshift, are typically designed as ground-based interferometer arrays, which I elaborate on in the following section. Other lines, including CO, [CII], and others, are typically probed through incoherent techniques which do not conserve phase information in the optical signal.[9] These lines probe a variety of scientific targets, typically focused on galaxy evolution. Some of these instruments are suborbital and space-based, as atmospheric noise provides a strong background signal at the relevant sub-millimeter wavelengths.

[9]See C.1 for details and context on coherent and incoherent detection techniques.

Name	Line(s)	Redshift	Type
COPSS	CO	$2.3 < z < 3.3$	Ground (dish array)
COMAP	CO	$2.4 < z < 3.4$	Ground (dish array)
CONCERTO	[CII]	$0.3 < z < 2.0$	Ground (single dish)
		$4 < z < 9$	
EXCLAIM	[CII]	$2.5 < z < 3.5$	Suborbital
	CO	$z < 0.6$	
mmIME	CO	$2 < z < 6$	Ground (dish array)
SPHEREx	Hα, Hβ, [OIII]	$0.5 < z < 5.$	Space
	Lyα	$6 < z < 10$	
SPT-SLIM	CO	$1. < z < 3.$	Ground (single-dish)
SuperSPEC	[CII]	$5 < z < 9$	Ground (single-dish)
TIM	[NII]	$0.5 < z < 1.7$	Suborbital
	[CII]	$5 < z < 9$	
TIME	CO	$0.5 < z < 2.0$	Ground (single-dish)
BINGO	HI	$0.13 < z < 0.45$	Ground (single-dish)
CHIME/CHORD	HI	$0 < z < 3.6$	Ground (interferometer)
HIRAX	HI	$0.775 < z < 2.55$	Ground (interferometer)
SKA	HI	$0 < z < 6$	Ground (dish array)
Tianlai	HI	$z < 2.55$	Ground (interferometer)
HERA	HI	$6 < z < 13$	Ground (interferometer)
MWA	HI	$4 < z < 20$	Ground (interferometer)

Table 1.1: Incomplete summary of LIM experiments.

1.4 A tale of two surveys

Here I provide an overview of two pathfinding intensity mapping surveys: the Tianlai Pathfinder Dish Array and the EXperiment for Cryogenic Large-aperture Intensity Mapping (EXCLAIM!). Tianlai is a first-generation dedicated HI intensity mapping instrument in the form of a ground-based radio interferometer. EXCLAIM is another first-generation instrument, based on a balloon-borne cryogenic telescope targeting far-infrared lines. Both present significantly different instrument designs, and feature many commonalities and differences.

Overall, the scientific signal and analytical techniques are similar between the radio and far-infrared regimes. Both feature large-scale maps of intensity overdensities,

which may be studied in cross-correlation with galaxy redshift surveys. Both have the goal of 'initial detection'. However, instrumentation strongly diverges between the two experiments. The coherent radio technology related to Tianlai is largely understood scientifically, whereas EXCLAIM features nascent spectrometer-detector technologies that are still actively researched. On the other hand, instrument calibration and characterization are challenges for Tianlai, owing to the presence of foregrounds much larger than the scientific signal. On the other hand, the far-infrared foregrounds associated with EXCLAIM are comparatively week, and can be removed from the signal with minimal loss of information.

The Tianlai Pathfinder Dish Array

The Tianlai Pathfinder Dish Array is one of three similar prototype late-time 21 cm (HI) intensity mapping interferometer arrays, with the others being CHIME [11] and HIRAX [108]. Generally, the goal of these experiments is to infer the dark energy equation of state by measuring BAO as a function of redshift. At higher redshifts, MWA [152] and HERA [45] are targeting the epoch of reionization (EoR) around $z \sim 6$. At present, our best understanding of the EoR signal is from the Gunn-Peterson Effect [67], in which high-redshift quasar signals are suppressed by Lyman-alpha (Lyα) absorption in the intervening HI, thereby measuring the redshift bound where the intergalactic medium (IGM) was ionized, i.e. the redshift of reioniation. By 21 cm intensity mapping may provide similar tomograph maps, without requiring the measurement of a high-redshift quasar. At even higher redshifts, 21 cm intensity mapping may be used to map the 'dark ages' between the recombination epoch and the EoR. This would not only provide a direct tracer of the ionization state of the universe over nearly its entire history, but also an unprecedented number of cosmological modes

for unprecedented levels of precision in large-scale structure cosmology.

Each of the existing 21 cm intensity mapping arrays operates by drift scanning, where cylinder telescopes (CHIME and the Tianlai Pathfinder Cylinder Array) and dish arrays (HIRAX, MWA, HERA, and the Tianlai Pathfinder Dish Array) remain stationary over times ranging from days to months. Dish arrays are pointable, so they may measure large portions of the sky by measuring one 'stripe' over at least a day, and re-pointing to different altitudes roughly every couple of days.

These 21 cm interferometer arrays all operate based on similar technological platforms. Each single feed antenna receives a coherent heterodyne signal; here, the signal in the feed is mixed with a local oscillator signal for a frequency downconversion, then amplified by a low-noise amplifier. The signals from every pair of feeds (generally, there are two feeds per antenna, one per polarization) are multiplied together and integrated in a correlator. Here, each sky pointing $\hat{s}$ contributes to the multiplied signal includes a phase delay factor $\exp\left(2\pi\mathbf{d}\cdot\hat{s}/\lambda\right)$, where λ is the observed wavelength and $\mathbf{d}$ is the displacement between the two antennas known as the *baseline* vector. The output is known as a 'visibility' for each baseline, and is roughly equivalent to the Fourier transform of the signal on the sky. This is the basis for interferometry, which presents dual advantages over single-dish antennas: many unique and redundant visibilities[10], and the spatial resolution is set by the maximum baseline length, i.e. the length between the furthest dishes. Thus, two small dishes located 100 apart has the same angular resolution as a single 100 m dish.

All of these 21 cm interferometer arrays are faced with a similar challenge: the intensity mapping signal is ~ 5 orders of magnitude fainter than galactic synchrotron and point source foregrounds. However, these foregrounds are spectrally smooth

[10]For N feeds, there $N(N-1)/2+N$ visibilities; N autocorrelations and $N(N-1)/2$ cross-correlations.

compared to the intensity mapping signal. Thus, the bulk of the foreground signal is expected to be in the lowest Fourier modes along the line of sight ($k_{||}$), so these modes may be filtered or removed without drastic loss to the 21 cm signal. Interferometers present an additional challenge to this problem: higher Fourier modes perpendicular to the line of sight ($k_{\perp}$) mix with the foreground signal, resulting in a 'foreground wedge' on a two-dimensional plot in k-space [90]. As a result, the bulk of the measurable cosmological signal is present in the lower-$k_{\perp}$ and higher $k_{||}$ modes, in what is known as the 'EoR window'[11] [91, 92]. To minimize this effect, it is necessary to have exquisite passband stability in the frequency direction, and precise knowledge of the beam pattern. Analytical methods are still being developed to combat these challenges.

At the time of this writing, the Tianlai Pathfinder Dish Array is analyzing first-light data on known galactic signals, including the Cygnus A and Cassiopeia A objects, to calibrate and understand the instrument. Wu et al. [162] summarizes these first-light data, including beam calibration and noise stability analyses I contributed to, and further described in Oxholm [111].

Each of these 21 cm instruments is a pathfinder, targeting the initial detection of the intensity mapping signal, while also providing an experimental testbed. These initial detections are analogous to the CMB: the first detection was of the global signal [118], while it took three decades to construct maps [53]. The first generations of 21 cm intensity mappers, including late-universe and EoR pathfinders, are targeting initial detections of the signal, while the coming generations of 21 cm experiements will be necessary to build precise maps. For example, the PUMA experiment [140] is an ambitious proposed array that may measure into the dark ages, providing leading measurements of $f_{\rm NL}$, the dark energy equation of state, and astronomical transients.

[11] The name is historical, based on the fact that it was first studied in the context of MWA studying the EoR. The same effect is present in the late-time experiments that are not targeting reionization.

EXCLAIM!

The Experiment for Cryogenic Large-aperture Intensity Mapping (EXCLAIM!) is a pathfinding instrument targeting CO at low-redshift ($z < 0.6$) and [CII] from $2.5 < z < 3.5$. EXCLAIM is based on a suborbital balloon to reduce atmospheric background radiation, which provides the strongest source of noise outside of the instrument. While EXCLAIM is a scientific pathfinder, it is also a technological one. Nascent microwave kinetic inductance detectors (MKIDs) and μSpec, an integrated spectrometer-on-a-chip, are state of the art mid- to far-infrared technologies that may be game-changing in other suborbital and space-based missions. The low noise, scalability, and small size, weight, and power (SWaP) requirements make these technologies crucial enablers for mission science for broad science goals in mid- to far-infrared astronomy missions.

Measurements of the CO and [CII] intensities will shed light on the cosmic star formation rate. Particularly, The $z \sim 3$ measurement of [CII] will provide a valuable datapoint on Figure 1.4, in the epoch just before the star formation peak. At lower redshifts, the CO intensity will trace cold, star-forming gas through the well-described CO-H_2 ratio [18] which can be used to infer the density of star-forming gas, ρ_{H_2}. This will help us to understand the role of the baryon cycle in star formation over cosmic time [159].

EXCLAIM will provide a definitive followup to the [CII] measurements of Pullen et al. [124] and Yang et al. [164], and analogous measurements of the CO $J = 6, 5, 4$ lines. However, there is a large discrepancy between models for each of these lines; which models are correct will determine whether a given observation is capable of measuring the power spectrum,making an initial detection, or setting upper limits. Even an upper limit can constrain the nature of star formation and gas densities by

ruling out models, similar to Anderson et al. [9].

Foregrounds are present for EXCLAIM, but are dramatically smaller compared to 21 cm cases. The foregrounds are primarily due to the CMB, cosmic infrared background (CIB), and Galactic Cirrus emission, though Zodiacal light from the solar system dominates at smaller wavelengths in the near- to mid-IR. Furthermore, having a single dish means EXCLAIM does not suffer from the wedge effect. It is most important that the passband is calibrated, in order to reduce mode mixing from in $k_{||}$ modes.

Lessons learned from data analysis and technology development for EXCLAIM will be directly applicable to future mid- to far-infrared suborbital and space telescopes. There is extensive interest in this spectral range in the ASTRO2020 decadal survey through the Origins Space Telescope [86] and the Galaxy Evolution Probe (GEP) [59], though neither was directly selected. At the time of this writing, successors to the GEP design, known as PRIMA and FIRSST, are under discussion and development. LIM is a potential technique for the PRIMA and FIRSST analyses. Furthermore, MKIDs may be chosen for the detector technologies, for which EXCLAIM will present one of the lowest-background mission tests to date.

1.5 How this thesis contributes to the development of line intensity mapping.

My thesis research has focused on modeling science and instrumentation for a new analytical method, line intensity mapping. My research has featured a blend of broad, system-level analyses of intensity mapping surveys and in-depth analyses of analytical techniques and instrumentation. In this thesis, I describe my work in a 'top-down'

fashion describing general scientific questions that can be addressed through LIM and techniques to maximize the signal, to specific instrumentation in the EXCLAIM survey. This structure is far from chronological order in terms of my thesis work; in this section, I intend to describe the circuitous path I've taken in these analyses. As a secondary focus, I describe EXCLAIM techniques and technologies in the context of being a pathfinder for space missions. The ultimate goal for this thesis is thus to contribute to a basis for designing future intensity mapping space missions.

I began my thesis research working to understand data from the Tianlai pathfinder dish array, a late-time ($z < 2.55$) 21 cm intensity mapping instrument. Tianlai is among the first densely-path interferometer arrays focused on measuring the intensity mapping signal. At the time I began this research, several months worth of of data were available at the Tianlai Analysis Center at Fermi National Laboratory (Fermilab). The primary goal of this research was to characterize and calibrate the instrument using known astronomical objects. I worked to understand the beam profiles, point source calibration, and the noise model of the instrument. A chief challenge is characterizing the array of 16 dishes, each featuring slightly different passband responses and beam patterns due to cross-coupling between antennas. It is critical to characterize and calibrate these responses due to the immense foreground challenge, including the 'foreground wedge' effect associated with LIM intererometers [91, 92, 90]. Though these studies are not a primary focus in my thesis, I published interim results in a proceedings article for the Wisconsin Space Conference in Oxholm [111], and these studies were included in Wu et al. [162]. Beyond the analytical results, my work on Tianlai provided a strong foundation for my scientific understanding of cosmology and Python-based computation, so I was able to 'hit the ball running' when I started work on EXCLAIM.

In Fall 2019, I shifted my efforts to NASA's Experiment for Cryogenic Large-

aperture Intensity Mapping (EXCLAIM!), a balloon-borne CO and [CII] intensity mapping mission. At the time, EXCLAIM was recently selected as a NASA mission, and was through the early stages of its preliminary design. As a remote collaborator, my primary contributions were modeling detectors and the optical system. Over time, however, these models became integral tools for other aspects of the instrument modeling, such as scanning strategy and thermal loading. Organically, what began as seemingly disparate modeling efforts grew into a high-fidelity system model. As I often state, I have benefitted immensely from the small yet diverse EXCLAIM collaboration, which has allowed me to 'touch' nearly all aspects of the experiment. Thus far, these efforts have been published in Essinger-Hileman et al. [51], Switzer et al. [149], and Oxholm et al. [114]. Furthermore, I have had the opportunity to participate in various NASA preliminary and critical design reviews (PDRs and CDRs).

My research trajectory had another sizeable change when I asked the right question to the EXCLAIM science & analysis team: "how does the scientific sensitivity change with different choices of cross-correlation survey?". The baseline EXCLAIM design features cross-correlation with galaxies from the BOSS Stripe-82 survey, but other photometric and spectroscopic surveys may be accessible, including Hyper Suprime-cam and HETDEX. An answer didn't yet exist to this question, so I took the plunge and began modeling the scientific sensitivity. These studies quickly evolved into me leading $P(k)$ analysis for the EXCLAIM forecast [125].

As I sought to understand the EXCLAIM sensitivities, we always had the big picture in mind; namely, how do these studies apply to future missions? Through EXCLAIM, we worked to identify the 'Key Performance Parameters' in the instrument that may affect scientific sensitivity. However, more questions arose, including 'how do we optimize survey area for a cross-correlation?' and 'what do we learn from intensity mapping as opposed to direction-detection instruments?'. We addressed

these questions in Oxholm and Switzer [113], and I also published an introductory proceedings paper targeting those entering the field, Oxholm [112].

At the time of this writing, EXCLAIM and mid- to far-infrared intensity mapping is still growing in interest and excitement. EXCLAIM is preparing for the Mission CDR, signifying the final design before building and executing the mission. The engineering flight will nominally take place in Fall 2023, while the science flight is poised for the following year. Beyond this timeline, mid- to far-infrared telescopes are constantly proposed for suborbital and space missions. These can be seen as successors to EXCLAIM, potentially utilizing similar detector and spectrometer technologies, and measuring the LIM signal with ever-increasing sensitivity.

The primary working group for the U.S.-based Tianlai analysis team included myself and then- UW postdoc Dr. Santanu Das, working for Professor Peter Timbie. We closely collaborated with Dr. Albert Stebbins and Dr. John Marriner, both at Fermilab, along with Professor Gregory Tucker at Brown University. Later, Anh Phan joined the group and has been leading many studies at UW. Throughout, there has been excellent work from David Kwak, Calvin Osinga, Lily Robinthal, Gage Siebert, and Yanlin Wu, on various aspects of beam modeling and data analysis. We also collaborated less closely with Professor Reza Ansari from France, along with Xuelei Chen and Fengquan Wu in China.

I've collaborated closely with Dr. Eric Switzer at NASA-Goddard Space Flight Center (GSFC) since I first started on EXCLAIM, and I've benefited enormously from his mentorship. On the detector modeling front, I have worked with a dedicated team of NASA-GSFC scientists & engineers including Dr. Emily Barrentine, Dr. Thomas Stevenson, Dr. Maryam Rahmani, and Dr. James Hays-Wehle, along with University of Maryland graduate student Carrie Volpert. On the optical modeling front, I have worked closely with Dr. Thomas Essinger-Hileman and Gage Siebert,

who has diligently performed challenging simulations. On the science & analysis team, I have primarily worked with Dr. Christopher Anderson, Professor Alberto Bolatto, Professor Anthony Pullen, Dr. Patrick Breysse, Dr. Abhishek Maniyar, Dr. Shengqi Yang, and Dr. Aaron Yung. Throughout, I have worked with various other students and interns have contributed to these analyses including Lee-Roger Chevres-Fernanadez, Jonas Mugge-Durum, Gina Pantano, Adrian Sinclair, Ryan Stephenson, and Tony Zhou. Other scientists and engineers include Dr. Giuseppe Cataldo, Dr. Jason Glenn, Professor Philip Mauskopf, and Tatsat Parekh.

1.6 Thesis structure and publication overview

My thesis is structured in a 'top-down' fashion, focused on science before presenting various instrumentation efforts in the final chapters. This presentation is by no means in chronological order of when I focused on each effort[12] but I chose this format to place EXCLAIM mission goals and instrumentation efforts in the context of major scientific goals.

I begin by providing a quantitative overview of LIM, focusing on generalized formalism that may be applied to HI or sub-millimeter targets. I then describe forecasting techniques using Fisher matrices, building up formalism for cosmic variance evasion developed in Oxholm and Switzer [113]. I then provide an overview of the EXCLAIM mission, including some of my contributions to Switzer et al. [149]. I describe the EXCLAIM detector model, before presenting an operational technique to optimize detector noise. Finally, I describe optical modeling of the instrument, including results presented in Essinger-Hileman et al. [51].

The publications and proceedings with portions directly included in this thesis are:

[12] In fact, it's much closer to reverse chronological!

- **T.M. Oxholm**, Eric R. Switzer, Emily M. Barrentine, Thomas Essinger-Hileman, James P. Hays-Wehle, Philip D. Mauskopf, Omid Noroozian, Maryam Rahmani, Adrian K. Sinclair, Ryan Stephenson, Thomas R. Stevenson, Peter T. Timbie, Carolyn Volpert, Eric Weeks. "Operational Optimization to Maximize Dynamic Range in EXCLAIM Microwave Kinetic Inductance Detectors" (2022). This comprises the entire Chapter 7 verbatim.

- Anthony R. Pullen, Christopher J.,Anderson, Alberto D. Bolatto, Patrick C. Breysse, Thomas Essinger-Hileman, Abhishek Maniyar, **Trevor Oxholm**, Rachel S. Somerville, Eric R. Switzer, Carrie Volpert, Shengqi Yang, L. Y. Aaron Yung, and Zilu Zhou. "Galactic Science with the Experiment for Cryogenic Large-aperture Intensity Mapping." (2022). My contributions are included in Chapter 5.

- **Oxholm, T.M.**. "A beginner's Guide to Line Intensity Mapping Power Spectra". Proceedings of the 2021 Wisconsin Space Conference (2022). Portions of this proceedings paper are included in this introductory chapter.

- Eric R Switzer, Emily M Barrentine, Giuseppe Cataldo, Thomas Essinger-Hileman, Peter AR Ade, Christopher J Anderson, Alyssa Barlis, Jeffrey Beeman, Nicholas Bellis, Alberto D Bolatto, Patrick C Breysse, Berhanu T Bulcha, Lee-Roger Chevres-Fernanadez, Chullhee Cho, Jake A Connors, Negar Ehsan, Jason Glenn, Joseph Golec, James P Hays-Wehle, Larry A Hess, Amir E Jahromi, Trevian Jenkins, Mark O Kimball, Alan J Kogut, Luke N Lowe, Philip Mauskopf, Jeffrey McMahon, Mona Mirzaei, Harvey Moseley, Jonas Mugge-Durum, Omid Noroozian, **Trevor M Oxholm**, Tatsat Parekh, Ue-Li Pen, Anthony R Pullen, Maryam Rahmani, Mathias M Ramirez, Florian Roselli, Konrad Shire, Gage Siebert, Adrian K Sinclair, Rachel S Somerville, Ryan Stephenson, Thomas

R Stevenson, Peter Timbie, Jared Termini, Justin Trenkamp, Carole Tucker, Elijah Visbal, Carolyn G Volpert, Edward J Wollack, Shengqi Yang, LY Aaron Yung. "Experiment for Cryogenic Large-Aperture Intensity Mapping: Instrument design." J. of Astronomical Telescopes, Instruments, and Systems 7(4), 044004, 2021. Portions of Chapters 4 were taken from this paper, and portions of Chapters 6 and 8 in this thesis contributed to the paper.

- **Oxholm, T.M.** and Switzer, E.R.. "Intensity Mapping without Cosmic Variance," Phys. Rev. D 104, 083501, 2021. Most of this paper appears verbatim in Chapter 3.

- Thomas Essinger-Hileman, **Trevor Oxholm**, Gage Siebert, Peter Ade, Christopher Anderson, Alyssa Barlis, Emily Barrentine, Jeffrey Beeman, Nicholas Bellis, Patrick Breysse, Alberto Bolatto, Berhanu Bulcha, Giuseppe Cataldo, Jake Connors, Paul Cursey, Negar Ehsan, Lee-Roger Fernandez, Jason Glenn, Joseph Golec, James Hays-Wehle, Larry Hess, Amir Jahromi, Mark Kimball, Alan Kogut, Luke Lowe, Philip Mauskopf, Jeffrey McMahon, Mona Mirzaei, Harvey Moseley, Jonas Mugge-Durum, Omid Noroozian, Ue-Li Pen, Anthony Pullen, Samelys Rodriguez, Konrad Shire, Adrian Sinclair, Rachel Somerville, Thomas Stevenson, Eric Switzer, Peter Timbie, Carole Tucker, Eli Visbal, Carolyn Volpert, Edward Wollack, Shengqi Yang. "Optical design of the experiment for cryogenic large-aperture intensity mapping (EXCLAIM)," Millimeter, Submillimeter, and Far- Infrared Detectors and Instrumentation for Astronomy X. Vol. 11453. International Society for Optics and Photonics, 2020. Portions of 8 contribute to this paper.

Other publications I contributed to that were not included directly in this thesis include

- Siebert, G.L., **Oxholm, T.M.**, et al.. "Modeling the Optical System of NASA's EXCLAIM Mission." Submitted to Proceedings of the Wisconsin Space Conference (2021). This study, led by Gage Siebert, describes CST modeling of the EXCLAIM optical system.

- Fengquan Wu, Jixia Li, Shifan Zuo, Xuelei Chen, Santanu Das, John P Marriner, **Trevor M Oxholm**, Anh Phan, Albert Stebbins, Peter T Timbie, Reza Ansari, Jean-Eric Campagne, Zhiping Chen, Yanping Cong, Qizhi Huang, Juhun Kwak, Yichao Li, Tao Liu, Yingfeng Liu, Chenhui Niu, Calvin Osinga, Olivier Perdereau, Jeffrey B Peterson, John Podczerwinski, Huli Shi, Gage Siebert, Shijie Sun, Haijun Tian, Gregory S Tucker, Qunxiong Wang, Rongli Wang, Yougang Wang, Yanlin Wu, Yidong Xu, Kaifeng Yu, Zijie Yu, Jiao Zhang, Juyong Zhang, Jialu Zhu. "The Tianlai Dish Pathfinder Array: design, operation and performance of a prototype transit radio interferometer," Monthly Notices of the Royal Astronomical Society, 506, 3, 2021. This paper summarizes analysis of first-light data on the Tianlai Pathfinder Dish Array. My contributions include analyzing point source sensitivity, beam stability, and beam characterization.

2 LIM: INTRODUCTION TO LINE INTENSITY MAPPING

Here, I provide a quantitative introduction to line intensity mapping. I begin with a discussion of the signal itself, and the observables measureable through LIM surveys. I focus on the power spectrum of cross-correlations between intensity maps and galaxy redshift surveys, laying the groundwork for forecasting studies later in the thesis. Portions of this chapter were published in my proceedings article, "A beginner's guide to line intensity mapping power spectra" in Proceedings of the Wisconsin Space Conference, 2021.

2.1 Tracing the matter overdensity

The primary observable in an intensity map is the intensity field δ_I, which traces large-scale matter fluctuations δ_m as

$$\delta_I(\mathbf{r}, z) = I(z)b(z)\delta_m(\mathbf{r}, z) + N(z), \tag{2.1}$$

where $\mathbf{r}$ represents spatial location and b is the linear clustering bias of the observed galaxies relative to the underlying matter overdensity δ_m. $I(z)$ is the intensity at mean density, representing the cumulative emission from all galaxies in the survey region. $N(z)$ describes map noise, which I assume is isotropic at a given frequency/redshift.

The intensity I is related to the first moment of the galaxy luminosity function, and its dependence on z probes galaxy evolution. The specific intensity (henceforth I will drop the 'specific') of a single galaxy is given by [157] [1]

$$I_{1\ \mathrm{gal}} = \frac{L}{4\pi d_L^2}\frac{1}{\delta\nu\Omega_{\mathrm{beam}}}, \tag{2.2}$$

[1] This is consistent with the famous formula from Carilli and Walter [24], where $4\pi *$ Jy GHz Mpc^2 (km/s/c) $= 1.04 \times 10^{-3} \mathrm{L}_\odot$.

where $L/(4\pi d_L^2 \delta\nu)$ provides a specific flux (units of $W\ m^{-2}\ Hz^{-1}$), d_L is the luminosity distance defined in Chapter 1, and $1/\Omega_{\rm beam}$ converts from flux to intensity. I define all the terms except L by

$$\frac{dF}{dL} \equiv \frac{1}{4\pi d_L^2 \delta\nu}, \tag{2.3}$$

and $dI/dL = \Omega_{\rm beam}^{-1}\ dF/dL$, where F is the flux through the detectors.

An intensity map provides an integral over all galaxies in a given region, resulting in

$$\begin{aligned} \bar{I} &= \int \frac{L}{4\pi d_L^2 \Omega_{\rm beam}} \frac{\partial V_{\rm co}}{\partial \nu} dn \\ &= \int \frac{L}{4\pi d_L^2 \Omega_{\rm beam}} \frac{\partial \chi}{\partial \nu} d_A^2 \Omega_{\rm beam} dn \\ &= \int \frac{L}{4\pi d_L^2} \frac{\lambda_{\rm rest}(1+z)^2}{H(z)} d_A^2 dn \\ &= \frac{\lambda_{\rm rest}}{4\pi H(z)} \int L d\tilde{n}. \end{aligned} \tag{2.4}$$

Here, dn is the differential number of line-emitting galaxies per comoving volume, and the differential comoving volume element $dV_{\rm co}$ provides the conversion from number density to number. d_A is the angular diameter distance and χ is the line-of-sight comoving distance. Note that $dn \propto (1+z)^{-2}$ (see Equation 1.7), and I have defined $d\tilde{n} = (1+z)^2 dn$ to remove the z-dependence for calculations to come[2].

Here, the prefactor is described by

$$\alpha(z) \equiv \frac{dI}{dL}\frac{dV_{\rm co}}{d\nu}\delta\nu = \frac{\lambda_{\rm rest}}{4\pi H(z)}, \tag{2.5}$$

converting the (comoving) integral of the luminosity to an intensity.

[2]Note that it is not a comoving inverse volume, but a comoving inverse area with fixed line-of-sight distance specified by dz. Hence, there are only two powers of $(1+z)$ rather than three.

The number density of galaxies can be calculated in a variety of ways, including

$$\begin{aligned} L d\tilde{n} &= L\frac{dn}{dL}(L)dL \quad \text{(Luminosity approach)} \\ &= L(M)\frac{dn}{dM}(M)dM \quad \text{(Halo mass approach)} \\ &= L(L_{\rm IR})\frac{dn}{dL_{\rm IR}}(L_{\rm IR})dL_{\rm IR} \quad \text{(IR luminosity approach).} \end{aligned}$$

For the rest of this section I will apply the halo mass function (HMF) approach [35]. Here,

$$\bar{I}(z) = \alpha(z)\int_{M_{\rm min}}^{\infty} L(M,z)\frac{dn}{dM}(M,z)dM, \tag{2.6}$$

given in units of Jy/sr.

The shot power $P_{\rm shot}$ is also critical to the calculation of the power spectrum of the line intensity map. It is given by [23]

$$P_{\rm shot}(z) = \alpha^2(z)\int_{M_{\rm min}}^{\infty} L^2(M,z)\frac{dn}{dM}(M,z)dM, \tag{2.7}$$

in units of $\mathrm{Jy}^2(\mathrm{Mpc}/h)^3/\mathrm{sr}^2$. The integrals in Equations 2.6 and 2.7 are known as the first and second moments of the luminosity function, respectively.

Figure 2.1 shows the components of Equation 2.6 corresponding to the [CII] model of Padmanabhan [116]. The [CII] luminosity (as with other lines) increases with halo mass because generally, high-mass halos are more luminous than low-mass ones. On the other hand, bottom-up structure formation dictates that low-mass halos are more common than high-mass ones. As a result, there is a clear peak in the first moment of the luminosity function for $M_h \sim 10^{12}\,\mathrm{M}_\odot$. Thus, these are the most heavily-weighted halos in the mean cosmic [CII] intensity. A similar peak occurs in the shot power,

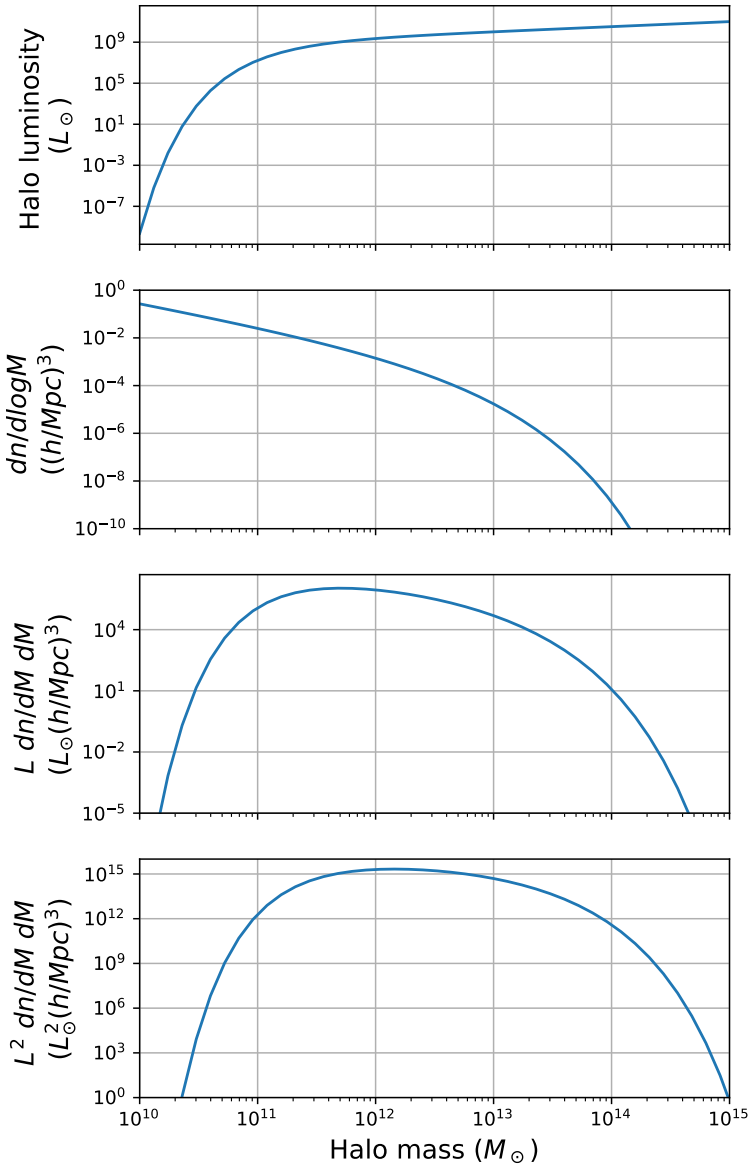

Figure 2.1: [CII] intensity parameters corresponding to Equations 2.6 and 2.7. The four panels show the [CII] luminosity function, the HMF, the integrand of the line intensity, and the integrand of the [CII] intensity, and the integrand of the [CII] shot power, respectively. The integrals of the latter two are given by the first and second moments of the luminosity function.

but the peak is at a higher halo mass because the second moment is more heavily weighted toward high-mass halos.

The clustering bias b between the intensity field and the underlying matter density field provides another observable that may be used to infer the mass-luminosity function. I calculate b as a weighted mean over the mass-luminosity function,

$$b(z) = \frac{\int_{M_{\rm min}} b_h(M,z) L(M,z) dn/dM(M,z) dM}{\int_{M_{\rm min}} L(M,z) dn/dM(M,z) dM} \tag{2.8}$$

where $b_h(M,z)$ is the bias of a given halo with respect to the underlying matter power spectrum [135, 153].

The intensity and bias are completely degenerate, so I group the terms together as the *biased intensity* $[Ib]$. In the calculations that follow, I define the biased intensity simply as the product between the intensity I and a constant bias b, specified by Equations 2.6 and 2.8, without the inclusion of redshift-space distortions (RSD) or scale-dependent bias. $[Ib]$ therefore contains information about the integral of the line mass-luminosity function $L(M,z)$ and the halo low-mass cutoff $M_{\rm min}$.

Using only information from the intensity map, $[Ib]$ is also degenerate with δ_m. The latter is subject to cosmic variance because it depends on the measurement of waves in the matter density field, with a variance limited by the number of observable modes. Because $[Ib]$ and δ_m are degenerate, cosmic variance in δ_m is coupled to variance in $[Ib]$.

Power spectrum

The power spectrum describing fluctuations in the intensity overdensity are given by the intensity power spectrum $P_I(\mathbf{k}, z)$, as

$$\langle \delta_I(\mathbf{k}, z)\delta_I(\mathbf{k'}, z)\rangle = P_I(\mathbf{k}, z)(2\pi)^3\delta(\mathbf{k} - \mathbf{k'}), \tag{2.9}$$

assuming Gaussian fluctuations. Here, δ denotes the Dirac delta function.

The intensity power spectrum has three primary contributions: a 2-halo (clustering) term, a 1-halo term, and a shot noise term. The clustering term describes linear fluctuations tracing the matter power spectrum on scales larger than individual halos.

Clustering (2-halo) power spectrum

The clustering term describes the linear clustering of the underlying dark matter overdensity on scales larger than individual halos.

$$P_I^{\text{clust}}(\mu, k, z) = [Ib]^2(z)F_{I,\text{RSD}}^2(\mu, k, z)P_m(k, z). \tag{2.10}$$

F_{RSD} accounts for redshift-space distortions, i.e. observable distortions in the matter distribution because we are observing galaxies in redshift space, rather than physical space. The main effects are the Kaiser and Fingers-of-God effects. The Kaiser effect arises from the peculiar velocities (i.e. velocities of galaxies against the Hubble flow), and generally contributes on large scales. The Fingers-of-God effect accounts for velocity dispersion of galaxies (or intergalactic gas within the halo) against dark matter halos, and contributes on smaller scales. The two terms contribute together as

$$F_{I,RSD}(\mu, k, z) = \left(1 + \beta_I(z)\mu^2\right)\exp\left[-\mu^2k^2\sigma_{k,\text{FOG}}^2\right], \tag{2.11}$$

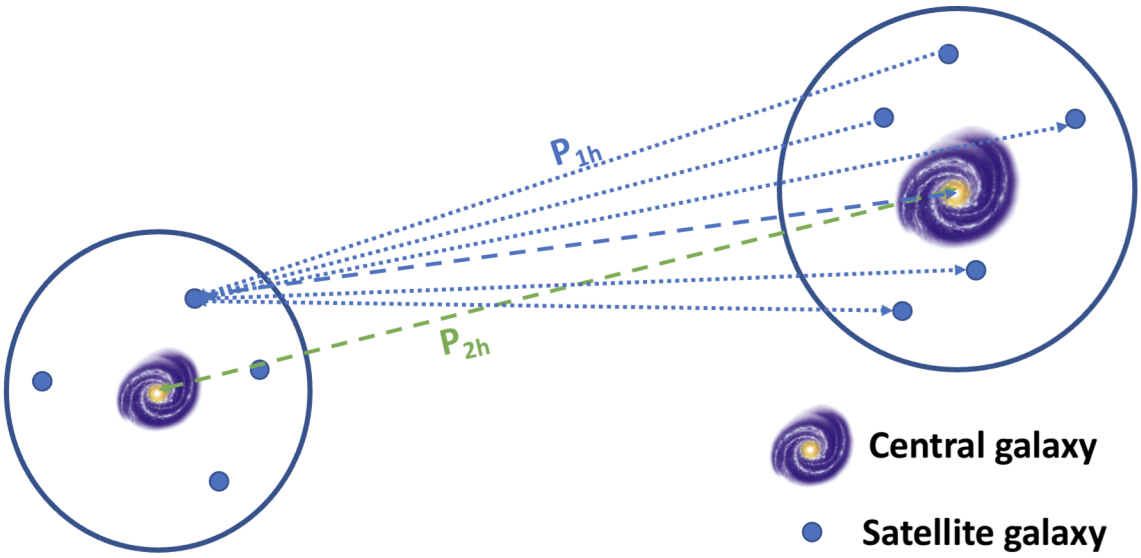

Figure 2.2: Pictorial representation of central and satellite galaxies. Central galaxy correlations are described by the 2-halo power spectrum $P_{\rm 2h}$ while correlations between satellites are represented by $P_{\rm 1h}$.

where $\beta_I = f/b_I$ and $\sigma_{k,\rm FOG} = (1+z)\left(0.5(1+z)v_{\rm disp}^2 + (0.001c(1+z))^2\right)^{1/2}$, with $v_{\rm disp}$ the velocity dispersion of matter about the center of the host halo.

1-halo power spectrum

The clustering/2-halo term describes fluctuations on scales large enough that halos can be treated as discrete objects. On smaller scales ($k \lesssim 0.1h^{-1}\,\rm Mpc$), the inner structure of dark matter halos becomes important. Figure 2.2 illustrates this effect. The 2-halo term ($P_{\rm 2h}$) describes vectors between halo centers. The 1-halo term (P_{1h}) describes vectors between galaxies dispersed throughout the halo, not located at the center.

The distribution of galaxies, or more precisely line-emitting gas, throughout the halos is crucial to the calculation of the 1-halo term. Galaxies tend to be separated into two populations: centrals and satellites. Central galaxies are located precisely at

the center of the halo, and tend to be the most massive galaxies in the halo. Satellite galaxies represent smaller galaxies that were accumulated by the central through mergers, and are dispersed throughout the halo.

It is enlightening to compare the 2-halo and 1-halo power spectra in terms of discrete galaxy statistics[3]. Here, the 2-halo term is given by (ignoring RSD and assuming all detected galaxies are centrals)

$$P_I^{2h}(k) = \alpha^2 P_m(k) \left[\int_{M_{\rm min}}^{\infty} L(M) b_h(M) u(k, M) \frac{dn}{dM}(M) dM \right]^2 \tag{2.12}$$

where the term in the brackets is $[Ib]^2$. The 1-halo power spectrum is given by (again ignoring RSD and satellite galaxies)

$$P_I^{1h}(k) = \alpha^2 \int_{M_{\rm min}}^{\infty} L^2(M) \left| u(k|M) \right|^2 \frac{dn}{dM} dM. \tag{2.13}$$

I show in Appendix A the sum of P_I^{1h} and $P_I^{\rm shot}$ can be expressed in the form

$$P_I^{\rm shot}(k) + P_I^{\rm 1h}(k) = \left(1 + \Sigma_{1h}(k)\right) P_I^{\rm shot}, \tag{2.14}$$

where $\Sigma_{1h} \leq 1$.

In Appendix A, I discuss how $\Sigma_{1h}(k)$ includes information about the line intensity attributed to central galaxies, as opposed to satellite galaxies or intrahalo dust. In the extreme case that 100% of the emission is attributed to satellites and/or intrahalo dust, Σ_{1h} approaches 1 on scales k that are larger than the the scale of the virial radii of the host halos. On the other hand, if all the intensity is attributed to centrals, Σ_{1h} approaches 1. Generally, the factor of u in the 2-halo power spectrum is not important because the shot and 1-halo power dominate on the small scales where it is relevant,

[3]This discussion was motivated by Schaan and White [131], which may be referenced for more in-depth discussion about the 1- and 2-halo power spectra.

so it is safely ignored throughout this thesis.

Autocorrelation - minimal set of parameters

The total LIM auto-power spectrum is given by

$$\begin{aligned} P_I(\mu,k,z) &= P_I^{\rm clust}(\mu,k,z) + \left[P_I^{\rm shot}(z) + P_I^{\rm 1h}(\mu,k,z)\right] \\ &= I^2(z)b^2(z)F_{I,RSD}^2(\mu,k,z)P_m(k,z) + \left(1+\Sigma_{1h}(\mu,k,z)\right)P_I^{\rm shot}(z), \end{aligned} \tag{2.15}$$

as shown by Figure 2.3. On large scales ($k \lesssim 0.05\,h/\mathrm{Mpc}$), the 2-halo term dominates the signal. Here, there is a clear degeneracy between I, b, $F_{I,\mathrm{RSD}}$, and P_m. The latter is the source of cosmic variance, a subject of our next chapter.

On intermediate scales where the shot and 1-halo power dominate the power spectrum ($0.05\,h/\mathrm{Mpc} \lesssim k \lesssim 10\,h/\mathrm{Mpc}$), there is a degeneracy between $(1+\Sigma_{1h})$ and the second moment of the luminosity function. This degeneracy can be broken by observing large scales where the clustering term provides a measurement of the first moment of the luminosity function, or on smaller scales where $u_S \to 0$ and the 1-halo term vanishes, leaving a measurement of the shot power on its own.

A measurement of P_I can be used to constrain a set of nondegenerate parameters:

$$[Ib],\ \beta_I = f/b,\ \sigma_{k,\mathrm{FOG}},\ P_m,\ I_2,\ \Sigma_{1h}. \tag{2.16}$$

Here, there is a degeneracy between I, b, and f, so the three cannot be simultaneously measured without prior information. However, f is known with much higher precision from CMB and galaxy redshift surveys than I or b. Taking $f(z) = \Omega(z)^\gamma$ with

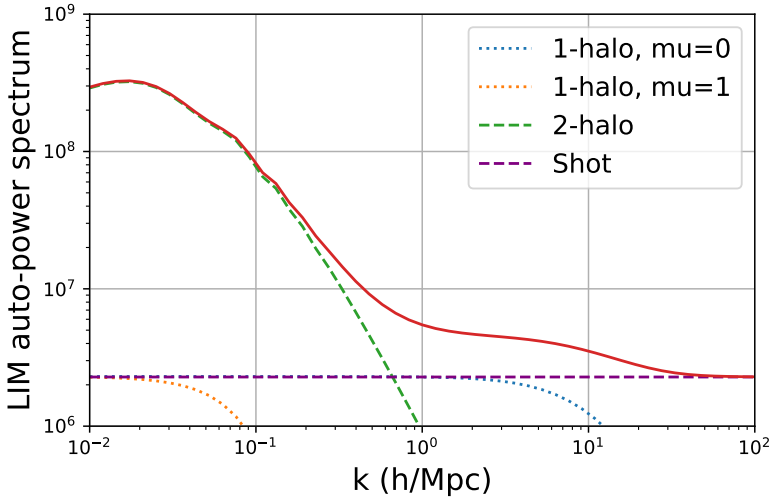

Figure 2.3: [CII] Autopower components using the Padmanabhan [116] model at $z = 1$.

$\Omega_m(z = 0) = 0.412 \pm 0.002$ from [3] and $\gamma = 0.55$ [49], the fractional uncertainty $\delta f/f = 0.008$; on the other hand, models for Ib are disparate by upwards of three orders of magnitude. With a strong prior on f, we can use RSD measurements to separate the bias from the intensity through joint measurements of Ib and f/b. Without RSD measurement, however, we can only constrain Ib; this is the goal of the present generation of LIM surveys at both 21 cm and sub-millimeter wavelengths. Furthermore, the current stage is unlikely to be able to distinguish between the 1-halo and shot power terms; here, the instrument must he highly sensitive and the beam must be narrow enough to resolve structure on the scales of individual dark matter halos.

Additional contributions to the IM signal

Instrument noise

Instrument noise is present in all intensity mapping surveys, and presents an unavoidable limit to achievable sensitivities. I describe the contribution of instrument noise to the intensity mapping power spectrum through a term P_n given by

$$\begin{aligned} P_n(z) &= \frac{\mathrm{NEI}^2(z) V_{\mathrm{surv}}}{N_{\mathrm{ch}} t_{\mathrm{surv}}} \\ &= \frac{\mathrm{NEI(z)}^2 V_{\mathrm{pix}}}{N_{\mathrm{ch}} t_{\mathrm{pix}}} \\ &= \frac{\mathrm{NEI}^2(z) V_{\mathrm{vox}}}{t_{\mathrm{pix}}} \\ &= \sigma_n^2 V_{\mathrm{vox}}, \end{aligned} \tag{2.17}$$

where NEI is the noise-equivalent intensity, given in units of Jy $\mathrm{sr}^{-1}\mathrm{s}^{1/2}$. σ_n dscribes the instrument noise per voxel volume. The NEI defines the intensity of instrument noise over one root-second of integration time. V_{surv} and t_{surv} represent the volume and observation time for the entire survey, while V_{pix} and t_{pix} represent the equivalent quantities for a single pixel on the sky, with the former corresponding to the integral along the line of sight for the total survey volume. V_{vox} is the volume corresponding to a single pixel and a single frequency bin, i.e. a differential along the line of sight. $N_{\mathrm{ch}} = V_{\mathrm{pix}}/V_{\mathrm{vox}}$ is the number of frequency channels across the band.

Equation 2.17 suggests that instrument noise can be reduced in one of three ways: decrease the NEI, decrease the pixel or survey volume, or increase observation time. Decreasing the NEI presents the strongest means to increasing sensitivity, as it features quadratic improvements in sensitivity. In the case of CO and [CII] intensity maps, the atmosphere presents a strong contribution to ground- and balloon-based instruments.

As I later quantify in Section 4.2, the limiting NEI in a 500 GHz balloon-based telescope at an altitude of 36 km is roughly a factor of 10 higher than an equivalent space telescope pointing away from the galactic plane. The balloon telescope would therefore require 100 times more integration time to achieve the same level of sensitivity. A space telescope could therefore provide roughly the same sensitivity in a 7-hour survey as a 30-day balloon campaign.

Decreasing the survey volume also decreases P_n, but it may or may not increase sensitivities. As I described in Oxholm and Switzer [113] and will further describe in the next chapter, the optimal survey volume depends on a slew of assumptions, including auto- vs. cross-correlations, the k scales of interest, and how P_n compares to the clustering (or shot) power spectrum.

Oftentimes, the NEI varies as a function of frequency. In this case, the NEI can be expressed as an inverse variance-weighted mean of the NEI per channel. I denote each frequency channel channel $1 \leq i \leq N_{\rm ch}$, with power spectrum noise, NEI, and voxel volumes given by $P_{n,i}$, NEI_i, and $V_{{\rm vox},i}$, so

$$\begin{aligned} P_n(z) &= N_{\rm ch}\left[\sum_{i=1}^{N_{\rm ch}} P_{n,i}(z)^{-1}\right]^{-1} \\ &= N_{\rm ch}\left[\sum_{i=1}^{N_{\rm ch}} \left(\frac{\mathrm{NEI}_i^2(z) V_{{\rm vox},i}}{t_{\rm pix}}\right)^{-1}\right]^{-1} \\ &\approx \frac{N_{\rm ch} V_{\rm vox}}{t_{\rm pix}}\left[\sum_{i=1}^{N_{\rm ch}} \mathrm{NEI}_i^{-2}(z)\right]^{-1}, \end{aligned} \tag{2.18}$$

assuming $V_{{\rm vox},i}$ is constant across the passband[4]. Comparing to Equation 2.17, I find

[4]Strictly speaking, the volume per channel is not constant for channels of constant bandwidth because the voxel volume increases with distance. Thus, Equation 2.18 does not perfectly minimize variance in the intensity map, but it is a useful guideline that is close enough for our forecasting purposes.

that

$$\mathrm{NEI}^2 = N_{\mathrm{ch}} \left[\sum_{i=1}^{N_{\mathrm{ch}}} \mathrm{NEI}_i^{-2}(z) \right]^{-1}, \tag{2.19}$$

the inverse-weighted NEI per channel.

In the case that the noise in each frequency channel is exactly the same, i.e. $\mathrm{NEI}_{\mathrm{bin},i} = \mathrm{NEI}$ for all i, $P_n(z) = \mathrm{NEI}^2 V_{\mathrm{vox}}/t_{\mathrm{pix}}$, consistent with Equation 2.17. Equation 2.18 is particularly useful in the case that instrument noise varies widely across the array, as pertains to the EXCLAIM instrument model as I later describe in Section 6.6.

Residual foregrounds

Residual foregrounds present another systematic challenge in IM surveys. Foregrounds from galactic, Zodiacal, and CIB emission contribute significantly to the IM signal. In 21cm experiments, galactic synchrotron emission presents the primary foreground signal. In the mid- to far-IR, galactic Cirrus, Zodiacal, and CMB emission are the primary contributors. These foreground signals are often orders of magnitude larger than the extragalactic IM signal, with a factor of 10^5 in the case of 21cm. The foreground contributors, however, are expected to be spectrally smooth, with much higher variation orthogonal to the line of sight. This makes it possible to remove the foregrounds without an excessive loss of IM signal. Here, passband stability is crucial to the ability to remove foregrounds. This may be done by removing the lowest $k_{||}$ modes[5].

[5]More sophisticated methods may be used, as highlighted in Switzer et al. [147], Anderson [8], Anderson et al. [10], Switzer et al. [148].

Interloping lines

Emission from other lines presents an additional contribution to the intensity mapping signal. Suppose the rest-frame frequency of our target line is given by $\nu_I^{\rm rest}$, so the observed frequency is $\nu_I^{\rm obs} = \nu_I^{\rm rest}/(1+z)$. An interloping contaminant with rest-frame frequency $\nu_{\rm IL}^{\rm rest}$ originating from redshift $z_{\rm IL} = \nu_{\rm IL}^{\rm rest}/\nu_I^{\rm obs} - 1$.

Because the interlopers originated from a different redshift than the target line, observed wavenumbers are warped as [88]

$$k_{\perp,\rm IL} = \frac{d_A(z)}{d_A(z_{\rm IL})} k_\perp \equiv \alpha_\perp k_\perp \tag{2.20}$$

$$k_{||,\rm IL} = \frac{H(z_{\rm IL})(1+z)}{H(z)(1+z_{\rm IL})} k_{||} \equiv \alpha_{||} k_{||}, \tag{2.21}$$

where $\alpha_\perp$ and $\alpha_{||}$ feature the same interpretations as the Alcock-Pacynski parameters [6]. The total contribution from all interlopers to the intensity mapping power spectrum is given by

$$P_I^{IL}(\mathbf{k}, z) = \sum_i \frac{1}{\alpha_{||}(z_i)\alpha_\perp^2(z_i)} P_{clust,i}\left(\frac{k_{||}}{\alpha_{||}(z_i)}, \frac{k_\perp}{\alpha_\perp(z_i)}, z_i\right), \tag{2.22}$$

where the index i runs over all interlopers. Here, the parameters $\alpha_{||}$ and $\alpha_\perp$ account for difference in volume when comparing the power spectra of the target redshifts compared to those of the interloping lines.

2.2 Cross-correlation with a galaxy redshift survey

The contaminating sources described in Section 2.1 result in additive biases and noise in the intensity map. Here, Equation 2.1 is modified as

$$\delta_I^{\rm tot} = \delta_I + N + F + \delta_I^{\rm IL} \tag{2.23}$$

where F denotes the foreground signal and $\delta_I^{\rm IL}$ describes fluctuations due to interloping lines.

Cross-correlating with a different tracer of the same underlying matter overdensity allows us to remove the additive biases in the signal due to instrument noise, foregrounds, and interloping lines. By cross-correlating with different frequency channels, foregrounds are uncorrelated between the two tracers. Furthermore, interloping lines emit at a different redshift from the target line (as long as redshift bins are sufficiently small that there is no overlap). Therefore, interloping lines are not correlated with the same galaxy population, and are similarly canceled out. I stress, however, that foregrounds, interlopers, and instrument noise still contribute to noise in the signal, unless they are adequately masked or removed.

Power spectrum formalism

Typically, an intensity map is cross-correlated with a galaxy redshift survey. This is due to the relative high noise in the intensity map, which can use known galaxy positions to bolster the signal and remove multiplicative biases. In future surveys with higher sensitivity, intensity maps will likely increasingly be used without the use of cross-correlation. Using the $P(k)$ formalism, I describe power spectra similar to P_I

in Equation 2.15 as

$$P_g(\mu,k,z) = b_g^2(z)F_{g,RSD}^2(\mu,k,z)P_m(k,z) + \frac{1+\Sigma_{1h}^g(\mu,k,z)}{\bar{n}(z)} \quad (2.24)$$

$$P_{I\times g}(\mu,k,z) = I(z)b(z)b_g(z)F_{I,RSD}(\mu,k,z)F_{g,RSD}(\mu,k,z)P_m(k,z) + \left[1+\Sigma_{1h}^{I\times g}(\mu,k,z)\right]P_{\rm shot}^{I\times g}(z), \quad (2.25)$$

where P_g is the power spectrum of the galaxy redshift survey and $P_{I\times g}$ is the cross-power spectrum between the intensity map and the galaxy redshift survey. Here, b_g is the bias of the galaxies in the galaxy redshift survey, and $\bar{n}$ is the mean number density of galaxies observed in the galaxy redshift survey. Σ_{1h}^g and $\Sigma_{1h}^{I\times g}$ denote the dimensionless 1-halo terms for the galaxy redshift survey and cross-power, respectively.

$P_{\rm shot}^{I\times g}$ is the cross-shot power between the two surveys, attributed to the number statistics of the correlated galaxies between the two surveys. Finally, $F_{g,RSD}$ is the redshift-space distortion in the galaxy survey, which is defined equivalently to Equation 2.11, but instead calculated with $\beta_g = f/b_g$ replacing β_I.

Calculation of galaxy redshift survey parameters

Terms in the galaxy redshift survey are also calculated using the halo mass function approach of Cooray and Sheth [35]. Here, the galaxy bias is given by

$$b_g(z) = \frac{\int_{M_{\rm min}^g} b_h(M,z)n_g(M,z)dn/dM(M,z)dM}{\int_{M_{\rm min}^g} n_g(M,z)dn/dM(M,z)dM} \quad (2.26)$$

where $n_g(M,z)$ is the galaxy halo occupation distribution (HOD) describing the average number density of observed galaxies in halos of mass range M to $M+dM$.

The average number density of galaxies $\bar{n}$ is given by

$$\bar{n}(z) = \int_{M^g_{\rm min}} n_g(M,z)\frac{dn}{dM}(M,z)dM. \tag{2.27}$$

In both cases, the minimum halo mass $M_{\rm min,g}$ describes a sharp cutoff halo mass that contains an observable galaxy. Generally, because galaxy luminosity increases with halo mass, $M_{\rm min,g}$ is a proxy for a luminosity cutoff. Caution must be taken to distinguish between the formalisms, however, as the symbol M is also often used to describe galaxy magnitude in the astronomy community.

Galaxy occupation statistics

The galaxy HOD depends on the population that is being surveyed. However, it is typically broken into central ($n^{\rm c}_g$) and satellite ($n^{\rm s}_g$) populations as

$$n_g(M,z) = n^{\rm c}_g(M,z) + n^{\rm s}_g(M,z). \tag{2.28}$$

Central galaxies are typically described through a log-normal distribution

$$n^{\rm c}_g(M,z) = \tau\left[1 + {\rm erf}\left(\frac{\log M - \log M_{\rm c}}{\log \sigma_m}\right)\right] \tag{2.29}$$

where $M_{\rm c} \sim 10^{12} M_\odot$ is the mean halo mass for central galaxies in a typical late-time ($z \lesssim 4$) galaxy redshift survey, and σ_m describes the width of the function. τ describes the duty cycle of the given survey. In local surveys that pick up nearly all central galaxies, $\tau \simeq 1$. However, higher-redshift surveys tend to have lower values owing to magnitude-limited samples; for example, eBOSS quasar sample mocks have $\tau \sim 10^{-2}$ [141].

Satellite galaxies are typically Poisson-distributed with a power law cutoff at low

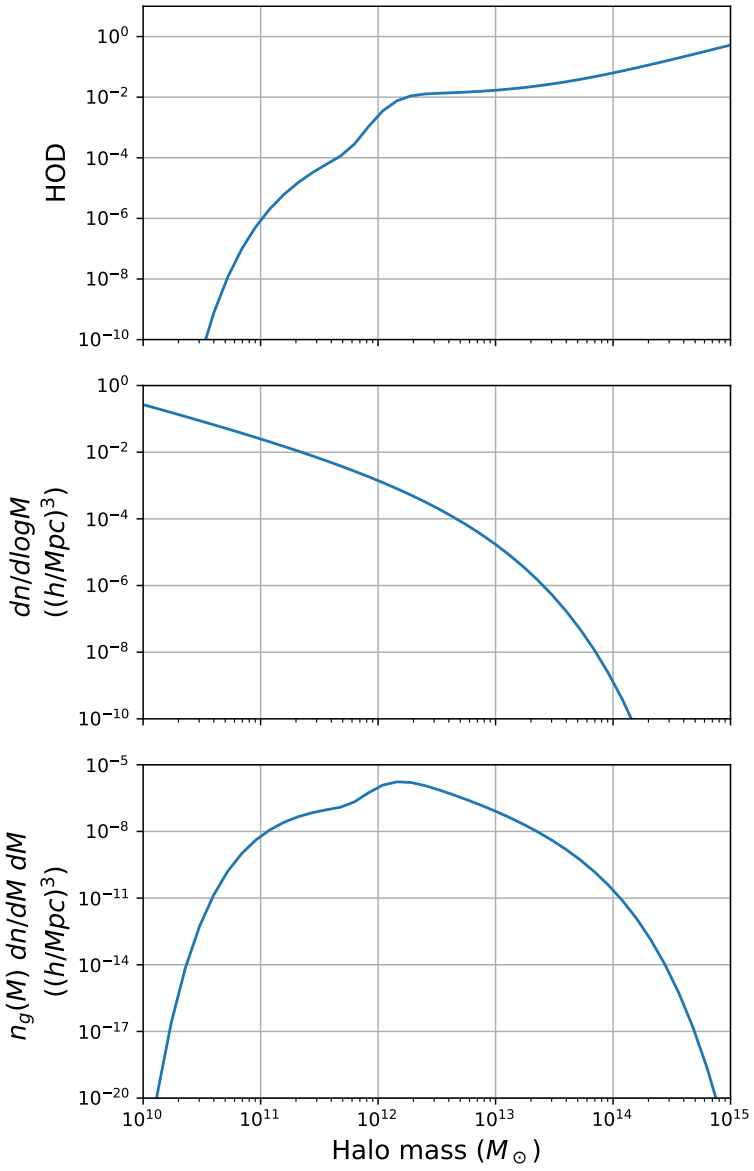

Figure 2.4: Calculations for the galaxy number density components of Equation 2.27. The top panel shows the eBOSS QSO galaxy HOD, the middle panel shows the HMF, and the bottom panel shows the integrand of the galaxy number density calculation.

mass. Here,

$$n_g^{\rm s}(M,z) = \left(\frac{M}{M_{\rm s}}\right)^{\alpha_{\rm s}} \exp\left(-\frac{M_{\rm cut}}{M}\right). \tag{2.30}$$

Figure 2.4 shows the components of the galaxy number density calculation for eBOSS QSOs. Here, the central component of the HOD is peaked at $M_h \sim 10^{12}\,{\rm M}_\odot$, while the satellite HOD grows with halo mass as a power law. This means the central halos most commonly occupy $\sim 10^{12}\,{\rm M}_\odot$ halos, but most halos do not have a visible QSO because the central peak HOD is not 1. Higher-mass halos tend to feature more visible objects; for low-redshift galaxy surveys, the central HOD can peak at nearly 1 at $M_h \sim 10^{12}\,{\rm M}_\odot$ while the satellite HOD can be upwards of 10 for the highest-mass halos at around $M_h \sim 10^{15}\,{\rm M}_\odot$ [141]. Like the [CII] intensity shown in Figure 2.1, this results in a peak halo mass in the integrand of the galaxy number density. This represents the most heavily represented halo mass in the eBOSS QSO sample.

Correlated shot noise

I estimate the cross-shot power as [23]

$$P_\times^{\rm shot}(z) = \alpha(z) \int_{M_{\rm min}^\times}^\infty L(M,z) n_g(M,z) n(M,z) dM, \tag{2.31}$$

Crosscorrelation - minimal set of parameters

The total cross-power spectrum is given by

$$\begin{aligned} P_\times(\mu,k,z) &= P_\times^{\rm clust}(\mu,k,z) + \left[P_\times^{\rm shot}(z) + P_\times^{\rm 1h}(\mu,k,z)\right] \\ &= I(z) b(z) b_g(z) F_{I,RSD}(\mu,k,z) F_{g,RSD}(\mu,k,z) P_m(k,z) + \\ &\quad + \left(1 + \Sigma_{1h}^\times(\mu,k,z)\right) P_\times^{\rm shot}(z). \end{aligned} \tag{2.32}$$

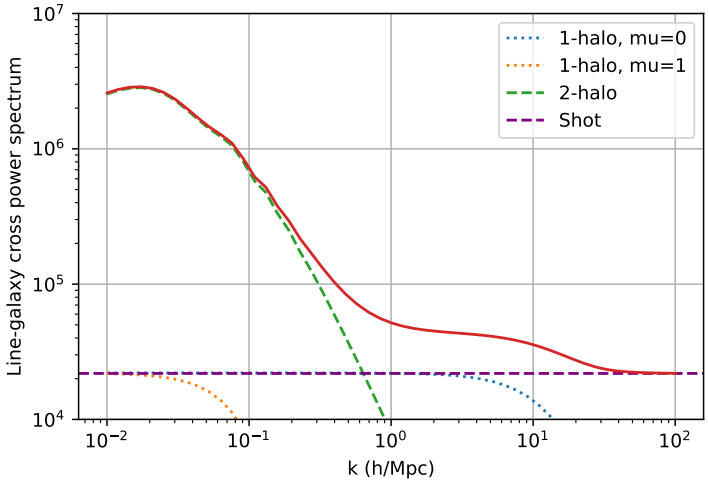

Figure 2.5: [CII] crosspower for based on the Padmanabhan [116] [CII] model and an arbitary galaxy redshift survey, at $z = 1$.

Again, the clustering power spectrum dominates on large scales (lower k), whereas the shot and 1-halo power spectra dominate on smaller scales. Using information from the cross-power only, we may constrain the parameters,

$$[Ib],\ b_g,\ \beta_I = f/b,\ \beta_g = f/b_g,\ \sigma_{k,\mathrm{FOG}},\ P_m,\ P_\times^{\mathrm{shot}},\ \Sigma_{1h}^{\times}. \tag{2.33}$$

Like the auto-power spectrum, RSD measurements are needed to separate the intensity from the bias. However, care must be taken that additional uncertainty is not introduced by priors in the galaxy redshift survey. For the current generation of LIM experiments exploiting cross-correlations with galaxy surveys, uncertainties in the intensity mapping parameters Ib, β_I, and $P_\times^{\mathrm{shot}}$ are much higher than that of the galaxy redshift survey.

Furthermore, as I will discuss in Chapter 3, the auto-power spectra from the LIM and galaxy redshift survey still contribute to their cross-correlation through errors. Here, instrument noise in the intensity map as well as shot noise in the galaxy survey

will both contribute to errors in the cross-correlation measurement.

Figure 2.5 shows the different components of the LIM cross-correlation power spectrum with a galaxy redshift survey. On large scales ($k \lesssim 0.1\,h/\mathrm{Mpc}$), the 2-halo term dominates the signal. Here, there is a clear degeneracy between I, b, $F_{I,\mathrm{RSD}}$, and P_m. The latter is the source of cosmic variance, a subject of our next chapter. On intermediate scales where the shot and 1-halo power dominate the power spectrum ($0.1\,h/\mathrm{Mpc} \lesssim k \lesssim 10\,h/\mathrm{Mpc}$), there is a degeneracy between $(1+\Sigma_{1h})$ and the second moment of the luminosity function. This degeneracy can be broken by observing large scales where the clustering term provides a measurement of the first moment of the luminosity function, or on smaller scales where $u_S \to 0$ and the 1-halo term vanishes, leaving a measurement of the shot power on its own.

2.3 Instrument effects

Resolution transfer functions

The beam transfer function has been well-developed by [87], for intensity maps, and in [30] in the case of cross-correlations between intensity maps and galaxy cross-correlations. I present a general discussion on the cross-correlation of two maps featuring different smoothing.

Finite resolution due to the instrument or redshift space uncertainties can be modeled as a convolution between the angular beam response and the underlying density field. In the case of smoothed galaxy maps and line intensity maps,

$$\begin{aligned} \delta_I^{sm}(\mathbf{r}) &= T_I(\mathbf{r}) \star \delta_I(\mathbf{r}) \\ \delta_g^{sm}(\mathbf{r}) &= T_g(\mathbf{r}) \star \delta_g(\mathbf{r}) \end{aligned} \tag{2.34}$$

where δ and δ^{sm} are the unsmoothed and smoothed density fields in position space, denoted as $\mathbf{r}$. $\star$ denotes a convolution. Based on these fields, the power spectra in the two autocorrelation maps and the cross-correlation map can be expressed as

$$\begin{aligned}
\left\langle \delta_I^{sm} \delta_I^{sm} \right\rangle (\mathbf{k}) &= T_I^2(\mathbf{k}) P_I(\mathbf{k}) \left(2\pi\right)^3 \delta(\mathbf{k}) \\
\left\langle \delta_I^{sm} \delta_g^{sm} \right\rangle (\mathbf{k}) &= T_I(\mathbf{k}) T_g(\mathbf{k}) P_\times(\mathbf{k}) \left(2\pi\right)^3 \delta(\mathbf{k}) \\
\left\langle \delta_g^{sm} \delta_g^{sm} \right\rangle (\mathbf{k}) &= T_g^2(\mathbf{k}) P_g(\mathbf{k}) \left(2\pi\right)^3 \delta(\mathbf{k}),
\end{aligned} \tag{2.35}$$

owing to the property that convolution in position space maps to multiplication in Fourier space. I define the smoothed power spectra as

$$\begin{aligned}
P_I^{sm}(\mathbf{k}) &= T_I^2(\mathbf{k}) P_I(\mathbf{k}) \\
P_\times^{sm}(\mathbf{k}) &= T_I(\mathbf{k}) T_g(\mathbf{k}) P_\times(\mathbf{k}) \\
P_g^{sm}(\mathbf{k}) &= T_g^2(\mathbf{k}) P_g(\mathbf{k}).
\end{aligned} \tag{2.36}$$

Here, T_I and T_g are the resolution transfer functions for the intensity map and galaxy redshift survey maps, respectively, given by [16, 30]

$$\begin{aligned}
T_{I(g)}(\mathbf{k}) &= T_{I(g)}^{||}(k_{||}) T_{I(g)}^{\perp}(k_\perp) \\
T_{I(g)}^{||}(k_{||}) &= \exp\left[-\frac{1}{2} \left(\frac{k_{||}}{k_{\mathrm{res,I(g)}}^{||}} \right)^2 \right] \\
T_{I(g)}^{\perp}(k_\perp) &= \exp\left[-\frac{1}{2} \left(\frac{k_\perp}{k_{\mathrm{res,I(g)}}^{\perp}} \right)^2 \right],
\end{aligned} \tag{2.37}$$

where the subscript $I(g)$ represents the intensity map (galaxy redshift survey). Here,

$$\begin{aligned} k_{\rm res}^{||} &= \frac{c\ \delta z}{H(z)} \\ k_{\rm res}^{\perp} &= \left[d_A^2 \delta\Omega\right]^{-1}, \end{aligned} \tag{2.38}$$

where d_A is the angular diameter distance, $\delta\Omega$ is the pixel size of the beam, and δz is the redshift resolution of the survey. In the case of the intensity map, $\delta z = (z+1)/R$, with R the resolving power of the instrument's spectrometer.

3 LIM SCIENCE: FORECASTS & COSMIC VARIANCE EVASION

In this chapter, I describe the forecasting formalism for intensity mapping cross-correlations. I apply the Fisher matrix formalism to the noise model assumed for LIM surveys, continuing the discussion from the previous chapter. I use theoretical space-based instrument focusing on measuring the [CII] intensity at $z = 1$, demonstrating that the sensitivity can be greatly improved through cross-correlation with a galaxy redshift survey like the Nancy Grace Roman Space Telescope. **The chapter is reproduced with minimal modifications from Oxholm and Switzer [113]**. For the reader unversed in the Fisher matrix formalism and Bayesian statistics, I provide a discussion in Appendix B.

3.1 Dimensionless noise parameters and cosmic variance evasion

The intensity and bias are completely degenerate, so we group the terms together as the *biased intensity* $[Ib]$. In the calculations that follow, we define the biased intensity simply as the product of the intensity I and a constant bias b, specified by Equations 2.6 and 2.8, without the inclusion of redshift-space distortions (RSD) or scale-dependent bias. $[Ib]$ therefore contains information about the integral of the line mass-luminosity function $L(M, z)$ and the halo mass cutoff $M_{\min}$. However, our formalism can be generalized to include RSD and scale-dependent biases in $[Ib]$ without significantly changing our conclusions. This generalization would provide information on structure growth, primordial non-Gaussianity, and nonlinear effects leading to scale-dependent biases on small scales. The mass of halos hosting star formation could also be measured through $M_{\min}$, using RSD to separate I from b.

Using only information from the intensity map, $[Ib]$ is also degenerate with δ_m. The

latter is subject to cosmic variance because it depends on the measurement of waves in the matter density field, with a variance limited by the number of observable modes. Because $[Ib]$ and δ_m are degenerate, cosmic variance in δ_m is coupled to variance in $[Ib]$.

The degeneracy may be broken through the inclusion of a second map tracing the matter overdensity, e.g. a galaxy redshift survey. In this case, the galaxy field δ_g is given by

$$\delta_g(\mathbf{r}, z) = b_g(z)\delta_m(\mathbf{r}, z), \tag{3.1}$$

where the bias b_g pertains to galaxies observed in the galaxy redshift survey. Generally, $b \neq b_g$ because intensity mapping and galaxy redshift surveys do not observe the same galaxy populations. This can be attributed to different halo mass cutoffs for the two tracers (set by luminosity cutoffs in galaxy redshift surveys) and scatter in the probability a given halo will be populated by line-emitting gas or a directly-observable galaxy.

Figure 3.1 shows a comparison between the three realistic simulated fields δ_m, δ_I, and δ_g. Because δ_g traces δ_m, we can use it to measure the fluctuations in the density field, allowing us to remove the contributions from δ_m to cosmic variance in δ_I.

Cross-correlation statistics

We forecast LIM cross-correlations using the Fisher matrix formalism. We begin with three power spectra,

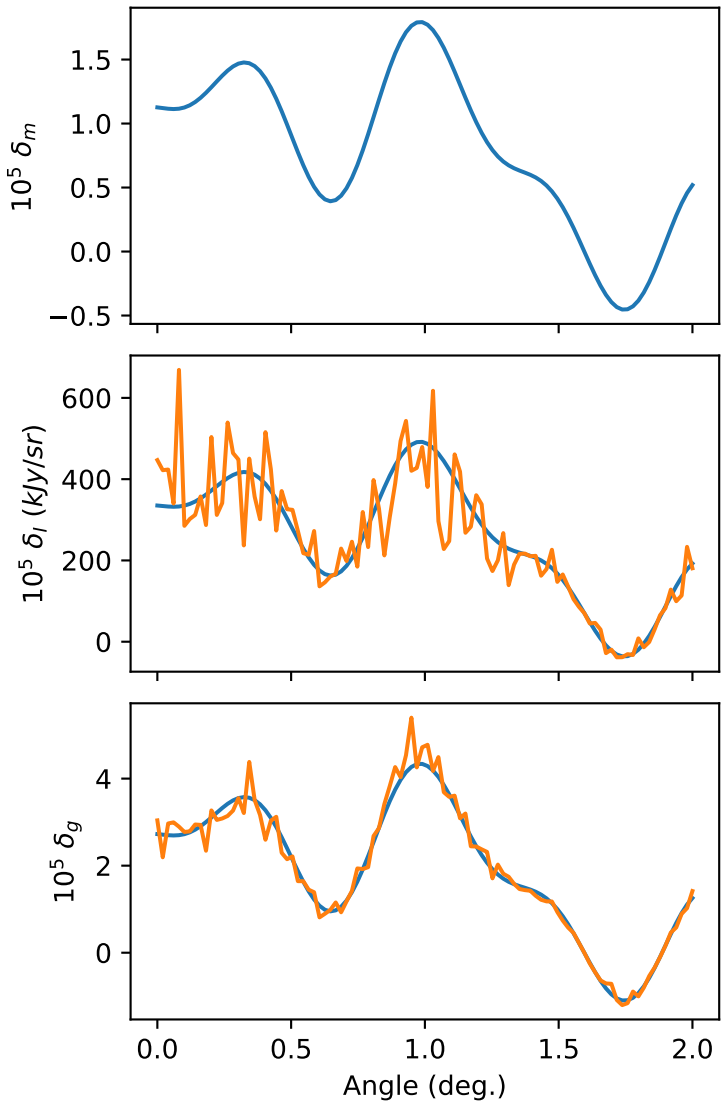

Figure 3.1: Overdensities over 2 deg. corresponding to the (top) matter, (middle) intensity, and (bottom) galaxy fields, where the latter two include arbitrary levels of Gaussian noise.

$$P_I(\mu,k,z) = T_I^2(\mathbf{k},z)\left([Ib]^2(z)P_m(k,z)+I_2(z)\right)+P_N(z) \tag{3.2}$$

$$P_{I\times g}(\mu,k,z) = T_I(\mathbf{k},z)T_g(\mathbf{k},z)\Bigg(I(z)b(z)b_g(z)F_{I,RSD}(\mu,k,z)F_{g,RSD}(\mu,k,z)P_m(k,z) + P_{\rm shot}^{I\times g}(z)\Bigg) \tag{3.3}$$

$$P_g(\mu,k,z) = T_g^2(\mathbf{k},z)\left(b_g^2(z)F_{g,RSD}^2(\mu,k,z)P_m(k,z)+\frac{1+\sigma_{1h}^g(\mu,k,z)}{\bar{n}(z)}\right), \tag{3.4}$$

For later convenience, we re-parameterize Equation 3.2 in terms of a dimensionless noise term W_I given by

$$W_I(\mathbf{k},z) = \frac{I_2(z)+P_N(z)/T_I^2(\mathbf{k},z)}{[Ib]^2(z)P_m(k,z)}, \tag{3.5}$$

with implied $\mathbf{k}, z$ dependence, representing fractional noise in the intensity mapping measurement of the clustering power spectrum due to shot noise and instrument noise. W_I can be generalized to also include residual foregrounds and interloping lines. With this substitution, Equation 3.2 evaluates to

$$P_I(\mathbf{k},z) = [Ib]^2(z)T_I^2(\mathbf{k},z)P_m(k,z)\left[1+W_I(\mathbf{k},z)\right]. \tag{3.6}$$

We can analogously define the power spectra associated with the galaxy redshift survey, P_g, and the cross-correlation between the two surveys, $P_\times$, as

$$P_g(k,z) = b_g^2P_m\left[1+W_g(k,z)\right] \tag{3.7}$$

$$P_\times(\mathbf{k},z) = T_I(\mathbf{k},z)[Ib]b_gP_m\left[1+W_\times(k,z)\right], \tag{3.8}$$

with associated dimensionless noise terms given by

$$W_g(k,z) = \frac{1}{\bar{n}(z) b_g^2(z) P_m(k,z)} \tag{3.9}$$

$$W_\times(k,z) = \frac{P^\times_{\rm shot}(z)}{[Ib](z) b_g(z) P_m(k,z)}. \tag{3.10}$$

Here, $\bar{n}$ represents the number density of galaxies observed in the galaxy redshift survey and $P^\times_{\rm shot}$ is the cross-shot power, representing correlated shot noise from the number of galaxies observed by both surveys. We estimate the cross-shot power as [23] (also listed in Equation 2.31)

$$P^\times_{\rm shot}(z) = \alpha(z) \int_{M^\times_{\rm min}}^{\infty} L(M,z) n_g(M,z) n(M,z) dM, \tag{3.11}$$

where $n_g(M)$ is the halo occupation distribution of the galaxy redshift survey, which contributes to the number density of detected galaxies as $\bar{n} = \int_{M^g_{\rm min}}^{\infty} n_g(M,z)\, n(M,z)\, dM$, with $M^g_{\rm min}$ the halo mass corresponding to the lower-luminosity threshold. $M^\times_{\rm min}$ is the minimum halo mass for galaxies observable in both surveys; we take $M^\times_{\rm min} = M^g_{\rm min}$ assuming the luminosity threshold in the galaxy redshift survey does not reach the smallest halos contributing to the $[CII]$ intensity. Note that Equation 2.31 is approximate, as we have left out potentially important physics, such as scatter between the two galaxy populations, a soft cutoff for $M^\times_{\rm min}$, and contributions from the 1-halo power spectrum. Later in the paper, we will explore marginalizing over $P^\times_{\rm shot}$, leading to increased variance on small scales where the shot power is non-negligible compared to the clustering power spectrum.

We stress that the dimensionless noise parameters W_I, $W_\times$, and W_g are scale-dependent; on large scales where the clustering power spectra tend to dominate, the parameters tend to be much smaller than one. On small scales where instrument

noise, shot power, and/or the 1-halo power spectrum dominate, the dimensionless noise parameters are larger than one, signifying increased variance in the maps.

Auto- and cross-correlation sensitivities

We derive the sensitivity of the cross-correlation using the Fisher matrix formalism. We begin with the assumption that we can utilize information from all three maps: the intensity map, the galaxy map, and the cross-correlation map. In this case, the covariance matrix of the the intensity map and galaxy redshift survey is given by

$$\Sigma = \begin{pmatrix} P_I & P_\times \\ P_\times & P_g \end{pmatrix}. \tag{3.12}$$

and the Fisher matrix is given by (see B for additional context) Tegmark et al. [151]

$$F_{ij} = \frac{1}{2}\mathrm{Tr}\left[\Sigma^{-1}\frac{\partial\Sigma}{\partial p_i}\Sigma^{-1}\frac{\partial\Sigma}{\partial p_j}\right], \tag{3.13}$$

where p_i corresponds to the varied parameters, e.g. $[Ib]$ and P_m.

As a first step, we calculate errors assuming information only in the line intensity map, i.e. the line intensity autocorrelation. Setting $\Sigma = P_I$ and inserting into Equation 3.13 with $p_i = [Ib]$, we arrive at the autopower errors,

$$\left.\frac{\sigma^2_{Ib}(\mathbf{k})}{(Ib)^2}\right|_{\mathrm{auto}} = \frac{(1+W_I(\mathbf{k}))^2}{N_{\mathrm{modes}}(\mathbf{k})}, \tag{3.14}$$

with N_{modes} the number of modes at a given wavenumber k. Note that z-dependence is implied. The first term in the parentheses describes the cosmic variance limit while the second describes variance in the map not originating from clustering of large-scale structure. Equation 3.14 is analogous to the Knox Formula describing errors in the

cosmic microwave background [81], and the Feldman-Kaiser-Peacock Formula for errors in galaxy redshift surveys [52].

We can estimate the number of modes for a given wavenumber k and line of sight angle μ by using the isotropic mode-counting formula,

$$N_{\rm modes}(\mathbf{k}) \approx \frac{k^2 V_{\rm surv}}{8\pi^2}\delta k \delta\mu, \tag{3.15}$$

where μ is the angle of $\mathbf{k}$ with respect to the line of sight, δk and $\delta\mu$ are the widths of the k and μ bins, and $V_{\rm surv}$ is the survey volume.

As a next step, we calculate errors in the inference of $[Ib]$ using information between both P_I and P_g, and the cross-correlation $P_\times$. Inserting the full covariance matrix (Equation 3.12) into the Fisher matrix, marginalizing over P_m, and varying over $[Ib]$, we arrive at the exact solution

$$\left.\frac{\sigma^2_{Ib}(\mathbf{k})}{[Ib]^2}\right|_\times = \frac{W_I - 2W_\times + W_g + W_I W_g - W_\times^2}{N_{\rm modes}(\mathbf{k})}. \tag{3.16}$$

The cosmic variance term is no longer present, while there are additional contributions from $W_\times$ and W_g. Note that $W_\times$ contributes negatively to the fractional errors; this feature was pointed out by Liu and Breysse [93] studying constraints on f_{NL} using intensity mapping cross-power spectra. This effect can be contextualized through the map cross-correlation coefficient $\mathcal{R}_\times = (1 + W_\times)/\sqrt{(1 + W_I)(1 + W_g)}$. Cross-correlation errors are generally minimized when $\mathcal{R}_\times \to 1$, so increased correlated shot noise leads to decreased variance.

Finally, we stress that the variances listed in this section correspond to specific $\mathbf{k}$ vectors, specified by a magnitude k and the cosine of the angle to the line-of-sight μ. Accurate variance per k must be performed by integrating Fisher matrices over μ, i.e.

$F_{ij}(k) = \int d\mu F_{ij}(k,\mu)$. This is particularly important when factoring in RSD, and in modes where the resolution transfer function approaches zero. μ-dependence enters the resolution transfer function because generally, the beam and frequency resolutions do not yield identical limits on perpendicular and parallel modes, respectively.

Note that while we focus on cross-correlation with galaxy redshift surveys, our formalism can be extended to other cross-correlations, including those between two intensity maps. However, this requires an understanding of correlated noise between the two maps and requires further study.

Robustness of the cross-correlation sensitivity

The qualitative features of the errors described by Equation 3.16 are robust to a variety of assumptions on the model and availability of data, namely, marginalizing over the cross-shot power, the non-inclusion of intensity mapping autocorrelation data, and additional sources of stochasticity in the cross-power spectrum.

Marginalizing over shot power and/or 1-halo terms in the cross-power spectrum

Our formalism for the cross-shot power given in Equation 2.31 is a rough estimate and leaves out many important details related to astrophysics and the 1-halo power spectrum. We therefore examine the conservative approach of marginalizing over $P^{\times}_{\rm shot}$.

Marginalizing over $W_\times$ and P_m, Equation 3.16 instead evaluates exactly to

$$\left.\frac{\sigma^2_{Ib}(\mathbf{k})}{[Ib]^2}\right|^{\text{marg.}}_{P^\times_{\text{shot}}} = \frac{W_I - 2W_\times + W_g + \frac{1}{2}(W_I^2 + W_g^2) - W_\times^2}{N_{\text{modes}}(\mathbf{k})} \tag{3.17}$$

$$\left.\frac{\sigma^2_{P^\times_{\text{shot}}}(\mathbf{k})}{P^2_{\times\text{shot}}}\right|^{\text{marg.}}_{Ib} = \frac{2 - 2\tilde{W} + \tilde{W}^2/2}{N_{\text{modes}}(\mathbf{k})}, \tag{3.18}$$

where we have also solved for errors in the cross-shot power for completeness, and we have defined $\tilde{W} = (W_I + W_g)/W_\times$ for brevity. Note that here, cosmic variance contributes to the cross-power spectrum errors as a factor of $2/N_{\text{modes}}$.

Comparing Equation 3.17 to Equation 3.16, we find that terms linear in the W parameters are identical. We refer to these terms linear in W as the first-order errors. Higher-order terms, however, are different between the two surveys; terms quadratic in W_I and W_g appear. On small scales where the clustering power spectrum is subdominant in either the intensity or galaxy redshift survey maps (W_I or $\mathrm{W_g} > 1$), marginalizing over $P^\times_{\text{shot}}$ results in higher errors. On large scales where W_I and $\mathrm{W_g} < 1$, marginalizing over $P^\times_{\text{shot}}$ has little effect on the variance.

Exclusion of information from the auto-power of the intensity map

The covariance matrix in Equation 3.12 assumes that information is usable in both the intensity map and the galaxy redshift survey. In many cases, the intensity mapping autocorrelation signal can be contaminated by additive biases due to foregrounds, interloping lines, and other systematics. It is therefore useful to calculate errors assuming no information from the intensity map autocorrelation.

In this case, we define the data vector Θ by the two-point correlation functions

defined by $\Theta = (P_\times, P_g)$. The covariance matrix is given by

$$\Sigma = \begin{pmatrix} C_{Ig}^{Ig} & C_{Ig}^{gg} \\ C_{Ig}^{gg} & C_{gg}^{gg} \end{pmatrix} \tag{3.19}$$

where $C_{Ig}^{Ig} = P_\times^2 + P_I P_g$, $C_{Ig}^{gg} = 2P_\times P_g$, and $C_{gg}^{gg} = 2P_g^2$ are the covariances per mode, assuming Gaussian fields in δ_I and δ_g.

Using the Fisher matrix for information in the mean (rather than the covariance),

$$F_{ij} = \frac{1}{2}\mathrm{Tr}\left[\Sigma^{-1}\left(\frac{\partial\Theta^T}{\partial p_i}\frac{\partial\Theta}{\partial p_j} + \frac{\partial\Theta^T}{\partial p_j}\frac{\partial\Theta}{\partial p_i}\right)\right], \tag{3.20}$$

and plugging Equation 21 and Θ into Equation 3.20, we again find that the first-order sensitivity in $[Ib]$ is identical to that shown in Equation 3.16, with differences appearing at second-order:

$$\begin{aligned} \left.\frac{\sigma_{Ib}^2(\mathbf{k})}{[Ib]^2}\right|_\times &= \frac{W_I - 2W_\times + W_g}{N_{\mathrm{modes}}} \\ &\quad + \frac{W_I W_g - 4W_\times W_g + W_\times^2 + 2W_g^2}{N_{\mathrm{modes}}}. \end{aligned} \tag{3.21}$$

Cosmic variance is still suppressed because P_m can be marginalized over through $P_\times$ and P_g.

For a final case, we calculate errors including only information from the cross-correlation $P_\times$. Using a covariance $\Sigma = C_{Ig}^{Ig}$ and data $\Theta = P_\times$ and plugging into Equation 3.20, we arrive at

$$\left.\frac{\sigma_{Ib}^2(\mathbf{k})}{[Ib]^2}\right|_{\times\ \mathrm{only}} = \frac{1}{N_{\mathrm{modes}}} + \frac{(1+W_I)(1+W_g)}{N_{\mathrm{modes}}(1+W_\times)^2}. \tag{3.22}$$

Here, cosmic variance variance has re-appeared because it is not possible to marginalize

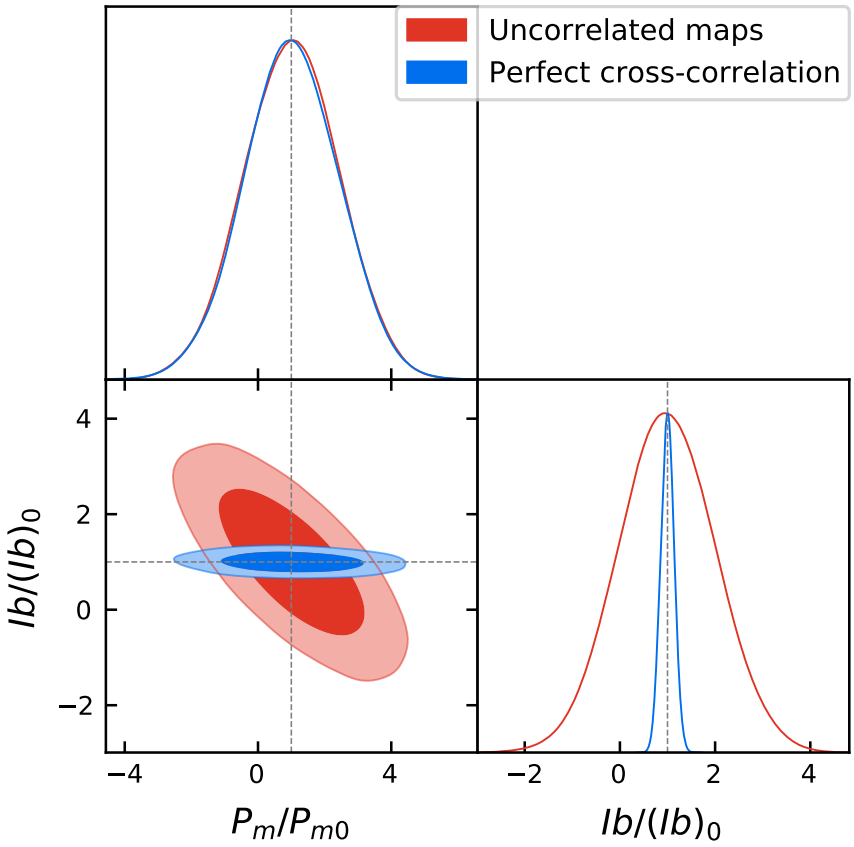

Figure 3.2: Illustration of cosmic variance evasion technique for a single mode in the cross-power spectra given by Equation 3.24 with noise parameters arbitrarily chosen as $(W_I, W_\times, W_g) = (0.01, 0, 0.01)$. The red ellipse shows the case where $r_\times = 0$, i.e. the maps are uncorrelated, resulting in a variance-limited measurement in $[Ib]$. Here, measurements of $Ib/(Ib)_0$ and P_m/P_{m0} are degenerate in P_I, resulting in coupling between errors in the P_m and $[Ib]$. The blue ellipse shows the $r_\times = 1$ case, where we are able to flatten the covariance ellipse in the $Ib/(Ib)_0 - P_m/P_{m0}$ plane, allowing us to marginalize the P_m errors with minimal residual errors.

over P_m.

Additional sources of stochasticity

The galaxy redshift survey and intensity mapping survey may not identically trace the underlying matter field. We benchmark this effect through a cross-correlation

(stochasticity) coefficient $r_\times$, contributing to the cross-power spectrum as

$$P_\times^r = [Ib] b_g P_m \left[r_\times + W_\times \right]. \tag{3.23}$$

This is purely a choice of convention, as all sources of decorrelation can also be absorbed into $W_\times$ and marginalized or measured. Marginalizing over $W_\times$ and P_m, residual stochasticity contributes to the fractional variance in the cross-power (analogous to Equation 3.17) as

$$\begin{aligned} \left.\frac{\sigma_{Ib}^2(\mathbf{k})}{[Ib]^2}\right|_{r_\times} &= \frac{1 - r_\times^2 - 2 r_\times W_\times + W_I + W_g}{N_{\rm modes}(\mathbf{k})} \\ &+ \frac{-W_\times^2 + (W_I^2 + W_g^2)/2}{N_{\rm modes}(\mathbf{k})}. \end{aligned} \tag{3.24}$$

Note that cosmic variance appears when the cross-correlation coefficient $r_\times \neq 1$, and Equation 3.17 is recovered in the limit that $r_\times \to 1$. In the limit that $r_\times \to 0$, we recover the same cosmic variance term as Equation 3.14. Note that nonlinear processes that cause $r_\times < 1$ tend to appear on small scales, similar to those where the shot power becomes dominant; effects include scale-dependent biases and contributions to the 1-halo power spectrum that may be incorrectly modeled.

Equation 3.24 is useful to illustrate the importance of highly-correlated maps in canceling cosmic variance. Figure 3.2 shows error contours for a single mode in the $[Ib]$-P_m plane for two cases: perfectly uncorrelated maps ($r_\times = 0$), and perfectly correlated maps ($r_\times = 1$). In the uncorrelated case, the degeneracy between P_m and $[Ib]$ is shown clearly in the error ellipse; cosmic variance errors in P_m are coupled to errors in $[Ib]$. Note, however, that the degeneracy is mildly broken by the appearance of P_m in the clustering power of the galaxy redshift survey. In the perfectly correlated case, the degeneracy is broken and errors in $[Ib]$ are no longer coupled to those in P_m,

so errors in the former are limited by noise in the maps, rather than cosmic variance.

3.2 Designing an intensity mapping survey without cosmic variance

Survey optimization

Given a fixed total time for a survey, Equations 3.14 and 3.16 can be used to optimize the total survey area $A_{\rm surv}$, in order to reduce errors in a given k. Throughout this section we assume W_I is dominated by instrument noise, rather than shot noise or residual foregrounds. Increased integration time per pixel linearly decreases instrument noise and therefore W_I. However, the increased integration time per pixel results in a smaller number of observed pixels, linearly decreasing the scan area $A_{\rm surv}$ and therefore $N_{\rm modes}$. Different terms present in Equations 3.14 and 3.16 scale with survey area (with fixed total survey time) as

$$\begin{aligned} \frac{1}{N_{\rm modes}} &\propto A_{\rm surv}^{-1} \\ \frac{W_I}{N_{\rm modes}} &\propto A_{\rm surv}^{0} \\ \frac{W_I^2}{N_{\rm modes}} &\propto A_{\rm surv}^{1}. \end{aligned} \tag{3.25}$$

Errors in the autocorrelation scale analogously to conclusions made in Knox [81]. When instrument noise dominates, there is a clear preference for small survey coverage with increased integration time per pixel. This is because, for an instrument noise-dominated survey, autocorrelation errors are proportional to $W_I^2/N_{\rm modes}$, which increase linearly with $A_{\rm surv}$. When $W_I < 1$, i.e. when cosmic variance dominates

the errors, it is best to widen the survey area. We therefore suggest optimizing the integration time per pixel for autocorrelation so that W_I is just below 1, over the widest area possible.

Cross-correlation errors scale slightly differently from autocorrelation errors. When we do not marginalize over $W_\times$, Equation 3.16 shows that W_I does not contribute beyond linear order. Based on the scaling of W_I with $N_{\rm modes}$, this would suggest no preference for wide or deep surveys when instrument noise dominates, but again, a clear preference for wide surveys when $W_I < 1$. On the other hand, if we marginalize over the cross-shot power, Equation 3.17 shows that the variance is quadratic in W_I, increasing proportionally to $A_{\rm surv}$; thus, a deep survey is preferred. Generally, however, deep surveys emphasize high-k modes, putting more weight on the modes where correlated shot modes is marginalized.

In the case where instrument noise is low, errors in the cross-power are not cosmic variance-limited. Instead, errors are limited by W_g, as described in Equations 3.16 and 3.17. Therefore, it is ideal to set the integration time such that the depths of the two surveys match, i.e. $W_I \approx W_g$. Increasing the integration time beyond this limit would only decrease W_I while W_g remains constant; increasing $A_{\rm surv}$, on the other hand, would increase $N_{\rm modes}$, thereby decreasing errors attributed to both W_I and W_g. This survey strategy extends the arguments of Knox [81] to the cross-power; errors in the cross-correlation are limited by noise in the galaxy redshift survey, rather than cosmic variance.

Realistic survey model

We benchmark our model by producing a realistic intensity mapping cross-correlation strategy for a realistic cross-correlation between a space-based [CII] line-intensity

mapping survey and the nominal 2000 deg^2 High-Latitude Survey for the Nancy Grace Roman Space Telescope [50] at $z = 1.5$.

The rest frequency of [CII] is $\nu_{\rm CII}^{\rm rest} = 1900$ GHz. We calculate the [CII] intensity by inserting the mass-luminosity function of Padmanabhan [116] into Equations 2.6 and 2.8, resulting in a biased intensity of $[Ib](z = 1.5) = 144\,{\rm Jy\ sr^{-1}}$. We model the Roman HOD through HOD0 in Smith et al. [141], with a multiplicative constant scaled to obtain an average galaxy number density of $\bar{n}(z = 1.5) = 0.0016\,{\rm h^3 Mpc^{-3}}$, and we calculate a bias $b_g(z = 1.5) = 2.3$.

We assume a 1/e beamwidth of 1 arcmin corresponding to a 70 cm primary mirror, and a spectral resolving power $R = 500$, resulting in a frequency resolution $\delta\nu = 1.27\,{\rm GHz}$, which we take to be equal to the single-channel bandwidth.

We assume the noise in the intensity map is background-limited with a background intensity of $I_{\rm bknd} = 9 \times 10^3\,{\rm kJy\ sr^{-1}}$, an accurate figure for the combined CMB, galactic Cirrus in typical clean regions out of the galactic plane, and CIB radiation [53, 54, 21]. Our strategy to calculate the NEI is to first relate $I_{\rm bknd}$ to the power absorbed by the detectors $P_{\rm det}$, through the relation $P_{\rm det} = \eta_{\rm det} I_{\rm bknd} \partial P/\partial I$, with $\eta_{\rm det}$ the detector efficiency and $\partial P/\partial I = A_d \Omega_{\rm inst} \delta\nu$, assuming an unpolarized source.

Here, the detector area A_d and the beam area $\Omega_{\rm inst}$ are related to the frequency $\nu = 760$ GHz and number of optical modes $N_{\rm opt}$ as $A_d \Omega_{\rm inst} = N_{\rm opt} \eta_{\rm opt} (c/\nu)^2$, with $\eta_{\rm opt}$ the optical efficiency. We assume $N_{\rm opt} = 1$ and $\eta_{\rm opt}\eta_{\rm det} = 0.20$. The resulting detector power is translated into a photon background-limited noise-equivalent power for a single mode $NEP = [h\nu P_{\rm det} + P_{\rm det}^2/\delta\nu]^{1/2}$ (e.g. [169]), where h is Planck's constant . This results in $NEP = 4.6 \times 10^{-20}\,{\rm W\ Hz^{-1/2}}$, a realistic but ambitious goal for, e.g. far-infrared kinetic inductance detectors [12, 22]. Finally, we calculate $NEI = NEP/\eta_{\rm det}/(\sqrt{2}\partial P/\partial I) = 69.2\,{\rm kJy\ sr^{-1}}$. The factor of $\sqrt{2}$ comes from the conversion from power spectral conventions of ${\rm Hz^{1/2}}$ to $s^{-1/2}$. The model survey

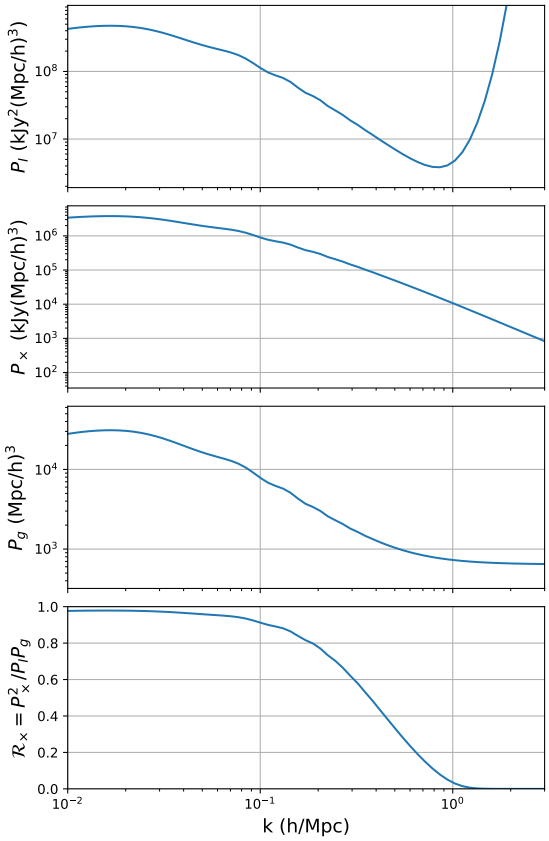

Figure 3.3: Power spectra corresponding to the wide survey model in 3.2: (top) intensity mapping auto-power spectrum, (upper middle) cross-power spectrum, (lower middle) galaxy auto-power spectrum, and (bottom) map-space cross-correlation coefficient.

occupies 2000 deg^2 over a range of redshift $\Delta z = 0.2$ over 417 days, (5 s per 1/e beamwidth) resulting in $V_{\rm surv} = 1.4\,h^{-3}$ Gpc^3.

The resulting power spectra are shown in Figure 3.3, and sensitivities are shown in Figure 3.4. The latter shows the fractional variance per k given three cases: autopower, cross-power errors using information from the cross-power only (labeled CV), and cross-power errors using information from all available maps, marginalized over P_m and $P_\times^{\rm shot}$; these errors are calculated by Equations 3.14, 3.22, and 3.17, respectively. We marginalize over $P_\times^{\rm shot}$ in the latter case to remain conservative about our simplified model describing Equation 2.31. We assume 32 bandpowers in k

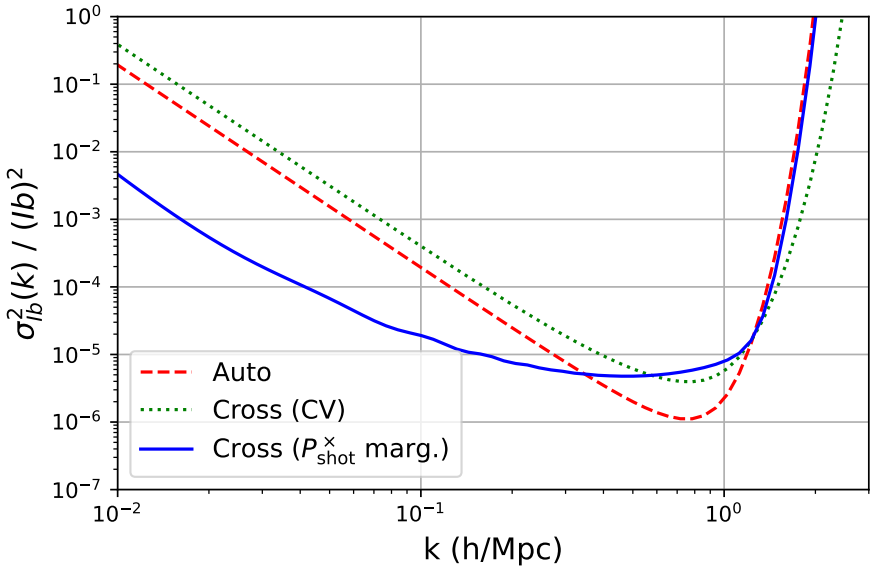

Figure 3.4: Fractional variance per mode in $[Ib]$. We model errors in the intensity map autocorrelation, and cross-correlation marginalized over $P^{\times}_{\rm shot}$, specified by Equations 3.14 and 3.17, respectively. The instrument design is specified in Section 3.2.

spanning $0.01 < k < 2.7\,\mathrm{hMpc}^{-1}$ equally spaced logarithmically, with Fisher matrices integrated over μ. We note that instrument noise dominates shot power, and we assume sufficient bandpass stability that noise due to residual foregrounds is also subdominant.

The cosmic variance-evading cross-power significantly outperforms the autopower and cross (CV) errors on large scales where the intensity and galaxy redshift survey maps are highly-correlated, i.e. $\mathcal{R}_{\times} \approx 1$. On smaller scales ($k \gtrsim 0.3\,\mathrm{hMpc}^{-1}$), autopower errors outperform crosspower errors because dimensionless noise in the galaxy redshift survey exceeds cosmic variance, i.e. $W_g > 1$. The cross (CV) case also outperforms the marginalized cross-power on smaller scales ($k \gtrsim 1.1\,\mathrm{hMpc}^{-1}$) because the latter is marginalized over the $P^{\times}_{\rm shot}$, thereby increasing errors.

Figure 3.5 shows variance per k as a function of survey area, assuming the same total survey time. We calculate the variance for two modes: $k = 0.02$ and $0.80\,\mathrm{hMpc}^{-1}$.

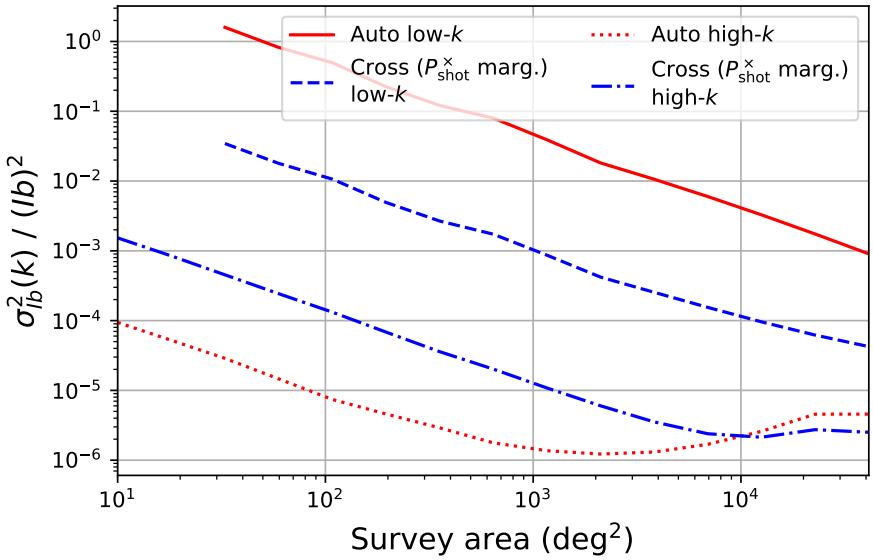

Figure 3.5: Fractional variance per mode in $[Ib]$ varying the survey area from 10 to 40000 deg^2 (full-sky) at fixed survey time.

Variance in the $0.02\,\mathrm{hMpc}^{-1}$ mode is minimized by increasing $A_{\rm surv}$ as much as possible. This is because $W_I < W_g$ even for the largest survey area, so increased survey depth does little to decrease variance in $[Ib]$. Furthermore, on these large scales the cross-power provides a drastic increase in sensitivity compared to the cosmic variance-limited autopower.

For $k = 0.80\,\mathrm{hMpc}^{-1}$ modes, the autopower produces smaller errors than the cross-power for almost all survey depths. Here, noise in the galaxy redshift survey exceeds cosmic variance, i.e. $W_g > 1$. For the largest survey areas, however, the crosspower outperforms the autopower, owing to a factor of 2 difference in terms proportional to W_I^2 in Equations 3.14 and 3.17. Though we marginalize over the cross-shot power, care must be taken to understand nonlinear physics on these scales to validate this conclusion. The autocorrelation variance for $k = 0.80\,\mathrm{hMpc}^{-1}$ is minimized for $A_{\rm surv} \approx 1100$ deg^2. This corresponds to the survey depth that matches cosmic variance, i.e. $W_I \approx 1$, matching conclusions described in Knox [81]. The

crosscorrelation variance features a similar minimum instead at $A_{\rm surv} \approx 10,000$ deg^2. On this scale, the depth of the intensity map matches that of the galaxy redshift survey, i.e. $W_I \approx W_g$. Finally, we note that in the case of increased noise in the intensity map, these minima would be pushed to proportionally smaller survey areas.

3.3 Conclusion

Intensity mapping cross-correlations provide a powerful means to measuring the biased intensity of a given tracer. Cross-correlation has well-established utility to rejectallows rejection of sources of contamination in the intensity map that are not correlated with the target galaxy population, such as interlopers and foregrounds [147, 37, 164]. Furthermore, cross-correlation measurements of the biased intensity can evade cosmic variance.

For a given k mode, cosmic variance can be mitigated if the fractional noise in the clustering power spectrum in both surveys (i.e. W_I and W_g) is less than 1, and if the stochasticity between the surveys is small. These requirements are straightforwardly achieved on large, linear scales. Smaller scales tend to feature higher fractional noise and higher stochasticity due to the dominance of nonlinear physics. On smaller scales, an intensity mapping autocorrelation may be preferable to a cross-correlation, because the latter introduces an additional source of noise from the cross-correlating survey, which may exceed cosmic variance. Note, however, that the use of the autocorrelation requires stronger control of contamination from foregrounds and interlopers. In either case, the depth of the intensity map is optimized when fractional noise in the intensity map matches that of the cross-correlating survey. We stress that this optimal depth depends on the scales of interest and the level of noise in the two surveys. There is therefore no one-size-fits-all optimum survey depth, but careful analyses using

the techniques and equations described in this paper provide a useful framework for designing a survey to achieve specific science goals.

4 EXCLAIM: MISSION OVERVIEW AND SYSTEMS ANALYSIS

Here, I provide an overview of the EXCLAIM instrument and survey. I begin with an introduction to the overall design of the instrument, before describing the anticipated background noise level. I then describe the survey scan strategy, and conclude by describing several important systems-level constraints on the instrument.

4.1 Introduction to EXCLAIM

In this section, I provide an overview of the EXCLAIM mission. I focus on the general design parameters, with a particular emphasis on the detector and optical systems. Then, I discuss the atmospheric background radiation, survey scan strategy, and systems-level considerations that will provide a foundation for the rest of the chapters in this thesis. Further details on the EXCLAIM instrument can be found in Switzer et al. [149]

The EXperiment for Cryogenic Large-aperture Intensity Mapping (EXCLAIM!) is a first-generation dedicated intensity mapping instrument. EXCLAIM is a suborbital balloon-borne mission led by NASA-Goddard Space Flight Center, equipped with superconducting microwave kinetic inductance detectors (MKIDs) and cryogenic optics. EXCLAIM is being built to map the intensities of [CII] and various CO lines, from $2.5 < z < 3.5$ and $z < 0.64$, respectively.

The primary scientific goal is to obtain cross-correlations of [CII] and CO with the BOSS-Stripe 82 region, spanning $\sim 270\,\mathrm{deg}^2$. Cross-correlation removes additive bias from the power spectrum signal. For EXCLAIM, atmospheric noise is too large to exploit cosmic variance evasion, i.e. $W_I \gg 1$ in Equation 3.14, and dominates the dimensionless noise parameter for the intensity map. In this sense, EXCLAIM is a pathfinder for future space missions that may exploit the cosmic variance evasion technique. Furthermore, it aims for the initial detection of the [CII] and CO line

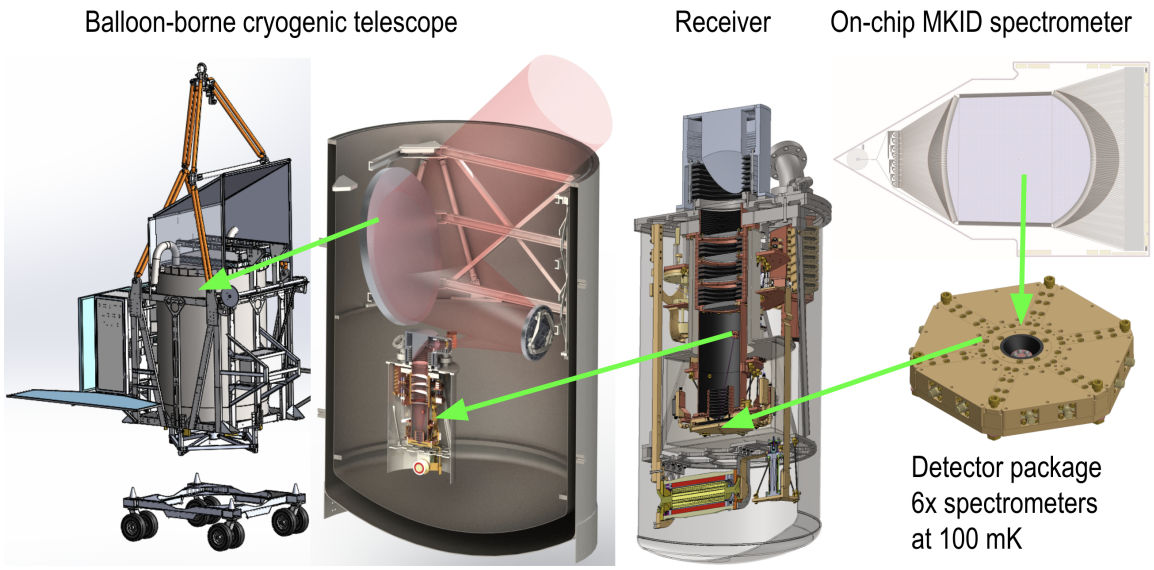

Figure 4.1: EXCLAIM instrument overview. Taken from Switzer et al. [149].

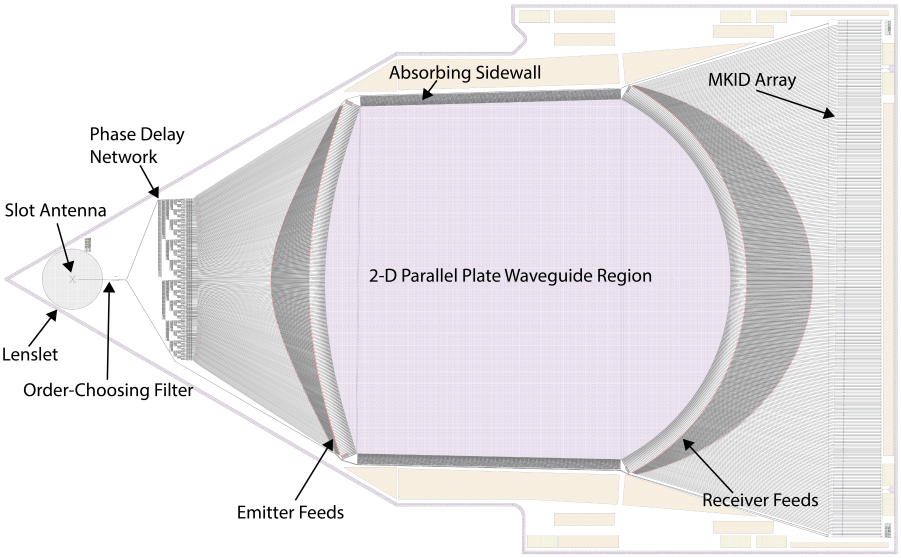

Figure 4.2: To-scale diagram of the EXCLAIM spectrometer. Taken from Switzer et al. [149].

intensity mapping signals, which may help to affirm or rule out models of galaxy evolution and cosmic star formation history.

EXCLAIM will be nearly atmospheric background-limited, owing to cooled mirrors,

an innovative spectrometer-on-a-chip (μ-Spec[1]), and low-noise MKIDs. The EXCLAIM instrument is shown in Figure 4.1. The leftmost panel shows the EXCLAIM dewar, roughly 2 m tall. The rotator on the top of the figure is where the balloon attaches to the ballast of the instrument[2]. The second panel from the left shows a cross-section of the dewar. Incident light (the red 'tube' in the figure) enters the dewar at an elevation of 45°, before reflecting off an 90 cm parabolic primary mirror. The beam reflects off a folding flat mirror (i.e. infinite focal length), converges to an intermediate focus, then reflects off a parabolic secondary mirror. Finally, the collimated beam passes through a cold stop and lens, focusing on the focal plane. The third figure from the left shows the 'submarine assembly' of the receiver, featuring filters and baffles. The rightmost panel shows the spectrometer package, sitting in the focal plane at the bottom of the submarine assembly.

The mirrors are cooled to 1.7 K, as they are coated by liquid helium throughout the flight (either directly submerged or sprayed with helium via the superfluid fountain effect). The effect of cooled mirrors on the anticipated sensitivity is shown in Figure 4.3, where Ambient refers to the temperature of the surrounding environment, and Cryogenic refers to a 1.7 K black body with 10% emissivity.

The μ-Spec spectrometers present a significant technological breakthrough for far-infrared telescope missions. μ-Spec features all elements of a grating spectrometer, fitting six on a single silicon wafer[3], representing an order of magnitude reduction in size compared to previous technologies. Figure 4.2 shows the design; light is coupled to the chip through a lenslet, which focuses onto a slot antenna. The light then passes through a niobium transmission line, then goes through a phase delay network. The

[1]Pronounced 'micro spec'

[2]The balloon expands to the size of a football field... I can't really wrap my head around how big that is.

[3]Roughly the size of a CD, for those who remember the ancient technology.

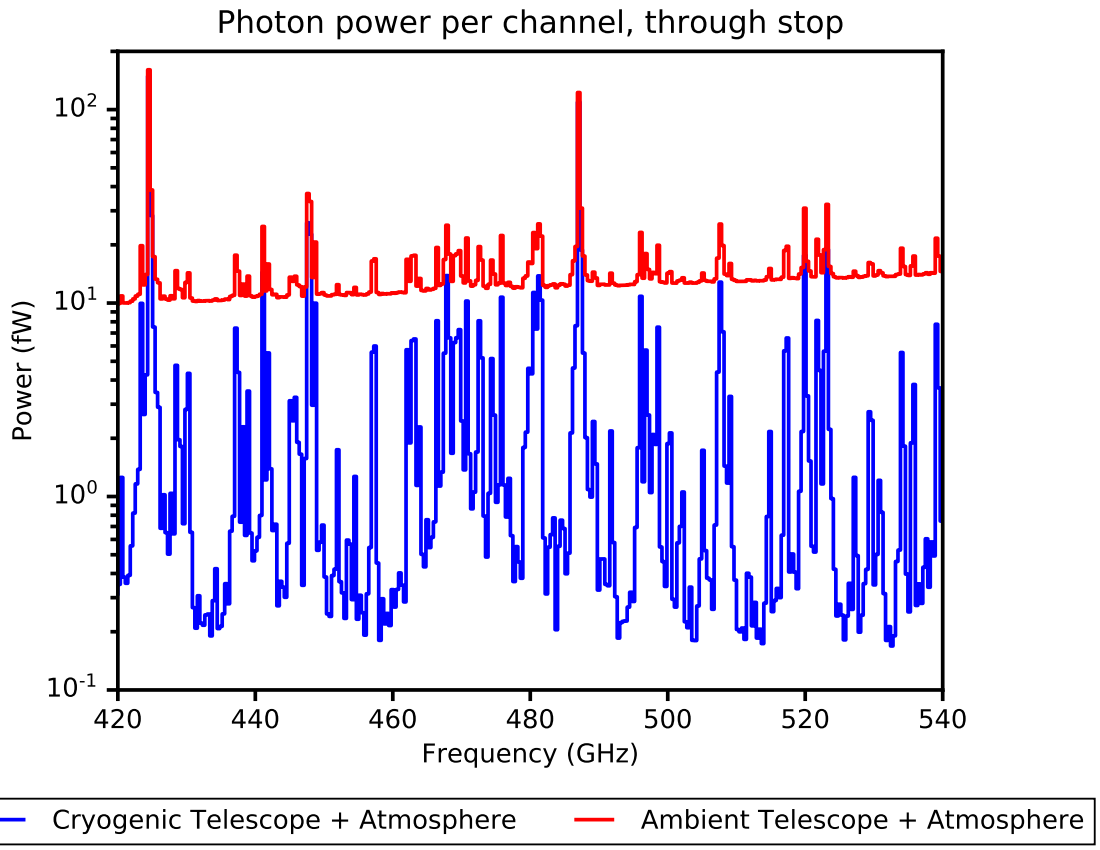

Figure 4.3: Anticipated EXCLAIM background loading assuming cooled and ambient optics. Taken from Switzer et al. [149].

phase delay network feeds into a set of emitters, where each emitter radiates with a unique phase. Light then passes through a 2-dimensional parallel plate waveguide region, and into the receiver feeds, each featuring a unique frequency. Finally, these receivers feed into the MKID array. The spectrometers developed for EXCLAIM will feature a resolving power $R \equiv (\text{frequency})/(\text{channel bandwidth}) = 512$.

4.2 Background signal

The extragalactic [CII] and CO signals are dwarfed by the atmospheric background and astrophysical foregrounds. While the atmospheric background, modeled using

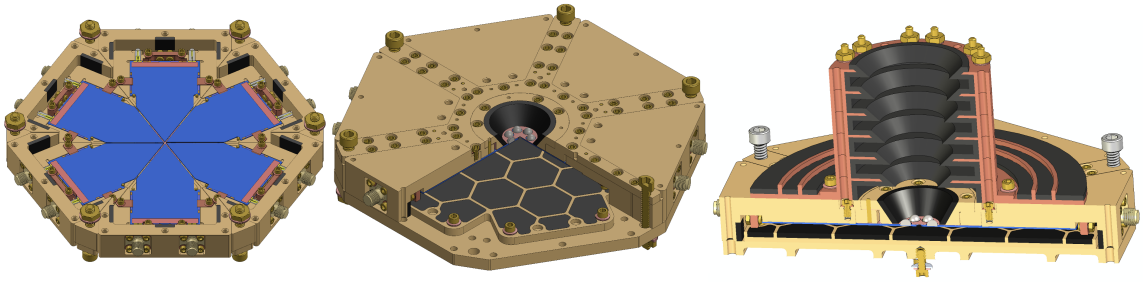

Figure 4.4: EXCLAIM focal plane, describing (left, center) the packaging for the six spectrometers and (right) baffles between the lenslet and lens. Taken from Switzer et al. [149].

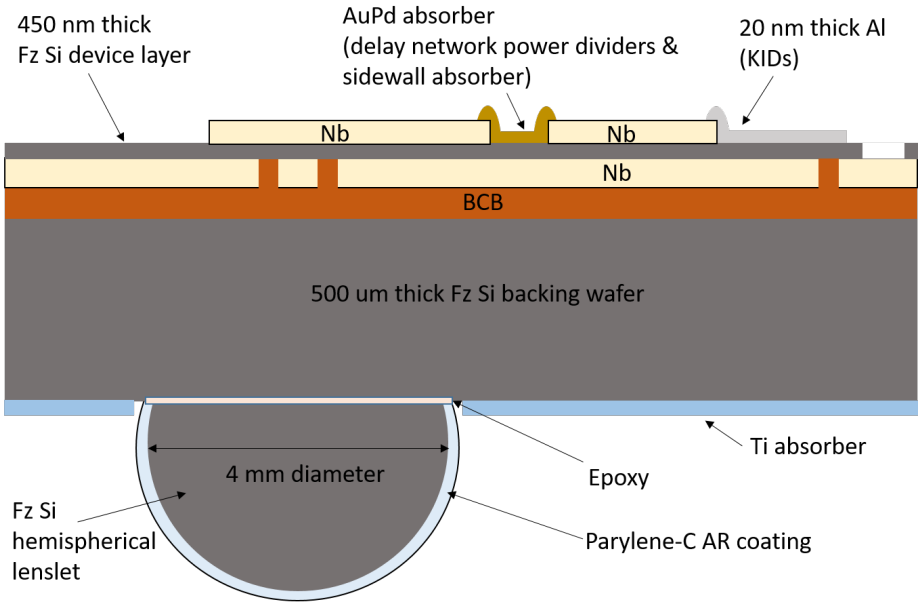

Figure 4.5: EXCLAIM spectrometer layers. Taken from Switzer et al. [149]. (Drawing is not to scale.)

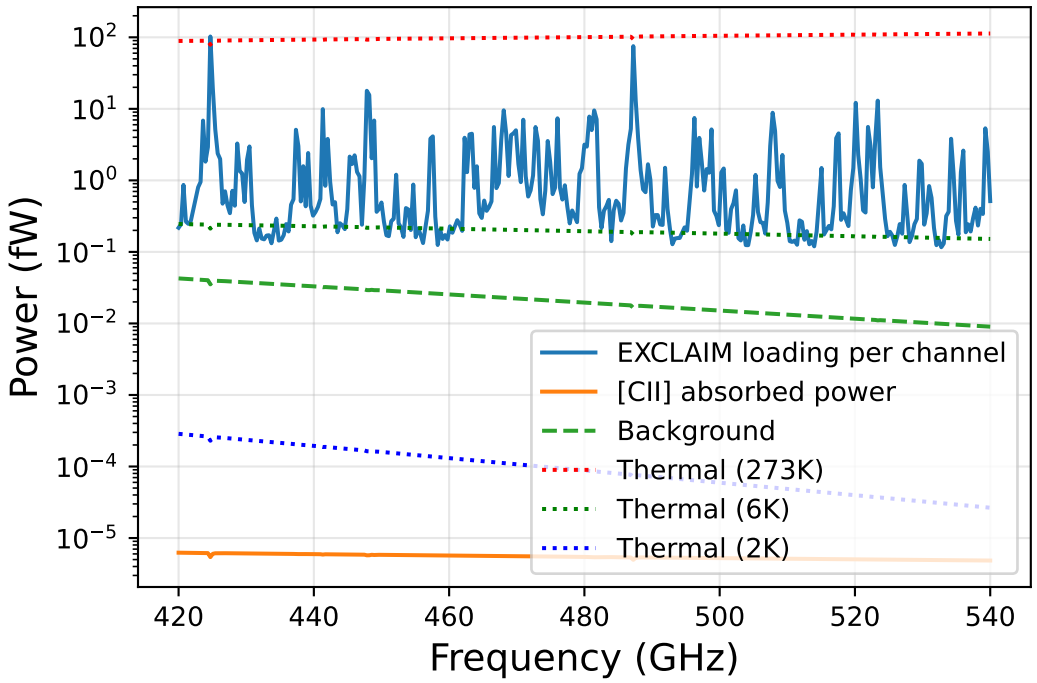

Figure 4.6: Demonstration of the various background levels of the EXCLAIM signal, including the space background signal (labeled Background).

Paine [117] based on an altitude of 36 km and a telescope elevation of 45°, is much lower than it is on the ground, it is still roughly an order of magnitude brighter than the background in space. The space background is primarily limited by the cosmic microwave background, cosmic infrared background, and galactic Cirrus emission, while shorter wavelengths are dominated by Zodiacal light.

Figure 4.6 shows a comparison between these levels of radiation; the atmospheric background varies between $\sim 0.2 - 100$ fW. The space background, on the other hand, is roughly an order of magnitude fainter. The figure also demonstrates the importance of a cooled telescope. Assuming a 10% emissivity, blackbody radiation from 273 K, 6 K, and 2 K mirrors are shown in the dotted curves. A 6 K telescope reduces the blackbody emission to the level of the faintest atmospheric channels, while the 273 K

emission would exceed all but the brightest channels. The incident power from a $10\,\mathrm{kJy\ sr^{-1}}$ is also shown, which equates to below $10^{-5}\,\mathrm{fW}$. This roughly equates to the expected [CII] intensity at $z = 3$ from the model of Padmanabhan [116].

4.3 Survey strategy

EXCLAIM seeks to perform extragalactic science by cross-correlating [CII] and CO intensity maps with galaxy redshift catalogs, and to perform galactic science by mapping neutral carbon ([CI]) in the Milky Way. The primary goal is to map the entirety of the BOSS-Stripe 82 (BOSS-S82) region, where galaxy redshift survey catalogs overlap with the EXCLAIM [CII] and CO surveys. BOSS-S82 spans the range where $21\mathrm{h} < \mathrm{RA} < 4\mathrm{h}$ and $-1.25 < \mathrm{DEC} < 1.25$, representing the right ascension and declination ranges, respectively.

The observations are projected to take place in a single overnight flight from Fort Sumner, New Mexico sometime between September 1 and October 15, 2023. This launch window would allow excellent coverage of the BOSS-S82 region, as well as other extragalactic and galactic science regions. Figure 4.7 shows the accessible regions from 8pm to 6am in Fort Sumner. The primary mission science will come from the Stripe-82 region, expected to be visible roughly between 9pm and sunrise; here, the instrument scans in azimuth, mapping to specific RA, declination coordinates. Visible regions are defined as those that pass through 45° elevation, the target pointing for the EXCLAIM instrument. During the beginning of the night, the Hyper Suprime-Cam (HSC) North region is visible. Starting around 9pm, the BOSS-S82 region is rising through the EXCLAIM horizon, and is visible until around 4am. Starting around 1am, the BOSS-S82 region is setting. Overlapping the S82 region are the HSC-Fall,

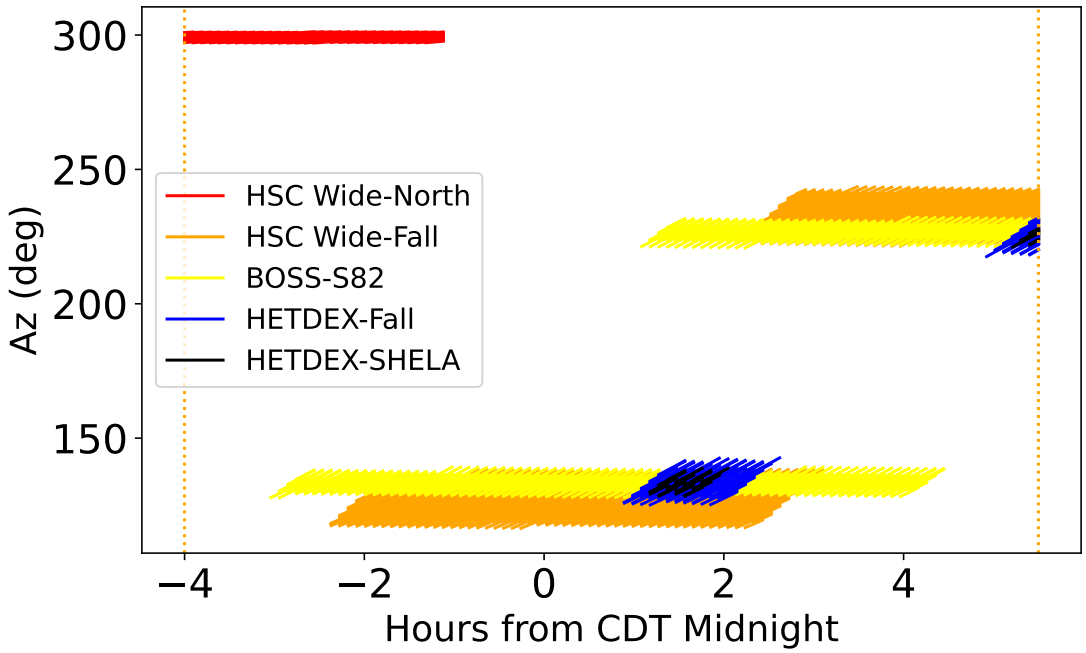

Figure 4.7: Azimuth pointing for various Hyper Suprime-Cam (HSC), BOSS-S82, and HETDEX fields.

HETDEX-Fall, and HETDEX-SHELA regions.[4]

Scan strategy: science

In EXCLAIM's regime of sensitivity, measurements of the biased intensity is largely independent of survey area, assuming the same survey time allocated to the particular measurements. In principle, smaller survey areas mean fewer k modes are measured, but there is a higher sensitivity per mode due to the higher integration time per pixel. Because EXCLAIM will be limited by instrument noise rather than cosmic variance, these competing effects largely cancel out.

[4]Previously, Palestine, Texas was a possible launch site to take place during a similar time frame. However, population growth in the surrounding regions, coupled with cost-benefit analyses by NASA Columbia Scientific Balloon Facility in case of the payload landing in a populated regions, renders an instrument the size of EXCLAIM unacceptable for launch.

In practice, this intuition is indeed correct for [CII], but less so for CO. Here, I studied the effect of declination span on sensitivity to the biased intensity, where declination spans ranged from $2.6 \pm 0.5\,\mathrm{deg}$. CO, on the other hand, has a weak trend toward higher sensitivities with larger declination span. In the most extreme example, CO(4-3) measurements are twice as sensitive for 3.1 deg declination span as they are for 2.1 deg. CO(6-5) sensitivities similarly increased by $\sim 40\%$. This is because, given a larger survey area, there is increased access to lower-k modes, which tend to be dominated by the clustering power spectrum over the shot power. Because the information in the biased intensity comes from the clustering power spectrum, it is advantageous to measure these lower-k modes. However, this is at the expense of measurements of the shot power, which also contain interesting information about the line intensity models, though they may be harder to interpret than the biased intensity, due to other competing terms such as interloper contamination and the 1-halo power spectrum.

Scan strategy: instrumentation

Beyond these effects on the power spectrum, a larger survey span may lead to gaps in the map, or an increased effective beamwidth. I assume the Raster scan is sinusoidal in azimuth at constant elevation, with the azimuth shown in Figure 4.8. Here, x and v describe the angular position and angular velocity of the scan relative to a central mean direction in azimuth. The vertical red dashes show the nominal time for the sky to rotate 1/3 of the beam size, relative to Earth. This is roughly the cutoff where sparser sampling leads to gaps in the map. These gaps are equivalent to convolving the sky signal with discrete sampling with angle $\delta\Theta = \omega_{\mathrm{Earth}} T_{\mathrm{scan}}/2$, with ω_{Earth} Earth's rotation rate and T_{scan} the period of the scan. I assume the period is roughly 14 s,

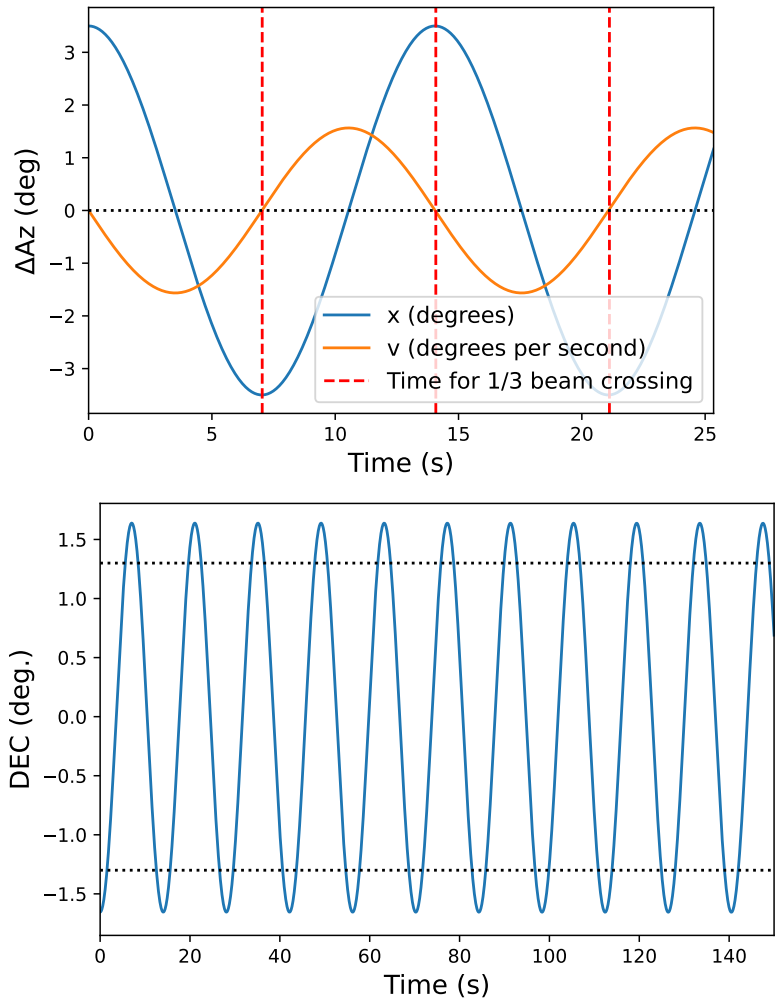

Figure 4.8: EXCLAIM Raster scan. The upper panel shows the angular position and angular velocity of the azimuth, while the bottom panel shows the declination, both as a function of time.

compliant with the requirement that half the scan period matche the time for the Earth to rotate 1/3 of the beam.

The bottom panel of Figure 4.8 shows the translation from azimuth to declination, assuming a September 1st flight from Ft. Sumner, NM. The nominal Raster scan pattern results in a declination throw of ± 1.6 deg. This completely covers the BOSS-S82 region, while extending slightly further in declination. This builds in resilience to

the effect of jitter, in which an anisotropic moment of intertia in the instrument may result in undesirable rotation modes which could limit the declination throw in some portions of the survey.

Figure 4.9 shows the RA, DEC of a Stripe-82 scan for 50 seconds of one potential observation with a throw of 1.7 deg. Here, the entire Stripe-82 declination is covered with some added padding to ensure the entire stripe is covered, even in the case of unwanted precession.

Precessional modes

Balloon-based instruments face the unique challenge of precessional modes. Ideally, the reaction wheel, a spinning wheel which rotates the instrument via angular momentum conservation, allows the instrument to scan in azimuth without affecting other degrees of freedom such as the elevation, which is set to be fixed at 45°. This slew in azimuth enables pointing over a range of sky coordinates (RA, declination). If the instrument's center of mass is perfectly located about the axis, the elevation is indeed fixed. However, if the center of mass is offset, the azimuthal rotation modes can couple to elevation rotation modes, leading to precession in the instrument[5]. A sine wave scan strategy was implemented to minimize the excitation of rotational modes that may contribute to this precession. Only a single frequency mode contributes to the signal, unlike other scan patterns like a step function, which features many higher-order rotational modes that may couple to precessional modes. Furthermore, changes in the liquid helium volume and ballast cause the moment of inertia tensor of the instrument to change throughout the duration of the flight. During the flight, the EXCLAIM team plans to alter the length of the rigging (i.e. the points where the dewar attaches to

[5]This can be calculated by diagonalizing the moment of intertia tensor and finding the principal axes of rotation.

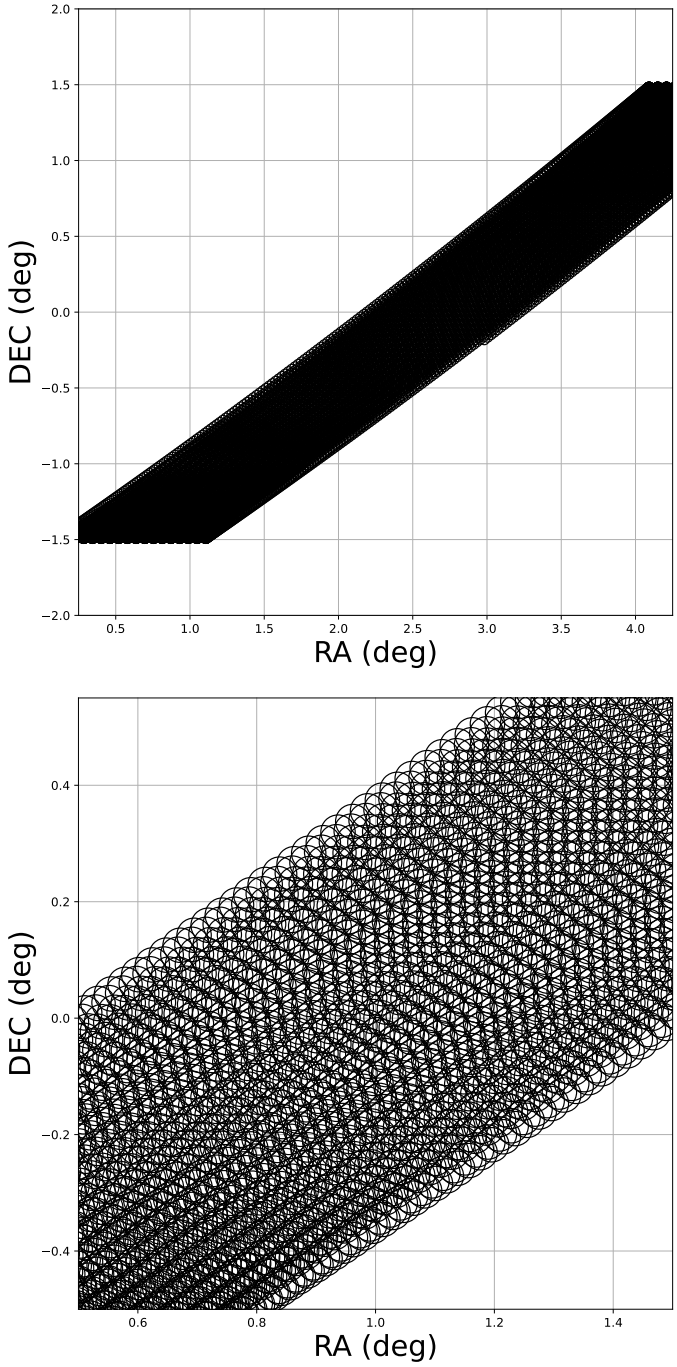

Figure 4.9: Raster scan image on the sky, after 50 seconds of observation. The top and bottom panels show the same curves, but the bottom plot is zoomed in to reflect the size of the beam relative to the scan coverage. The circles represent the FWHM of the beam.

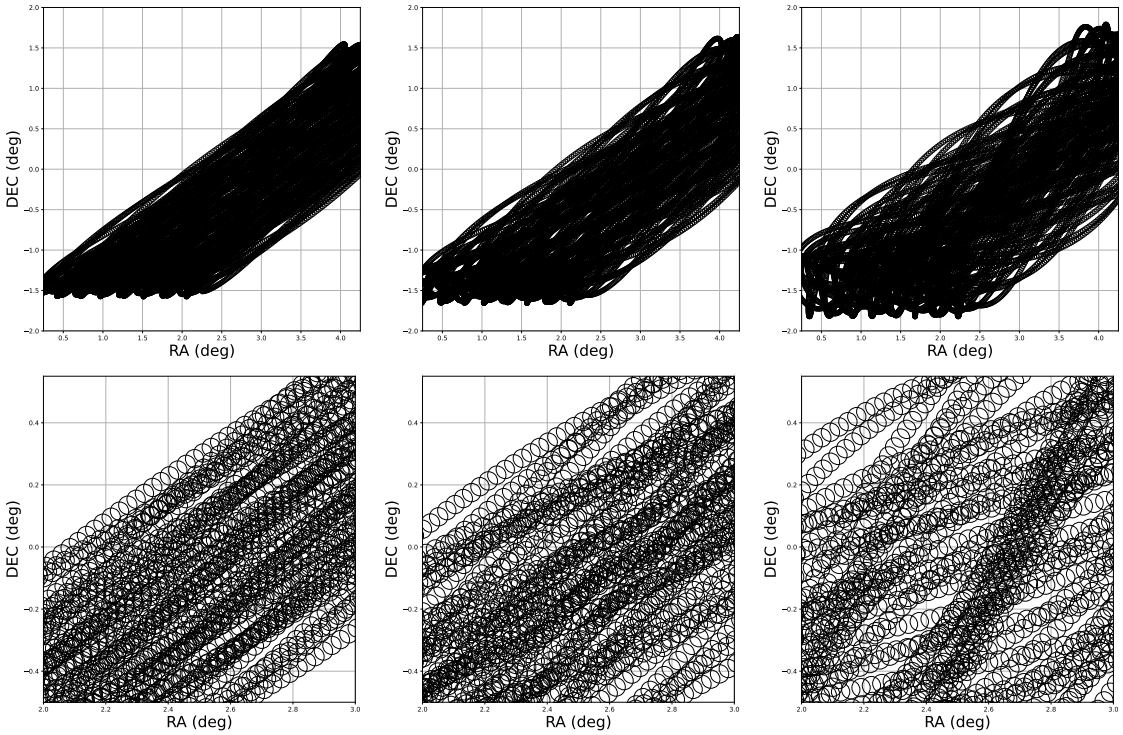

Figure 4.10: Stripe-82 coverage with precession due to a center-of-mass offset. The three columns correspond to a sinusoidal throw in azimuth with peak-to-peak amplitudes of $6, 12, 24$ arcmin, from left to right. The bottom row shows the same scan as the top, zoomed in to see the increased pointing modulation associated with the higher-throw cases.

the balloon hook) to ensure that the center of mass is centered throughout the flight, despite a decreasing helium volume. This should minimize jitter in the survey, but this chapter shows the effects if this solution were not feasible.

Figure 4.10 illustrates the effect of jitter on the survey coverage for a nominal Stripe-82 survey corresponding to Figure 4.9. Here, the precession is modeled by a sinusoid in the beam altitude with a period of 4.2 s and peak-to-peak amplitudes of $6, 12, 24$ arcmin. Here, the nominal center of mass offset is 69 mm in the direction parallel to the ground, and 20 mm vertically, corresponding to the 12 arcmin case. Note, however, the EXCLAIM instrument is designed for the center of mass to be through the vertical axis [26] so this can be seen as deviations from non-ideality. The effects of

precession are twofold: the beam envelope is modulated, and the effective beamwidth is increased. The beam envelope can be seen by the first row, where increased precision causes a fluctuating minimum and maximum declination. If the precession is large enough, some of Stripe-82 is not covered. The effective beamwidth increase is caused by the gaps in survey coverage, where the circles correspond to 1/3 of the nominal 540 GHz beamwidth of 3.78 arcmin. The top row of the figure shows minimal gaps for the small-precession case, but these gaps increase with precessional amplitude. Ultimately, this increase in effective beamwidth leads to a decrease in sensitivity to small-scale modes, leading to a decreased number of observable cosmological modes.

4.4 System constraints and Key Performance Parameters

In the following chapters, I will discuss scientific forecasts, detector design, and optical modeling for the EXCLAIM instrument. These components form vital portions of the EXCLAIM system. One of the chief challenges for pre-flight modeling of the EXCLAIM instrument is to build a holistic understanding of the telescope, in conjunction with complicated models for the specific subsystems; the instrument is ultimately a *system of systems*. Ultimately, sensitivities to the [CII] and CO power spectra are the primary goals driving the requirements for all the other aspects of the mission.

It is important to note that the interplay between these subsystems is nonlinear, as requirements intersect between the scientific sensitivity, detector noise, optical loading, readout firmware, attitude determination and control systems, and more. The goal of this section is to demonstrate how these subsystems relate through a subset of mission requirements I have directly contributed to. I will return to these requirements later

in the thesis, after describing physical modeling of these subsystems in detail.

Ideally, our approach for understanding the EXCLAIM instrument would be a *model-based systems engineering* approach. Here, all of the EXCLAIM subsystems are built into a singular computational model with a common, limited set of system requirements. At the other extreme, a *document-based system engineering* treats the various subsytems in a modular fashion, where each subsystem features a unique set of requirements. The EXCLAIM collaboration uses a hybrid approach, where high-fidelity models are used in conjunction with discrete requirements, all dictated mission goals defined in preparation for design reviews.

In this thesis, I will particularly focus on *Key Performance Parameters* which relate specific mission goals to margins and uncertainties in the instrument. These are typically summarized in a *Requirements Traceability Matrix*. The most important parameter I will discuss is the noise-equivalent intensity, which directly affects instrument noise per channel. I introduce this formalism in Chapter 6, which will be applied to the EXCLAIM detector array as described in Section 6.6. Based on this model, I describe the current best estimate for scientific sensitivities in Chapter 5. In Chapter 8, I describe the EXCLAIM optical modeling and its relation to the sensitivity model. The effective NEI, introduced in Equation 2.19, provides the key science requirement describing the instrument sensitivity. Other parameters, such as the survey time and beam resolution, affect the number of observable cosmological modes; in the KPP table, these effects are modeled by an effective increase in NEI, summarizing the impact on overall science sensitivity[6].

Figure 4.11 shows the Key Performance Parameters of the EXCLAIM survey. The primary effects I focus on are excess NEP due to stray light, survey coverage, and

[6]For example, an increased FWHM would block our ability to detect high-k modes. This would impact the sensitivity roughly as NEI $\sim \sqrt{\mathrm{N}^{\mathrm{nom}}_{\mathrm{modes}}/\mathrm{N}^{\mathrm{cut}}_{\mathrm{modes}}}$, with $N^{\mathrm{nom}}_{\mathrm{modes}}$ describing the number of modes in the nominal case, and $N^{\mathrm{cut}}_{\mathrm{modes}}$ the number of modes when cutting off at high k.

Parameter name	System	Current best estimate	Units	Maximum (worst) Expected Value (hardware)	Maximum (worst) Possible Value (science)	NEP under MPV (instrument), impact in quadrature	NEI under MPV (science). Impact as product.
Telescope efficiency	Optics	0.876	fraction	0.800	0.740	0.9	N/A
Spectrometer efficiency	Spectrometer	0.23	fraction	0.13	0.07	1.8	N/A
Excess NEP	Spectrometer	1.00	fraction	N/A	2.6	2.6	N/A
Spectral resolving power	Spectrometer	512	unitless	438	364	1.1	0.89
Stray power: In-band diffraction reflected (ghosts)	Spectrometer	-38	dB	-32	-30	1.9	N/A
Stray power: In-band Optical Chain Thermal Emission (Diffraction)	Optics Spectrometer	0.10	fW	0.20	0.40	1.5	N/A
Altitude	Survey	36	km	33	29	2.3	N/A
Detector/Spectrometer Yield	Spectrometer	0.97	fraction	0.67	0.30	N/A	0.56
Cosmic ray deadtime	Spectrometer	0.003	fraction	0.030	0.050	N/A	0.97
Effective angular FWHM	ADCS	4.3	arcmin	5.0	7.0	N/A	0.75
Integration time	Survey	8	hours	8	6	N/A	0.87
					Multiplier	4.2	0.31

Derived Instrument Sensitivity	NEP @ Stop	NEP @ detectors		Instrument	NEI
CBE NEP	1.7E-18	3.9E-19	W/rtHz	1.5E+03	kJy/sr rtsec
MPV NEP, all terms	7.1E-18	4.9E-19	W/rtHz	7.6E+03	kJy/sr rtsec

Derived science requirement		
CBE NEI	2.5E+04	kJy/sr rtsec
MPV NEI	7.6E+03	kJy/sr rtsec

Figure 4.11: EXCLAIM Key Performance Parameters. Taken from Switzer et al. [149].

thermal loading.

Stray light and excess NEP: The goal of the EXCLAIM detectors, as well as most other modern mid- to far-infrared missions, is to bring the detector noise as close as possible to the photon background limit. While noise within the instrument, including thermal loading and amplifier noise, may limit the sensitivity, excess light on the detectors presents an additional nuisance. Various types of stray light can enter the detectors: blackbody radiation from the mirrors and dewar walls, reflections within the detector focal plane, and out-of-band loading[7].

Coverage: While the baseline goal is to fully sample BOSS-S82, there are uncertainties in our ability to fully sample the region. Attitude Determination and Control System (ADCS) requirements may prevent us from fully samplihg the region (including jitter effects). The instrument is being carefully designed to minimize these effects,

[7]The EXCLAIM passband of $420 - 540\,\mathrm{GHz}$ was chosen in part to avoid the $557\,\mathrm{GHz}$ water vapor line. This contributes to out-of-band stray light, but care was taken in the EXCLAIM design to ensure filters block out this light to acceptable levels. In this thesis, I do not specifically analyze this effect, but it would contribute similarly to other sources of stray light I discuss in later chapters.

but we model the potential detriments. For example, jitter may cause an increase in effective beamwidth, or we may not be able to cover the S82 region completely.

5 EXCLAIM SCIENCE: LIM FORECASTS

In this chapter, I describe the extragalactic science forecasts for EXCLAIM using the $P(k)$, i.e. flat-sky power spectrum, formalism. Here, I aim to calculate the sensitivity of EXCLAIM to measurements of the biased intensity and cross-shot power for [CII] and CO lines for cross-correlation with BOSS galaxies. I apply the methodologies of Chapters 2-3 to the background model described in Chapter 4 using the optimized MKID model we later describe in Chapters 6-7 and the optical model described in Chapter 8. In short, this forecast utilizes holistic modeling from the rest of the thesis. Despite the fact that this chapter utilizes results from later chapters, I present these scientific forecasts here to help bridge the gap between science and instrumentation, and to help motivate the importance of maximizing sensitivity in the detectors. These results will be presented in Pullen et al. [125]; note that these forecast numbers are preliminary.

5.1 Instrument and survey models

The instrument model is described in Table 5.1. The effective NEI is given by the EXCLAIM background model described in Chapter 4, applied to an MKID array model given by Chapter 6. The array is separated into three different redshift bins, each with 110 channels and a 40 GHz bandwidth. The instrument noise per voxel, σ_n is the instrument noise divided by the voxel volume, calculated through the effective NEI in Equation 2.19, contributing to the LIM signal as in Equation 2.17. The center redshifts per line per channel are also shown for each of the four target lines ([CII] and three CO lines), along with the beamwidth which scales with inverse frequency.

The survey models for the BOSS-S82, HSC-N, and HETDEX-SHELA regions are shown in Table 5.2. Here, the number density, survey area, redshift ranges, and

freq (GHz)	n_{ch}	$\Delta\nu$ (GHz)	$\mathrm{NEI_{eff}}$ (kJy/sr)	σ_n^2 ($\mathrm{kJy^2/sr^2Mpc^3}$)	z_{CII}	z_{CO65}	z_{CO54}	z_{CO43}	$\Delta\Theta$ (arcmin)
440	110	40	1952	6.340e+05	3.32	0.57	0.31	0.048	1.97
480	110	40	2650	1.170e+06	2.96	0.44	0.20	-	1.81
520	110	40	2194	8.03e+05	2.66	0.33	0.11	-	1.67

Table 5.1: EXCLAIM instrument model separated into three redshift bins. Here, n_{ch} describes the number of frequency channels in the bin, $\Delta\nu$ is the bandwidth of the bin, the σ_n^2 is the instrument noise per voxel, and the following four columns describe the redshift of the [CII] and CO measurements for $J = 6, 5, 4$, respectively. Finally, $\Delta\Theta$ describes the $1/e$ angular resolution of the beam.

	nh^3 ($\mathrm{Mpc^{-3}}$)	A ($\mathrm{deg^2}$)	z range	σ_z
BOSS-S82	$10^{-6}/3\times10^{-4}/10^{-4}/2\times10^{-2}$	273	2.5-3.5/0–0.6	0 (effectively)
HETDEX-F	$7\times10^{-4}/2.7\times10^{-3}/10^{-2}/10^{-2}$	350	1.9–3.5/0–0.5	$(6/2/2/2)\times10^{-3}$
HETDEX-SHELA	$7\times10^{-4}/2.7\times10^{-3}/10^{-2}$	34	1.9–3.5/0–0.5	$(6/2/2)\times10^{-3}$
HSC-N	3.6×10^{-3}/0.11/0.38/0.38	125	2.5–3.5/0–0.6	0.03/0.03/0.1/0.1

Table 5.2: Survey region parameters. For the n and σ_z columns, the four entries correspond to [CII] / CO(6-5) / CO(5-4) / and CO(4-3), and for the z range column, the two entries correspond to [CII] and the aggregate CO.

redshift uncertainties are shown[1]. For a given area, it is an open question whether photometric surveys (high n, high σ_z) or spectroscopic surveys (low n, low σ_z) are preferred, though forecasts in Chung et al. [31] suggests that spectroscopic surveys yield higher sensitivities when cross-correlating with COMAP intensity maps.

Note that for the rest of this chapter, I will assume the cross-correlation with BOSS-S82 with [CII] and CO models from Padmanabhan [116] and Keating et al. [77], respectively .

Plots of the power spectra are shown in Figure 5.1. Instrument noise dominates the intensity maps, and increases on smaller scales (larger k) due to the effective resolution limits of the instrument. For the BOSS-S82 quasars used in the [CII] survey, Poisson variance dominates the clustering power spectrum because relatively few objects are observed. In the lower-redshift BOSS surveys relevant to CO(6-5), however, enough galaxies are observed to bring Poisson noise to a similar level to the clustering power

[1]For the HSC survey, σ_z refers to the bias in Nishizawa et al. [109].

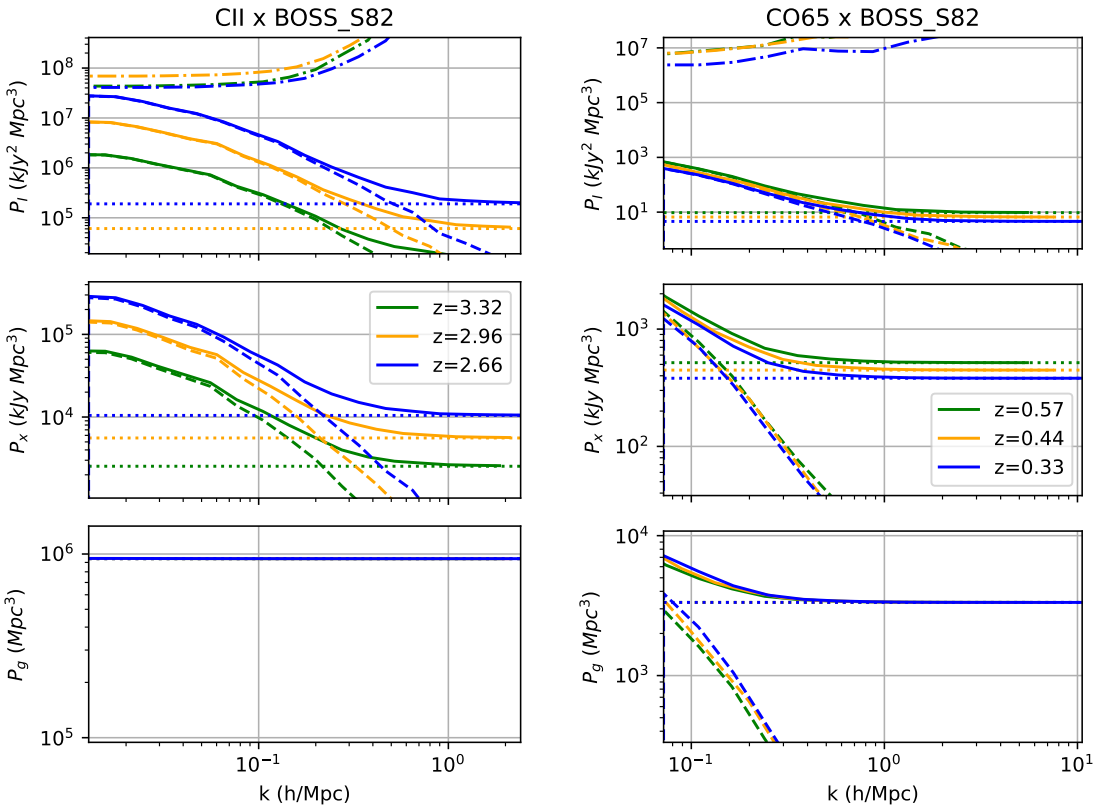

Figure 5.1: EXCLAIM-tracer auto and cross power spectra with [CII]-quasar on the left and CO(4-3)-galaxy on the right using Stripe 82. The top, middle, and bottom panels show the intensity auto, intensity-tracer cross, and tracer auto-power, respectively. All power spectra are spherically averaged in k-space. The dashed (dotted) curves show the clustering (shot) power spectra, the solid curves show the total power spectra, and the dash-dotted curve shows instrument noise. The quasar power spectrum (bottom left) is dominated by shot noise, while the CO(4-3) auto-power (top right) is dominated by instrument noise.

spectrum. Note that, based on the conclusions from Chapter 3, noise from both the LIM and galaxy auto-power spectra contribute to errors in the cross-power spectra, though they do not present additive biases to the signal.

	[CII]			CO(6-5)		
z	3.32	2.96	2.66	0.57	0.44	0.33
$\Delta L_{\|\|}$	231	220	210	309	281	256
$\Delta L_{\perp}$	209	199	189	67.1	53.6	41.3
$V_{\rm surv}$	1.06×10^7	8.67×10^6	7.49×10^6	1.39×10^6	8.08×10^5	4.37×10^5
$dL_{\|\|}$	5.44	5.18	4.96	7.29	6.63	6.03
$dL_{\perp}$	2.64	2.30	2.02	0.848	0.620	0.441
dV	37.8	27.4	20.1	5.24	2.55	1.18
P_n	4.35×10^7	6.91×10^7	4.09×10^7	6.03×10^6	6.45×10^6	2.39×10^6
	CO(5-4)			**CO(4-3)**		
z	0.31	0.20	0.11	0.05	-	-
$\Delta L_{\|\|}$	301	269	241	278	-	-
$\Delta L_{\perp}$	39.1	26.0	14.4	6.54	-	-
$V_{\rm surv}$	4.61×10^5	1.83×10^5	4.98×10^4	1.19×10^4	-	-
$dL_{\|\|}$	7.11	6.35	5.68	6.55	-	-
$dL_{\perp}$	0.494	0.301	0.154	0.083	-	-
dV	1.73	0.577	0.134	0.0447	-	-
P_n	1.99×10^6	1.46×10^6	2.72×10^5	5.139×10^4	-	-

Table 5.3: Distance, volume, and noise for each line and redshift bin for the BOSS-S82 survey. $\Delta L_{||}$, $\Delta L_{\perp}$, and $V_{\rm surv}$ correspond to the dimensions and total volume of the redshift bin bin consisting of 100 frequency channels, while $dL_{||}$, $dL_{\perp}$, and dV correspond to single voxels. Distances are in units of Mpc/h, volumes in Mpc$^3/h^3$, and instrument noise in kJy^2/sr^2 Mpc$^3/h^3$.

5.2 Mode-counting

Based on the survey areas described in Table 5.2, cosmological distance measurements are shown in Table 5.3. For simplicity, we will break each survey region into square regions; for example, the total BOSS-S82 region is $105 \times 2.6\,$deg., which makes up 40.4 distinct square regions[2]. Each survey region contains 40 line-of-sight modes, and 80 modes in each orthogonal direction.

I first construct a three-dimensional data cube by taking a Fourier series with the number of modes equal to the number of frequency channels or the number of $1/e$

[2]Breaking up the survey into square-shaped sections is justified because there are few large-$k_{\perp}$ modes lost by cutting off the survey at 2.6 deg.

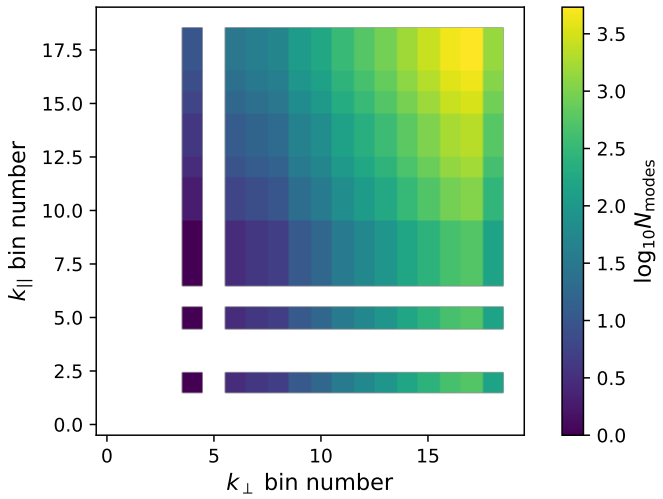

Figure 5.2: Number of modes per $k_{||}$, $k_\perp$ bin for [CII] at $2.83 < z < 3.16$. Each axis features 20 bins equally spaced logarithmically from $k_{||}h^{-1} = 0.0052\,\mathrm{Mpc}^{-1}$ to $0.62\,\mathrm{Mpc}^{-1}$, and from $k_\perp h^{-1} = 0.015\,\mathrm{Mpc}^{-1}$ to $2.00\,\mathrm{Mpc}^{-1}$. White regions contain no modes.

beamwidths, for the parallel or perpendicular modes, respectively. Furthermore, the total number of modes per k bin is multiplied by the resolution transfer function to account for the loss of information on small scales. This results in 3620, 4340, and 5160 total effective modes for the three redshift bins, from highest to lowest.

From here, I flatten the data cube to a two-dimensional array with dimensions corresponding to $k_{||}$ and $k_\perp$ modes, shown in Figure 5.2. Here, for each $k_{||}$, $k_\perp$ pair, the number of modes, k, and $\mu = k_{||}/k$ were calculated.

5.3 Covariance forecasts

For each $k_{||}$, $k_\perp$ pair, the Fisher matrix is calculated using various assumptions. A simplified power spectrum model is calculated assuming the [CII] model given in

Equation 1.21, re-presented here for clarity as

$$L(M) = A(z)\left(\frac{M}{N_1}\right)^{\beta} e^{-N_1/M}, \tag{5.1}$$

with

$$A(z) = \left(\frac{N_1}{M_1}\right)^{\beta} \mathrm{SFR}^{\alpha}(z), \tag{5.2}$$

and

$$\begin{aligned} M_1 &= (2.39 \pm 1.86) \times 10^{-5} \\ N_1 &= (4.19 \pm 3.27) \times 10^{11} \\ \alpha &= 1.79 \pm 0.30 \\ \beta &= 0.49 \pm 0.38 \\ \mathrm{SFR}(z) &= \frac{(1+z)^{2.7}}{1+[(1+z)/2.9]^{5.6}}. \end{aligned}$$

The model of Keating et al. [77] was used for the CO lines. Here, the star formation rate density was calculated using the models of Behroozi et al. [14], converted to IR luminosities via Kennicutt relation [79], and related to CO luminosities via power laws of the form of Equation 1.27 according to Kamenetzky et al. [76].

The mass-luminosity function models are integrated to calculate the LIM power spectra according to the calculations in Chapter 2. These power spectra are used to calculate Fisher matrix covariances over $[Ib]$ and $I_{\times\mathrm{shot}}$. I also calculate Fisher matrices fitting redshift-space distortions, though these are not detected with high significance for the EXCLAIM model. For each of these configurations, I also calculate each Fisher matrix with and without marginalizing over interlopers, and again setting the interlopers to known, fixed values without marginalizing.

Foregrounds can be effectively removed by excliding the lowest nonzero $k_{||}$ mode (s)[3]. I calculate these $k_{||}$, $k_{\perp}$ arrays (i) including all $k_{||}$ modes, (ii) excluding the lowest nonzero $k_{||}$ mode, and (iii) excluding the two lowest nonzero $k_{||}$ modes. For the rest of the chapter, forecasts will exclude the single lowest $k_{||}$ mode, unless otherwise specified.

These Fisher matrices are then added per spherically-averaged k, resulting in a single data vector with a unique signal-to-noise for each mode. Note that the addition of Fisher matrices from many line-of-sight angles μ helps to break degeneracies. Given a sufficiently sensitive instrument, measurements over many angles μ could be used to break the degeneracy between the bias and the intensity through RSD via the Kaiser effect term, which multiplies Ib by $(1 + f\mu^2/b)$. Figure 5.3 shows the resulting sensitivity per k mode. Arbitrarily, I take 20 k values. Note that the $z = 2.7$ bin is the only one where single modes may be measured with signal-to-noise greater than 5, while the ratio decreases with increasing redshift.

Finally, the resulting array of Fisher matrices is added, to obtain the total Fisher matrix describing the measurement, including information on all measured angular scales. Here, the biased intensity and correlated shot noise are jointly fitted, resulting in the triangle plots[4] shown in Figure 5.4. Here, I compare the case of marginalizing over interlopers to assuming they are fixed, and there is a slight penalty for marginalizing. Note that the case of fixed interlopers is virtually identical to not including them at all, because the interloping CO signal is much fainter than the target [CII] signal.

[3]I verified this assumption by performing the signular-value decomposition (SVD) calculations described in Switzer et al. [147], Anderson [8], and Anderson et al. [10] for detections of the HI signal through single-dish radio antennas. The largest SVD mode is dominantly described by the lowest $k_{||}$ mode, verifying my assumption that the foreground signal can be effectively removed as such.

[4]A triangle plot is a way to visualize covariance matrices for a large number of variables. In the plots included in this thesis, the inner and outer ellipses signify the 1- and 2-σ confidence, while the single-dimensional plots at the top of each column show the variance of each parameter. In the covariance ellipses, all the parameters not explicitly included in each figure are marginalized over.

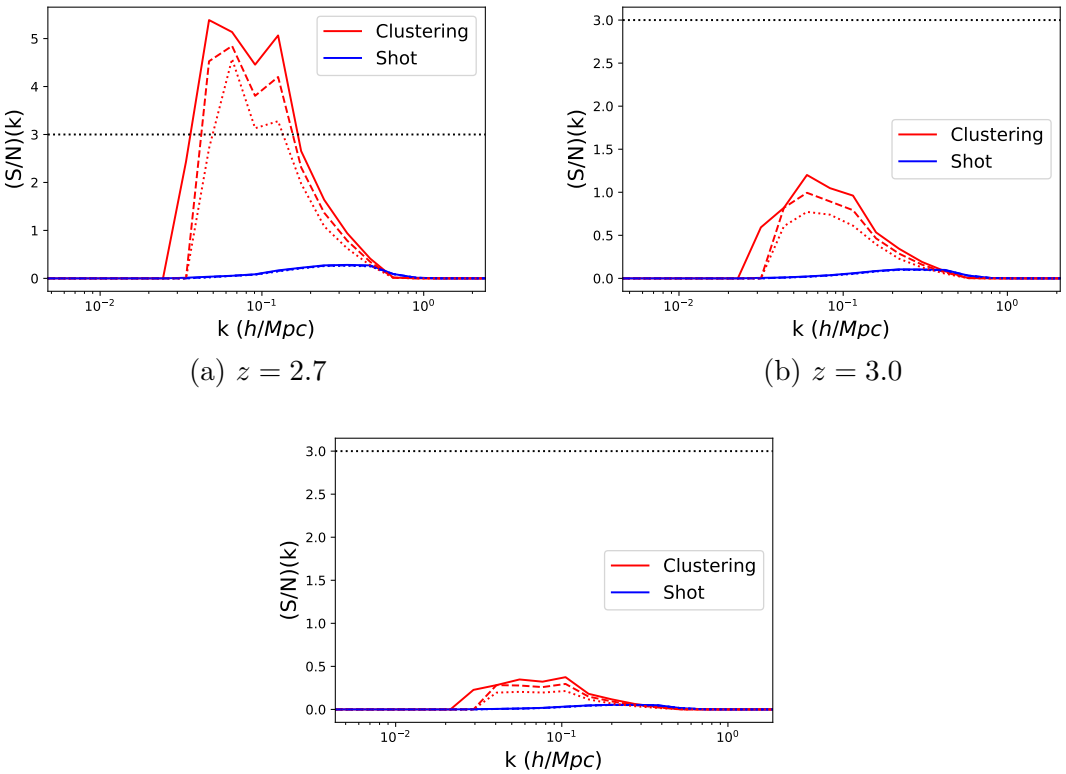

(a) $z = 2.7$ (b) $z = 3.0$

(c) $z = 3.3$

Figure 5.3: Spherically averaged signal-to-noise per k for [CII] cross-correlated with BOSS-S82, for three redshift bins. The solid, dashed, and dotted curves correspond to including all modes, excluding the lowest nonzero $k_{||}$ mode, and excluding the two lowest nonzero $k_{||}$ modes, respectively, suggesting the effect of foreground removal.

Again, these figures show that the $z = 2.7$ bin is the only one we expect to measure the biased intensity signal with statistical significance (roughly 4σ). On the other hand, the shot power signal is not expected to be measured with statistical signicance in any of the three redshift bins.

Corresponding plots for the three CO lines are shown in Figure 5.5. Because the signal is fainter than [CII], I only include a single redshift bin for each CO line. Here, only the cross-shot power in CO(6-5) is expected to be measured with any significance, while the biased intensity is not expected to be measured for any of the lines.

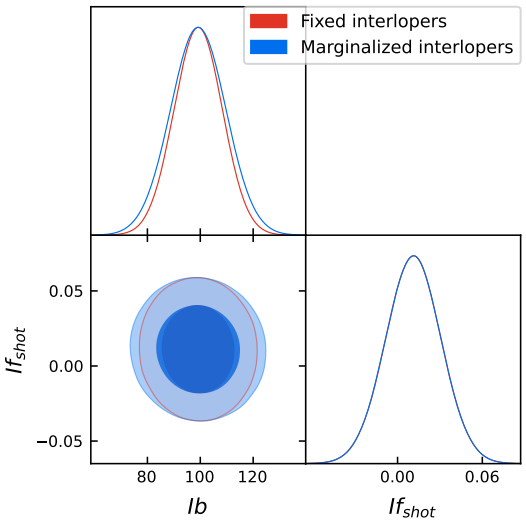

(a) z=2.7

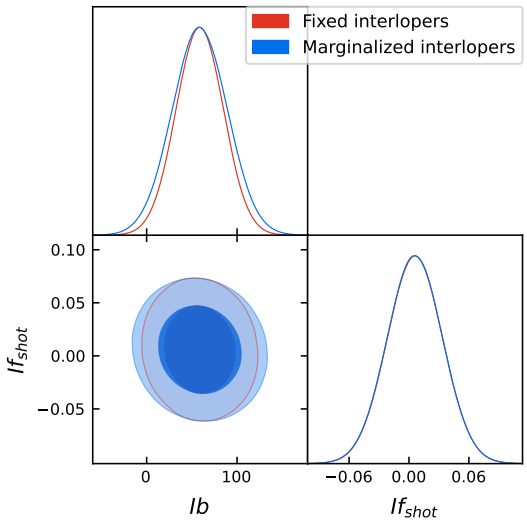

(b) z=3.0

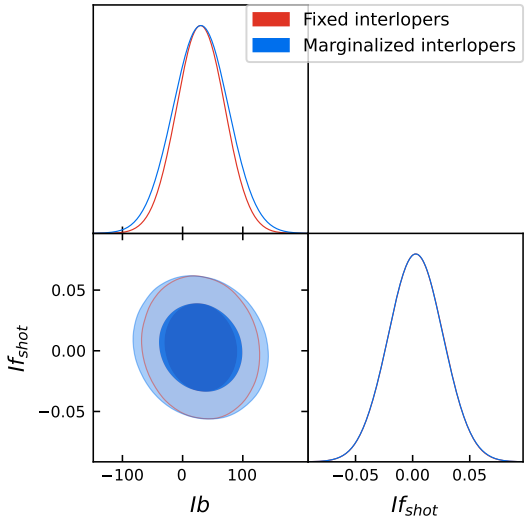

(c) z=3.3

Figure 5.4: Triangle plots for [CII] forecasts, jointly fitting Ib and $I_{\times\mathrm{shot}}$.

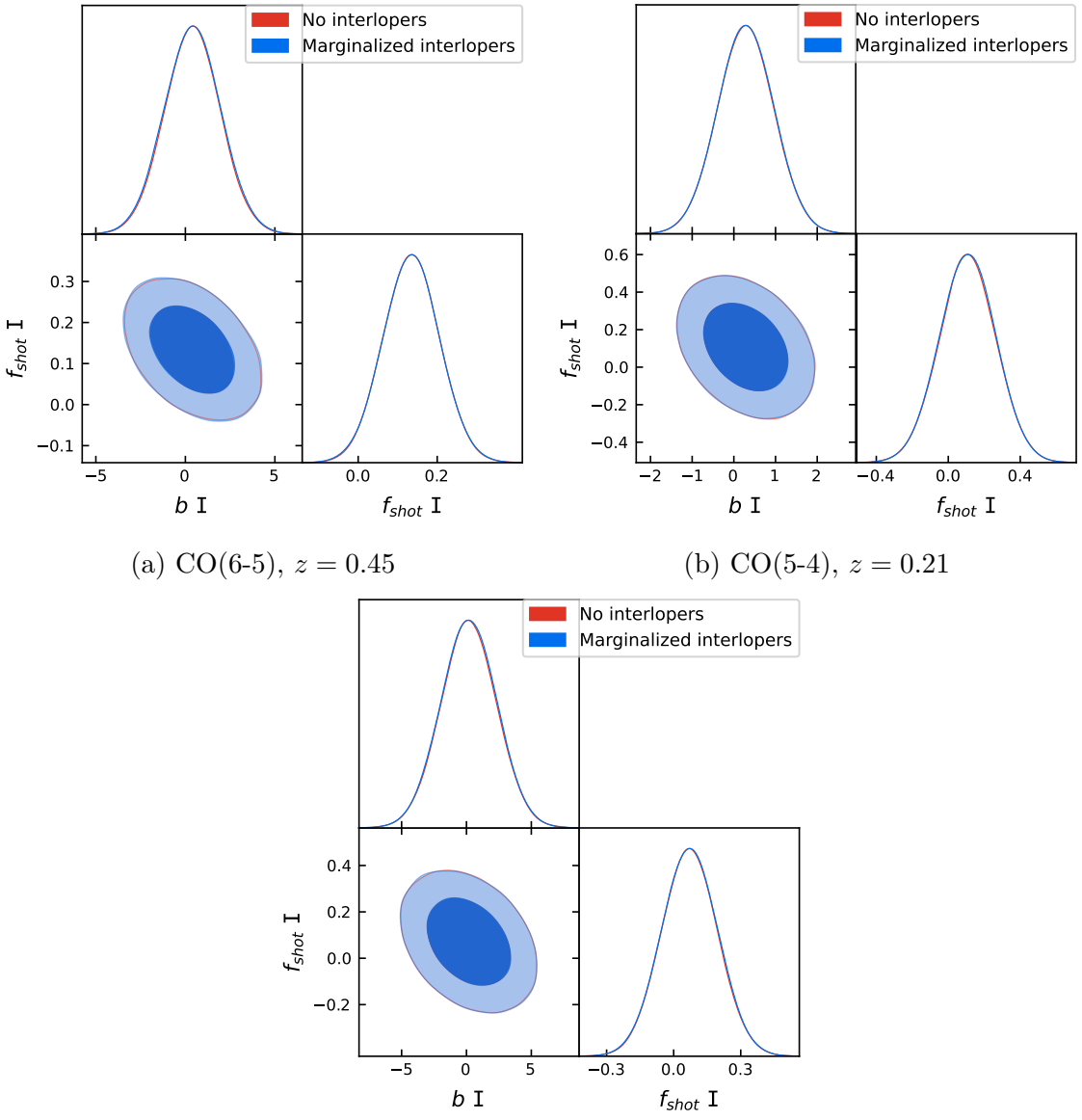

(a) CO(6-5), $z = 0.45$

(b) CO(5-4), $z = 0.21$

(c) CO(4-3), $z = 0.05$

Figure 5.5: Triangle plots for CO forecasts, jointly fitting Ib and $I_{\times \mathrm{shot}}$.

5.4 Science interpretation

Starting with the Fisher matrices over Ib and $I_{\times shot}$, we can calculate errors in the line luminosity model through the Fisher matrix error propagation formula, Equation B.12. Here, I use priors according to the model parameters presented after Equation 1.21. The results are shown in Figure 5.6, demonstrating the improvement EXCLAIM brings in inferring the the parameters of our updated Padmanabhan [116] model. Compared to the priors, the primary improvements are in the amplitude term $A(z)$, while the other terms have limited improvement. There is also a slight degeneracy between $A(z)$ and N_1 primarily at the lower redshifts, demonstrated by the slope of the covariance matrix between the two parameters.

A higher-significance result for a measurement of $A(z)$ would provide insight into the star formation rate density before its peak around $z \sim 2$. An instrument with an order of magnitude greater sensitivity (consistent with a space-based instrument with similar architecture to EXCLAIM, limited by the space background noise level in Figure 4.6) may be used to calculate redshift evolution in $A(z)$, and therefore measure the relation between the [CII] intensity and the star formation rate, nominally given by Equation 5.2.

Figure 5.7 places these measurements in the context of other models for the [CII] and CO intensities. Clearly, there are orders of magnitude in variation between the models for both sets of lines. The [CII] models of Gong et al. [62] and Padmanabhan [116] both depend on the cosmic star formation rate, leading to a signal that strongly decreases with redshift after $z \sim 2$. Bounds on low-redshift measurements are consistent with this conclusion [9], though measurements are needed to verify this conclusion.

Note that because instrument noise dominates the instrument errors, according

to our derivations in Chapter 3, errors in the biased intensity should not strongly depend on the model of choice. Thus, while we may detect the signal from a brighter model (such as our [CII] model of choice), our measurements may only provide an upper bound on a fainter model. However, even an upper bound would be insightful in ruling out specific models, and would add to our understanding of galaxy evolution through [CII] emission. Forecasts on the star formation rate density based on these measurements are in preparation in Pullen et al. [125].

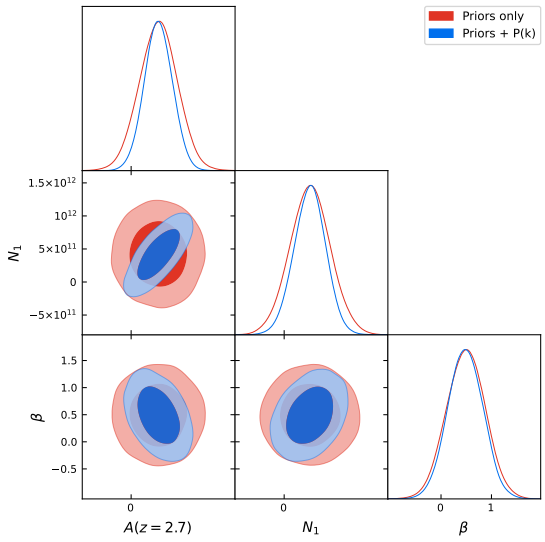

(a) z=2.7

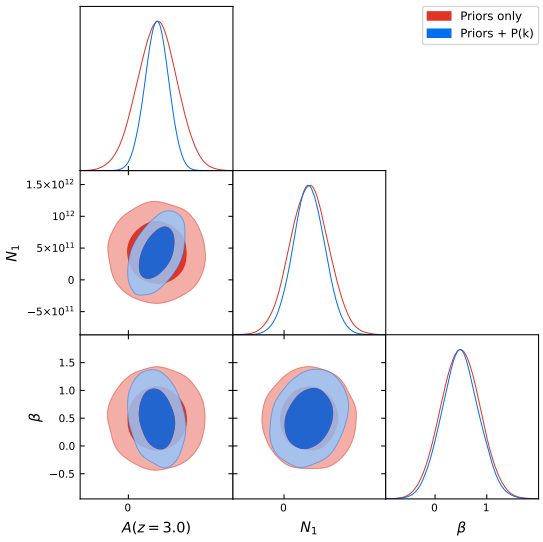

(b) z=3.0

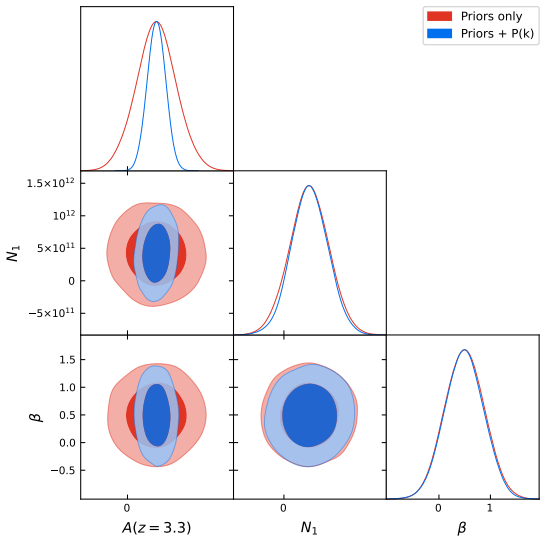

(c) z=3.3

Figure 5.6: Forecasts for the modified Padmanabhan [116] [CII] model, comparing Gaussian priors to Gaussian priors with the $P(k)$ analysis.

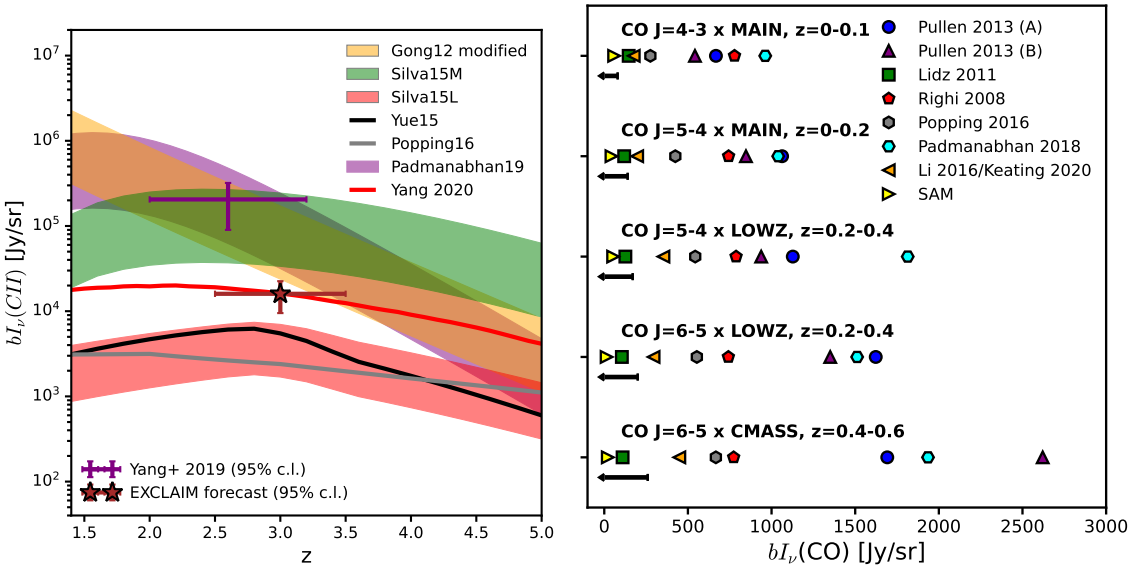

Figure 5.7: Comparison between CII (left) and CO (right) models near the EXCLAIM band. The [CII] models are from [62], [137], [167], [122], [116], and [165]; while the CO models are from [123], [89], [122], [115], [87]/[77], and [165].

6 EXCLAIM DETECTORS: MKID MODEL

In this chapter, I describe the microwave kinetic inductance detector (MKID) model used for the EXCLAIM instrument. I begin with a toy model describing the general operation of the detectors, relying on the kinetic inductance effect. I then describe the in-depth 'quasiparticle model' describing the particle dynamics within the detectors, followed by calculations of the detector noise. I then describe testing routines for MKID parameters, before describing the system-level performance of the EXCLAIM MKID array. Appendix C.1 provides a backing for background-limited performance in generic detector technologies, comparing the sensitivities of incoherent detectors like MKIDs to incoherent detectors like the radio heterodyne receivers relevant to the Tianlai interferometers.

6.1 MKIDs: illustrative toy model

MKIDs operate by coupling the kinetic inductance effect with a resonator array. The kinetic inductance effect occurs in superconducting AC circuits, where the nonzero inertia of oscillating bound electron pairs, i.e. Cooper pairs, leads to a resistance and inductance within the film. By fabricating the superconducting thin film in a resonator (modeled by an LRC circuit), changes in the kinetic inductance can be measured through changes in the absorption profile of the resonator (i.e. the S_{21} parameter). The level of kinetic inductance depends on the number of broken Cooper pairs, i.e. quasiparticles (akin to holes in normal conductors), which are produced through absorption of radiation. The process is modeled by the following:

Absorbed photons $\rightarrow$ quasiparticles $\rightarrow$ kinetic inductance changes $\rightarrow$ S_{21} changes,

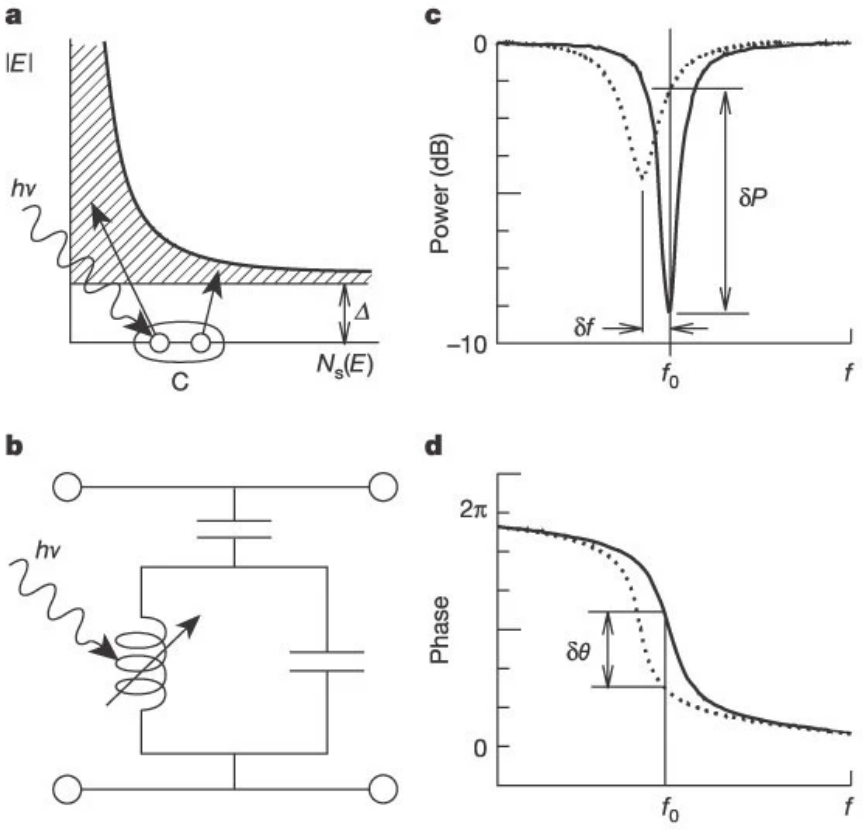

Figure 6.1: Illustration of MKID operation (taken from Day et al. [42]).

shown in Figure 6.1, taken from Day et al. [42]. Panel a demonstrates the density of quasiparticle states as a function of energy ($N_s(E)$), where quasiparticles are produced by the breaking of a Cooper pair by an incoming photon. The resonator impedance changes are shown in panel b, where the horizontal lines represent a common feedline between many resonators designed to be sensitive to unique frequencies. Panels c and d represent the real and imaginary components, respectively, of the S_{21} changes of the detector. In the rest of this section, I will add intuition for this in a toy model.

Superconductors are known for their ability to provide zero resistance to direct (i.e. zero-frequency) currents. However, at high frequencies, this intuition breaks down, as the inertia of massive quasiparticles under an oscillating electric field (current) results

in a change in complex impedance, which generally includes a resistive component. We will build this intuition through a two-fluid model, beginning with a classical picture of the electron current. In the two-fluid model, the conductivity σ features real and imaginary components, given by σ_1 and σ_2, respectively. Additionally, there are two classes of particles: normal conducting particles and superconducting particles, with number densities described by n_n and n_s, respectively.

We assume electrons of mass m moving at a velocity $\mathbf{v}$ are subject to an electric field $\mathbf{E}$. The electrons are accelerated as

$$m\frac{d\mathbf{v}}{dt} = e\mathbf{E} - \frac{m\mathbf{v}}{\tau}, \tag{6.1}$$

where τ is the phenomenological relaxation time it takes for the electron to reach zero velocity, given its classical momentum $m\mathbf{v}$. τ describes 'frictional forces' acting on the electron. It can be shown [154] that, under the application of an alternating current of frequency $\omega \ll \tau^{-1}$, the resulting conductivity σ takes on a complex value

$$\sigma = \sigma_1 - i\sigma_2, \tag{6.2}$$

where

$$\sigma_1(\omega) = \frac{\pi n_s e^2}{2m}\delta(\omega) + \frac{n_n e^2 \tau}{m} \tag{6.3}$$

$$\sigma_2(\omega) = \frac{n_s e^2}{m\omega}. \tag{6.4}$$

Here, the delta function in the σ_1 equation describes DC current, i.e. $\omega = 0$. The other term in the first equation is constant with frequency. The term in σ_2 diverges as $\omega \to 0$, and $\sigma_2(\omega)/\sigma_1(\omega) \to \infty$, resulting in zero dissipation.

Equation 6.2 is analogous to the (inverse) impedance of a circuit. Here, $\sigma = Z^{-1}$, $\sigma_1 = R^{-1}$ and $\sigma_2 = (\omega L)^{-1}$, with R the resistance and L the inductance. Also add in a parallel capacitance C, describing a resonance LRC circuit . This circuit features an absorptive inverse quality factor

$$Q^{-1} = \frac{R}{\omega L} = \frac{n_s}{\omega \tau n_n} \tag{6.5}$$

and resonance frequency

$$\omega_r = \frac{1}{\sqrt{LC}} = \sqrt{\frac{m}{n_s e^2 C}}. \tag{6.6}$$

Suppose the number of superconducting particles changes by a small perturbation δn_s, thereby changing the inductance term σ_2. Here, the quality factor and resonance change as

$$\begin{aligned} \delta Q_{-1} &= \frac{\delta n_s}{\omega \tau n_n} \\ \frac{\delta \omega_r}{\omega_r} &= -\frac{\delta n_s}{2 n_s}. \end{aligned} \tag{6.7}$$

Equation 6.7 represents the operation of a kinetic inductance detector [42]. Incident radiation of power P_{opt} increases the number of superconducting states by an amount $\delta n_s(P_{\text{opt}}) > 0$. This causes a decrease in the quality factor of the resonator circuit, while also decreasing the resonance frequency. The resulting shifts in resonance curves can be simultaneously read out by hundreds of individual resonators within a single feedline, allowing for a powerful means to scaling to large arrays.

Parameter	Symbol	Value
Material	-	Aluminum
Resonator volume	V	374 μm
Microwave readout center frequency	ν_{res}	3.50 GHz
Microwave readout bandwidth	-	0.50 GHz
Coupling quality factor	Q_c	Aluminum
Residual quality factor	Q_{i0}	1.75×10^6
Kinetic inductance fraction	α	0.775
Feedline readpower	$P_{\text{read}}^{\text{feed}}$	100 fW
Readout generation efficiency	η_{read}	9.24×10^{-4}
Acoustic frequency	ν_{ac}	10 Hz
Amplifier temperature	T_{amp}	4.1 K
Bath temperature	T_{bath}	100 mK
TLS exponent	α_{TLS}	-0.69
TLS spectral density at 1 Hz	$S_{0,\text{TLS}}$	1.49×10^{-16} Hz^{-1}
TLS photon number	N_{TLS}	241

Table 6.1: Nominal EXCLAIM MKID design parameters.

6.2 From quasiparticles to resonances

After having motivated MKID operation through an intuitive explanation of the kinetic inductance effect in Section 6.1, we will develop a rigorous MKID model in the following sections. Throughout, we will assume an aluminum MKID device matching those designed for EXCLAIM, with parameters specified by Table 6.1.

Quasiparticle resonances

A full calculation for the complex conductivity given in Equation 6.2 requires the use of Bardeen–Cooper–Schrieffer (BCS) theory. The complex conductivity is described

by [101].

$$\begin{aligned}
\frac{\sigma_1(\omega)}{\sigma_n} &= \frac{2}{\hbar\omega}\int_{\Delta}^{\infty}\frac{E^2+\Delta^2+\hbar\omega E}{\sqrt{E^2-\Delta^2}\sqrt{(E+\hbar\omega)^2-\Delta^2}}\left[f(E)-f(E+\hbar\omega)\right] \\
&\approx \frac{4\Delta}{\hbar\omega}e^{-\Delta_0/k_BT}\sinh\left(\frac{\hbar\omega}{2k_BT}\right)\mathrm{K}_0\left(\frac{\hbar\omega}{2k_BT}\right) \qquad (6.8)\\
\frac{\sigma_2(\omega)}{\sigma_n} &= \frac{1}{\hbar\omega}\int_{\Delta}^{\Delta+\hbar\omega}\frac{E^2+\Delta^2-\hbar\omega E}{\sqrt{E^2-\Delta^2}\sqrt{(\Delta^2-(E-\hbar\omega)^2}}\left[1-2f(E)\right], \\
&\approx \frac{\pi\Delta_0}{\hbar\omega}\left[1-\frac{1}{16}\left(\frac{\hbar\omega}{\Delta_0}\right)^2+\mathcal{O}\left(\frac{\hbar\omega}{\Delta_0}\right)^2\right] \qquad (6.9)
\end{aligned}$$

where $f(E)$ is the quasiparticle distribution function and K_0 is the Bessel function of the 0^{th} kind. The second lines of each of the above equations assume $\hbar\omega \ll \Delta_0$ and $k_BT \ll \Delta_0$. Here, the zero-temperature gap energy $\Delta_0 = 1.764k_BT_c$, while temperature-dependent gap Δ may vary at higher temperatures; for the temperatures of interest in this thesis, we assume $\Delta = \Delta_0$ because $T \ll T_c$. The density of quasiparticles is given by the integral

$$n_{\text{qp}} = 4N_0\int_0^{\infty}dE\rho(E)f(E) \approx 4N_0\Delta_0K_1(\Delta_0/k_BT). \qquad (6.10)$$

Here, $\rho(E) = Re\left(E/\sqrt{E^2-\Delta^2}\right)$ the quasiparticle density of states, $N_0 = 1.72 \times 10^{10}\,\mu\text{m}^{-3}\text{eV}^{-1}$ is the electron number density at the Fermi level for aluminum, and K_1 is the Bessel function of the first kind. In the case where $k_BT \ll \Delta$, the distribution is approximated by the thermal distribution

$$n_{\text{qp}}^{\text{th}} \approx 4N_0\Delta_0\sqrt{\frac{\pi k_BT}{2\Delta_0}}e^{-\Delta_0/k_BT}. \qquad (6.11)$$

Matching the approximations in Equations 6.8 and 6.9 to Equation 6.10, we find that

$$\begin{aligned}
\delta x_{\rm qp} &\equiv \left.\frac{\delta\omega_r}{\omega_r}\right|_{\rm TLS} = \frac{\delta L}{L(0)} = \frac{\alpha\delta X_s}{2X_s(0)} \\
&= \frac{\alpha\gamma}{4N_0\Delta_0} S_1(\omega)\delta n_{\rm qp} \qquad (6.12) \\
\delta Q_{\rm qp}^{-1} &= \frac{\alpha R_s}{X_s(0)} \\
&= \frac{\alpha\gamma}{2N_0\Delta_0} S_2(\omega)\delta n_{\rm qp}, \qquad (6.13)
\end{aligned}$$

where $x_{\rm qp}$ is the fractional resonance frequency shift and $Q_{\rm qp}$ is the quality factor, both due to quasiparticle production. Here, R_s and X_s contribute to the complex impedance Z_s as $Z_s = R_s + iX_s$ and S_1 and S_2 are respectively given by the real and imaginary components of the dimensionless response function

$$\begin{aligned}
S_1 &= \frac{2}{\pi}\sqrt{\frac{2\Delta_0}{\pi k_B T}}\sinh(\xi)K_0(\xi) \qquad (6.14) \\
S_2 &= 1 + \sqrt{\frac{2\Delta_0}{\pi k_B T}}e^{-\xi}I_0(\xi), \qquad (6.15)
\end{aligned}$$

where $\xi \equiv \hbar\omega/(2k_BT)$. These expressions are related to the S_{21} curve as discussed in the MKID readout subsection.

Two-level system resonance terms

It has been observed that dielectric properties in resonator thin films also contribute to dissipation and frequency shifts in low-temperature devices featuring amorphous dielectric materials (e.g. aluminum oxide). Two-level systems (TLS) form at the interface between the superconducting film and the other layers in the device. The TLS effect is due to the tunneling of atoms between regions of different energy levels

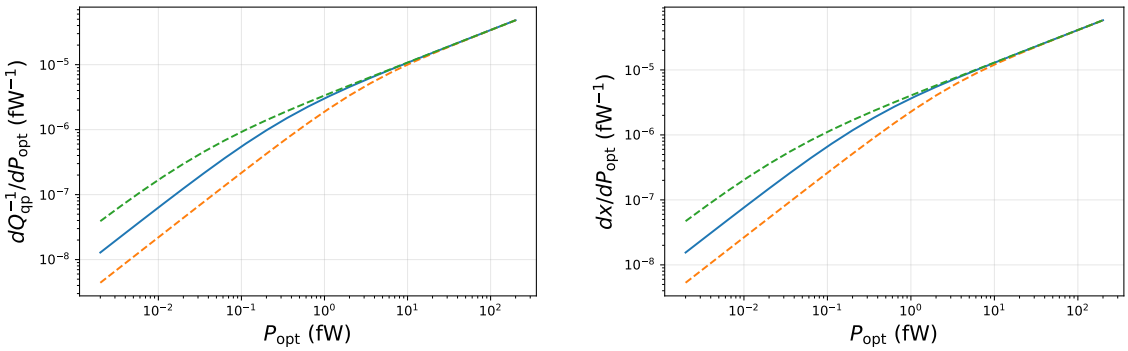

(a) dQqp/dP (b) dx/dP

Figure 6.2: Fesponsivities of the quasiparticle-induced quality factor Q_{qp} and the fractional frequency shift x.

and results in a continuous distribution of energy discontinuities. A dipole moment is introduced, thus altering the dielectric constant within the film, affecting the resonance of the device.

The sea of electric dipoles in the TLS-hosting material is characterized by a complex permeability $\epsilon_{\mathrm{TLS}}(\omega, T)$, with dependencies on the resonator frequency and temperature. In the absence of microwave readout power, the imaginary part results in a dielectric loss tangent given by

$$\delta_{\mathrm{TLS}}\left(\omega, T, P_{\mathrm{read}}^{\mathrm{feed}}=0\right)=\frac{\mathrm{Im}\ \epsilon_{\mathrm{TLS}}}{\mathrm{Re}\ \epsilon}=\delta_0 \tanh\left(\frac{\hbar\omega}{2k_BT}\right), \tag{6.16}$$

where δ_0 is a phenomenological term describing the ground state ($\hbar\omega \gg k_BT$) of the TLS material. In the presence of readout power, there is an additional contribution,

$$\delta_{\mathrm{TLS}}(\omega, T, P_{\mathrm{read}}^{\mathrm{feed}})=\frac{\delta_{\mathrm{TLS}}(P_{\mathrm{read}}^{\mathrm{feed}}=0)}{\sqrt{1+\chi_a P_{\mathrm{read}}^{\mathrm{feed}}/P_{\mathrm{TLS}}}}, \tag{6.17}$$

where χ_a is the portion of the feedline readpower absorbed by the resonator, quantitatively defined in the following subsection.

The dielectric loss tangent contributes to dissipation in the MKID through the TLS quality factor with an inverse given by

$$Q_{\mathrm{TLS}}^{-1} = F_{\mathrm{TLS}}\delta_{\mathrm{TLS}}(\omega, T, P_{\mathrm{read}}^{\mathrm{feed}}), \tag{6.18}$$

where F_{TLS} is the fraction of the energy of the electric field contained in the portion of the film containing TLS.

Similarly, the real part of the permeability contributes to resonance frequency shifts given by

$$\begin{aligned} x_{\mathrm{TLS}} &= -\frac{F_{\mathrm{TLS}}}{2}\frac{\mathrm{Re}\ \epsilon_{\mathrm{TLS}}}{\mathrm{Re}\ \epsilon} \\ &= \frac{F_{\mathrm{TLS}}\delta_0}{\pi}\left[\mathrm{Re}\Psi\left(\frac{1}{2}+\frac{1}{2\pi i}\frac{\hbar\omega}{k_BT}\right)-\ln\frac{\hbar\omega}{k_BT}\right], \end{aligned} \tag{6.19}$$

where Ψ is the complex digamma function.

MKID readout

The MKID detector can be modeled as a resonant RLC circuit. Changes in surface impedance due to changes in quasiparticle population will change the resistor and inductor in the circuit model, thus altering the response curve. The S_{21} parameter, defined as the power transmitted through the transmission line that is coupled to the resonator monitors the resonator response. A detailed derivation of S_{21} can be found in Appendix 1 of Noroozian [110], resulting in

$$S_{21} = 1 - \frac{Q_r}{Q_c}\frac{1}{1+i2Q_rx}. \tag{6.20}$$

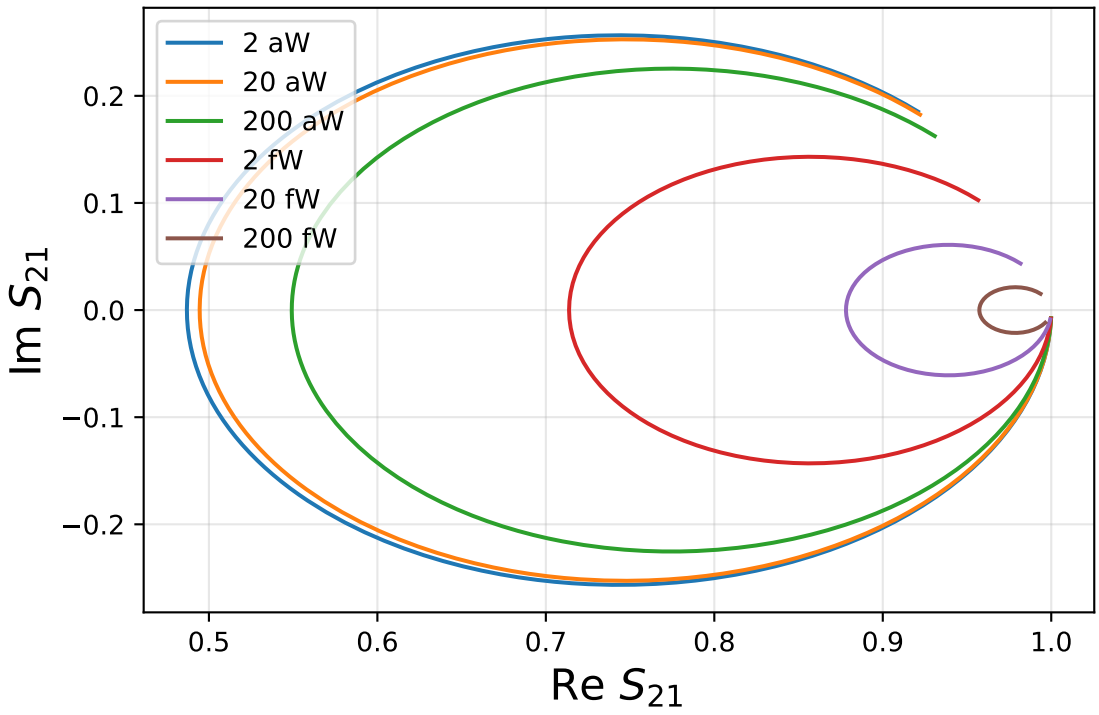

Figure 6.3: S21 curve for six background loads from 2 aW to 200 fW.

Here $Q_r^{-1} = Q_i^{-1} + Q_c^{-1}$ is the resonator quality factor, where Q_i and Q_c are the internal and coupling quality factors, respectively. Equation 6.20 traces a circle in the complex plane, with a radius proportional to the dissipation terms and phase determined by x. Given a measurement of S_{21} over a range of loadings (optical power, readout power, or temperature), the internal and coupling quality factors can be determined by $Q_i = Q_r / \min(|S_{21}|)$ and $Q_c = Q_r/(1 - \min(|S_{21}|))$, respectively. The amount of dissipation (i.e. the depth of the S_{21} ellipse) on the complex plane increases with absorbed optical power while the frequency shift (the 'start' of the ellipse in a counterclockwise direction) decreases with power, as shown in Figure 6.3.

The internal quality factor Q_i accounts for impedance properties of the supercon-

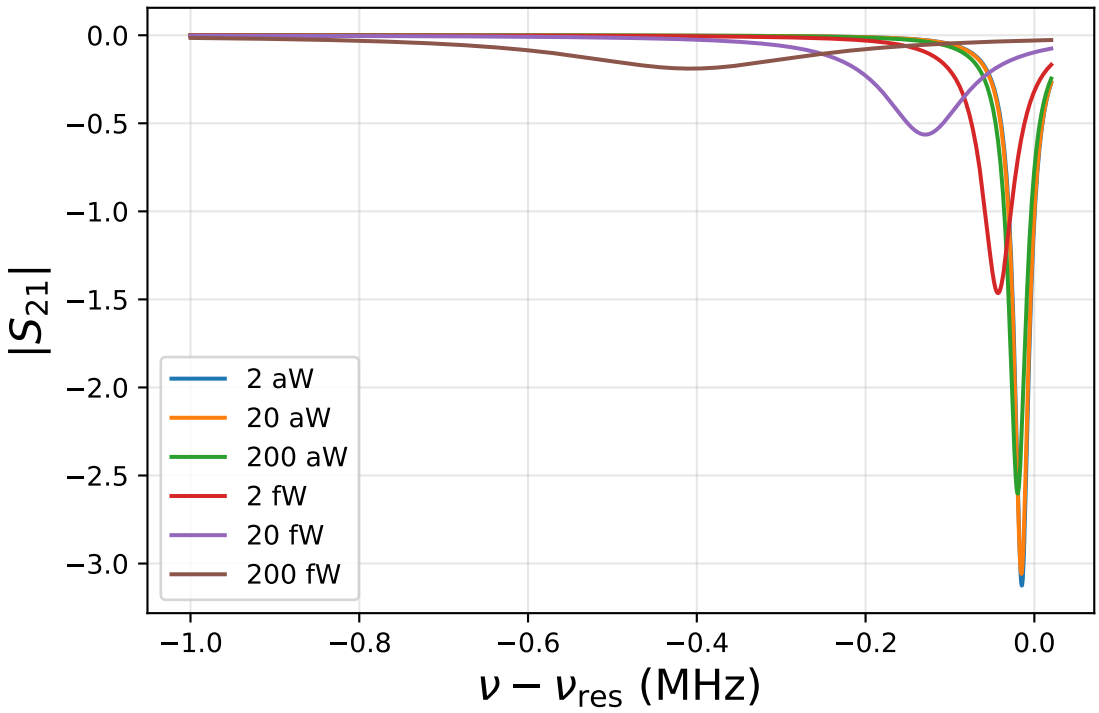

Figure 6.4: Magnitude of the S_{21} curve corresponding to Figure 6.3.

ducting film, and is given by

$$Q_i^{-1} = Q_{\mathrm{qp}}^{-1} + Q_{\mathrm{TLS}}^{-1} + Q_{i0}^{-1}, \tag{6.21}$$

where Q_{i0} accounts for other dissipative phenomena that may degrade the quality factor, such as trapped flux [55].

Similarly, the resonance frequency shift x is given by

$$x = x_{\mathrm{qp}} + x_{\mathrm{TLS}}. \tag{6.22}$$

For slow perturbations to x and Q_i^{-1} due to slow changes in quasiparticle generation, we can model changes in S_{21} through the resonator response coefficients (Z30-31)

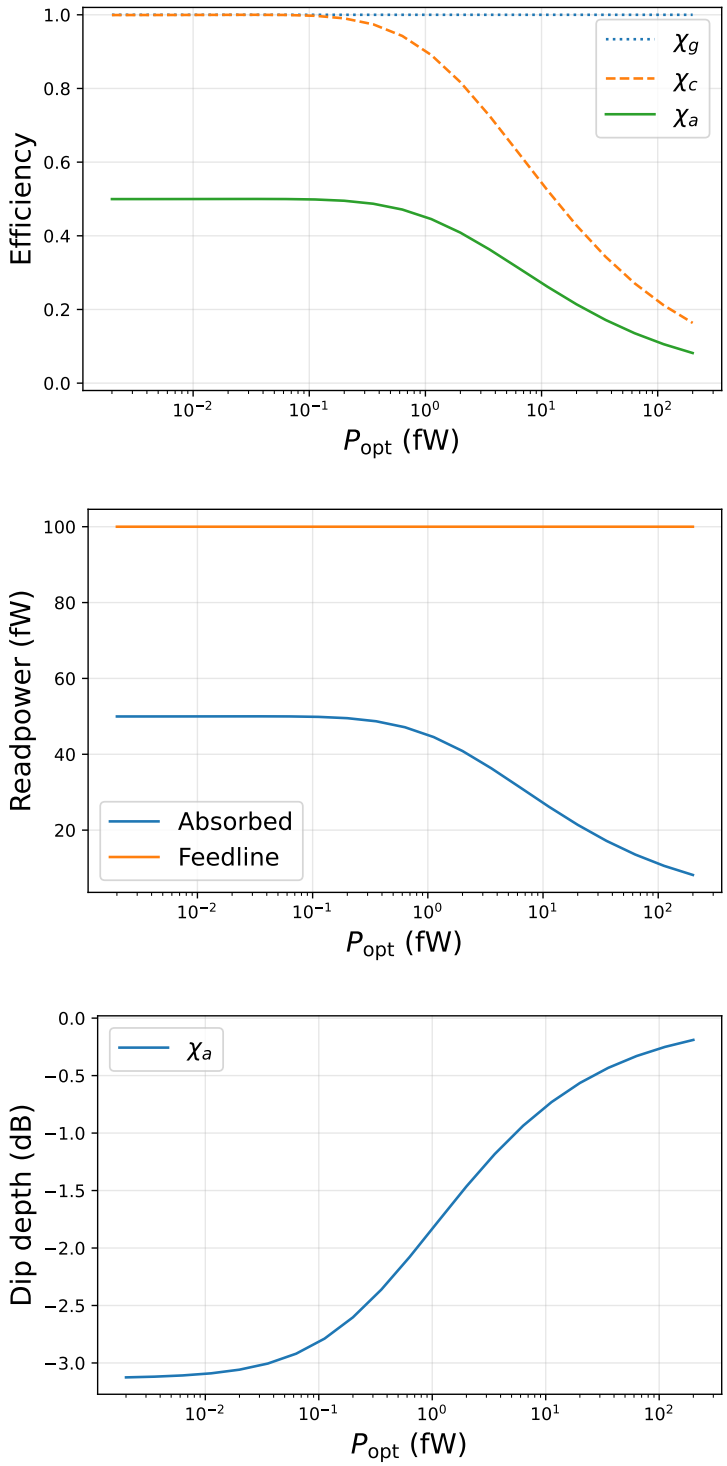

Figure 6.5: Summary of efficiencies (χ_g, χ_c, χ_a), readpowers (absorbed, feedline), and dip-depth, each as a function of optical load.

$$\delta S_{21}(t) = A(\omega)\delta x(t) + B(\omega)\delta Q_i^{-1}, \tag{6.23}$$

where A is tangent to the S_{21} curve in the complex plane, and B is orthogonal. The two terms are calculated as

$$A(\omega) = \frac{\partial S_{21}}{\partial x} = 2jQ_c\left(1 - S_{21}(\omega)\right)^2 \tag{6.24}$$

$$B(\omega) = \frac{\partial S_{21}}{\partial Q_i^{-1}} = \frac{1}{2j}A(\omega) \tag{6.25}$$

Using these response coefficients, we find that

$$\delta S_{21}(\omega) = \frac{1}{4}\chi_c\chi_g Q_i e^{-2j\phi_g}\left(2j\delta x(\omega) + \delta Q_i^{-1}(\omega)\right)\psi(\omega) + \delta S_{\mathrm{amp}}(\omega) \tag{6.26}$$

where we have introduced the amplifier noise term $\delta S_{\mathrm{amp}}(\omega) = \delta I_{\mathrm{amp}}(\omega) + j\delta Q_{\mathrm{amp}}(\omega)$. We have also introduced ϕ_g, defined as the phase of $1 - S_{21}$, as well as the coupling and generation efficiencies (each less than or equal to 1):

$$\chi_c(\omega) = \frac{4Q_cQ_i}{\left(Q_c + Q_i\right)^2} = \frac{4Q_r^2}{Q_cQ_i} \tag{6.27}$$

$$\chi_g(\omega) = \frac{1}{1 + 4Q_r^2x^2} \tag{6.28}$$

The combined effect of the two efficiencies, χ_g and χ_c, gives a new efficiency term,[1]

$$\chi_a(\omega) = \frac{\chi_c(\omega)\chi_g(\omega)}{2}, \tag{6.29}$$

[1] Yippee χ_a, a la McClane [103].

which is maximized when $Q_i = Q_c = 2Q_r$, i.e. $\chi_c = \chi_g = 1$ and $\chi_a = 1/2$. For a given feedline readpower $P_{\text{read}}^{\text{feed}}$, the detector absorbs a readpower $P_{\text{read}}^{\text{abs}}$ given by

$$P_{\text{read}}^{\text{abs}} = \chi_a P_{\text{read}}^{\text{feed}}. \tag{6.30}$$

In practice, χ_a must be calculated numerically. The calculation for χ_a depends on Q_i, which depends on the absorbed readpower through Equation 6.21. However, the absorbed readpower depends on χ_a through Equation 6.30. In the EXCLAIM MKID modeling code, an initial term for χ_a is given, which is used to calculate $P_{\text{read}}^{\text{abs}}$, which is used to calculate Γ_{read} and Γ_{tot}, which then re-calculate χ_a, while the previous χ_a is referred to as χ_a^{previous}. The loop iterates until $\left(\chi_a - \chi_a^{\text{previous}}\right)/\chi_a^{\text{previous}} < 10^{-5}$ (or whatever other threshold is chosen for convergence)[2].

Figure 6.4 shows the magnitudes of simulated MKID S_{21} responses for absorbed optical loads ranging from 2 aW to 200 fW. As the optical load increases, the depth of the resonance curve, which we will refer to as the *dip depth*, and the resonance frequency both decrease. This is consistent with the toy model presented in Section 6.1, illustrating the kinetic inductance effect.

Figure 6.5 demonstrates the effect of the incident optical power on the efficiencies χ_a, χ_c, and χ_g, as well as the readpower and dip depth. The $P_{\text{read}}^{\text{abs}}$ peaks at $P_{\text{read}}^{\text{feed}}/2$, where $\chi_a = 1/2$.

Bifurcation

A high readout power is ideal for reducing TLS losses, as well as noise due to TLS and the amplifier. However, under high readout power, nonlinear effects are seen in

[2]This procedure benefited from discussion with Perido and Glenn [119].

the frequency response of the resonators [170]. The bifurcation appears in the kinetic inductance under a strong current,

$$L_k(I) = L_k(0)\left(1 + \frac{I^2}{I_2^2} + ...\right) \tag{6.31}$$

The effect is thought to be caused by strong circulating currents in the film, which are highly susceptible to changing magnetic fields.

See [145] for nonlinear response of the resonator (going into more detail than Zmuidzinas review), and [80] for other terms which result in asymmetric resonances.

At resonance (see Zmuidzinas for calculating off-resonance effects) the effect changes the fractional frequency shift as

$$\delta x' = \delta x - 2a\delta Q_i^{-1} \tag{6.32}$$

where $a = (2Q_r^3/Q_c\omega_r E_*)P_g$ and $E_* = 2L_k I_*^2/\alpha\kappa_*$. $I_* = J_* V = (\pi N_0 \Delta_0^3/\hbar\rho_n)^{1/2} V$, two model parameters quoted in Zmuidzinas.

The full expression for a is

$$a = \left(\frac{\alpha Q_r^3}{V^2 Q_c}\right)\left(\frac{\hbar}{\pi\omega_r N_0 \Delta^3}\right)\left(\frac{\kappa_*\rho_n}{L_k}\right) P_{\text{read}} \tag{6.33}$$

According to Zmuidzinas, the effects of bifurcation dominate when $a > 0.77$. This effect can be ameliorated by reducing the first grouping of terms or by reducing P_{read}.

6.3 Quasiparticle model

Equations 6.12 and 6.13 describe the contributions of perturbations in the excess quasiparticle density to changes in S_{21}. In this subsection, we describe the sources of

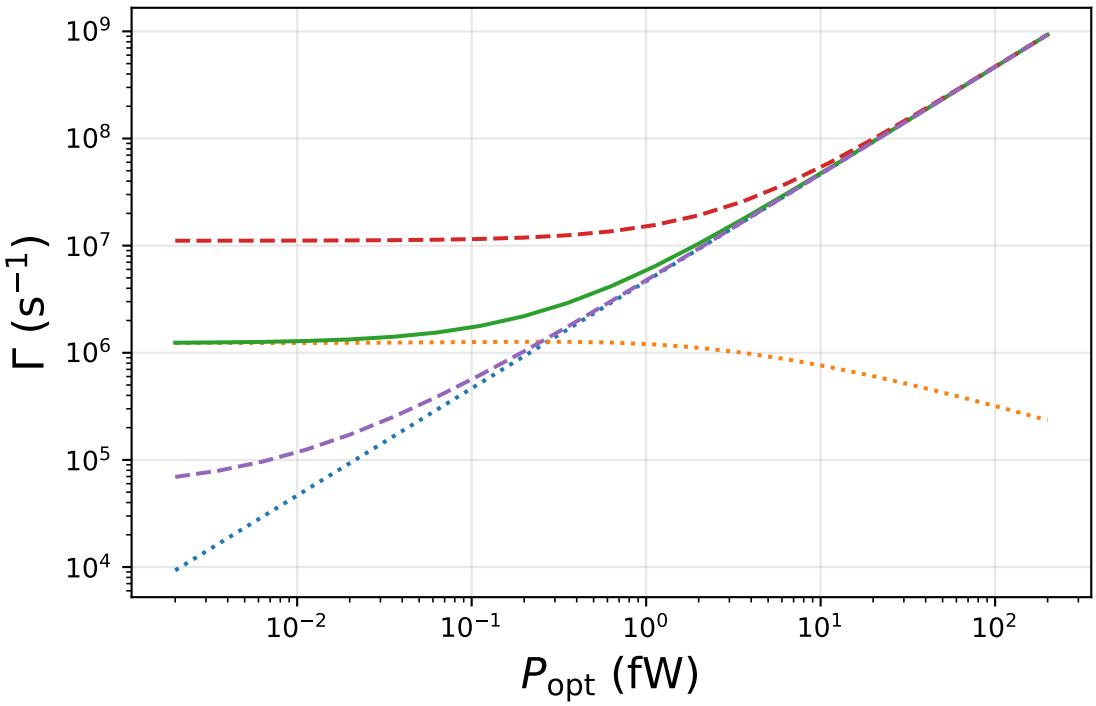

Figure 6.6: Quasiparticle generation efficiency. The blue and orange dotted curves show the optical and readout quasiparticle generation efficiencies, respectively. The solid curve describes the total quasiparticle generation efficiency, while the two dashed curves show the total generation efficiency if the readpower is doubled (upper) or halved (lower). Note that the readout generation efficiency drops at higher optical because χ_a decreases, as is shown in Figure 6.5

these excess quasiparticles.

Photons and phonons with energies greater than 2Δ can generate a quasiparticle pair. The total quasiparticle generation rate Γ_{tot} features contributions from incident optical photons, thermal noise, and readout noise, and is given by

$$\Gamma_{\rm tot} = \Gamma_{\rm opt} + \Gamma_{\rm th} + \Gamma_{\rm read}. \tag{6.34}$$

Ideally, the optical quasipartical generation rate exceeds the readout and thermal generation rates, i.e. $\Gamma_{\rm opt} > \Gamma_{\rm th}, \Gamma_{\rm read}$.

Optical generation can occur when an incident photon generates quasiparticles. An optical photon will generate $q \geq 2$ quasiparticles with a pair-breaking efficiency η_{pb}:

$$\eta_{pb} = \frac{q\Delta}{h\nu}. \tag{6.35}$$

The associated quasiparticle generation rate is

$$\Gamma_{\text{opt}} = \frac{qP_{\text{opt}}}{h\nu} = \frac{\eta_{pb}P_{\text{opt}}}{\Delta}. \tag{6.36}$$

Thus, $\partial\Gamma_{\text{opt}}/\partial P_{\text{opt}} = q/h\nu = \eta_{\text{pb}}/\Delta$.

Phonon annihilation also produces quasiparticles, where the phonon population is attributed to thermal vibrations in the film. The thermal generation rate is given by

$$\Gamma_{\text{th}} = VRn_{\text{th}}^2(T) = V\sqrt{\frac{\pi k_B T}{2\Delta_0}}e^{-\Delta/k_B T}, \tag{6.37}$$

where R is the *recombination constant* given by

$$R = \frac{(2 \times 1.764)^3}{4N_0\Delta_0\tau_0}. \tag{6.38}$$

Because the device temperature is well below T_c, we expect most thermal phonons to barely reach the gap energy. Assuming the energy of each phonon equals that of the gap, each annihilated phonon generates 2 quasiparticles.

The readout generation rate Γ_{read} occurs due to microwave photons nbreaders may not know that the resonances are in the microwave frequency range. redistributing the quasiparticle distribution function. This is given by [110]

$$\Gamma_{\text{read}} = \frac{\eta_{\text{read}}P_{\text{read}}^{\text{abs}}}{\Delta}. \tag{6.39}$$

It can also be expressed in terms of the readout power, which is an observable in actual MKID devices. Per Noroozian [110], the readout power efficiency can be modeled as $\eta_{\rm read} = N_{\rm qp}^{read}\Delta/\tau_{\rm qp}\chi_{\rm qp}P_{\rm read}$. Here, $N_{\rm qp}^{read}$ is the population of readout-generated quasiparticles, and $\chi_{\rm read}$ is the proportion of the readout power reaching quasiparticles to the total readout power. Like thermal generation, we expect 2 quasiparticles to be produced per readout photon event.

Pair recombination

A quasiparticle pair can combine to form a Cooper pair plus a phonon with energy $\Omega = E_1 + E_2$, with E_1 and E_2 the two quasiparticle energies. The inverse process also occurs (as is relevant to the previously-described thermal generation rate that peaks at the gap energy), but to a much lesser extent due to much lower number densities of resultant phonons.

At low temperatures in thermal equilibrium, pairs have a recombination lifetime

$$\tau_{\rm rec} = \frac{V}{RN_{\rm qp}} = \frac{N_{\rm qp}}{\Gamma_{\rm rec}}, \tag{6.40}$$

and $\Gamma_{\rm rec}$ is the thermal recombination rate

$$\Gamma_{\rm rec} = \frac{RN_{\rm qp}^2}{V} = \frac{N_{\rm qp}}{\tau_{\rm rec}}. \tag{6.41}$$

For a process in thermal equilibrium without any optical generation (i.e. *bare recombination*), the rate of thermal generation equals the rate of thermal recombination:

$$\frac{dN_{\rm qp}}{dt} = 0 = \Gamma_{tot} - \Gamma_{\rm rec}. \tag{6.42}$$

Thus, the thermal generation rate is given by

$$\Gamma_G = \tau_R^{-1} \frac{dR}{dt} = \frac{RN_{\rm qp}^2}{V}. \tag{6.43}$$

Phonon generation

As quasiparticles recombine to form a Cooper pair, they emit a phonon with enough energy to break another Cooper pair. The phonon has a lifetime before breaking another Cooper pair τ_{br}. However, in thin-film devices including MKIDs the phonon has a certain likelihood of passing through the film and into the substrate, quantified by the escape time τ_{esc}. Thus, the recombination lifetime is increased (i.e. phonon-quasiparticle interactions are less likely) by the geometry-dependent phonon trapping factor

$$f_{trap} = 1 + \frac{\tau_{esc}}{\tau_{br}} \tag{6.44}$$

In practical experiments, f_{trap} is a measured quantity.

Phonon trapping effects can be accounted for by replacing R with $R_* = R/f_{trap}$ in the preceding equations.

Perturbations to the quasiparticle density

As we showed in Sections 6.3 and 6.3, the quasiparticle number rate equation is given by

$$\frac{dN_{\rm qp}}{dt} = \Gamma_{tot}(t) - \Gamma_{\rm rec}(t) = \Gamma_{tot}(t) - R_* N_{\rm qp}(t)^2. \tag{6.45}$$

In the steady state, as shown above, $\Gamma_{tot,av} = R_* N_{qp,av}^2$, so

$$N_{qp,av} = \left(\frac{V \Gamma_{tot,av}}{R_*} \right)^{1/2}, \tag{6.46}$$

where $N_{qp,av}$ and $\Gamma_{tot,av}$ are the steady-state averages of the quasiparticle number and generation rate, respectively.

In typical MKID operation, we are interested in small perturbations in the total quasiparticle number induced by optical photons. Thus, we introduce perturbations $\delta N_{\rm qp} \equiv N_{\rm qp} - N_{qp,av}$ and $\delta \Gamma_{tot} \equiv \Gamma_{tot} - \Gamma_{tot,av}$. Inserting them into the number density equation the steady-state values cancel as above, resulting in

$$\frac{dN_{\rm qp}}{dt} = \delta \Gamma_{tot} - \frac{R_*}{V} (\delta N_{\rm qp})^2 - \tau_{\rm qp}^{-1} \delta N_{\rm qp}. \tag{6.47}$$

Here, we introduce the quasiparticle relaxation time. $\tau_{\rm qp}$ is important when considering the Fourier solution to the number density equation, which appears with a Lorenzian profile,

$$\delta N_{\rm qp}(\nu_{\rm ac}) = \frac{\tau_{\rm qp}}{1 + 2\pi i \nu_{\rm ac} \tau_{\rm qp}} \delta \Gamma_{tot}(\phi). \tag{6.48}$$

Here, $\delta N_{\rm qp}(\nu_{\rm ac})$ and $\delta \Gamma_{tot}(\nu_{\rm ac})$ are Fourier conjugates to $\delta N_{\rm qp}(t)$ and $\delta \Gamma_{tot}(t)$. Thus, there is a pole at $\nu_{\rm ac} = (2\pi \tau_{\rm qp})^{-1}$ with a linewidth characterized by $\tau_{\rm qp}$. Note that this solution is valid for small perturbations $\delta N_{\rm qp}$. Pulse decay and quasiparticle band experiments can be used to determine $\tau_{\rm qp}$. In the case that $\nu_{\rm ac} \tau_{\rm qp} \ll 1$, we arrive at

$$\tau_{\rm qp} = \frac{\partial N_{qp,av}}{\partial \Gamma_{tot,av}} = \frac{V}{2 N_{qp,av} R_*} = \frac{N_{qp,av}}{2 \Gamma_{tot,av}}. \tag{6.49}$$

Note that in the acoustic frequency domain (the frequency band over which the detector output is sampled due to the Raster scan of the instrument), Equations 6.12

and 6.13 generalize as

$$\delta x_{\rm qp}(\nu_{\rm ac}) = -\frac{\alpha\gamma S_1(\omega)}{4N_0\Delta_0 V}\left(\frac{\tau_{\rm qp}}{1+2\pi i\nu_{\rm ac}\tau_{\rm qp}}\right)\delta\Gamma_{\rm tot}(\nu_{\rm ac}) \quad (6.50)$$

$$\delta Q_{\rm qp}^{-1}(\nu_{\rm ac}) = \frac{\alpha\gamma S_2(\omega)}{2N_0\Delta_0 V}\left(\frac{\tau_{\rm qp}}{1+2\pi i\nu_{\rm ac}\tau_{\rm qp}}\right)\delta\Gamma_{\rm tot}(\nu_{\rm ac}), \quad (6.51)$$

mapping to the total quasiparticle generation rate given by Equation 6.34, with contributions from Equations 6.36, 6.37, and 6.39.

Absent the acoustic frequency effects (i.e. taking $\nu_{\rm ac} = 0\,\text{Hz}$, the number of additive quasiparticles is shown by Figure 6.7 as a function of optical power. Here, the solid curve shows the baseline readpower described in Table 6.1, where readout-induced quasiparticles dominate at lower loads $P_{\rm opt} \lesssim 0.1\,\text{fW}$. The upper and lower dashed curve show the effect of increasing and decreasing the readpower by $10\times$, respectively.

6.4 MKID noise model

In our MKID model there are many possible sources of noise, including optical photon noise, quasiparticle generation noise, quasiparticle recombination noise, amplifier noise, and TLS noise. In this section, we will derive the NEP of each of these terms using the quasiparticle number model.

The total NEP by all of these sources depends on whether the S_{21} curve is read out in the dissipation direction or the frequency direction, corresponding to Q_i or x, respectively. The total dissipation NEP is given by

$$\text{NEP}_{\rm diss}^2 = \text{NEP}_{\rm opt}^2 + \text{NEP}_{\rm gen}^2 + \text{NEP}_{\rm rec}^2 + \text{NEP}_{\rm amp,diss}^2, \quad (6.52)$$

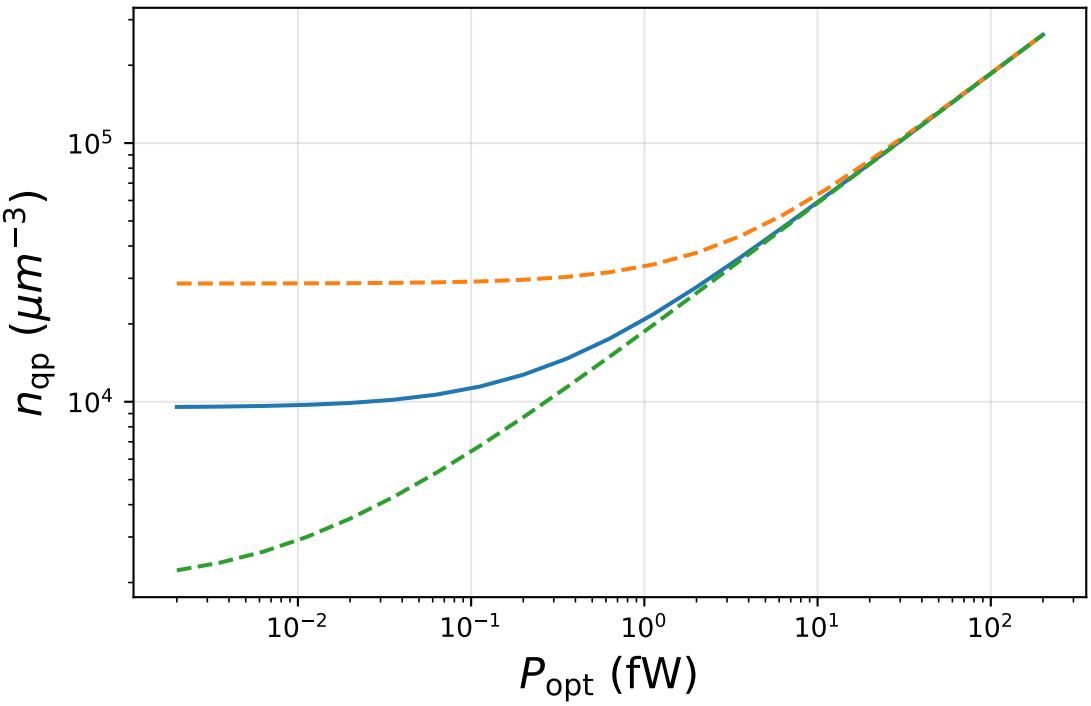

Figure 6.7: Quasiparticle number as a function of optical load. The upper and lower dashed curves represent the cases where the feedline readpower is an order of magnitude above and below that of Table 6.1, respectively.

with terms corresponding to optical, generation, recombination, and amplifier noise in the dissipation quadruture. Here,

$$\mathrm{NEP}^2_{\mathrm{gen}} = \mathrm{NEP}^2_{\mathrm{read}} + \mathrm{NEP}^2_{\mathrm{th}} \tag{6.53}$$

accounts for non-optical generation noise. On the other hand, the total frequency NEP is given by

$$\mathrm{NEP}^2_{\mathrm{freq}} = \mathrm{NEP}^2_{\mathrm{opt}} + \mathrm{NEP}^2_{\mathrm{gen}} + \mathrm{NEP}^2_{\mathrm{rec}} + \mathrm{NEP}^2_{\mathrm{amp,freq}} + \mathrm{NEP}^2_{\mathrm{TLS}}, \tag{6.54}$$

which contains amplifier noise in the frequency direction and TLS noise.

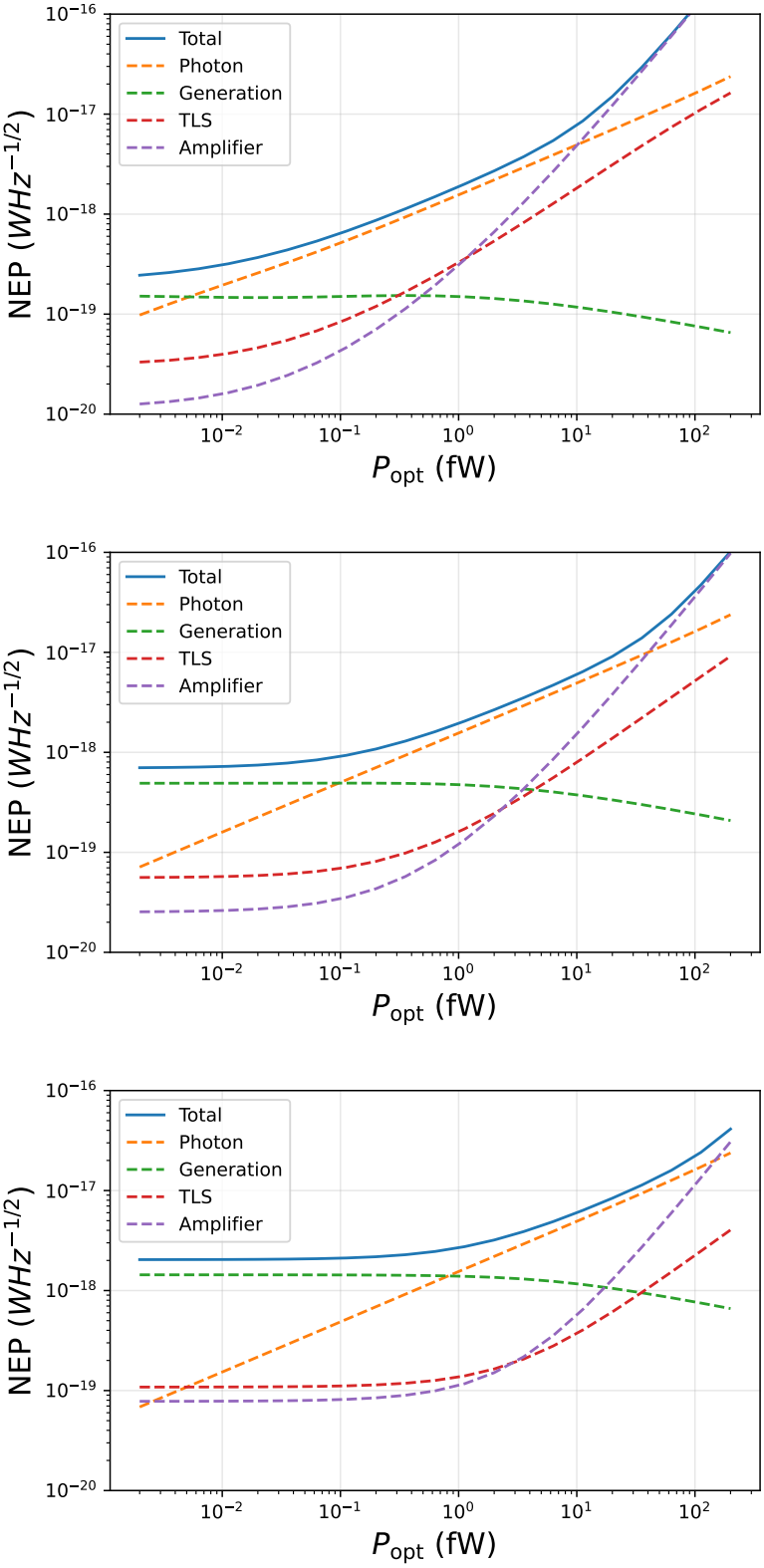

Figure 6.8: NEP components for three fixed feedline readpowers: (top) 10 fW, (middle) 100 fW, (bottom) 1000 fW. Note that the rest of the plots in this section correspond to the middle plot, unless specified otherwise.

Generally, the NEP for a given quantity X can be found by

$$\mathrm{NEP}_X^2 = S_{\mathrm{xx}} \left(\frac{\partial X}{\partial P} \right)^{-2} \tag{6.55}$$

.

Here, $S_{\mathrm{xx}} = \langle \delta X \delta X \rangle$ is the single-sided spectral density due to a particular component X. For a white noise process about zero mean, $S_{\mathrm{xx}} = 2\sigma_X^2 \tau$ with σ_X the standard error of the mean and τ the rate of event occurrence. The NEP can also be interpreted as the standard error of the mean power averaged over 0.5s [55].

Photon noise

Photon noise is described by a Poisson statistical process plus a photon bunching correction:

$$\sigma_{\gamma,n}^2 \tau = \frac{n}{\eta_{\mathrm{opt}} \Delta\nu} (1 + \eta_{\mathrm{opt}} n) \tag{6.56}$$

where n is the photon number density, η_{opt} is the optical efficiency, and $\Delta\nu$ is the received bandwidth. The optical power $P = \eta_{\mathrm{opt}} n \Delta\nu h\nu$, so

$$NEP_\gamma^2 = 2\sigma_{\gamma,n}^2 \tau \left(\frac{\partial P}{\partial n} \right)^2 = 2 \left(h\nu P_{\mathrm{opt}} + \frac{P_{\mathrm{opt}}^2}{\Delta\nu} \right), \tag{6.57}$$

consistent with the incoherent NEP given by Equation C.8, multiplied by 2 for two polarizations.

NEP_γ^2 can also be determined via the optical generation rate $\Gamma_{\mathrm{opt}} = qP/h\nu$. The variance in this case is

$$\sigma_{\gamma,\Gamma_{\mathrm{opt}}}^2 = \left(q\Gamma_{\mathrm{opt}} + \frac{\Gamma_{\mathrm{opt}}^2}{\Delta\nu} \right) \tag{6.58}$$

Thus, the NEP is given by

$$\begin{aligned} NEP_{\gamma}^{2} &= 2\sigma_{\gamma,\Gamma_{\rm opt}}^{2}\left(\frac{\partial\Gamma_{\rm opt}}{\partial P}\right)^{-2} \\ &= 2\sigma_{\gamma,\Gamma_{\rm opt}}^{2}\left(\frac{h\nu}{q}\right)^{2} \\ &= 2\left(h\nu P_{\rm opt}+\frac{P_{\rm opt}^{2}}{\Delta\nu}\right), \end{aligned} \tag{6.59}$$

matching the value obtained starting with σ_n.

Generation and recombination noise

Recombination noise, thermal noise, and readout noise are all modeled by shot noise where each event produces two quasiparticles. We can make this approximation because the energy level of each of these components is below the gap energy so any generation is likely to yield exactly two quasiparticles.

The recombination rate includes contributions from optical photons $\Gamma_{\rm opt}$ and phonons produced from the readout and thermal fluctuations. For a system in equilibrium, we will have $\Gamma_{tot} = \Gamma_{\rm rec}$. Thus, $\Gamma_{tot} = \Gamma_{\rm rec} = \Gamma_{\rm opt} + \Gamma_{\rm th} + \Gamma_{\rm read}$.

Ignoring the phonon sources $\Gamma_{\rm th}$ and $\Gamma_{\rm read}$, we can model the recombination noise as

$$\mathrm{NEP}_{\rm rec}^{2} = 2\sigma_{\Gamma_{\rm rec}}^{2}\left(\frac{\partial\Gamma_{\rm rec}}{\partial P}\right)^{-2}. \tag{6.60}$$

Here, $\sigma_{\Gamma_{\rm rec}}^{2} = 2\Gamma_{\rm rec}$ is the variance due to the generation rate due to quasiparticle recombination. Because we are ignoring phonon sources, $\Gamma_{\rm rec} = \Gamma_{\rm opt} = \frac{q}{h\nu}P_{\rm opt}$ and $\frac{\partial P}{\partial\Gamma_{\rm rec}} = \frac{\partial P}{\partial\Gamma_{\rm opt}} = \frac{h\nu}{q} = \Delta/\eta_{pb}$. Thus,

$$\mathrm{NEP}_{\rm rec}^{2}\Big|_{\rm noopt} = 4\Gamma_{\rm rec}\left(\frac{\partial\Gamma_{\rm rec}}{\partial P}\right)^{-2} = 4\frac{\Delta P_{\rm opt}}{\eta_{\rm pb}}. \tag{6.61}$$

This approximation is valid in cases where optical generation dominates.

Amplifier noise

Amplifier noise can be found through the term $\delta S_{\rm amp} = \delta I_{\rm amp} + j\delta Q_{\rm amp}$ that appears in δS_{21}. Here,

$$S_{I_a I_a} = S_{Q_a Q_a} = \frac{k_B T_{\rm amp}}{2P_{\rm read}^{\rm feed}}, \tag{6.62}$$

with $T_{\rm amp}$ the amplifier temperature, and $P_{\rm read}^{\rm feed}$ the power incident on the feedline. Thus,

$$\mathrm{NEP}^2_{\rm amp,diss} = \frac{k_B T_{\rm amp}}{P_{\rm read}^{\rm feed}} \left(\frac{\delta Re(S_{21})}{\delta P}\right)^{-2} \tag{6.63}$$

$$\mathrm{NEP}^2_{\rm amp,freq} = \frac{k_B T_{\rm amp}}{P_{\rm read}^{\rm feed}} \left(\frac{\delta Im(S_{21})}{\delta P}\right)^{-2}. \tag{6.64}$$

TLS noise

In addition to noise in the dissipation and frequency directions described in Section 6.2, TLS also causes an additional source of noise.

At low power the TLS noise is expected to be independent of incident power (similar to $Q_{\rm TLS}$ in Equation 6.18, whereas at high power it is expected to scale as $P^{-1/2}$). Thus, the TLS spectral density in fractional energy shift can be modeled as

$$S_{\rm xx,TLS}(\nu, P) = \langle \delta x \delta x \rangle = S_{0,\rm TLS} \left(\frac{\nu_{\rm ac}}{\nu_{\rm TLS,ref}}\right)^{\alpha_{\rm TLS}} \delta_{\rm TLS}, \tag{6.65}$$

where $\nu_{\rm TLS,ref}$ and $\alpha_{\rm TLS}$ are phenomenological factors found in Table 6.1.

The NEP due to fluctuations in the resonant frequency are given by $\mathrm{NEP}^2_{\rm TLS} =$

$S_{\mathrm{xx,TLS}}(\partial x/\partial P)^{-2}$. Using the *fractional frequency responsivity*, we have

$$R_x = \frac{\delta x}{\delta P_{\mathrm{opt}}} = \frac{\alpha S_2(\nu)\eta_{\mathrm{opt}}\tau_{\mathrm{qp}}}{4N_0\Delta_0^2 V}. \tag{6.66}$$

Therefore,

$$\mathrm{NEP}^2_{\mathrm{TLS}} = \frac{S_{\mathrm{xx,TLS}}}{R_x^2} = \left(\frac{4N_0\Delta_0^2 V}{\alpha S_2(\nu)\eta_{\mathrm{opt}}\tau_{\mathrm{qp}}}\right)^2 S_{\mathrm{xx,TLS}}(\nu, P). \tag{6.67}$$

General KID noise behavior

Figure 6.8 shows the general KID performance for three different feedline readpowers: 10 fW, 100 fW, and 1000 fW. Generally, TLS and/or generation noise dominates for small optical loads. At high loads, amplifier noise tends to dominate. In the middle range of optical loads, photon noise dominates and the detector is primarily background-limited. By increasing the readpower, we increase the optical loads where this background-limited performance occurs. We will describe an operational optimization procedure based on these principles in the next chapter.

6.5 MKID model: numerical implementation and laboratory testing

The results in this chapter were generated through MKID modeling code modified from Daniel Flanigan's code[3], developed for the EXCLAIM detectors. The code was upgraded for EXCLAIM by Dr. Eric Switzer and myself to reflect our version of the model.

[3] github/danielflanigan/physics/blob/master/mkid/model.py

The model inputs a set of `params` and a set of `extparams`, for each MKID iteration. `params` features parameters related to the MKID design, including α, Q_{i0}, T_c, η_{pb}, V, T_{amp}, ${\eta_{\mathrm{pb}}}^4$, τ_{max}, and the TLS parameters. `extparams` define the external parameters applied to each MKID design, including P_{abs}, $P_{\mathrm{read}}^{\mathrm{feed}}$, and the resonator temperature. Each MKID is defined as a Python object, which is initially calculated using a dictionary of `params`. A single iteration of the MKID object is then calculated using `extparams`, running through the iterative procedure to calculate χ_a.

Various laboratory tests can be performed to evaluate the performance of the MKID array. Generally, the detectors are first measured through dark tests, i.e. where no optical photons are present and the quasiparticle fluctuations are due to readout and thermal generation. The resonance curves can be measured over a range of readpowers at fixed temperature or vice-versa. Assuming Q_c is known, resulting S_{21} curves can be used to measure of Q_i and x as a function of readpower or temperature. The resulting curves can be directly measured against theoretical models to verify detector performance. Likewise, the NEP may be measured by cataloging the fluctuations overa long timescale, though this tends to be more time- and computationally intensive. Following the dark tests, a blackbody source can be used to illuminate detectors with a range of known optical loads, and used to measure Q_i, x, and the NEP.

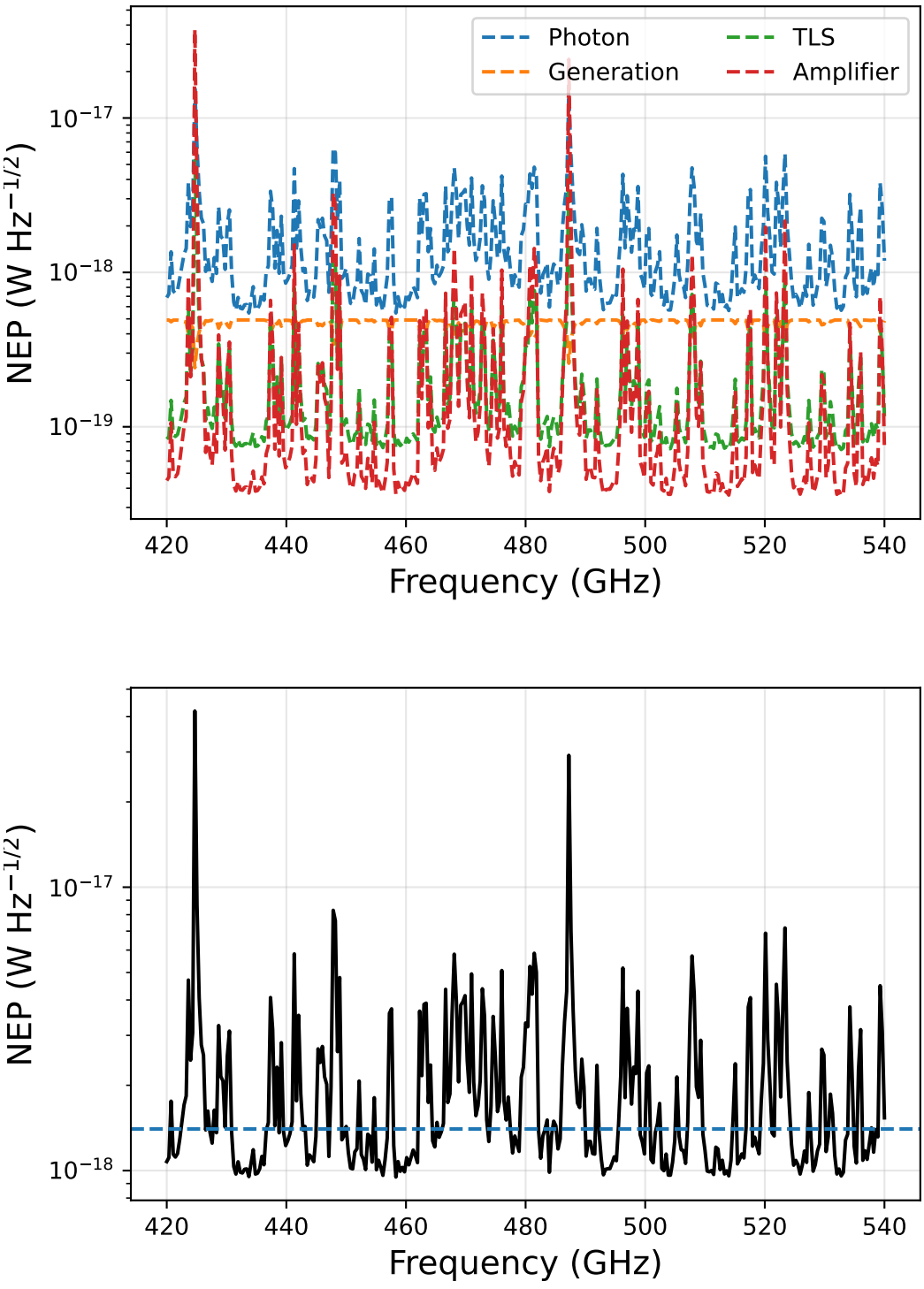

Figure 6.9: Top: Photon, generation, TLS, and amplifier NEP per channel for the MKID model specified by Table 6.1 given the background model of Section 4.2, with a fixed feedline readpower. Bottom: total NEP per channel (solid curve) and the effective NEP (dashed horizontal).

6.6 The impact of the MKID model on the EXCLAIM detector array

Effective NEP

As we described in Section 4.2, the EXCLAIM detectors are subject to nearly three orders of magnitude in variation in the atmospheric signal. The NEP therefore varies by approximately 1.5 orders of magnitude across the array, where bright atmospheric channels have higher noise. In Section 3.1 we showed that the noisiest modes contribute less to the signal to noise of the intensity mapping signals, compared to the dark channels. We therefore describe an *effective NEP per channel* to define the performance of the entire array, based on which modes contribute the most to the survey sensitivity. The effective NEP is a single metric defining performance across the optical passband, with the contributions of $N_{\rm det}$ individual channels weighted by inverse variance [149]:

$$\mathrm{NEP}_{\rm eff} = \left(\frac{\sum_{i=1}^{N_{\rm det}} \hat{\mathrm{NEP}}_i^{-2}}{N_{\rm det}} \right)^{-1/2}, \tag{6.68}$$

where

$$\hat{\mathrm{NEP}}_i = \left(\frac{\sum_j W(\nu_j) \mathrm{NEP}_i^{-2}(\nu_j)}{\sum_j W(\nu_j)} \right)^{-1/2}. \tag{6.69}$$

The factor $W(\nu_i)$ further weights each channel by acoustic frequency, where acoustic frequencies larger than the detector time constant lead to increased noise per channel. For the purposes of this chapter, we apply uniform weighting per channel, i.e. $W(\nu_i) = 1$ for all acoustic frequencies ν_i. However, for a Raster scanning instrument with 1/f noise, a more precise weighting per channel can be calculated through the techniques of Crawford [36]; the calculation for EXCLAIM is shown in Figure 22b in

[4]The model for a constant $\eta_{\rm pb}$ and $\eta_{\rm read}$ are approximate, and a more in-depth discussion on the dependence on $P_{\rm opt}$ and $P_{\rm read}^{\rm abs}$ can be found in Goldie and Withington [60].

Switzer et al. [149], with the bulk of the acoustic frequency weight from $10 - 20\,\mathrm{Hz}$.

Figure 6.9 shows the modeled NEP performance of the EXCLAIM MKID array under constant readout power loading. The top figure shows the photon, generation, TLS, and amplifier noise components. In all but the brightest channels, the incident photon background is the dominant source of noise. In the brightest channels, amplifier noise tends to dominate, consistent with the conclusions of Figure 6.8. The bottom panel shows the total NEP, along with the effective NEP, which evaluates in this case to $\mathrm{NEP}_{\mathrm{eff}} = 1.4 \times 10^{-18}\,\mathrm{W\ Hz^{-1/2}}$. The figure demonstrates the skewed weighting towards the darker channels, due to the inverse variance weighting of the effective NEP metric.

As a consistency check, consider the case that every channel features the same $\hat{\mathrm{NEP}}$. In this case, $\mathrm{NEP}_{\mathrm{eff}} = \hat{\mathrm{NEP}}$, i.e. the effective NEP equals the NEP of each channel. Critically, this distinguishes the effective NEP per channel from the variance of the entire array, which is given by $NEP_{\mathrm{eff}}/N_{\mathrm{det}}^{1/2}$. Note that the effective NEI, the analog of the effective NEP given by Equation 6.68, is applicable to Equation 2.19 describing instrument noise in an intensity map. Here, the effective NEI is defined in the same way as $\mathrm{NEP}_{\mathrm{eff}}$ in Equation 6.68, instead using the NEI per channel. The two quantities are effectively the same if $\partial P/\partial I$ is roughly constant across the passband.

Stray light

As we described in Section 4.4, one of the key performance concerns of the EXCLAIM MKID array is the minimization of stray light. Here, primary concerns include out-of-band light from e.g. strong atmospheric lines outside of the EXCLAIM band, blackbody radiation from warm parts of the telescope, undesired reflections within the detector-spectrometer packaging, and crosstalk between spectral channels. The results

of this section were included in Section 7.2 of Switzer et al. [149], and expanded in this thesis.

First, we will introduce a new vector notation to describe the MKID loading array. Here, $\overrightarrow{P}$ describes the optical loading across the array.

We begin by considering the effect of a flat excess loading per channel, roughly corresponding to the response to blackbody radiation from warm parts of the telescope. Here, we add fixed optical power to each channel in Figures 4.3 and 4.6 that increases the NEP per channel in Figure 6.9. We define this excess loading vector $\overrightarrow{P}^{\rm flat}_{\rm excess}$ where each element is the same. Here, the total loading is simply

$$\overrightarrow{P}^{\rm flat}_{\rm tot} = \overrightarrow{P} + \overrightarrow{P}^{\rm flat}_{\rm excess}. \tag{6.70}$$

For excess loading below $\sim 1\,\mathrm{fW}$, there is little effect on the effective NEP because the excess loading is much smaller than the nominal atmospheric loading. However, beyond this threshold, the excess loading will cause an increase in the effective NEP with a power law form,

$$\mathrm{NEP}_{\rm eff}(P^{\rm flat}_{\rm stray}) = \mathrm{NEP}_{\rm eff}(P_{\rm stray}=0)\left(1+\frac{P_{\rm stray}}{0.25\,\mathrm{fW}}\right)^{0.41}. \tag{6.71}$$

Note that in the case that loading far exceeds the nominal atmospheric loads, Equation 6.71 increases roughly as $\mathrm{NEP}_{\rm eff} \sim P^{1/2}_{\rm stray}$. This corresponds to the Poisson term for the NEP in Equation C.8, evaluated with the stray power.

Second, we consider the effect of optical 'ghosts'[5], where the power from a single channel spreads uniformly across all other channels. Reflections in the detector-spectrometer packaging would produce such an effect, as power in each channel is

[5]Note that 'optical ghosts' is somewhat of an oxymoron, given that ghouls tend to be invisible.

reflected and spread uniformly into other channels. Here, we consider a mixing matrix $\overleftrightarrow{\Lambda}(\alpha_{\text{ghost}})$, which for an array of N frequency channels is given by

$$\overleftrightarrow{\Lambda}(\alpha_{\text{ghost}}) = \begin{pmatrix} 1-\alpha_{\text{ghost}} & \alpha_{\text{ghost}}/(N-1) & \alpha_{\text{ghost}}/(N-1) & ... \\ \alpha_{\text{ghost}}/(N-1) & 1-\alpha_{\text{ghost}} & \alpha_{\text{ghost}}/(N-1) & ... \\ \alpha_{\text{ghost}}/(N-1) & \alpha_{\text{ghost}}/(N-1) & 1-\alpha_{\text{ghost}} & ... \\ \vdots & \vdots & \vdots & \ddots \end{pmatrix}, \tag{6.72}$$

summing to 1 in each row and column.

Here, the effective NEP is given by

$$\overrightarrow{P}_{\text{ghost}}(\alpha_{\text{ghost}}) = \overleftrightarrow{\Lambda}(\alpha_{\text{ghost}})\overrightarrow{P}. \tag{6.73}$$

Here, the total power in the system is conserved. Calculating the effective NEP for $\overrightarrow{P}_{\text{ghost}}$ using the EXCLAIM background model, we find

$$\text{NEP}_{\text{eff}}(\alpha_{\text{ghost}}) = \text{NEP}_{\text{eff}}(\alpha_{\text{ghost}}=0)\left(1+\alpha_{\text{ghost}}/3\times10^{-4}\right)^{0.42}. \tag{6.74}$$

The increase in the effective NEP with α_{ghost} is driven by the bright spectral channels, which add loading to the faint channels. Because the effective NEP is inverse variance-weighted, the dark channels contribute disproportionately to the effective NEP, resulting in decreased sensitivity.

EXCLAIM design - optimizing Q_c

The effective NEP is also a useful tool for evaluating the system-wide noise performance as a function of various MKID design parameters, such as Q_c and V. As a demonstrative example, I examine its use to optimize Q_c in based on the EXCLAIM

detector array and anticipated atmospheric loading.

Q_c affects the portion of $P_{\text{read}}^{\text{feed}}$ that gets absorbed by the detectors, and the absorption occurs when $Q_i = Q_c$, and $\chi_c = \chi_g = 2\chi_a = 1$, demonstrated by Equations 6.27, 6.28, and 6.29, assuming the readout frequency is on resonance. As we show in the next chapter, when as long as NEP is dominated by quasiparticle generation and recombination noise (i.e. TLS and amplifier noise are subdominant), the NEP is minimized in a single detector when $Q_i \approx Q_c$. Noting that Q_i increases with the optical power, Q_c can be tuned such that the NEP is minimized for specific optical loads. Note, however, that Q_c is fixed by the geometry of the resonators, and cannot be tuned during the flight.

In Figure 6.10, we show how the ratio Q_i/Q_c and the NEP vary with Q_c given the EXCLAIM background model. We assume a single $P_{\text{read}}^{\text{feed}}$ value. Here, the top panel shows the ratio Q_i/Q_c, which reaches 1.0 for $Q_c \sim 10^5$ in dark channels, maximizing χ_a in Equation 6.29 and therefore $P_{\text{read}}^{\text{feed}}$. The bright channels clearly show a much lower ratio Q_i/Q_c because Q_i is greatly reduced with the increased photon background. These brighter channels clearly display a higher total NEP, shown in the second panel (also shown in the third panel, truncated at $10^{-17}\,\text{W Hz}^{-1/2}$ to better show the behavior of darker channels). The fourth panel shows the generation NEP, which peaks at $Q_c \sim 10^5$, where Q_i is minimized. Finally, the amplifier noise is shown in the fifth panel, clearly peaking for the lower and higher values for Q_c.

The cumulative effect of the plots in Figure 6.10 is shown in Figure 6.11. The figure shows the effective NEP as a function of Q_c. Two minima are shown for $Q_c \sim 10^4$ and $\sim 5 \times 10^6$. These two minima occur when the squared sum of the generation and amplifer NEP is minimized. Because generation noise peaks around $Q_c \sim 10^5$ and amplifier noise peaks for lower and higher values for Q_c, there are effectively two minima surrounding $Q_c \sim 10^5$. However, the effective NEP only varies by $\sim 12\%$ for

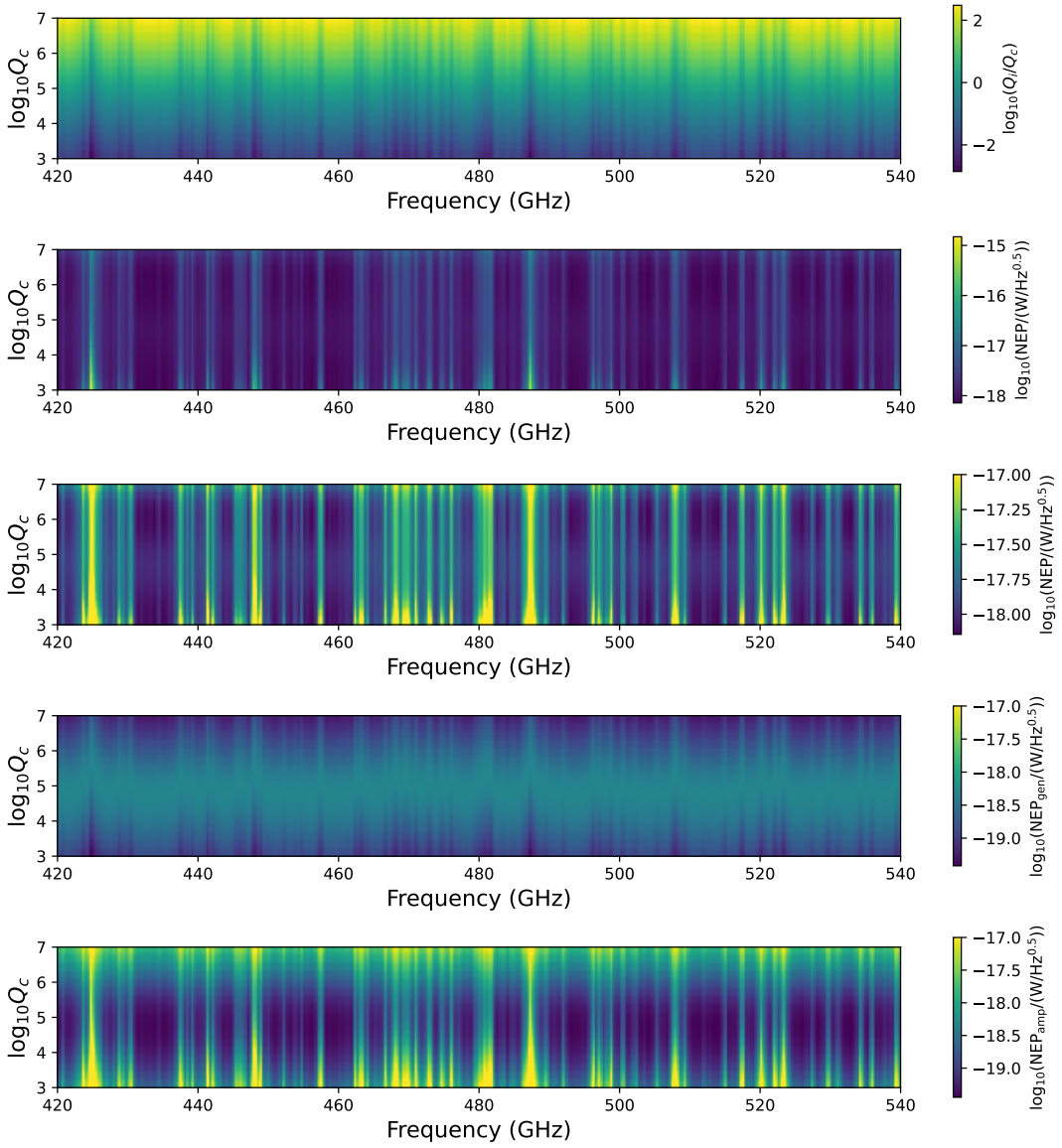

Figure 6.10: From top to bottom: Q_i/Q_c, $\mathrm{NEP_{tot}}/(\mathrm{W/Hz^{1/2}})$, $\mathrm{NEP_{tot}}/(\mathrm{W/Hz^{1/2}})$ (colorbar saturated at 10^{-17} to emphasize behavior at faint loads), $\mathrm{NEP_{gen}}/(\mathrm{W/Hz^{1/2}})$, and $\mathrm{NEP_{amp}}/(\mathrm{W/Hz^{1/2}})$, each as a function of frequency and Q_c, assuming the EXCLAIM background load and the MKID model.

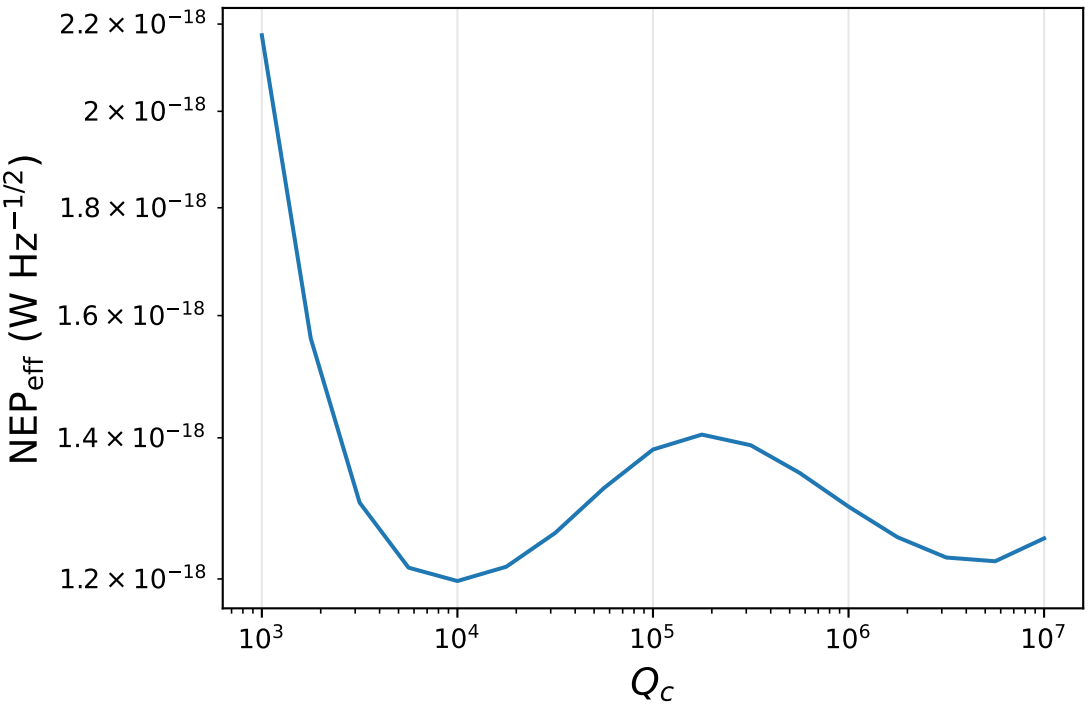

Figure 6.11: Effective NEP vs. Q_c. Can be thought of as the weighted mean of the total NEP in the second panel of Figure 6.10 over the range of frequencies.

$Q_c \gtrsim 10^4$.

It is possible that the EXCLAIM background model shown in Section 4.2 underestimates the loading per channel. This can be because of extra optical loading from reflections or warm portions of the instrument, or a miscalculation in the background mode itself. Decreasing Q_c provides a safeguard against this. If the loading exceeds expectation, then Q_i will be decreased from its expected value. This margin of uncertainty in Q_i due to uncertainty in the optical power can be ameliorated by tuning the readpower delivered to each detector. This procedure, as well as the demonstration that $\mathrm{NEP_{eff}}$ is not significantly impacted by changes in Q_c, results in the decision to use $Q_c = 2 \times 10^5$ for the EXCLAIM MKID array.

7 EXCLAIM DETECTORS: OPERATIONAL OPTIMIZATION TO MAXIMIZE DYNAMIC RANGE IN EXCLAIM MICROWAVE KINETIC INDUCTANCE DETECTORS

In this chapter, I restate verbatim a paper I wrote with Dr. Eric Switzer and the EXCLAIM detector group [114], describing a technique for in-situ optimizations of MKID arrays, entitled 'Operational Optimization to Maximize Dynamic Range in EXCLAIM Microwave Kinetic Inductance Detectors', accepted for publication in the 19th International Workshop on Low Temperature Detectors (LTD19) proceedings in the Journal of Low Temperature Physics. Co-authors include Eric R. Switzer, Emily M. Barrentine, Thomas Essinger-Hileman, James P. Hays-Wehle, Philip D. Mauskopf, Omid Noroozian, Maryam Rahmani, Adrian K. Sinclair, Ryan Stephenson, Thomas R. Stevenson, Peter T. Timbie, Carolyn Volpert, Eric Weeks.

7.1 Introduction

MKIDs are pair-breaking superconducting microwave resonators capable of highly sensitive detection of radiation, with applications ranging from millimeter waves to X-rays [42, 170, 102]. Arrays of numerous MKID detectors can be multiplexed on a single transmission line [158] and are highly tunable to maximize sensitivity to a wide range of optical loading, making them ideal for use in terrestrial, suborbital, and space-based telescopes [156]. MKIDs operate through the kinetic inductance effect, whereby energetic photons absorbed in a superconducting thin film break Cooper pairs, altering the inductance and resistance of the film. A single feedline can contain a comb of superconducting resonant circuits, each responding in amplitude and phase to an optical power delivered to the MKID.

MKID characteristics are tuned both by the geometry and materials, and dynamically as a function of their readout. The resonator geometry, including the active volume and the coupling capacitance, can be chosen to maximize sensitivity. The readout system permits additional detector optimization during operation by tuning

the frequency and readout power transmitted to each detector. These readout optimizations can be performed uniquely for each detector and optical power, significantly increasing the dynamic range. This tunability is especially advantageous in spectroscopy, where the optical power varies widely across individual channels. In contrast, TESs can be designed to operate at higher optical power by increasing the saturation power through increased leg conduction, and compensating Joule power to target operating conditions. Higher conduction increases the intrinsic phonon noise [102], making it difficult to achieve operation at high optical power without compromising noise at low optical power.

EXCLAIM [25] is a balloon-borne cryogenic telescope featuring an aluminum MKID array and designed to demonstrate the line intensity mapping technique [83] to obtain tomographic maps of extragalactic carbon monoxide and singly-ionized carbon emission, which may be used to infer the cosmic star formation history [24]. EXCLAIM features a set of six μSpec spectrometers-on-a-chip with resolving power $R = 512$ [104] read out in a 3.25-3.75 GHz microwave band by a Xilinx RFSoC.

MKIDs have already demonstrated nearly background-limited performance in balloon [99, 64] and space-like [12] backgrounds in the far-infrared. Like other balloon- and space-based mid- to far-infrared missions, EXCLAIM detectors must accommodate a wide range of background loads spanning three orders of magnitude. MKIDs proposed for next-generation space instruments[59, 86] require high sensitivity over loads ranging from three [59] to five [22] orders of magnitude, owing to the wide variety of science cases targeted by a single instrument. While the EXCLAIM mission does not require sensitivity to the brightest background loads, it will provide a valuable testbed for dynamic range optimization for future far-IR missions.

This study describes the optimization of the EXCLAIM MKID design over a wide range of background loads and the underlying device physics for general MKID

applications. We focus on optimizing the readout system with a purely model-based approach, which can support dynamic range optimization during operation. Throughout, we simplify the model by choosing a single signal modulation frequency of 1 Hz and constant quasiparticle pair-breaking efficiencies, and we describe how these effects may be accounted for in the discussion section.

7.2 MKID sensitivity to a widely-varying background

The anticipated incident background load for EXCLAIM ranges from $P_{\mathrm{opt}} \approx 0.1$ to 100 fW at the input of the spectrometer throughout the $420-540$ GHz passband, with strong frequency-to-frequency variation driven by narrow atmospheric emission lines subject to low pressure broadening in the upper atmosphere [25]. Once the flight stabilizes, observations occur at 45° elevation at an altitude of $\sim$34 km. Hence, dynamic range requirements apply to temporally stable loading rather than requiring significant real-time response. The space background is one to two orders of magnitude below the dark windows in upper atmospheric emission in the EXCLAIM band. Light passes through a cold stop to minimize stray light, then through the lenslet-coupled spectrometer, then into the MKID array. We estimate antenna efficiency (to the input of the spectrometer formed by the cold stop) $\eta_{\mathrm{ant}} = 0.85$ and detector efficiency (through the cold stop to the detectors) of $\eta_{\mathrm{det}} = 0.23$. Throughout, P_{opt} and NEP are defined at the cold stop (incident on the spectrometer lenslet) rather than at the detector in the on-chip spectrometer.

Assuming a model similar to Zmuidzinas [170] and Mauskopf [102] with MKID

Parameter	Symbol	Parameter type	Value
Resonator volume	V	Design choice	374 μm^3
Coupling quality factor	Q_c	Design choice	2.3×10^5
Residual quality factor	Q_{i0}	Measured	1.75×10^6
Kinetic inductance fraction	α	Measured/designed/material	0.775
Readout qp generation efficiency	η_{read}	Measured	9.24×10^{-4}
Modulation frequency	f_{mod}	Operational constraint	1 Hz
Amplifier temperature	T_{amp}	Design choice	4.1 K
Bath temperature	T_{bath}	Design choice	100 mK
TLS exponent	α_{TLS}	Measured	-0.69
TLS spectral density at 1 kHz	$S_{0,\mathrm{TLS}}$	Measured	1.49×10^{-16} Hz^{-1}
TLS photon number	N_{TLS}	Measured	241
Critical temperature	T_c	Measured	1.33 K

Table 7.1: MKID design reference parameters for the EXCLAIM detector array.

design parameters shown in Tab. 7.1, we calculate the total NEP per detector through

$$\mathrm{NEP}^2_{\mathrm{tot}} = \mathrm{NEP}^2_{\mathrm{opt}} + \mathrm{NEP}^2_{\mathrm{gen}} + \mathrm{NEP}^2_{\mathrm{rec}} + \mathrm{NEP}^2_{\mathrm{amp}} + \mathrm{NEP}^2_{\mathrm{TLS}}, \tag{7.1}$$

representing the total, optical, quasiparticle generation and recombination, amplifier, and two-level system (TLS) noise, respectively. Throughout, we assume frequency readout and signal modulation at a nominal frequency $f_{\mathrm{mod}} = 1\,\mathrm{Hz}$. The dominant sources of noise depend on the level of background radiation, which we specify in three regimes:

Low-background Loads: for low absorbed optical power, the detector NEP is typically dominated by generation noise and TLS noise, where the latter only affects readout in the frequency direction. Generation noise is caused by an increase in the number of quasiparticles from thermal phonons and readout photons, while TLS noise is produced by two-level systems at the boundaries of dielectric layers in the film. The NEP of these contributions is

$$\mathrm{NEP}^2_{\mathrm{gen}} + \mathrm{NEP}^2_{\mathrm{TLS}} = 4\left(\Gamma_{\mathrm{th}} + \Gamma_{\mathrm{read}}\right)\left(\frac{d\Gamma}{dP_{\mathrm{opt}}}\right)^{-2} + S_{\mathrm{TLS}}\left(\frac{dx}{dP_{\mathrm{opt}}}\right)^{-2}, \tag{7.2}$$

where Γ_{th} and Γ_{read} are the quasiparticle generation rates due to thermal phonons and readout photons, respectively, and dx is the differential fractional frequency shift due to changes in optical power. We model the readout generation rate as $\Gamma_{\mathrm{read}} = \eta_{\mathrm{read}} P^{\mathrm{abs}}_{\mathrm{read}}/\Delta$, with $P^{\mathrm{abs}}_{\mathrm{read}}$ the absorbed readout power and $\Delta = 1.764 k_B T_c = 180\,\mathrm{meV}$ the gap energy, where T_c is the critical temperature. We assume a constant η_{read}, though generally it may depend on the optical and readout powers (see Discussion below). Within the TLS noise term, $S_{\mathrm{TLS}} = S_{0,\mathrm{TLS}}(f_{\mathrm{mod}}/\nu_{\mathrm{TLS}})^{\alpha_{\mathrm{TLS}}}\delta_{\mathrm{TLS}}$ is the TLS power spectral density with $\nu_{\mathrm{TLS}} = 1\,\mathrm{kHz}$ pivot, and $\delta_{\mathrm{TLS}} = \tanh[h\nu_{\mathrm{read}}/(2k_BT)]^{1.5} \cdot (N_{\mathrm{ph}} + N_{\mathrm{TLS}})^{-1/2}$

describes losses due to TLS, with $N_{\rm ph} = P_{\rm read}^{\rm abs} Q_i (2\pi h \nu_{\rm read}^2)^{-1}$ the number of readout photons. Here, $\nu_{\rm read}$ is the microwave readout frequency and h is Planck's constant. This form matches measurements of resonators with $\nu_{\rm read} = 3.4\,\mathrm{GHz}$ by Gao [57] suggesting $S_{\rm TLS} \sim T^{-1.5}$ for $T > 100\,\mathrm{mK}$. $dx/dP_{\rm opt} \equiv R_x \propto \tau_{\rm qp}/V$ is the frequency responsivity describing variations in resonator frequency due to the kinetic inductance effect, and $d\Gamma/dP_{\rm opt} = q/h\nu$, where $q \equiv h\nu\eta_{\rm pb}/\Delta$ is the number of quasiparticles produced per photon, and $\eta_{\rm pb}$ describes the pair-breaking efficiency, evaluating to $\eta_{\rm pb} = 0.57$ when the photon energy $> 2\Delta$, as is the case for the optical frequencies of interest here [84]. Note that noise from single-quasiparticle interactions may also contribute to generation noise due to e.g. magnetic field flux trapping [55].

Photon Background-limited Loads: the background-limited noise-equivalent power (NEP) for unpolarized radiation at the input of an incoherent detector such as an MKID is [169]

$$\mathrm{NEP}_{\rm opt}^2 = 2\mathrm{h}\nu\mathrm{P}_{\rm opt} + \frac{2\mathrm{P}_{\rm opt}^2}{\mathrm{B}}, \tag{7.3}$$

where ν is the frequency of the incident radiation, B is the spectrometer optical bandwidth per channel, and $P_{\rm opt}$ is the incident optical power.

Recombination noise due to optically-generated quasiparticles produces an additional irreducible source of noise [94]. $\mathrm{NEP}_{\rm rec}^2 \approx 4h\nu q^{-1} P_{\rm opt}$ in the case that quasiparticle generation is dominated by optical photons. For EXCLAIM we find that $\mathrm{NEP}_{\rm rec}/\mathrm{NEP}_{\rm photon} \approx \sqrt{2q^{-1}}$, producing a ∼23% increase in NEP compared to the photon background at 480 GHz.

High-background Loads: for high optical power, amplifier noise dominates the EXCLAIM detector noise, with NEP given by

$$\mathrm{NEP}_{\rm amp}^2 = \frac{k_B T_{\rm amp}}{P_{\rm read}^{\rm feed}} \left(\left| \frac{\partial S_{21}}{\partial x} \right| R_x \right)^{-2} = \frac{k_B T_{\rm amp}}{P_{\rm read}^{\rm feed}} \left(\chi_a Q_i R_x \right)^{-2}. \tag{7.4}$$

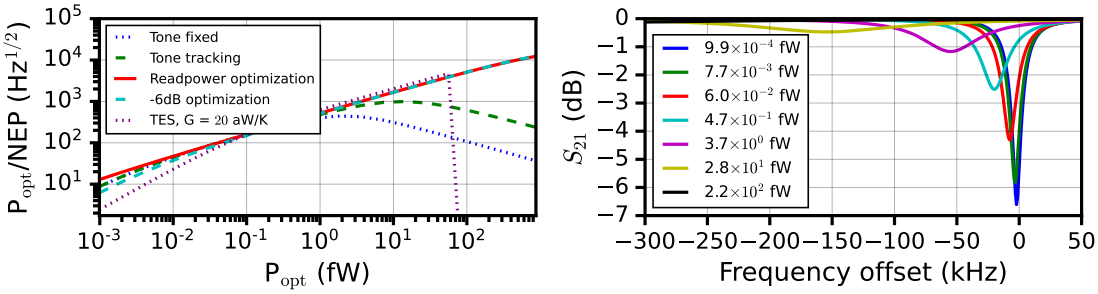

Figure 7.1: Simulated comparison between the three operational regimes. Left: instantaneous dynamic range, defined as the ratio of the optical power to the total NEP, akin to the signal-to-noise for one second of integration time. Right: magnitude of transmission S_{21} for a selection of incident optical power across the EXCLAIM band.

where $\chi_a = 2(Q_r^2 Q_i^{-1} Q_c^{-1})\,(1 + 2Q_r x)^{-1}$ is the absorption efficiency, with x the fractional frequency detuning, which equals zero when the readout tone frequency is on resonance. Here, the resonator quality factor is $Q_r^{-1} = Q_c^{-1} + Q_i^{-1}$, and the χ_a is maximized when $Q_i = Q_c$. χ_a represents the fraction of the delivered readout power $P_{\text{read}}^{\text{feed}}$ that is absorbed by the MKID, as $P_{\text{read}}^{\text{abs}} = \chi_a P_{\text{read}}^{\text{feed}}$.

7.3 Readout tone-tracking and readpower optimization

Several design parameters (e.g. V and Q_c) may be used to optimize detectors for a given application but are functions of the resonator geometry, and therefore cannot be optimized operationally. On the other hand, the readout system may implement in-situ NEP optimization as a function of optical power. The readout system enables two techniques:

Resonance tone-tracking: the tracking of each readout tone to be exactly on-resonance, i.e. x=0 for χ_a in Eqn. 7.4, minimizing amplifier noise. Without

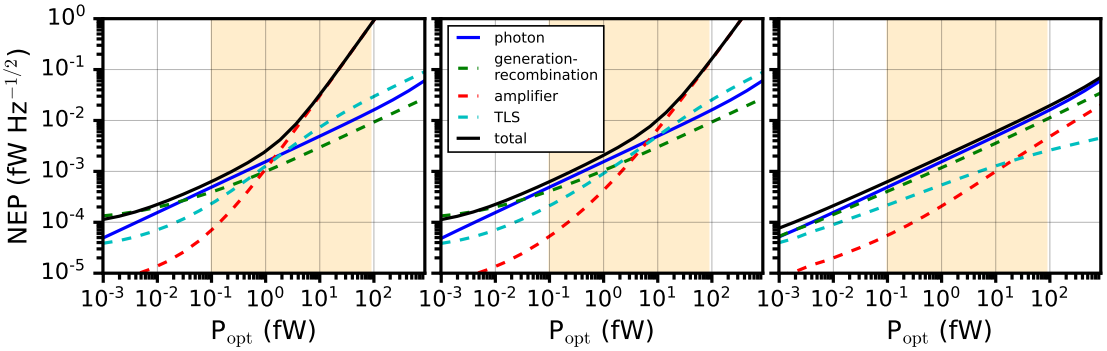

Figure 7.2: Simulated NEP curves for three cases: (left) fixed readpower without tone-tracking, (center) fixed readpower with tone-tracking, and (right) optimized readpower with tone-tracking. The shaded orange region represents the range of anticipated incident optical power for the EXCLAIM mission. In the left two plots, the readpower is fixed to minimize NEP at $P_{\rm opt} = 0.15\,\mathrm{fW}$, whereas the right plot optimizes at all input optical powers. In the left plot, the lack of tone-tracking causes a frequency mismatch, thereby increasing amplifier noise at high input optical power.

tone-tracking, we assume the readout tone equals the resonance frequency under a nominal optical loading and that the resonator can move away from this fixed tone under changing optical power (Fig. 7.1, right). Note that a similar dependence occurs when reading out in dissipation quadrature, where $\mathrm{NEP}_{\rm amp,diss} \propto \chi_a^{-1}$.

Readout power optimization: an adjustable readout power $P_{\rm read}^{\rm feed}$ delivered to each detector, minimizing the NEP per frequency channel. For low optical powers, a decrease in $P_{\rm read}^{\rm feed}$ leads to a decrease in $\mathrm{NEP}_{\rm gen}$, provided the resonator is cold enough for thermal quasiparticle generation and TLS noise to be subdominant. For high optical powers, an increase in $P_{\rm read}^{\rm feed}$ suppresses amplifier noise, up to the regime where the resonator response begins to bifurcate [145] or otherwise display signs of nonlinear response.

These in-situ optimizations are significant for EXCLAIM because they maximize the sensitivity per channel without uniquely fabricating each detector to its anticipated flight loading. In EXCLAIM's expected flight operation, the tone-tracking and

readpower optimization steps will be performed once the altitude stabilizes through measurements of quality factor and resonator frequencies as a function of several readpowers, requiring roughly a minute of data. We anticipate only requiring this optimization once, after the altitude stabilizes. Approaches for real-time optimization of readpower in response to optical power are deferred to future work, but may measure derivatives between tones on and near resonance. A low-power pulsed optical reference emitter will enable periodic responsivity [149]. Within the proposed RFSoC-based readout design for EXCLAIM [144], a PID loop style tone tracking algorithm can be applied after the digital down conversion stage in a time-division multiplexed fashion. Two PIDs will be used, each with an estimated resource utilization of 3 DSP48 multipliers, 2 FIFOs of length 512, and 5 adders. This uses only a fraction of the resources compared to the front-end FFT.

In the low optical power regime where noise is dominated by quasiparticle generation-recombination and TLS, the readpower that minimizes noise also maximizes the internal quality factor $Q_i = \left(Q_{\mathrm{qp}}^{-1} + Q_{\mathrm{TLS}}^{-1} + Q_{i0}^{-1}\right)^{-1}$. Here, Q_{i0} is an empirical residual quality factor, $Q_{\mathrm{TLS}} = 2.61 \times 10^4 \delta_{\mathrm{TLS}}^{-1}$ is the dissipation due to two-level systems with δ_{TLS} defined after Eqn. 7.2, and $Q_{\mathrm{qp}} \propto \delta n_{\mathrm{qp}}^{-1}$ is the dissipation due to quasiparticles in the film, which decreases with an increased number of quasiparticles. Note that readpower optimization differs from the typical operational procedure to maximize χ_a by setting $Q_i = Q_c$. Utilizing readpower optimization, a design with Q_c lower than Q_i can achieve near-ideal noise performance while also providing robustness to changes in optical loading, realized quality factors, and resonance-finding. Because Q_i can be measured directly through S_{21} in a readpower sweep, this technique is less time- and computation-intensive compared to measuring and minimizing the noise directly. The relation between maximal Q_i and minimal NEP breaks down for high optical powers where amplifier noise dominates; in this case, increasing the readpower reduces the

noise. For EXCLAIM, however, these optically bright, high-noise channels do not contribute as strongly to the extragalactic science signal, so the Q_i optimization step will suffice. More work will be needed to define the readpower optimization routine in future missions requiring higher sensitivities to brighter sources.

Based on these techniques, we analyze the noise performance of the EXCLAIM detector design under three regimes: (i) fixed tone (i.e. the tone frequency is fixed to the resonance under nominal loading) with fixed readpower; (ii) resonance tone-tracking with fixed readpower; (iii) resonance tone-tracking with optimized readpower. While the first two regimes have been demonstrated in laboratory and operational environments [72], the active readout power optimization represents a new technique; previous approaches have optimized the readout power by e.g. setting it to $-6\,\mathrm{dB}$ below the bifurcation power threshold [64]. In the model presented here, setting the feedline readpower $-6\,\mathrm{dB}$ below the bifurcation threshold and including tone tracking leads to a 26% increase in NEP compared to our optimization method for $0.01\,\mathrm{fW}$ loads and a 108% increase for $10\times$ lower loads, while $1000\,\mathrm{fW}$ loads are similar. The $-6\,\mathrm{dB}$ below the bifurcation threshold with fixed tones yields a similar NEP increase for the darkest loads, and a 53% increase in NEP for the brightest loads compared to the optimal readpower case.

Fig. 7.1 (left) shows the dynamic range performance and Fig. 7.2 shows the noise contributions in each operational regime, with minimum loads set a decade lower than the EXCLAIM minimum. In the case of the fixed readpower, $P_{\mathrm{read}}^{\mathrm{feed}} = 4.8\,\mathrm{fW}$ ($P_{\mathrm{read}}^{\mathrm{abs}} = 2.4\,\mathrm{fW}$) minimizes the NEP at $P_{\mathrm{opt}} = 0.15\,\mathrm{fW}$, representing a typical dark channel in the EXCLAIM passband. The case with optimized readpower scales approximately as $P_{\mathrm{read}}^{\mathrm{feed}} \approx 1.6\ \mathrm{fW} + 27\ P_{\mathrm{opt}}$. A basic TES sensitivity model is also shown, including noise from phonons and photons, as well as saturation. Here, we follow the model of Mauskopf [102] taking $G = 20\,\mathrm{aW/K}$ and $F_{\mathrm{link}} = 0.6$.

7.4 Discussion

We have investigated and modeled the physical effects of MKID optimizations through the readout system, including resonance tone-tracking and the optimization of the readout power as a function of optical power. These conclusions have several caveats that we will study through future measurements. In particular, nonlinear behavior has been observed in MKIDs with high incident background loads, due to bifurcation and nonlinear heating. In Goddard Al CPW test devices, this behavior has tentatively been observed at higher readpowers than the range described here. Future models can employ quasiparticle kinetic equations[27, 60] representing the local heating and cooling of quasiparticles, resulting in non-constant values for η_{read} and, to a lesser extent, η_{pb} [68]. The simple model used here agrees with readpower sweeps in the critical regime across the maximum of the quality factor.

Second, the quasiparticle lifetime may limit sensitivities at lower power levels and rapid signal variations. As a function of signal modulation frequency f_{mod}, the finite quasiparticle lifetime leads to increased TLS noise as $\mathrm{NEP}_{\mathrm{TLS}} \propto f_{\mathrm{mod}}^{\alpha_{\mathrm{TLS}}/2}$ and decreased responsivities through the multiplication of the responsivity R_x (following Eqn. 7.4) by $[1 + (2\pi f_{\mathrm{mod}}\tau_{\mathrm{qp}})^2]^{-1}$, leading to an increase in TLS and amplifier NEP. Note that τ_{qp} is inversely proportional to the number of quasiparticles in this model. However, for low-quality films or low quasiparticle densities, this quantity may saturate, resulting in a maximum lifetime τ_{max} [170]. Furthermore, the quasiparticle free-decay time may also limit sensitivities for f_{mod}, though τ_{qp} provides a more stringent constraint for the MKIDs described here.

With careful accounting for these caveats, the readpower optimization and tone-tracking techniques we describe can provide nearly background-limited sensitivity over a wide range of optical power. This tunability provides an incentive for developing

MKIDs for instruments requiring a wide dynamic range, including proposed space telescopes. In the EXCLAIM band, the simpler technique of setting P_{read} to 6 dB below the bifurcation approximates the optimal noise performance on all but the darkest loads. The widely-ranging background anticipated for the EXCLAIM mission will offer a testbed for these techniques.

Acknowledgements This work was supported by a 5-year NASA Astrophysics Research and Analysis (APRA 17-APRA17-0077) grant and NASA-Goddard Internal Research and Development funds, and TMO acknowledges support from the NASA-Goddard internship program and the UW-Madison graduate program.

8 EXCLAIM OPTICS: MODELING

Here, I describe optical modeling techniques for the EXCLAIM system. The primary goals of these ongoing studies are to (i) ensure the beam profile tapers enough at the edge of the primary mirror to minimize loading from warm parts of the instrument onto the detectors, and (ii) to characterize the far-field profile of the beam. These studies present some of the initial steps of this characterization procedure, while more advanced computational tools are being developed for higher-fidelity modeling. After giving an overview of the optical design, I describe various tools for characterizing the near-field profile of the beam. Note that throughout, I think of the optics in the 'time-reversal sense' where the input of the beam is located in the focal plane, propagated out through the primary mirror and into the far field.

8.1 EXCLAIM optical design

In this chapter, I discuss optical modeling in support of the EXCLAIM mission. Optical modeling is crucial for the EXCLAIM mission for two reasons: minimizing the beamwidth on the sky to access cosmological information on smaller scales, and minimizing the amount of optical 'spill' arising from blackbody radiation emitted by warm parts of the instrument. I will describe how the EXCLAIM mission design is compliant with system requirements based on these limitations, and the modeling considerations behind our analyses.

EXCLAIM features a three-mirror off-axis design, which is summarized in the cross-sectional view in the left panel of Figure 8.1. The left panel of the figure shows the optical assembly within the dewar, with a 'submarine' receiver assembly. Here, the red shaded region shows the primary envelope of the beam, which is incident on the primary mirror at an elevation of 45°. After reflecting off the parabolic primary mirror, the incident rays reflect off a folding flat mirror, off a parabolic secondary

Element	Distance from cold stop	Parameters
Lens aperture	0	FWHM = 2.302 cm
Cold stop	0	$r = 3.810$ cm
Optics tube baffles	0.89 - 11.81 cm	$r = 3.874$ cm
Secondary mirror	33.06 cm	$f = 19.50$ cm
Intermediate focus baffle	54.00 cm	$r = 4$ cm
Primary mirror	188.06 cm	$f = 155.0$ cm

Table 8.1: Simulation parameters for POPPY simulation using the `Fresnel Optical System` setting. The aperture at the lens is simulated as a Gaussian with FWHM provided above. The mirrors are simulated through POPPY as lenses with focal lengths denoted by f. The baffles and the Cold Stop are simulated as pupils with radii given by r. Note that we consider 9 optics tube baffles, each with the same radius of truncation, and we do not consider the finite sizes of the lenses/mirrors because they contribute negligibly.

mirror, and into the optics tube. Within the optics tube, shown in the right panel of the figure, the beam passes through a collimated region that includes a vacuum window and various low- and high-pass filters, before passing through a lens that focuses the beam on the focal plane. Within the collimated region, absorptive baffles reduce sidelobes for angles beyond the image of the cold stop. Table 8.1 shows the main parameters in the optics analysis.

The effects of beamwidth and excess detector loading on science sensitivities were described in Section 4.4. Here, increases in the beamwidth lead to the suppression of information on smaller spatial scales, minimizing the number of observable modes and particularly affecting measurements of the shot power spectrum. Furthermore, wider illumination of the optics may lead to increased loading on the detectors due to blackbody radiation spilling onto warm parts of the instrument, thereby increasing noise in the detectors. Here, the primary requirement is that the response at the edge of the primary mirror be at least 40 dB below the peak. Our analyses use three tools, listed here in order of increasing sophistication and accuracy:

1. **Ray-tracing:** basic analysis purely based on geometry. In the original design, Zemax OpticStudio was used for off-axis ray-tracing analysis. In this thesis, however, I utilize basic on-axis ray-tracing to provide intuition and baseline characteristics for the EXCLAIM optical system, with off-axis mirrors replaced by on-axis lenses of equivalent focal lengths.

2. **Gaussian optics:** next-level analysis based on the Gaussian optics formalism. I utilize Physical Optics Propagation in Python (POPPY) [121] software[1], which also uses on-axis lenses to substitute off-axis mirrors. The Gaussian optics formalism is used to calculate diffraction in the EXCLAIM system; this is not achievable by pure ray-tracing analysis. POPPY is used to calculate diffraction from the lenses/mirrors, cold stop, and baffles, though it only calculates scalar transmission, while missing polarization information. This calculation is computationally efficient, and can simulate the full EXCLAIM band in seconds to minutes.

3. **Electromagnetic simulation:** full-scale simulations, done by meshing all surfaces in the optical assembly and solving Maxwell's Equations over the grid. This is done using Computer Simulation Technology (CST)[2], which allows full polarization analysis of off-axis mirrors. The main drawbacks are that CST is extremely computationally demanding (taking est. months to simulate at 420 GHz), and it is not feasible to calculate absorptive elements like lenses or perfect stops. This is because the `integral equation solver` setting used for these analyses does not work with three-dimensional gridding, and perfect absorption on a two-dimensional surface is not physically possible through the

[1]This research made use of POPPY, an open-source optical propagation Python package originally developed for the James Webb Space Telescope project.

[2]CST Studio Suite https://www.3ds.com/products-services/simulia/products/cst-studio-suite/

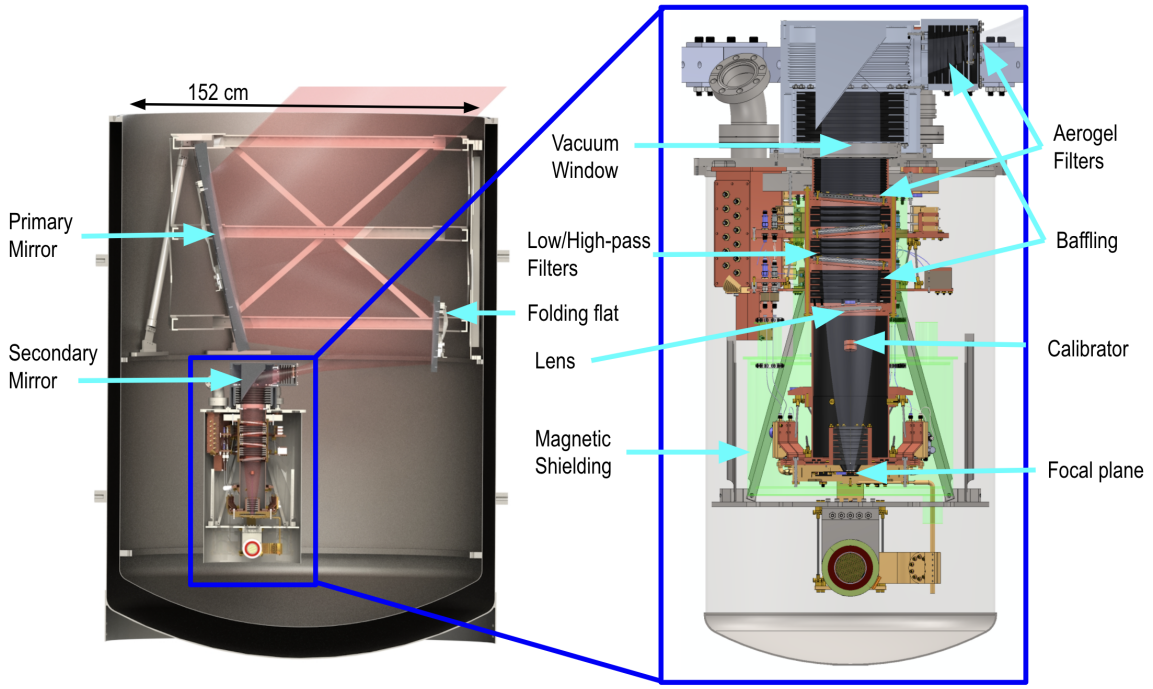

Figure 8.1: EXCLAIM optics overview. The features relevant to this section include the primary and secondary mirrors, folding flat, baffling, and lens.

parameters defining materials in CST.

8.2 EXCLAIM Gaussian beam analysis

Here, I describing ray-tracing and Gaussian optics calculations to the EXCLAIM optical system, with Gaussian optics utilizing POPPY. Note that portions of this analysis were published in Essinger-Hileman et al. [51] and Switzer et al. [149]. Here, the primary goal is to ensure that the optical spill is below $-40\,\mathrm{dB}$ at the edge of the primary.

The simulation parameters for the POPPY simulation are shown in Table 8.1. The simulation begins at the lens, at which the wavefront has a Gaussian profile truncated by the cold stop. The mirrors are simulated as lenses with corresponding focal lengths

Optical Element	Ray-tracing (cm)	Analytical GO (cm)	POPPY (cm)
Lens	∞	24.0	24.0
Secondary	19.5	19.5	19.5
Primary	6.36×10^4	1.28×10^4	5.04×10^4

Table 8.2: Positions of the beam waist/focus, using time-reversed propagation (i.e. from the lens to the primary). The first column describes the optical element that was most recently propagated through, where e.g. the first row describes the optical rays between the lens and the secondary mirror. The three columns describe the positions of the focus via ray-tracing, beam waist via analytic Gaussian optics, and beam waist via POPPY. Zero distance corresponds to the position of the lens.

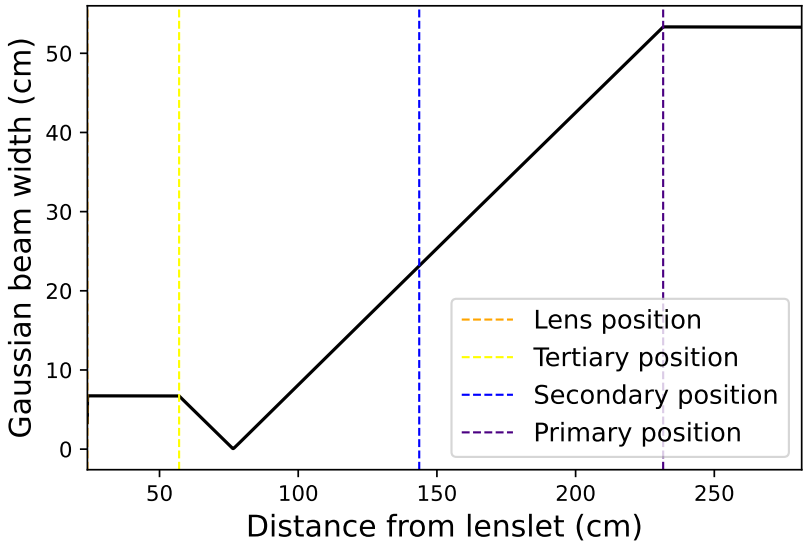

Figure 8.2: Gaussian beamwidth as a function of propagation distance from the lenslet through POPPY simulation. The plot starts from the cold stop and lens.

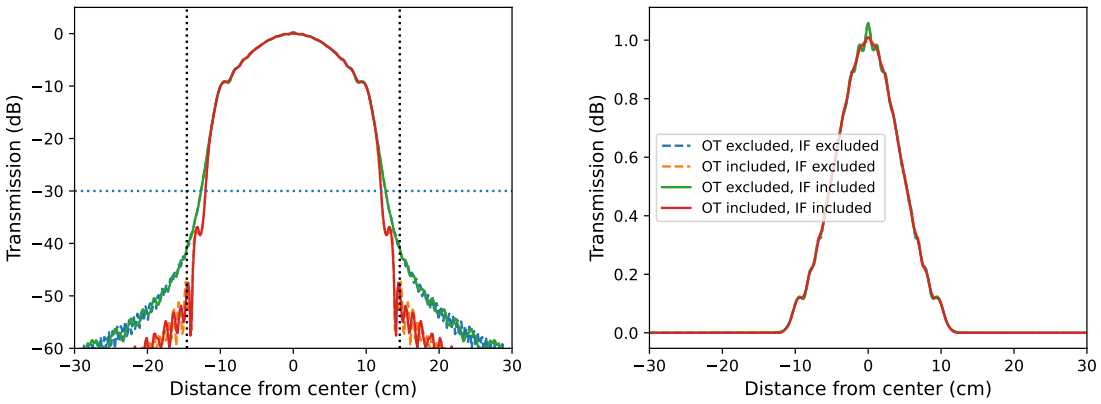

Figure 8.3: Illumination on the secondary mirror. We consider four different cases corresponding to the inclusion/exclusion of the optics tube (OT) baffles the inclusion/exclusion of the intermediate focus (IF) baffle. *Left*: logarithmic scale with vertical dotted lines corresponding to the effective beam edges 38 cm from the beam center, and the horizontal dotted line corresponding to the −40 dB level. Note that the two "OT included" curves are nearly indistinguishable on this plot. *Right*: linear scale highlighting diffraction effects on the main lobe. Here, the two 'IF included' curves are nearly indistinguishable.

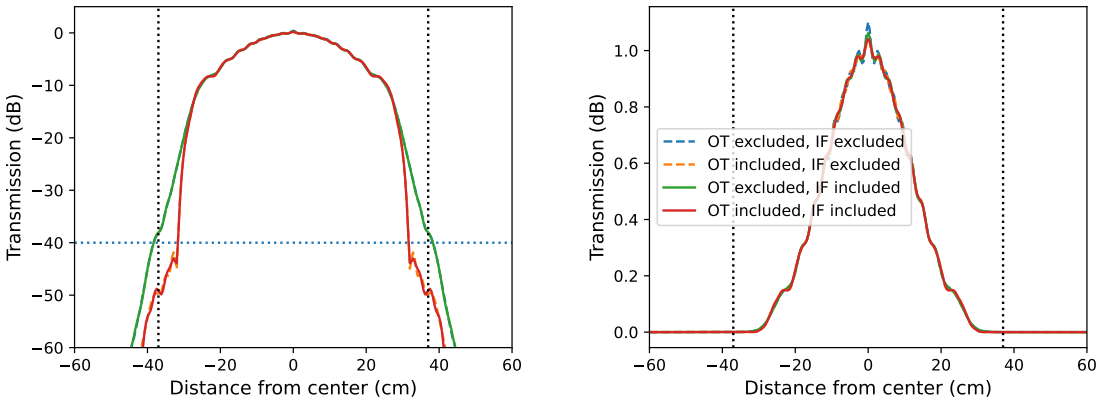

Figure 8.4: Illumination on the primary mirror. We consider four different cases corresponding to the inclusion/exclusion of the optics tube (OT) baffles the inclusion/exclusion of the intermediate focus (IF) baffle. *Left*: logarithmic scale with vertical dotted lines corresponding to the effective beam edges 38 cm from the beam center, and the horizontal dotted line corresponding to the −40 dB level. Note that the two "OT included" curves are nearly indistinguishable on this plot. *Right*: linear scale highlighting diffraction effects on the main lobe. Here, the two 'IF included' curves are nearly indistinguishable.

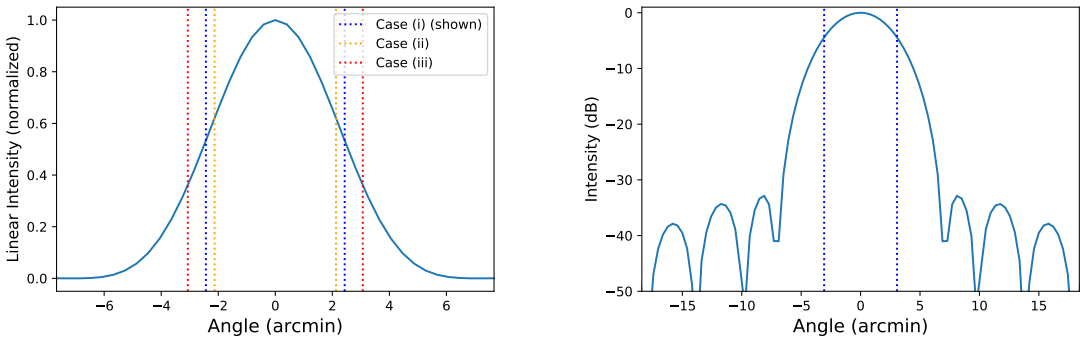

Figure 8.5: Far-field beam. *Left*: Radial cut through the beam center with a linear scale. The three pairs of vertical lines correspond to the three different $\Theta_{\mathrm{FWHM}}^{\mathrm{far-field}}$ cases: (i) (blue) full POPPY simulation (shown); (ii) (orange) estimate based on the primary FWHM $\Theta_{\mathrm{FWHM}}^{\mathrm{primary}}$; (iii) (red) estimate based the primary edge taper $T_E(\mathrm{dB})$ *Right*: Radial cut through the beam center with a log scale. The vertical lines corresponds to Case (i).

and the baffles are simulated as pupils. We used the `Fresnel Optical System` setting to obtain the results shown in Figure 8.4. Four different cases are shown: (i) baffles at both the intermediate focus (IF) and optics tube (OT); (ii) IF baffle only; (iii) optics tube baffles only; (iv) no baffles. These simulations were performed for an optical frequency of 480 GHz.

As shown in Figure 8.4, the optics tube baffling is necessary and sufficient to reduce spill at the edge of the primary to well below the -40 dB target. In the case that OT and IF baffles are included, the main lobe is nearly Gaussian with a FWHM $\Theta_{\mathrm{FWHM}}^{\mathrm{primary}} = 22.4$ cm and edge taper $T_E(\mathrm{dB}) = 85\,\mathrm{dB}$. The edge taper is defined as the absolute value of the primary illumination at the effective mirror radius of 38 cm, and it is heavily suppressed through the inclusion of OT baffles as shown in the left figure. The baffle at the intermediate focus smooths out diffraction wiggles in the main lobe, as shown in the right figure, which we attribute to the truncation of the beam at the cold stop. In either case, the diffraction wiggles in the main lobe disappear when propagating to the far field.

The far-field beam for the fully-baffled POPPY simulation is shown in Figure 8.5. The two plots show a slice through the beam center in a linear scale (left) and logarithmic scale (right). The far-field calculations were performed for three different cases for the illumination on the primary mirror: (i) full POPPY simulation; (ii) Gaussian with $\Theta_{\mathrm{FWHM}}^{\mathrm{primary}} = 22.4$ cm, truncated at the primary effective radius; (iii) Gaussian with $T_E(\mathrm{dB}) = 85$ dB.

In Case (i) we calculated the far-field pattern $\Theta_{\mathrm{FWHM}}^{\mathrm{far-field}}$ by Fourier transforming the primary illumination shown in Figure 8.4, resulting in $\Theta_{\mathrm{FWHM}}^{\mathrm{far-field}} = 4.33$ arcmin. For the latter two cases we calculated $\Theta_{\mathrm{FWHM}}^{\mathrm{far-field}}$ using Equation D.2 assuming a Gaussian illumination of the primary mirror, truncated at an edge taper of $T_E(\mathrm{dB})$, where λ is the wavelength and D is the effective diameter of the primary. For Cases (ii) and (iii) the truncated Gaussian estimates $\Theta_{\mathrm{FWHM}}^{\mathrm{far-field}}$ were 3.78 arcmin and 5.44 arcmin, respectively. $\Theta_{\mathrm{FWHM}}^{\mathrm{far-field}}$ was underestimated in Case (ii) by 0.55 arcmin because the mirror edges were over-illuminated, roughly corresponding to the exclusion of OT baffles. $\Theta_{\mathrm{FWHM}}^{\mathrm{far-field}}$ was overestimated in Case (iii) because the bright main lobe was underestimated by only considering the heavily-suppressed edge illumination. While the analytical estimates were both incorrect, the fully-simulated beam did exhibit the expected linear scaling with wavelength to a precision of one part in 10^7, demonstrating strong agreement with the scaling in Equation D.1. Comparing Cases (i) and (ii), we see only a modest increase in $\Theta_{\mathrm{FWHM}}^{\mathrm{far-field}}$, demonstrating that the inclusion of OT baffles accomplishes our goal of decreasing the spill on the primary, while not causing an unacceptable degradation in the far-field performance of the telescope.

The CST simulations have not yet been completed at the time of this writing. Our strategy is to utilize CST Microwave Studio Suite's `Integral Equation Solver`, which is ideal for computations featuring reflective mirrors with diameters much larger than the simulated wavelength, as for the EXCLAIM reflectors. The parameters for

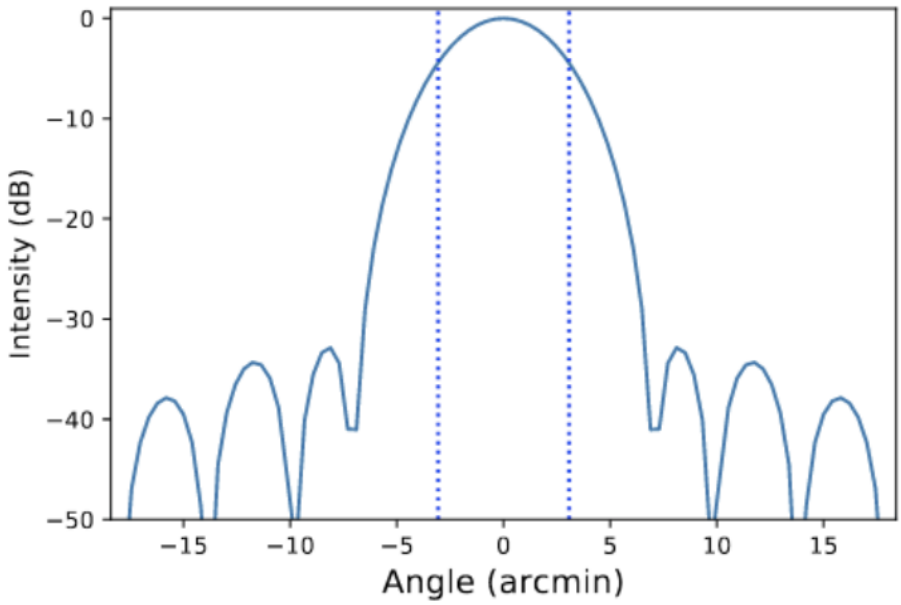

Figure 8.6: Farfield beam based on the fast Fourier transform of the POPPY-modeled beams at the output of the primary mirror.

the CST simulation are identical to those in Table 8.1 except for the baffles. We are investigating ways to include the effects of both the optics tube and IF baffles. The primary computational limit is system memory requirements; we estimate a computation at 100 GHz calculated at the location of the primary mirror would require ∼2.4 TB of RAM. We have successfully simulated the full set of mirrors at lower frequencies and find that memory requirements scale roughly as frequency squared. We are currently investigating high-throughput computing resources to complete the high-frequency simulations.

9 CONCLUSION AND THE FUTURE OF INTENSITY MAPPING

EXCLAIM and Tianlai are important pathfinders in the nascent field of line intensity mapping. While the field emerged as a tool for large-scale structure cosmology, it has since bloomed into a tool for studying galaxy evolution. As an exploratory technique, we are likely to find surprising ways that intensity mapping may add to our current knowledge of the Cosmos. In this thesis, I explored ways we can maximize scientific output from these first-generation surveys through the use of high-fidelity forecasts and the use of cross-correlation as a tool to evade cosmic variance. It is my hope that these studies will help influence surveys in the decades to come, and help realize the great potential of the intensity mapping technique. Furthermore, they will be critical for understanding the EXCLAIM flight data, as processes like calibration and map-making rely on an exquisite understanding of the instrument and the science of the target signal.

At the time of this writing, LIM is gaining traction in the astrophysics community, and will likely help influence the coming generations of mid- to far-infrared space telescopes. For these space-borne instruments, EXCLAIM is not only a scientific pathfinder, but also a technological testbed. MKIDs and μSpec are essential technologies for these coming surveys. I have assisted in these efforts through careful MKID modeling, and demonstrated a powerful technique for their operational optimization over a varying background signal.

While these targeted studies have proven insightful, my greatest contribution has been building a holistic 'system of systems' perspective on the EXCLAIM system. Not only does this help maximize the scientific impact of the instrument, but it also provides a framework for building future instruments. While most studies that forecast intensity mapping science rely on generalized assumptions, this systems-level understanding will be crucial in accurately understanding the true capabilities of the technique.

The efforts in this thesis focus on the EXCLAIM design phase, and there are many challenges to overcome before the planned Fall 2023 engineering flight. A necessarily incomplete list of areas that may benefit from my studies include the fabrication and characterization of the final MKID-μSpec system, time-ordered data simulations, and interpreting the map data from the flight(s). While I am saddened that I will not be actively involved in these efforts, I am confident that my colleagues and collaborators will be up to the challenge, and EXCLAIM will emerge as a pioneering experiment in the growing field of intensity mapping.

A 1-HALO POWER SPECTRUM

A.1 1-halo power spectrum limits - derivation

$$P_I^{2h}(k) = \alpha^2 P_m(k) \left[\int_{M_{\rm min}}^{\infty} L(M) b_h(M) u(k,M) \frac{dn}{dM}(M) dM \right]^2 \tag{A.1}$$

$$P_I^{1h}(k) = \alpha^2 \int_{M_{\rm min}}^{\infty} L^2(M) \left| u(k|M) \right|^2 \frac{dn}{dM} dM. \tag{A.2}$$

Equations 2.12 and 2.13 (reproduced above) do not fully account for the different populations of galaxies: namely, centrals and galaxies.

Here, the number statistics of L are crucial. I will first assume that all of the line-emitting gas resides in discrete galaxies. Here,

$$L N_L u(k) \rightarrow L_C N_C + L_S N_S u(k) \tag{A.3}$$

where L_C and L_S describe luminosities of central and satellite galaxies, respectively, and N_C and N_S describe the number of galaxies in the two respective populations. Finally, u_S describes the density profiles of satellite galaxies and/or continuum line emission in the intrahalo medium; I assume central galaxies are all located at the center of the host halo.

Now, I take scales larger than the size of a single halo so $u(k) \rightarrow 1$. I also define the satellite fraction f_s such that $N_s = f_s N$ and $N_c = (1 - f_s) N$, where N describes the number of galaxies in a single halo. Here, the term within the 1-halo term goes to

$$\begin{aligned} L^2 u(k) \;&\rightarrow\; L_c^2 \langle N_c \left(N_c - 1 \right) \rangle + L_s^2 \langle N_s \left(N_s - 1 \right) \rangle \\ &\quad + 2 L_c L_s \langle N_c N_s \rangle \\ &=\; L_s^2 \langle N_s \rangle^2 + 2 L_c L_s \langle N_c \rangle \langle N_s \rangle, \end{aligned} \tag{A.4}$$

where $\langle\rangle$ represents the mean per halo. In the second line I note that $\langle N_c^2 \rangle = \langle N_c \rangle$,

$\langle N_s\,(N_s-1)\rangle = N_s^2$ for a Poisson process, and the central and satellite galaxy statistics are independent such that $\langle N_c N_s\rangle = \langle N_c\rangle\langle N_s\rangle$.

Next, I define the satellite fraction as

$$f_s = \frac{N_s}{N_c + N_s} \tag{A.5}$$

and $N_c + N_s = N$. Here, I find that

$$L^2(M)\langle N\,(N-1)\rangle = \left[2L_cL_sf_s(1-f_s) + L_s^2f^2\right]\langle N\rangle^2 \tag{A.6}$$

The four parameters L_c, L_s, f_s, and $\langle N\rangle$ are degenerate and not well-understood, so I combine them into a single term σ_{1h},

$$\sigma_{1h}^2(M)L^2(M) \equiv L^2(M)\langle N\,(N-1)\rangle(M) \tag{A.7}$$

that can be marginalized over or targeted as an observable. Here, I have reinstated the M-dependence to emphasize that this is a mass-dependent parameter.

It is illuminating to examine the behavior of σ_{1h} under various conditions. First, I ask, given central and satellite luminosities L_c and L_s per halo mass, what satellite fraction maximizes the 1-halo term? Taking the derivative of the contents of Equation A.7 and setting it equal to zero, I find that

$$\sigma_{1h}^2L^2 > \frac{L_c^2L_s}{2L_c - L_s}\langle N\rangle^2. \tag{A.8}$$

If the centrals are much brighter than the satellites, i.e. $L_c \gg L_s$, the limit evaluates to

$$\sigma_{1h}^2L^2\Big|_{L_c\gg L_s} > \frac{L_cL_s}{2}\langle N\rangle^2. \tag{A.9}$$

On the other hand, if centrals are equally luminous, i.e. $L_c = L_s = L$, it instead evaluates to

$$\sigma_{1h}^2 L^2 \Big|_{L_c \gg L_s} > L^2 \langle N \rangle^2. \tag{A.10}$$

The notation of Equation A.7 is useful in comparing the 1-halo power spectrum to the shot power (Equation 2.7). Here, setting $L^2\langle N\rangle^2 = L(M)$, and plugging into Equation 2.13, I arrive at

$$\begin{aligned} P_I^{1h}(k,z)_{\tilde{u}_S \to 1} &= \int_{M_{\rm min}}^{\infty} \sigma_{1h}^2(M,k) L^2(M) \frac{dn}{dM} dM \\ &= \Sigma_{1h} \int_{M_{\rm min}}^{\infty} L^2(M,z) \frac{dn}{dM} dM \\ &= \Sigma_{1h} P_I^{\rm shot} \end{aligned} \tag{A.11}$$

where on the final line I matched to the previous notation where $\tilde{L}\langle \mathcal{N} \rangle = L(M)$, with the shot power evaluated by Equation 2.7.

B GAUSSIAN ERROR ESTIMATION IN COSMOLOGY

B.1 Gaussian error estimation

Gaussian likelihoods & Bayes' theorem

I begin this section on scientific forecasts for line intensity mapping experiments with an overview of statistics useful in cosmology. The central idea is that we have a set of measurements, and we want to find the likelihood of these measurements specifying a given model. Much of the discussion on Gaussian likelihoods follows Dodelson [49], providing a foundation for forecasts on intensity mapping measurements.

We begin with a likelihood $\mathcal{L}(\theta|\bar{\theta},\mathcal{C})$, signifying the probability distribution of a given measurement of a parameter vector θ with mean value $\bar{\theta}$, and a covariance matrix $\mathcal{C}$. Here, $\mathcal{L}$ typically takes some assumed functional form, specified by the data d with mean $\bar{d}$. Assuming a Gaussian distribution, the likelihood is given by

$$\mathcal{L}(d|\bar{d},\mathcal{C}) \equiv P(d|\bar{d},\mathcal{C}) = \frac{1}{2\pi\sqrt{\det\mathcal{C}}} \exp\left[-(d-\bar{d})^T\mathcal{C}^{-1}(d-\bar{d})\right], \tag{B.1}$$

where $P(A|B)$ signifies probability of some outcome A given a parameter B.

We can use Equation B.1 to find the probability of observable parameters $\bar{\theta}$ given a measurement θ through Bayes' theorem. Here,

$$P(\bar{d},\mathcal{C}|d) = \frac{P(d|\bar{d},\mathcal{C})P(\bar{d},\mathcal{C})}{P(d)}. \tag{B.2}$$

The four parameters are defined as

- **Posterior** $P(\bar{d},\mathcal{C})$: the probability of a model specified by $\bar{\theta}$, $\mathcal{C}$, given an observable θ.
- **Likelihood** $P(d|\bar{d},\mathcal{C})$: the probability of an observable given a model.
- **Prior** $P(\bar{d},\mathcal{C})$: an existing constraint on the model by previous measurements.

- **Marginal** $P(d)$: the probability that the measurement θ is true.

The likelihood is maximized when the measurement θ is equal to the true model value $\bar{\theta}$. We can show this by first taking the derivative to zero,

$$0 = \sum_{i=1}^{n} \frac{\partial \mathcal{L}}{\partial d_i}, \tag{B.3}$$

evaluating to

$$0 = \sum_{i=1}^{n} (d_i - \bar{d}). \tag{B.4}$$

Maximum-likelihood estimator is given by

$$\frac{\hat{d}}{\hat{\sigma}(\hat{d})} = \frac{1}{n} \left[\sum_{i=1}^{n} \frac{d_i^2}{\sigma^2(d_i)} \right], \tag{B.5}$$

where

$$\hat{\sigma}^2(\hat{d}) = \frac{1}{n} \sum_{i=1}^{n} (d_i - \bar{d})^2 \tag{B.6}$$

Fisher matrix

Suppose we want to explore how our model, described by data d with covariance $\mathcal{C}$, changes based on some observables θ. We Taylor expand the likelihood given by Equation B.1 to second order in θ, resulting in

$$\mathcal{L}(\theta) = \mathcal{L}(\bar{\theta}) + \sum_i (\theta_i - \bar{\theta}_i) \frac{\partial \mathcal{L}}{\partial \theta_i} + \frac{1}{2} \sum_{ij} (\theta_i - \bar{\theta}_i)^T \frac{\partial^2 \mathcal{L}}{\partial \theta_i \partial \theta_j} (\theta_j - \bar{\theta}_j). \tag{B.7}$$

If we take the expectation value of $\mathcal{L}$, the first derivative term goes to zero following the definition of maximum likelihood. The second derivative is known as the Fisher

Information Matrix

$$\begin{aligned}\mathcal{F}_{ij} &= \left\langle \frac{\partial^2 \mathcal{L}}{\partial\theta_i \partial\theta_j} \right\rangle \\ &= \frac{1}{2}\mathrm{Tr}\left[\mathcal{C}^{-1}\frac{\partial \mathcal{C}}{\partial\theta_i}\mathcal{C}^{-1}\frac{\partial \mathcal{C}}{\partial\theta_j} + \left(\mathcal{C}^{-1}\frac{\partial d}{\partial\theta_i}^T \frac{\partial d}{\partial\theta_j} + i \leftrightarrow j\right)\right]. \end{aligned} \tag{B.8}$$

The second term is equal to $\partial^2\chi^2/\partial\theta_i\partial\theta_j$, i.e. the variation in chi-squared due to changes in θ_i and θ_j. The first term appears from the normalization factor ($\sim (\det \mathcal{C})^{-1/2}$). Note that the first line in Equation B.8 is generally true, but the second line is specific to Gaussian likelihoods as given in Equation B.1.

Equation B.8 allows us to estimate the covariance matrix between various model parameters prior to performing a measurement. In practice, the first or second term is used in different scenarios; we will use both throughout this chapter. The first term describes errors based on model covariances alone; for example, two-point correlation functions describing variance in an overdensity. The second term describes errors based on variances in observed data; for example, data vectors obtained from maps.

Equation B.8 has a number of useful properties. First, the Fisher matrix is the inverse of the covariance matrix between the parameters θ_i. We can therefore find the variance in θ_i fixing all other parameters through

$$\sigma^2_{\theta_i} = \frac{1}{\mathcal{F}_{ii}}. \tag{B.9}$$

Suppose we instead want to marginalize over all parameters not equal to i. In a remarkable result, we have

$$\sigma^2_{\theta_i}\Big|_{\text{marg.}} = (\mathcal{F}^{-1})_{ii}. \tag{B.10}$$

We can generalize Equation B.10 to marginalizing over all parameters not equal to

i and j to find a covariance matrix

$$\Sigma_{ij} = (\mathcal{F}^{-1})_{ij}. \tag{B.11}$$

The Fisher matrix over some parameters θ_i can also be used to propogate errors to other parameters p_α, as

$$\mathcal{F}_{\alpha\beta} = \sum_{ij} \mathcal{F}_{ij} \frac{\partial \theta_i}{\partial p_\alpha} \frac{\partial \theta_j}{\partial p_\beta}. \tag{B.12}$$

C EXCLAIM DETECTORS: RELATING SKY INTENSITY TO DETECTOR POWER FOR COHERENT AND DIRECT DETECTORS

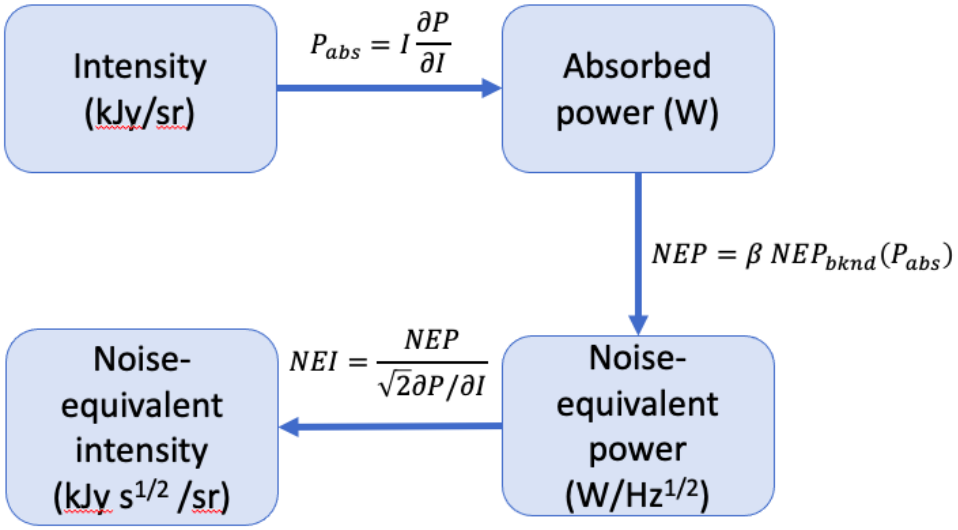

Figure C.1: Conversion from intensity to noise-equivalent intensity

In this appendix, I focus on comparing the background-limited performance of coherent and incoherent detectors, presenting similar information to Zmuidzinas [168]. Here, coherent detectors are defined as those that preserve phase information, such as the heterodyne receivers used in the Tianlai radio interferometers. Incoherent detectors, on the other hand, do not include phase information, instead measuring the total power absorbed by the detectors. Incoherent detectors include MKIDs and bolometers, as well as higher-energy detectors including optical CCDs and virtually all detectors measuring smaller wavelengths. The far-infrared represents a 'turning point' regime where one detector technology is clearly advantageous over another, and the choice depends heavily on the application.

C.1 The sensitivities of coherent and incoherent detectors

Figure C.1 demonstrates the calculation of sky sensitivity given a detector design. Here, the incident intensity I is converted to power absorbed by the detectors $P_{\rm abs}$ as

$$P_{\rm abs} = I\frac{\partial P}{\partial I}, \tag{C.1}$$

where $\partial P/\partial I$ is specific to the given optical system. This results in a noise-equivalent power (NEP) specific to each absorbed power. The NEP, given in units of W $\mathrm{Hz}^{-1/2}$, gives the power given by 0.5 s of integration of the noise. Ideally, the detection is background-limited, meaning noise inherent to the statistical distribution of optical photons is larger than sources within the detector, such as thermal fluctuations in the absorbing materials and amplifiers. Finally, this detector NEP is converted to the noise-equivalent intensity (NEI), given in units of Jy $\mathrm{s}^{1/2}$, through

$$\mathrm{NEI} = \frac{\mathrm{NEP}}{\sqrt{2}\partial P/\partial I}. \tag{C.2}$$

Note that the $\sqrt{2}$ appears through RMS averaging over frequency in the conversion from units of $\mathrm{Hz}^{-1/2}$ to $\mathrm{s}^{1/2}$.

Relating sky intensity to absorbed power

The ultimate job of an astrophysical detector is to convert radiation on the sky to detectable power. The target signal is the flux of incident power in a given frequency range (units of W m^{-2} Hz^{-1} sr^{-1} or Jy sr^{-1}), known as spectral brightness or specific intensity; we will follow conventions from the literature and simply refer to this as

intensity.

In a telescope, the conversion from intensity on the sky to power absorbed by the detectors is given by

$$\begin{aligned} \frac{\partial P}{\partial I} &= A_d \Omega_{\rm beam} \delta\nu \\ &= \eta_d N_{\rm modes}^{\rm opt} \lambda^2 \delta\nu \end{aligned}$$

In the case of an unpolarized source and an apodized beam, the effective area is related to the wavelength as $A_e\Omega_{\rm beam} = \lambda^2$. Here, the product $A_e\Omega_{\rm beam}$ is known as the antenna etendue. The effective area A_e is related to the physical detector area as, $A_d = \eta_d A_e$, with η_d the detector efficiency. Generalizing the unpolarized source or one where the image of the detector is smaller than the diameter of the primary mirror, the etendue is multiplied by the number of optical modes, $N_{\rm modes}^{\rm opt}$.

Coherent and incoherent detector noise

Next, we convert power absorbed by the detectors to detector NEP. In what follows, we calculate the photon background noise, i.e. the noise inherent to the incident radiation. Later in this chapter, we will also model other sources of noise in kinetic inductance detectors. Note that this subsection may be skipped without loss of continuity, noting the derivation of the incoherent detector NEP in Equation C.8 relevant to MKIDs studied later in the chapter.

This relation depends on the type of detector. We describe two categories of detector; coherent receivers maintain the phase information of the incident light, while incoherent receivers are insensitive to phase. For example, a heterodyne receiver, as is typically used for a radio communications, is coherent, whereas a charge-coupled device (CCD), the semiconductor technology relying on the photoelectric effect to

convert optical photons to electrons, is incoherent.

As we describe in the sections below, the decision of whether to use a coherent or incoherent detector is highly dependent on frequency and application. For example, nearly all long-wavelength (radio) receivers are coherent detectors. This owes to the relative simplicity and commercial technologies for local oscillators that may be used to downconvert the optical frequency to frequencies tractable with readout technologies. On the other hand, most detectors at optical wavelengths and below (i.e. ultraviolet, X-ray, and gamma-ray) rely on coherent detection, where photon detection relies on a cascade of particle interactions, ranging from electrons in semiconductors at optical and near-infrared frequencies, to lattice interactions in scintillating detectors at gamma-ray frequencies.

At infrared and microwave frequencies, the choice between coherent and incoherent detectors is less straightforward, and depends on the requirements of the experiment. Coherent heterodyne detectors can easily achieve high frequency resolution $R \geq 10^5$ [128]. Incoherent detectors rely on spectrometers to resolve individual frequencies; this typically entails diffraction or thin-film spectroscopy, which are limited in their abilities to obtain high frequency resolution. Resolutions up to $R \sim 10^4$ can be achieved through post-dispursed spectrometer technologies (i.e. an additional spectrometer is placed in front of a second spectrometer), such as a Fourier Transform Spectrometer (FTS) in conjunction with a grating spectrometer [22]. On the other hand, coherent detectors may feature higher noise than incoherent ones at frequencies higher than the GHz-THz range, depending on the quantum efficiency and spatial resolution of the detectors C.2. Coherent mid-infrared to microwave telescopes increasingly rely on superconducting materials for mixers and low-noise amplifiers, which are costly in terms of to power and cooling. For example, the Herschel-Heterodine Instrument for the Far-Infrared (HIFI) utilized hot electron bolometers (HEB) [29] and superconducting-insulating-

superconductor (SIS) mixers [75], for the 1410-1910 GHz and 480-1250 GHz bands, respectively [43].

In the following subsections, we will derive the equation for the photon background NEP for coherent and incoherent detector technologies. Note that these NEP values represent the minimum possible noise for a given technology, given by the statistics of the incident photon population. Detectors may generally be subject to other sources of noise, including thermal, readout, and quasiparticle generation-recombination.

Photon statistics

We begin by modeling the absorbed power for a single optical mode through blackbody statistics as

$$P_{\rm abs} = B_\nu A\Omega\Delta\nu = \frac{h\nu\Delta\nu}{e^{h\nu/k_BT}-1}, \tag{C.3}$$

where B_ν is the Planck radiation formula describing the intensity of a blackbody, $A\Omega$ is the detector etendue, and $\Delta\nu$ is the bandwidth of the detector.

Here, the probability of a given photon number n is given by

$$P(n) = \frac{e^{-nh\nu/k_BT}}{\sum_{n=0}^{\infty} e^{-nh\nu/k_BT}}, \tag{C.4}$$

resulting in a mean photon number $\bar{n}$ of

$$\bar{n} = \sum_{n=0}^{\infty} nP(n) = \frac{1}{e^{h\nu/k_BT}-1} = \frac{P_{\rm abs}}{2h\nu\Delta\nu}, \tag{C.5}$$

where in the last line we used Equation C.3 to relate from absorbed power ot the number of photons. The variance in the number of photons is given by

$$(\delta n)^2 = \sum_{n=0}^{\infty} (n-\bar{n})^2 P(n) = \bar{n} + \bar{n}^2. \tag{C.6}$$

Incoherent detector NEP

The responsivity of an incoherent detector, e.g. an MKID or a transition edge sensor (TES), is determined by the total number of photons absorbed without measuring the phase of the incident radiation. Detector noise $\delta P_{\rm abs}^{\rm inc}$ is therefore limited by the variance of the number of photons. For a single optical mode and a single polarization,

$$\begin{aligned} \delta P_{\rm abs}^{\rm inc} &= \eta_{\rm inc}^{-1} h\nu\Delta\nu\delta n = h\nu\Delta\nu\sqrt{\bar{n}+\bar{n}^2} \\ &= \sqrt{2h\nu\Delta\nu\eta_{\rm inc}^{-1}P_{\rm abs} + P_{\rm abs}^2}, \end{aligned} \tag{C.7}$$

where $\eta_{\rm inc}$ is the optical efficiency of the incoherent detector, i.e. the portion of photon power that is converted to usable energy in the detector.

We can relate this to an NEP through

$$\mathrm{NEP}^{\rm inc} = \frac{\delta P_{\rm abs}^{\rm inc}}{\sqrt{\Delta\nu}} = \sqrt{h\nu\eta_{\rm inc}^{-1}P_{\rm abs} + \frac{P_{\rm abs}^2}{\Delta\nu}}. \tag{C.8}$$

Here, the first term represents Poisson fluctuations in the photon background. The second describes "Dicke Bunching", and represents the Dicke radiometer equation for high photon occupation numbers and high spectral resolution [47, 169], as is typically the case at radio frequencies.

Coherent detector NEP

While the signal received by an incoherent detector may feature only a single optical path (e.g. the signal incident on a bolometer is directly converted to usable signal), coherent detectors generically rely on the multiplication of an optical signal with an intermediate frequency (IF) mixer signal. Here, photons generated by the mixer (or generally, whatever circuit element is mixed to measure phase in the optical signal)

present an additional source of quantum noise. We assume this produces another photon population $\bar{n}_c$, which combines with the overall photon population to produce the phase coherent signal. Here, we have

$$\begin{aligned} \delta P_{\text{abs}}^{\text{coh}} &= \eta_{\text{coh}} h\nu\Delta\nu\sqrt{\left((\bar{n}+\bar{n}_c)+(\bar{n}+\bar{n}_c)\right)^2} \\ &= \sqrt{h\nu\eta_{\text{coh}}^{-1}\left(P_{\text{abs}}+P_c\right)+\frac{\left(P_{\text{abs}}+P_c\right)^2}{\Delta\nu}}, \end{aligned} \tag{C.9}$$

where η_{coh} is the coherent detector efficiency contributing to both P_{abs} and P_c.

Taking $P_c = h\nu\Delta\nu$, we have

$$\text{NEP}^{\text{coh}} \approx \eta_{\text{coh}}^{-1} h\nu\sqrt{\Delta\nu} + \frac{P_{\text{abs}}}{\sqrt{\Delta\nu}}. \tag{C.10}$$

Here, the $\eta_{\text{coh}}^{-1} h\nu\sqrt{\Delta\nu}$ term tends to be much larger than the first term in the first line of Equation C.9, so we can safely ignore it for our purposes of comparing the NEP of coherent and incoherent detectors. Physically, this means we are assuming the Dicke bunching noise from the photon population added to the optical signal exceeds the single-photon statistics in both signals (i.e. $\bar{n}_c \gg \bar{n}, \bar{n}_c$). The $\eta_{\text{coh}}^{-1} h\nu\sqrt{\Delta\nu}$ term behaves like a system temperature term, which adds a fixed intensity following blackbody statistics of the instrument.

Figures C.2 and C.3 show the comparison between the background-limited NEP in incoherent (Equation C.8) and coherent (Equation C.10) receivers as a function of frequency. The former shows the NEP per channel, while the latter shows the instantaneous dynamic range (P / NEP), roughly defined as the signal-to-noise per root-second. The five plots in the figures point toward a number of conclusions:

- At high frequencies, coherent receivers are noisier than incoherent ones, while

their noise performance is equivalent at low frequencies.

- The threshold frequency where incoherent noise exceeds coherent noise increases with resolution R, and decreases with absorbed optical power P. For absorbed optical powers ranging from $\sim 1\,\mathrm{pW} - 1\,\mathrm{fW}$, this threshold tends to occur at microwave to far-infrared frequencies.

- At high frequencies, incoherent detector noise is insensitive to resolution.

- At low frequencies, NEP $\propto R^{-1/2}$ for coherent and incoherent detectors alike, matching Dicke's radiometer equation [47].

- Both coherent and incoherent detectors feature signal-to-noise peaks, where specific optical loads and intensities peak at specific frequencies. For example, the signal-to-noise for $I = 1\,\mathrm{MJy}$ (Figure C.3d) corresponds to a peak at $\sim 40\,\mathrm{GHz}$ for all R.

Clearly, the decision of whether to equip an instrument in the microwave to far-infrared depends on the specific instrument. As a result, current, past, and future detectors have included a wide array of detector technologies. For example, the first detections of the CMB in 1965 by Penzias & Wilson [118] and Dicke, Peebles, Role, & Wilkinson [46] relied on Dicke radiometers, a coherent receiver technology. Today, both coherent and incoherent detector technologies are employed for CMB observations, with coherent detectors used by Planck [33], and incoherent detectors (superconducting transition edge sensors) are used by BICEP3 [4], ACT [146] and CMB-S4 [2]. Furthermore, a technological hybrid between coherent and incoherent detectors, was implemented by the Q & U Bolometric Interferometer[1] for Cosmology (QUBIC) [106]. Suborbital balloon missions have utilized both coherent and incoherent

[1]Previously, I was convinced the terms bolometer and interferometer were mutually exclusive!

technologies, where ARCADE [138] utilized a radiometer to obtain the CMB spectrum; OLIMPO, on the other hand, utilized incoherent kinetic inductance [99] detectors. Future CMB experiments, such as PIXIE [82] and PICO [69], proposed explorer- and probe-class space missions, may be equipped with MKIDs similar to those described here. At the time of this writing, mid-IR probe missions are being proposed with both technologies: FIRSST [34] and PRIMA [58] may be equipped with incoherent receivers, while SPIRIT may employ interferometry through coherent detectors [85].

Finally, for the purpose of the rest of the chapter, at EXCLAIM's frequency range ($420 - 540\,\mathrm{GHz}$) and low resolution ($R = 512$), incoherent receivers outperform coherent ones by 2-3 orders of magnitude. The brightest channels feature incident detector loads on the order of $\sim 1\,\mathrm{fW}$, so Figure C.2 demonstrates a strong advantage for incoherent detector technologies.

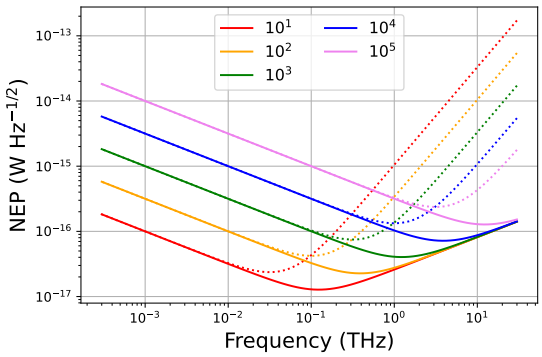

(a) $P = 1\,\mathrm{pW}$

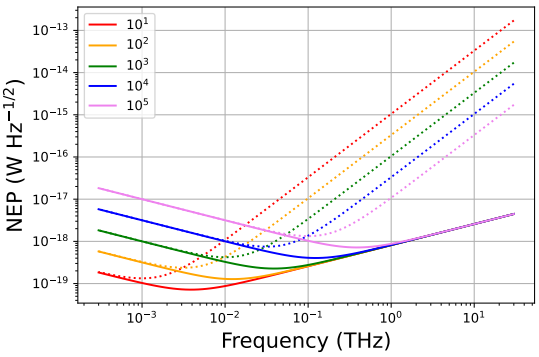

(b) $P = 1\,\mathrm{fW}$

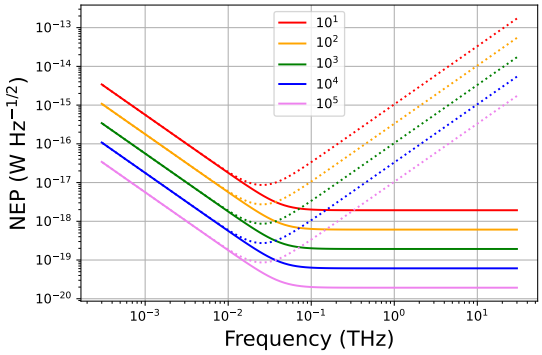

(c) $I = 1\,\mathrm{GJy/sr}$

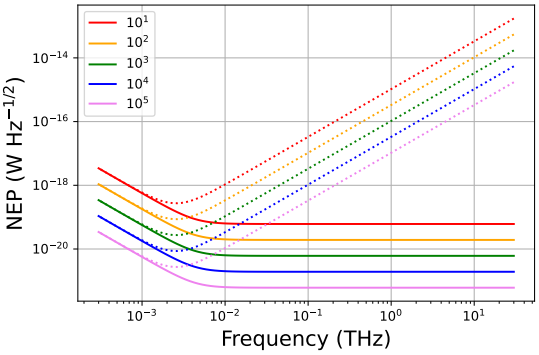

(d) $I = 1\,\mathrm{MJy/sr}$

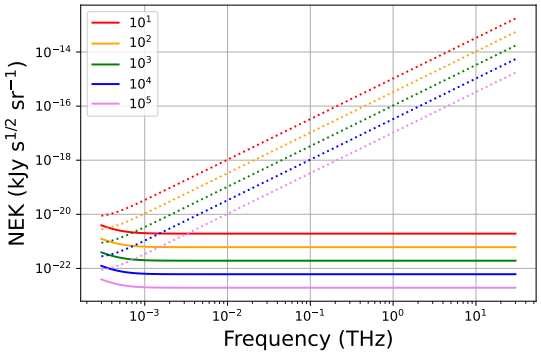

(e) $I = 1\,\mathrm{kJy/sr}$

Figure C.2: Background-limited NEP for incoherent (solid) and coherent (dotted) receivers over four decades in frequency, roughly spanning the microwave ($\sim 0.3 - 300\,\mathrm{GHz}$) to far-infrared band ($\sim 0.3 - 20\,\mathrm{THz}$). The two top panels represent fixed incident powers per channel $P = 1\,\mathrm{pW}$ and $1\,\mathrm{fW}$, while the bottom three represent fixed intensities $I = 1\,\mathrm{GJy}$, $1\,\mathrm{MJy}$, and $1\,\mathrm{kJy}$. The five curves in each panel correspond to frequency resolution $R = 10^1$ through 10^5.

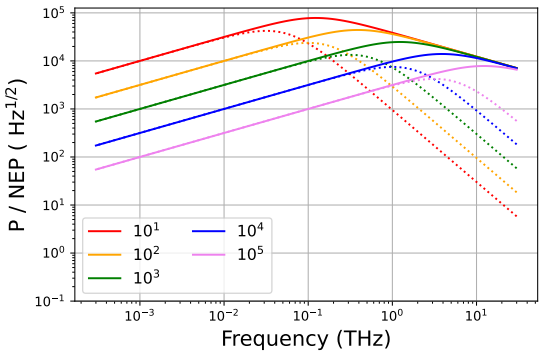

(a) $P = 1\,\mathrm{pW}$

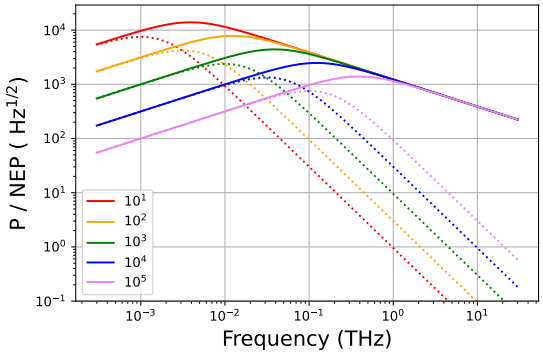

(b) $P = 1\,\mathrm{fW}$

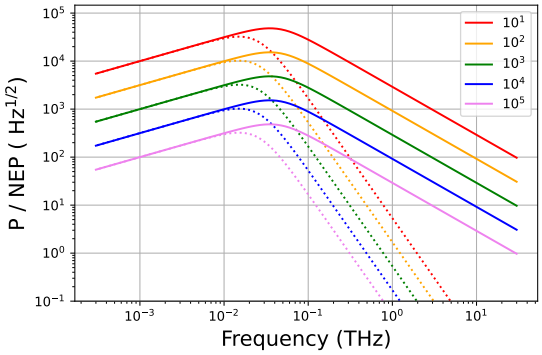

(c) $I = 1\,\mathrm{GJy}$

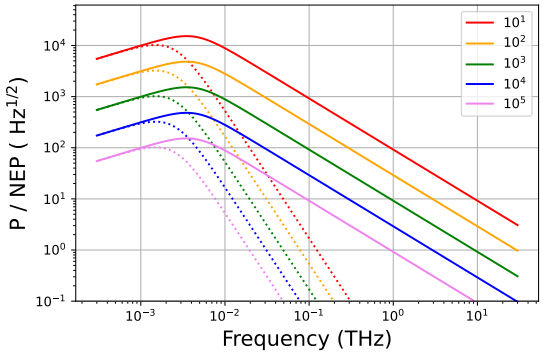

(d) $I = 1\,\mathrm{MJy}$

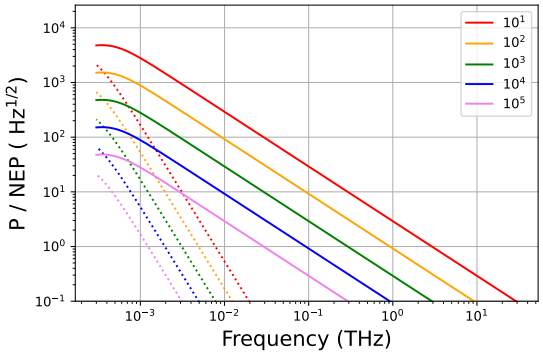

(e) $I = 1\,\mathrm{kJy}$

Figure C.3: Background-limited instantaneous dynamic range (P / NEP) for incoherent (solid) and coherent (dotted) receivers over four decades in frequency, roughly spanning the microwave ($\sim 0.3 - 300\,\mathrm{GHz}$) to far-infrared band ($\sim 0.3 - 20\,\mathrm{THz}$). The two top panels represent fixed incident powers per channel $P = 1\,\mathrm{pW}$ and $1\,\mathrm{fW}$, while the bottom three represent fixed intensities $I = 1\,\mathrm{GJy}$, $1\,\mathrm{MJy}$, and $1\,\mathrm{kJy}$. The five curves in each panel correspond to frequency resolution $R = 10^1$ through 10^5.

D OPTICS: DIFFRACTION ANALYSIS

D.1 Optical modeling

Rules of thumb

The entrance pupil diameter D_{ep} sets the resolution of the telescope. In the case of a plane wave, the resolution is given by the Rayleigh criterion,

$$\delta\theta_{plane} = 1.22\frac{\lambda}{D_{ep}} \tag{D.1}$$

In the case of a Gaussian wave with edge taper $T_e(dB)$ at the entrance pupil [61],

$$\delta\theta_{Gaussian} = [1.02 + 0.0135T_e(dB)]\,\frac{\lambda}{D_{ep}}. \tag{D.2}$$

These calculations may be used for first-order forecasts based on a given instrument. For example, in the middle of the EXCLAIM band (480 GHz) with a $D_{ep} = 0.8$ m aperture, we would expect a plane wave beamwidth of 3.3 arcmin. For a Gaussian with a 15 dB edge taper, we would come up with the same value, 3.3 arcmin, while it would be widened to 4.2 arcmin for a 40 dB edge taper. These numbers provide an effective estimate for the EXCLAIM instrument, which we refine through more advanced techniques. Furthermore, these numbers are only relevant to the main lobe of the optical beam pattern, and do not account for sidelobes present in the near-field that may be important in calculating optical spill from warm parts of the instrument.

Diffraction analysis and the Fourier transform

We will study the effects of diffraction through careful analysis of a propagating optical wavefunction. We begin with the Helmholtz Equation,

$$\left(\nabla^2 + k^2\right)\psi = 0, \tag{D.3}$$

defining the propagation of a wavefunction ψ. The solution can be found through the use of a Green's function

$$G(r) = \frac{e^{ik\cdot r}}{r}. \tag{D.4}$$

Now, suppose we want to examine the electric field $E(r)$ at a point a distance r away from the center of an aperture A. Here, taking x' and y' as the coordinates in the plane of the aperture,

$$U(x,y,z) = \frac{1}{i\lambda}\int\int_A U(x',y',0)\frac{e^{ikr}}{r}cos\theta dx'dy'. \tag{D.5}$$

Here, A imposes the constraint that $x'^2 + y'^2 < R^2$ with R the aperture radius and

$$\begin{aligned} r &= \sqrt{(x-x')^2 + (y-y')^2 + z^2} \\ &\approx z + \frac{\rho^2}{2z}, \end{aligned} \tag{D.6}$$

where $\rho^2 = (x-x')^2 + (y-y')^2$. This approximation relies on the Fresnel limit, which can be expressed as

$$\frac{\rho^2}{\lambda z} \gg 1. \tag{D.7}$$

We can rewrite Equation D.5 as

$$\begin{aligned} U(x,y,z) &= \frac{e^{ikz}}{ikz}\int_{-\infty}^{\infty}\int_{-\infty}^{\infty} U(x',y',0)\exp\left[\frac{ik}{2z}\left((x-x')^2+(y-y')^2\right)\right]dx'dy' \\ &= \frac{e^{ikz+ik(x^2+y^2)/2z}}{ikz}\int_{-\infty}^{\infty}\int_{-\infty}^{\infty}\Bigg(U(x',y',0) \\ &\quad \times\exp\left[\frac{ik(x'^2+y'^2)}{2z}\right]\Bigg)\exp\left[-\frac{ik}{z}(x'x+y'y)\right]dx'dy' \\ &= \frac{e^{ikz+ik(x^2+y^2)/2z}}{ikz}\left(\frac{z}{k}\right)^2\mathcal{F}\left[U(x',y',0)\exp\left(\frac{ik(x'^2+y'^2)}{2z}\right)\right], \end{aligned} \tag{D.8}$$

where $\mathcal{F}\left[f(x',y')\right]$ denotes a two-dimensional Fourier Transform of f from coordinates x', y', to $kx/z, ky/z$ located a line-of-sight distance z away from the aperture. Here, $U(x',y',0)$ defines the beam response at the initial position. Note that the Fresnel approximation in Equation D.7 makes the Fourier transform-based computation significantly less computationally intensive, as discussed in Goodman [63].

Suppose $U(x',y',0)$ is a perfect circular aperture of radius R illuminated by a plane wave, and the Gaussian within the Fourier transform evaluates to 1 (i.e. $x', y' \gg z/k$). Here, the Fourier transform evaluates to an Airy disk pattern, which is proportional to $J_1(kR\rho/z)/(kRr/z)$, where J_1 is the Bessel function of the first kind and $\rho = \sqrt{x^2+y^2}$. Here, the first zero in the Airy disk occurs at $kRr/z = 3.83$, corresponding to $\sin\theta \equiv r/z = 1.22\lambda/(2R)$, where $\lambda = k/2\pi$ and θ is the angle corresponding to the first zero in the Airy disk pattern. Thus, we have derived the Rayleigh criterion in Equation D.1. If we took the Gaussian to be non-unity with a width defined by the edge taper T_e at the edge of the aperture, it can be shown that D.2 applies.

Gaussian optics

Consider again the Helmholtz equation (Equation D.3). We will assume the wavefunction u can be defined by a plane wave multiplied by another wavefunction Ψ,

$$u(z) = e^{-ikz}\Psi(x, y, z). \tag{D.9}$$

For a well-collimated beam,

$$\left|\frac{\partial^2\Psi}{\partial z^2}\right| << 2k\left|\frac{\partial\Psi}{\partial z}\right|, \tag{D.10}$$

so plugging into the Helmholtz equation, we arrive at

$$\left(\frac{\partial^2}{\partial x^2} + \frac{\partial^2}{\partial y^2} - 2ik\frac{\partial}{\partial z}\right)\Psi = 0 \tag{D.11}$$

This is known as the paraxial approximation. The general solution to Equation D.11 is given by

$$\Psi(x, y, z) = \frac{\Psi_0}{q(z)}\exp\left[\frac{jk(x^2 + y^2)}{2q(z)}\right], \tag{D.12}$$

known as the Gaussian beam solution. Here,

$$q(z) = z - jz_0 \tag{D.13}$$

$$q^{-1}(z) = R^{-1}(z) + j\frac{\lambda}{\pi w_0^2(z)}, \tag{D.14}$$

where z_0 is known as the Rayleigh Range or Confocal Distance, defined as the distance it takes for the beamwidth to spread by a factor of $\sqrt{2}$, and $w(z)$ is the e^{-1} half-width of the Gaussian beam profile at a particular position z [70]. $R(z)$ is the curvature of the wavefront.

The expanded solution is given by

$$\Psi(x,y,z) = \Psi_0 \frac{w_0}{w(z)} \exp\left[-\frac{r^2}{w^2(z)}\right] \exp\left[jkz + jk\frac{r^2}{2R(z)} - j\psi(z)\right], \tag{D.15}$$

where

$$w(z) = w_0\sqrt{1+\frac{z^2}{z_0^2}} \tag{D.16}$$

$$w_0 = \sqrt{\frac{\lambda z_0}{\pi}} \tag{D.17}$$

$$R(z) = z\left(1+\left(\frac{z_0}{z}\right)^2\right) \tag{D.18}$$

$$\psi(z) = \tan^{-1}\left[\frac{z}{z_0}\right]. \tag{D.19}$$

These parameters are the 1/e beamwidth, 1/e beamwidth at the waist, wavefront curvature, and Guy phase, respectively.

The beam intensity is also Gaussian, and is given by [63]

$$I(x,y,z) = |V_0|^2 \left[\frac{w_0}{w(z)}\right]^2 \exp\left[-\frac{2(x^2+y^2)}{w^2(z)}\right] \tag{D.20}$$

As an illustrative example, we will examine the response of a collimated Gaussian beam with beamwidth corresponding to a $-15\,\mathrm{dB}$ edge taper at a radius of $3.81\,\mathrm{cm}$ at a frequency of $480\,\mathrm{GHz}$. This corresponds to the EXCLAIM beam in the collimated region between the lens and the secondary mirror. The mirror then passes through a lens of focal length $19.5\,\mathrm{cm}$, an on-axis analog of the EXCLAIM secondary mirror.

BIBLIOGRAPHY

[1] Timothy Abbott, Filipe B Abdalla, J Aleksić, S Allam, Adam Amara, D Bacon, Eduardo Balbinot, M Banerji, Keith Bechtol, Aurélien Benoit-Lévy, et al. The dark energy survey: more than dark energy–an overview. *Monthly Notices of the Royal Astronomical Society*, 460(2):1270–1299, 2016.

[2] Maximilian H Abitbol, Zeeshan Ahmed, Darcy Barron, Ritoban Basu Thakur, Amy N Bender, Bradford A Benson, Colin A Bischoff, Sean A Bryan, John E Carlstrom, Clarence L Chang, et al. Cmb-s4 technology book. *arXiv preprint arXiv:1706.02464*, 2017.

[3] Nabila Aghanim, Yashar Akrami, Mark Ashdown, J Aumont, C Baccigalupi, M Ballardini, AJ Banday, RB Barreiro, N Bartolo, S Basak, et al. Planck 2018 results-vi. cosmological parameters. *Astronomy & Astrophysics*, 641:A6, 2020.

[4] Z Ahmed, M Amiri, SJ Benton, JJ Bock, R Bowens-Rubin, I Buder, E Bullock, J Connors, JP Filippini, JA Grayson, et al. Bicep3: a 95ghz refracting telescope for degree-scale cmb polarization. In *Millimeter, Submillimeter, and Far-Infrared Detectors and Instrumentation for Astronomy VII*, volume 9153, page 91531N. International Society for Optics and Photonics, 2014.

[5] Hiroaki Aihara, Nobuo Arimoto, Robert Armstrong, Stéphane Arnouts, Neta A Bahcall, Steven Bickerton, James Bosch, Kevin Bundy, Peter L Capak, James HH Chan, et al. The hyper suprime-cam ssp survey: overview and survey design. *Publications of the Astronomical Society of Japan*, 70(SP1):S4, 2018.

[6] Charles Alcock and Bohdan Paczyński. An evolution free test for non-zero cosmological constant. *Nature*, 281(5730):358–359, 1979.

[7] Marcelo Alvarez, Tobias Baldauf, J Richard Bond, Neal Dalal, Roland de Putter, Olivier Doré, Daniel Green, Chris Hirata, Zhiqi Huang, Dragan Huterer, et al. Testing inflation with large scale structure: connecting hopes with reality. *arXiv preprint arXiv:1412.4671*, 2014.

[8] Christopher Anderson. *Studying Cosmic Evolution with 21 cm Intensity Mapping*. The University of Wisconsin-Madison, 2017.

[9] Christopher J Anderson, Eric R Switzer, and Patrick C Breysse. Constraining low redshift [cii] emission by cross-correlating firas and boss data. *arXiv preprint arXiv:2202.00203*, 2022.

[10] CJ Anderson, NJ Luciw, Y-C Li, CY Kuo, J Yadav, KW Masui, TC Chang, X Chen, N Oppermann, YW Liao, et al. Low-amplitude clustering in low-redshift 21-cm intensity maps cross-correlated with 2df galaxy densities. *Monthly Notices of the Royal Astronomical Society*, 476(3):3382–3392, 2018.

[11] Kevin Bandura, Graeme E Addison, Mandana Amiri, J Richard Bond, Duncan Campbell-Wilson, Liam Connor, Jean-François Cliche, Greg Davis, Meiling Deng, Nolan Denman, et al. Canadian hydrogen intensity mapping experiment (chime) pathfinder. In *Ground-based and Airborne Telescopes V*, volume 9145, pages 738–757. SPIE, 2014.

[12] JJA Baselmans, J Bueno, Stephen JC Yates, O Yurduseven, Nuria Llombart, K Karatsu, AM Baryshev, L Ferrari, A Endo, DJ Thoen, et al. A kilo-pixel imaging system for future space based far-infrared observatories using microwave kinetic inductance detectors. *Astronomy & Astrophysics*, 601:A89, 2017.

[13] Jurek B Bauer, David JE Marsh, Renée Hložek, Hamsa Padmanabhan, and Alex Laguë. Intensity mapping as a probe of axion dark matter. *Monthly Notices of the Royal Astronomical Society*, 500(3):3162–3177, 2021.

[14] Peter S Behroozi, Risa H Wechsler, and Charlie Conroy. The average star formation histories of galaxies in dark matter halos from z= 0-8. *The Astrophysical Journal*, 770(1):57, 2013.

[15] AJ Benson, RG Bower, CS Frenk, Cedric G Lacey, CM Baugh, and Shaun Cole. What shapes the luminosity function of galaxies? *The Astrophysical Journal*, 599(1):38, 2003.

[16] José Luis Bernal, Patrick C Breysse, Héctor Gil-Marín, and Ely D Kovetz. User's guide to extracting cosmological information from line-intensity maps. *Physical Review D*, 100(12):123522, 2019.

[17] José Luis Bernal, Andrea Caputo, and Marc Kamionkowski. Strategies to detect dark-matter decays with line-intensity mapping. *Physical Review D*, 103(6): 063523, 2021.

[18] Alberto D Bolatto, Mark Wolfire, and Adam K Leroy. The co-to-h2 conversion factor. *Annual Review of Astronomy and Astrophysics*, 51:207–268, 2013.

[19] Rychard J Bouwens, GD Illingworth, PA Oesch, M Trenti, I Labbé, M Franx, M Stiavelli, C Marcella Carollo, Pieter van Dokkum, and D Magee. Lower-luminosity galaxies could reionize the universe: Very steep faint-end slopes to the uv luminosity functions at z[U+2A7E] 5–8 from the hudf09 wfc3/ir observations. *The Astrophysical Journal Letters*, 752(1):L5, 2012.

[20] Judd D Bowman, Alan EE Rogers, Raul A Monsalve, Thomas J Mozdzen, and Nivedita Mahesh. An absorption profile centred at 78 megahertz in the sky-averaged spectrum. *Nature*, 555(7694):67–70, 2018.

[21] Andrea Bracco, Asantha Cooray, M Veneziani, A Amblard, P Serra, J Wardlow, MA Thompson, G White, R Auld, Maarten Baes, et al. Herschel-atlas: statistical properties of galactic cirrus in the gama-9 hour science demonstration phase field. *Monthly Notices of the Royal Astronomical Society*, 412(2):1151–1161, 2011.

[22] Charles M Bradford, Bruce A Cameron, Bradley D Moore, Steven Hailey-Dunsheath, Edward G Amatucci, Damon C Bradley, James A Corsetti, David T Leisawitz, Michael J DiPirro, James G Tuttle, et al. Origins survey spectrometer: revealing the hearts of distant galaxies and forming planetary systems with far-ir spectroscopy. *Journal of Astronomical Telescopes, Instruments, and Systems*, 7 (1):011017, 2021.

[23] Patrick C Breysse and Rachael M Alexandroff. Observing agn feedback with co intensity mapping. *Monthly Notices of the Royal Astronomical Society*, 490(1): 260–273, 2019.

[24] CL Carilli and Fabian Walter. Cool gas in high-redshift galaxies. *Annual Review of Astronomy and Astrophysics*, 51:105–161, 2013.

[25] G Cataldo, PAR Ade, CJ Anderson, EM Barrentine, NG Bellis, AD Bolatto, PC Breysse, BT Bulcha, JA Connors, PW Cursey, et al. The experiment for cryogenic large-aperture intensity mapping (exclaim). *Journal of Low Temperature Physics*, pages 1–11, 2020.

[26] Giuseppe Cataldo. Private communication. 2022.

[27] Jhy-Jiun Chang and DJ Scalapino. Nonequilibrium superconductivity. *Journal of Low Temperature Physics*, 31(1):1–32, 1978.

[28] Tzu-Ching Chang, Ue-Li Pen, Kevin Bandura, and Jeffrey B Peterson. An intensity map of hydrogen 21-cm emission at redshift z$\approx$ 0.8. *Nature*, 466(7305): 463–465, 2010.

[29] Sergey Cherednichenko, Vladimir Drakinskiy, Therese Berg, Pourya Khosropanah, and Erik Kollberg. Hot-electron bolometer terahertz mixers for the herschel space observatory. *Review of scientific instruments*, 79(3):034501, 2008.

[30] Dongwoo T Chung. A partial inventory of observational anisotropies in single-dish line-intensity mapping. *The Astrophysical Journal*, 881(2):149, 2019.

[31] Dongwoo T Chung, Marco P Viero, Sarah E Church, Risa H Wechsler, Marcelo A Alvarez, J Richard Bond, Patrick C Breysse, Kieran A Cleary, Hans K Eriksen, Marie K Foss, et al. Cross-correlating carbon monoxide line-intensity maps with spectroscopic and photometric galaxy surveys. *The Astrophysical Journal*, 872 (2):186, 2019.

[32] Dark Energy Spectroscopic Instrument Collaboration, Amir Aghamousa, Jessica Aguilar, Steve Ahlen, Shadab Alam, Lori E Allen, Carlos Allende Prieto, James Annis, Stephen Bailey, Christophe Balland, et al. The desi experiment part i: Science, targeting, and survey design. 2016.

[33] Planck Collaboration, PAR Ade, N Aghanim, C Armitage-Caplan, M Arnaud, et al. Planck 2015 results. *XVI. Cosmological parameters*, 1303:v1, 2013.

[34] Asantha Cooray. Firsst: Overview of the far-infrared spectroscopy space telescope probe concept. Infrared Astrophysics Workshop 2022, 2022.

[35] Asantha Cooray and Ravi Sheth. Halo models of large scale structure. *Physics reports*, 372(1):1–129, 2002.

[36] Tom Crawford. Power spectrum sensitivity of raster-scanned cmb experiments in the presence of 1/f noise. *Physical Review D*, 76(6):063008, 2007.

[37] Rupert AC Croft, Jordi Miralda-Escudé, Zheng Zheng, Michael Blomqvist, and Matthew Pieri. Intensity mapping with sdss/boss lyman-α emission, quasars, and their lyman-α forest. *Monthly Notices of the Royal Astronomical Society*, 481(1):1320–1336, 2018.

[38] O Cucciati, L Tresse, O Ilbert, O Le Fèvre, B Garilli, V Le Brun, P Cassata, P Franzetti, D Maccagni, M Scodeggio, et al. The star formation rate density and dust attenuation evolution over 12 gyr with the vvds surveys. *Astronomy & Astrophysics*, 539:A31, 2012.

[39] Tomas Dahlen, Bahram Mobasher, Mark Dickinson, Henry C Ferguson, Mauro Giavalisco, Claudia Kretchmer, and Swara Ravindranath. Evolution of the luminosity function, star formation rate, morphology, and size of star-forming galaxies selected at rest-frame 1500 and 2800 å. *The Astrophysical Journal*, 654 (1):172, 2007.

[40] Neal Dalal, Olivier Dore, Dragan Huterer, and Alexander Shirokov. Imprints of primordial non-gaussianities on large-scale structure: Scale-dependent bias and abundance of virialized objects. *Physical Review D*, 77(12):123514, 2008.

[41] Kyle S Dawson, David J Schlegel, Christopher P Ahn, Scott F Anderson, Éric Aubourg, Stephen Bailey, Robert H Barkhouser, Julian E Bautista, Alessandra Beifiori, Andreas A Berlind, et al. The baryon oscillation spectroscopic survey of sdss-iii. *The Astronomical Journal*, 145(1):10, 2012.

[42] Peter K Day, Henry G LeDuc, Benjamin A Mazin, Anastasios Vayonakis, and Jonas Zmuidzinas. A broadband superconducting detector suitable for use in large arrays. *Nature*, 425(6960):817–821, 2003.

[43] Th De Graauw, FP Helmich, TG Phillips, J Stutzki, E Caux, ND Whyborn, P Dieleman, PR Roelfsema, Henri Aarts, R Assendorp, et al. The herschel-heterodyne instrument for the far-infrared (hifi). *Astronomy & Astrophysics*, 518:L6, 2010.

[44] Jelte TA de Jong, Gijs A Verdoes Kleijn, Konrad H Kuijken, and Edwin A Valentijn. The kilo-degree survey. *Experimental Astronomy*, 35(1):25–44, 2013.

[45] David R DeBoer, Aaron R Parsons, James E Aguirre, Paul Alexander, Zaki S Ali, Adam P Beardsley, Gianni Bernardi, Judd D Bowman, Richard F Bradley, Chris L Carilli, et al. Hydrogen epoch of reionization array (hera). *Publications of the Astronomical Society of the Pacific*, 129(974):045001, 2017.

[46] Robert H Dicke, P James E Peebles, Peter G Roll, and David T Wilkinson. Cosmic black-body radiation. *The Astrophysical Journal*, 142:414–419, 1965.

[47] Robert Henry Dicke. The measurement of thermal radiation at microwave frequencies. In *Classics in Radio Astronomy*, pages 106–113. Springer, 1946.

[48] Benedikt Diemer. Colossus: A python toolkit for cosmology, large-scale structure, and dark matter halos. *The Astrophysical Journal Supplement Series*, 239(2):35, 2018.

[49] Scott Dodelson. *Modern cosmology*. Elsevier, 2003.

[50] Olivier Doré, Christopher Hirata, Yun Wang, David Weinberg, Ivano Baronchelli, Andrew Benson, Peter Capak, Ami Choi, Tim Eifler, Shoubaneh Hemmati, et al. Wfirst science investigation team" cosmology with the high latitude survey" annual report 2017. *arXiv e-prints*, pages arXiv–1804, 2018.

[51] Thomas Essinger-Hileman, Trevor Oxholm, Gage Siebert, Peter Ade, Christopher Anderson, Alyssa Barlis, Emily Barrentine, Jeffrey Beeman, Nicholas Bellis, Patrick Breysse, et al. Optical design of the experiment for cryogenic large-aperture intensity mapping (exclaim). In *Millimeter, Submillimeter, and Far-Infrared Detectors and Instrumentation for Astronomy X*, volume 11453, page 114530H. International Society for Optics and Photonics, 2020.

[52] Hume A Feldman, Nick Kaiser, and John A Peacock. Power-spectrum analysis of three-dimensional redshift surveys. *The Astrophysical Journal*, 426:23–37, 1994.

[53] DJ Fixsen, ES Cheng, JM Gales, John C Mather, RA Shafer, and EL Wright. The cosmic microwave background spectrum from the full cobe* firas data set. *The Astrophysical Journal*, 473(2):576, 1996.

[54] DJ Fixsen, EMJC Dwek, John C Mather, CL Bennett, and RA Shafer. The spectrum of the extragalactic far-infrared background from the cobe* firas observations. *The Astrophysical Journal*, 508(1):123, 1998.

[55] Daniel Flanigan, Bradley R Johnson, Maximilian H Abitbol, Sean Bryan, Robin Cantor, P Day, Glenn Jones, Philip Mauskopf, Heather McCarrick, Amber Miller, et al. Magnetic field dependence of the internal quality factor and noise performance of lumped-element kinetic inductance detectors. *Applied Physics Letters*, 109(14):143503, 2016.

[56] Masataka Fukugita and PJE Peebles. The cosmic energy inventory. *The Astrophysical Journal*, 616(2):643, 2004.

[57] Jiansong Gao. *The physics of superconducting microwave resonators*. PhD thesis, California Institute of Technology, 2008. http://thesis.library.caltech.edu/2530.

[58] Jason Glenn. Science and mission concept for the prima far-infrared probe. Infrared Astrophysics Workshop 2022, 2022.

[59] Jason Glenn, Charles M Bradford, Erik Rosolowsky, Rashied Amini, Katherine Alatalo, Lee Armus, Andrew J Benson, Tzu-Ching Chang, Jeremy Darling, Peter K Day, et al. Galaxy evolution probe. *Journal of Astronomical Telescopes, Instruments, and Systems*, 7(3):034004, 2021.

[60] DJ Goldie and S Withington. Non-equilibrium superconductivity in quantum-sensing superconducting resonators. *Superconductor Science and Technology*, 26 (1):015004, 2012.

[61] Paul F Goldsmith. Radiation patterns of circular apertures with gaussian illumination. *International Journal of Infrared and Millimeter Waves*, 8(7): 771–781, 1987.

[62] Yan Gong, Asantha Cooray, Marta Silva, Mario G. Santos, James Bock, C. Matt Bradford, and Michael Zemcov. Intensity Mapping of the [C II] Fine Structure Line during the Epoch of Reionization. , 745(1):49, January 2012. doi: 10.1088/0004-637X/745/1/49.

[63] JW Goodman. Introduction to fourier optics, 4w. h, 2017.

[64] Sam Gordon, Adrian Sinclair, Philip Mauskopf, Gabriele Coppi, Mark Devlin, Bradley Dober, Laura Fissel, Nicholas Galitzki, Jiansong Gao, Johannes Hubmayr, et al. Preflight detector characterization of blast-tng. *Journal of Low Temperature Physics*, 200(5):400–406, 2020.

[65] J Green, P Schechter, C Baltay, R Bean, D Bennett, R Brown, C Conselice, M Donahue, X Fan, BS Gaudi, et al. Wide-field infrared survey telescope (wfirst) final report. *arXiv preprint arXiv:1208.4012*, 2012.

[66] C Gruppioni, F Pozzi, G Rodighiero, I Delvecchio, S Berta, L Pozzetti, G Zamorani, P Andreani, Alessandro Cimatti, O Ilbert, et al. The herschel pep/hermes luminosity function–i. probing the evolution of pacs selected galaxies to z$\simeq$ 4. *Monthly Notices of the Royal Astronomical Society*, 432(1):23–52, 2013.

[67] James E Gunn and Bruce A Peterson. On the density of neutral hydrogen in intergalactic space. *The Astrophysical Journal*, 142:1633–1636, 1965.

[68] T Guruswamy, DJ Goldie, and S Withington. Quasiparticle generation efficiency in superconducting thin films. *Superconductor Science and Technology*, 27(5): 055012, 2014.

[69] Shaul Hanany, Marcelo Alvarez, Emmanuel Artis, Peter Ashton, Jonathan Aumont, Ragnhild Aurlien, Ranajoy Banerji, R Belen Barreiro, James G Bartlett, Soumen Basak, et al. Pico: probe of inflation and cosmic origins. *arXiv preprint arXiv:1902.10541*, 2019.

[70] Eugene Hecht. *Optics*. Pearson Education India, 2012.

[71] David W Hogg. Distance measures in cosmology. *arXiv preprint astro-ph/9905116*, 1999.

[72] Jonathan R. Hoh, Adrian Sinclair, and Ryan Stephenson. Maximizing dynamic range of microwave kinetic inductance detectors through high-speed tone tracking. In Jonas Zmuidzinas and Jian-Rong Gao, editors, *Millimeter, Submillimeter, and Far-Infrared Detectors and Instrumentation for Astronomy X*, volume 11453. International Society for Optics and Photonics, SPIE, 2020. doi: 10.1117/12.2559899. URL `https://doi.org/10.1117/12.2559899`.

[73] E Hubble. A relation between distance and radial velocity among extra-galactic nebulae from the proceedings of the national academy of sciences. 1929.

[74] Dragan Huterer and Daniel L Shafer. Dark energy two decades after: Observables, probes, consistency tests. *Reports on Progress in Physics*, 81(1):016901, 2017.

[75] Brian D Jackson, Gert de Lange, Tony Zijlstra, Matthias Kroug, Jacob W Kooi, Jeffrey A Stern, and Teun M Klapwijk. Low-noise 0.8-0.96-and 0.96-1.12-thz superconductor-insulator-superconductor mixers for the herschel space observatory. *IEEE transactions on microwave theory and techniques*, 54(2): 547–558, 2006.

[76] J Kamenetzky, N Rangwala, J Glenn, PR Maloney, and A Conley. Relations with co rotational ladders of galaxies across the herschel spire archive. *The Astrophysical Journal*, 829(2):93, 2016.

[77] Garrett K Keating, Daniel P Marrone, Geoffrey C Bower, and Ryan P Keenan. An intensity mapping detection of aggregate co line emission at 3 mm. *The Astrophysical Journal*, 901(2):141, 2020.

[78] Ryan P Keenan, Garrett K Keating, and Daniel P Marrone. An intensity mapping constraint on the co-galaxy cross power spectrum at redshift˜ 3. *arXiv preprint arXiv:2110.02239*, 2021.

[79] Robert C Kennicutt Jr. The global schmidt law in star-forming galaxies. *The Astrophysical Journal*, 498(2):541, 1998.

[80] M Stoutimore Khalil, MJA Stoutimore, FC Wellstood, and KD Osborn. An analysis method for asymmetric resonator transmission applied to superconducting devices. *Journal of Applied Physics*, 111(5):054510, 2012.

[81] LLoyd Knox. Determination of inflationary observables by cosmic microwave background anisotropy experiments. *Physical Review D*, 52(8):4307, 1995.

[82] Alan Kogut, David T Chuss, Jessie Dotson, Eli Dwek, Dale J Fixsen, Mark Halpern, Gary F Hinshaw, Stephan Meyer, S Harvey Moseley, Michael D Seiffert, et al. The primordial inflation explorer (pixie). In *Space Telescopes and Instrumentation 2014: Optical, Infrared, and Millimeter Wave*, volume 9143, page 91431E. International Society for Optics and Photonics, 2014.

[83] Ely D Kovetz, Marco P Viero, Adam Lidz, Laura Newburgh, Mubdi Rahman, Eric Switzer, Marc Kamionkowski, James Aguirre, Marcelo Alvarez, James Bock, et al. Line-intensity mapping: 2017 status report. *arXiv preprint arXiv:1709.09066*, 2017.

[84] AG Kozorezov, AF Volkov, JK Wigmore, A Peacock, A Poelaert, and R Den Hartog. Quasiparticle-phonon downconversion in nonequilibrium superconductors. *Physical Review B*, 61(17):11807, 2000.

[85] David Leisawitz. The space infrared interferometric telescope (spirit): A far-ir probe candidate. Infrared Astrophysics Workshop 2022, 2022.

[86] David Leisawitz, Edward G Amatucci, Lynn N Allen, Jonathan W Arenberg, Lee Armus, Cara Battersby, James M Bauer, Porfirio Beltran, Dominic J Benford, Denis Burgarella, et al. Origins space telescope: baseline mission concept. *Journal of Astronomical Telescopes, Instruments, and Systems*, 7(1):Art–No, 2021.

[87] Tony Y Li, Risa H Wechsler, Kiruthika Devaraj, and Sarah E Church. Connecting co intensity mapping to molecular gas and star formation in the epoch of galaxy assembly. *The Astrophysical Journal*, 817(2):169, 2016.

[88] Adam Lidz and Jessie Taylor. On removing interloper contamination from intensity mapping power spectrum measurements. *The Astrophysical Journal*, 825(2):143, 2016.

[89] Adam Lidz, Steven R. Furlanetto, S. Peng Oh, James Aguirre, Tzu-Ching Chang, Olivier Doré, and Jonathan R. Pritchard. Intensity Mapping with Carbon Monoxide Emission Lines and the Redshifted 21 cm Line. , 741(2):70, Nov 2011. doi: 10.1088/0004-637X/741/2/70.

[90] Adrian Liu and J Richard Shaw. Data analysis for precision 21 cm cosmology. *Publications of the Astronomical Society of the Pacific*, 132(1012):062001, 2020.

[91] Adrian Liu, Aaron R Parsons, and Cathryn M Trott. Epoch of reionization window. i. mathematical formalism. *Physical Review D*, 90(2):023018, 2014.

[92] Adrian Liu, Aaron R Parsons, and Cathryn M Trott. Epoch of reionization window. ii. statistical methods for foreground wedge reduction. *Physical Review D*, 90(2):023019, 2014.

[93] R Henry Liu and Patrick C Breysse. Coupling parsec and gigaparsec scales: Primordial non-gaussianity with multitracer intensity mapping. *Physical Review D*, 103(6):063520, 2021.

[94] AE Lowitz, EM Barrentine, SR Golwala, and PT Timbie. A comparison of fundamental noise in kinetic inductance detectors and transition edge sensors for millimeter-wave applications. *Journal of Low Temperature Physics*, 176(3): 504–510, 2014.

[95] Knut Lundmark. The determination of the curvature of space-time in de sitter's world. *Monthly Notices of the Royal Astronomical Society*, 84:747–770, 1924.

[96] Piero Madau and Mark Dickinson. Cosmic star-formation history. *Annual Review of Astronomy and Astrophysics*, 52:415–486, 2014.

[97] B Magnelli, D Elbaz, RR Chary, M Dickinson, D Le Borgne, DT Frayer, and CNA Willmer. Evolution of the dusty infrared luminosity function from z= 0 to z= 2.3 using observations from spitzer. *Astronomy & Astrophysics*, 528:A35, 2011.

[98] B Magnelli, P Popesso, S Berta, F Pozzi, D Elbaz, D Lutz, M Dickinson, B Altieri, P Andreani, H Aussel, et al. The deepest herschel-pacs far-infrared survey: number counts and infrared luminosity functions from combined pep/goods-h observations. *Astronomy & Astrophysics*, 553:A132, 2013.

[99] S Masi, P De Bernardis, A Paiella, F Piacentini, L Lamagna, A Coppolecchia, PAR Ade, ES Battistelli, MG Castellano, I Colantoni, et al. Kinetic inductance detectors for the olimpo experiment: in-flight operation and performance. *Journal of Cosmology and Astroparticle Physics*, 2019(07):003, 2019.

[100] KW Masui, ER Switzer, N Banavar, K Bandura, C Blake, L-M Calin, T-C Chang, X Chen, Y-C Li, Y-W Liao, et al. Measurement of 21 cm brightness fluctuations at z 0.8 in cross-correlation. *The Astrophysical Journal Letters*, 763(1):L20, 2013.

[101] Daniel C Mattis and John Bardeen. Theory of the anomalous skin effect in normal and superconducting metals. *Physical Review*, 111(2):412, 1958.

[102] PD Mauskopf. Transition edge sensors and kinetic inductance detectors in astronomical instruments. *Publications of the Astronomical Society of the Pacific*, 130(990):082001, 2018.

[103] John McClane. Die hard. *Silver Pictures*, 281(5730):358–359, 1988.

[104] Mona Mirzaei, Emily M Barrentine, Berhanu T Bulcha, Giuseppe Cataldo, Jake A Connors, Negar Ehsan, Thomas M Essinger-Hileman, Larry A Hess, Samuel H Moseley, Jonas W Mugge-Durum, et al. μ-spec spectrometers for the exclaim instrument. In *Millimeter, Submillimeter, and Far-Infrared Detectors and Instrumentation for Astronomy X*, volume 11453, page 114530M. International Society for Optics and Photonics, 2020.

[105] Houjun Mo, Frank Van den Bosch, and Simon White. *Galaxy formation and evolution*. Cambridge University Press, 2010.

[106] L Mousset, MM Lerena, ES Battistelli, P de Bernardis, P Chanial, G d'Alessandro, G Dashyan, M De Petris, L Grandsire, J-Ch Hamilton, et al. Qubic ii: Spectro-polarimetry with bolometric interferometry. *arXiv preprint arXiv:2010.15119*, 2020.

[107] Julio F Navarro, Carlos S Frenk, and Simon DM White. A universal density profile from hierarchical clustering. *The Astrophysical Journal*, 490(2):493, 1997.

[108] LB Newburgh, K Bandura, MA Bucher, T-C Chang, HC Chiang, JF Cliche, R Davé, M Dobbs, C Clarkson, KM Ganga, et al. Hirax: a probe of dark energy and radio transients. In *Ground-based and Airborne Telescopes VI*, volume 9906, page 99065X. International Society for Optics and Photonics, 2016.

[109] Atsushi J Nishizawa, Bau-Ching Hsieh, Masayuki Tanaka, and Tadafumi Takata. Photometric redshifts for the hyper suprime-cam subaru strategic program data release 2. *arXiv preprint arXiv:2003.01511*, 2020.

[110] Omid Noroozian. *Superconducting microwave resonator arrays for submillimeter/far-infrared imaging*. California Institute of Technology, 2012.

[111] Trevor M Oxholm. Calibration and beam-mapping techniques for the tianlai pathfinder dish array. In *Proceedings of the Wisconsin Space Conference*, volume 1, 2019.

[112] Trevor M Oxholm. A beginner's guide to line intensity mapping power spectra. In *Proceedings of the Wisconsin Space Conference*, volume 1, 2021.

[113] Trevor M Oxholm and Eric R Switzer. Intensity mapping without cosmic variance. *Physical Review D*, 104(8):083501, 2021.

[114] Trevor M. Oxholm, Eric R. Switzer, Emily M. Barrentine, Thomas Essinger-Hileman, James P. Hays-Wehle, Philip D. Mauskopf, Omid Noroozian, Maryam Rahmani, Adrian K. Sinclair, Ryan Stephenson, Thomas R. Stevenson, Peter T. Timbie, Carolyn Volpert, and Eric Weeks. Operational optimization to maximize dynamic range in exclaim microwave kinetic inductance detectors. *Low-Temperature Detectors (accepted for publication)*, 2022.

[115] Hamsa Padmanabhan. Constraining the CO intensity mapping power spectrum at intermediate redshifts. , 475(2):1477–1484, April 2018. doi: 10.1093/mnras/stx3250.

[116] Hamsa Padmanabhan. Constraining the evolution of [c ii] intensity through the end stages of reionization. *Monthly Notices of the Royal Astronomical Society*, 488(3):3014–3023, 2019.

[117] Scott Paine. The am atmospheric model (version 11.0). zenodo, 2019.

[118] Arno A Penzias and Robert Woodrow Wilson. A measurement of excess antenna temperature at 4080 mc/s. *The Astrophysical Journal*, 142:419–421, 1965.

[119] Joanna Perido and Jason Glenn. Private communication. to appear in thesis. 2020.

[120] Saul Perlmutter, Goldhaber Aldering, Gerson Goldhaber, RA Knop, Peter Nugent, Patricia G Castro, Susana Deustua, Sebastien Fabbro, Ariel Goobar, Donald E Groom, et al. Measurements of ω and λ from 42 high-redshift supernovae. *The Astrophysical Journal*, 517(2):565, 1999.

[121] Marshall Perrin, Joseph Long, Ewan Douglas, Anand Sivaramakrishnan, Christine Slocum, et al. Poppy: physical optics propagation in python. *Astrophysics Source Code Library*, pages ascl–1602, 2016.

[122] Gergö Popping, Eelco van Kampen, Roberto Decarli, Marco Spaans, Rachel S. Somerville, and Scott C. Trager. Sub-mm emission line deep fields: CO and [C II] luminosity functions out to z = 6. , 461(1):93–110, September 2016. doi: 10.1093/mnras/stw1323.

[123] Anthony R. Pullen, Tzu-Ching Chang, Olivier Doré, and Adam Lidz. Cross-correlations as a Cosmological Carbon Monoxide Detector. , 768(1):15, May 2013. doi: 10.1088/0004-637X/768/1/15.

[124] Anthony R Pullen, Paolo Serra, Tzu-Ching Chang, Olivier Doré, and Shirley Ho. Search for c ii emission on cosmological scales at redshift z 2.6. *Monthly Notices of the Royal Astronomical Society*, 478(2):1911–1924, 2018.

[125] Anthony R. Pullen, Christopher J. Anderson, Alberto D. Bolatto, Patrick C. Breysse, Thomas Essinger-Hileman, Abhishek Maniyar, Trevor Oxholm, Rachel S. Somerville, Eric R. Switzer, Carrie Volpert, Shengqi Yang, L. Y. Aaron Yung, and Zilu Zhou. Article in preparation. *arXiv preprint arXiv:2003.01511*, 2022.

[126] Naveen A Reddy and Charles C Steidel. A steep faint-end slope of the uv luminosity function at z 2-3: Implications for the global stellar mass density and star formation in low-mass halos. *The Astrophysical Journal*, 692(1):778, 2009.

[127] Adam G Riess, Alexei V Filippenko, Peter Challis, Alejandro Clocchiatti, Alan Diercks, Peter M Garnavich, Ron L Gilliland, Craig J Hogan, Saurabh Jha, Robert P Kirshner, et al. Observational evidence from supernovae for an accelerating universe and a cosmological constant. *The Astronomical Journal*, 116(3):1009, 1998.

[128] Christophe Risacher and Willem Jellema. Heterodyne technology for space missions. The next generation mid/far-IR space missions - Formulating a European perspective, 2022.

[129] Aaron SG Robotham and Simon P Driver. The galex–sdss nuv and fuv flux density and local star formation rate. *Monthly Notices of the Royal Astronomical Society*, 413(4):2570–2582, 2011.

[130] DB Sanders, JM Mazzarella, D-C Kim, JA Surace, and BT Soifer. The iras revised bright galaxy sample. *The Astronomical Journal*, 126(4):1607, 2003.

[131] Emmanuel Schaan and Martin White. Astrophysics & cosmology from line intensity mapping vs galaxy surveys. *Journal of Cosmology and Astroparticle Physics*, 2021(05):067, 2021.

[132] Matthew A Schenker, Brant E Robertson, Richard S Ellis, Yoshiaki Ono, Ross J McLure, James S Dunlop, Anton Koekemoer, Rebecca AA Bowler, Masami Ouchi, Emma Curtis-Lake, et al. The uv luminosity function of star-forming galaxies via dropout selection at redshifts z 7 and 8 from the 2012 ultra deep field campaign. *The Astrophysical Journal*, 768(2):196, 2013.

[133] David Schiminovich, O Ilbert, S Arnouts, B Milliard, L Tresse, O Le Fèvre, M Treyer, TK Wyder, T Budavári, E Zucca, et al. The galex-vvds measurement of the evolution of the far-ultraviolet luminosity density and the cosmic star formation rate. *The Astrophysical Journal*, 619(1):L47, 2005.

[134] David J Schlegel, Juna A Kollmeier, Greg Aldering, Stephen Bailey, Charles Baltay, Christopher Bebek, Segev BenZvi, Robert Besuner, Guillermo Blanc, Adam S Bolton, et al. Astro2020 apc white paper: The megamapper: az¿ 2 spectroscopic instrument for the study of inflation and dark energy. *arXiv preprint arXiv:1907.11171*, 2019.

[135] Ravi K Sheth and Giuseppe Tormen. An excursion set model of hierarchical clustering: ellipsoidal collapse and the moving barrier. *Monthly Notices of the Royal Astronomical Society*, 329(1):61–75, 2002.

[136] Joseph Silk and Martin J Rees. Letter to the editor quasars and galaxy formation. *Astron. Astrophys*, 331:L1–L4, 1998.

[137] Marta Silva, Mario G. Santos, Asantha Cooray, and Yan Gong. Prospects for Detecting C II Emission during the Epoch of Reionization. , 806(2):209, June 2015. doi: 10.1088/0004-637X/806/2/209.

[138] Jack Singal, DJ Fixsen, A Kogut, S Levin, M Limon, P Lubin, P Mirel, M Seiffert, T Villela, E Wollack, et al. The arcade 2 instrument. *The Astrophysical Journal*, 730(2):138, 2011.

[139] Vesto M Slipher. Nebulae. *Proceedings of the American Philosophical Society*, pages 403–409, 1917.

[140] Anze Slosar, Zeeshan Ahmed, David Alonso, Mustafa A Amin, Evan J Arena, Kevin Bandura, Nicholas Battaglia, Jonathan Blazek, Philip Bull, Emanuele Castorina, et al. Packed ultra-wideband mapping array (puma): A radio telescope for cosmology and transients. *Bulletin of the American Astronomical Society*, 51(7):53, 2019.

[141] Alex Smith, Etienne Burtin, Jiamin Hou, Richard Neveux, Ashley J Ross, Shadab Alam, Jonathan Brinkmann, Kyle S Dawson, Salman Habib, Katrin Heitmann, et al. The completed sdss-iv extended baryon oscillation spectroscopic survey: N-body mock challenge for the quasar sample. *Monthly Notices of the Royal Astronomical Society*, 499(1):269–291, 2020.

[142] Rachel S Somerville and Romeel Davé. Physical models of galaxy formation in a cosmological framework. *Annual Review of Astronomy and Astrophysics*, 53: 51–113, 2015.

[143] Luigi Spinoglio, Kalliopi M Dasyra, Alberto Franceschini, Carlotta Gruppioni, Elisabetta Valiante, and Kate Isaak. Far-ir/submillimeter spectroscopic cosmological surveys: Predictions of infrared line luminosity functions for z¡ 4 galaxies. *The Astrophysical Journal*, 745(2):171, 2012.

[144] Ryan Stephenson. paper in preparation.

[145] LJ Swenson, PK Day, BH Eom, HG Leduc, N Llombart, CM McKenney, O Noroozian, and J Zmuidzinas. Operation of a titanium nitride superconducting microresonator detector in the nonlinear regime. *Journal of Applied Physics*, 113(10):104501, 2013.

[146] DS Swetz, Peter AR Ade, M Amiri, JW Appel, ES Battistelli, B Burger, J Chervenak, MJ Devlin, SR Dicker, WB Doriese, et al. Overview of the atacama cosmology telescope: Receiver, instrumentation, and telescope systems. *The Astrophysical Journal Supplement Series*, 194(2):41, 2011.

[147] ER Switzer, KW Masui, K Bandura, L-M Calin, T-C Chang, X-L Chen, Y-C Li, Y-W Liao, A Natarajan, U-L Pen, et al. Determination of z 0.8 neutral hydrogen fluctuations using the 21 cm intensity mapping autocorrelation. *Monthly Notices of the Royal Astronomical Society: Letters*, 434(1):L46–L50, 2013.

[148] ER Switzer, CJ Anderson, AR Pullen, and S Yang. Intensity mapping in the presence of foregrounds and correlated continuum emission. *The Astrophysical Journal*, 872(1):82, 2019.

[149] Eric R Switzer, Emily M Barrentine, Giuseppe Cataldo, Thomas Essinger-Hileman, Peter AR Ade, Christopher J Anderson, Alyssa Barlis, Jeffrey Beeman, Nicholas Bellis, Alberto D Bolatto, et al. Experiment for cryogenic large-aperture intensity mapping: instrument design. *Journal of Astronomical Telescopes, Instruments, and Systems*, 7(4):044004, 2021.

[150] Tsutomu T Takeuchi, Kohji Yoshikawa, and Takako T Ishii. The luminosity function of iras point source catalog redshift survey galaxies. *The Astrophysical Journal Letters*, 587(2):L89, 2003.

[151] Max Tegmark, Andy N Taylor, and Alan F Heavens. Karhunen-loeve eigenvalue problems in cosmology: How should we tackle large data sets? *The Astrophysical Journal*, 480(1):22, 1997.

[152] Steven John Tingay, Robert Goeke, Judd D Bowman, David Emrich, Stephen M Ord, Daniel A Mitchell, Miguel F Morales, Tom Booler, Brian Crosse, Randall B Wayth, et al. The murchison widefield array: The square kilometre array precursor at low radio frequencies. *Publications of the Astronomical Society of Australia*, 30, 2013.

[153] Jeremy L Tinker, Brant E Robertson, Andrey V Kravtsov, Anatoly Klypin, Michael S Warren, Gustavo Yepes, and Stefan Gottlöber. The large-scale bias of dark matter halos: numerical calibration and model tests. *The Astrophysical Journal*, 724(2):878, 2010.

[154] Michael Tinkham. *Introduction to superconductivity*. Courier Corporation, 2004.

[155] J Anthony Tyson. Large synoptic survey telescope: overview. *Survey and Other Telescope Technologies and Discoveries*, 4836:10–20, 2002.

[156] Gerhard Ulbricht, Mario De Lucia, and Eoin Baldwin. Applications for microwave kinetic induction detectors in advanced instrumentation. *Applied Sciences*, 11(6):2671, 2021.

[157] Bade D Uzgil, Chris Carilli, Adam Lidz, Fabian Walter, Nithyanandan Thyagarajan, Roberto Decarli, Manuel Aravena, Frank Bertoldi, Paulo C Cortes, Jorge González-López, et al. The alma spectroscopic survey in the hudf: Constraining cumulative co emission at $1\lesssim z\lesssim 4$ with power spectrum analysis of aspecs lp data from 84 to 115 ghz. *The Astrophysical Journal*, 887(1):37, 2019.

[158] Joris van Rantwijk, Martin Grim, Dennis van Loon, Stephen Yates, Andrey Baryshev, and Jochem Baselmans. Multiplexed readout for 1000-pixel arrays of microwave kinetic inductance detectors. *IEEE Transactions on Microwave Theory and Techniques*, 64(6):1876–1883, 2016.

[159] Fabian Walter, Chris Carilli, Marcel Neeleman, Roberto Decarli, Gergö Popping, Rachel S Somerville, Manuel Aravena, Frank Bertoldi, Leindert Boogaard, Pierre Cox, et al. The evolution of the baryons associated with galaxies averaged over cosmic time and space. *The Astrophysical Journal*, 902(2):111, 2020.

[160] L Wolz, SG Murray, C Blake, and JS Wyithe. Intensity mapping cross-correlations ii: Hi halo models including shot noise. *Monthly Notices of the Royal Astronomical Society*, 484(1):1007–1020, 2019.

[161] Laura Wolz, Alkistis Pourtsidou, Kiyoshi W Masui, Tzu-Ching Chang, Julian E Bautista, Eva-Maria Müller, Santiago Avila, David Bacon, Will J Percival, Steven Cunnington, et al. Hi constraints from the cross-correlation of eboss galaxies and green bank telescope intensity maps. *arXiv preprint arXiv:2102.04946*, 2021.

[162] Fengquan Wu, Jixia Li, Shifan Zuo, Xuelei Chen, Santanu Das, John P Marriner, Trevor M Oxholm, Anh Phan, Albert Stebbins, Peter T Timbie, et al. The tianlai dish pathfinder array: design, operation, and performance of a prototype transit radio interferometer. *Monthly Notices of the Royal Astronomical Society*, 506(3):3455–3482, 2021.

[163] Ted K Wyder, Marie A Treyer, Bruno Milliard, David Schiminovich, Stéphane Arnouts, Tamás Budavári, Tom A Barlow, Luciana Bianchi, Yong-Ik Byun, José Donas, et al. The ultraviolet galaxy luminosity function in the local universe from galex data. *The Astrophysical Journal Letters*, 619(1):L15, 2005.

[164] Shengqi Yang, Anthony R Pullen, and Eric R Switzer. Evidence for c ii diffuse line emission at redshift z 2.6. *Monthly Notices of the Royal Astronomical Society: Letters*, 489(1):L53–L57, 2019.

[165] Shengqi Yang, Rachel S Somerville, Anthony R Pullen, Gergö Popping, Patrick C Breysse, and Abhishek S Maniyar. Multitracer cosmological line intensity mapping mock light-cone simulation. *The Astrophysical Journal*, 911(2):132, 2021.

[166] Donald G York, J Adelman, John E Anderson Jr, Scott F Anderson, James Annis, Neta A Bahcall, JA Bakken, Robert Barkhouser, Steven Bastian, Eileen Berman, et al. The sloan digital sky survey: Technical summary. *The Astronomical Journal*, 120(3):1579, 2000.

[167] B. Yue, A. Ferrara, A. Pallottini, S. Gallerani, and L. Vallini. Intensity mapping of [C II] emission from early galaxies. , 450(4):3829–3839, July 2015. doi: 10.1093/mnras/stv933.

[168] J Zmuidzinas. Progress in coherent detection methods. In *The Physics and Chemistry of the Interstellar Medium*, 1999.

[169] Jonas Zmuidzinas. Thermal noise and correlations in photon detection. *Applied optics*, 42(25):4989–5008, 2003.

[170] Jonas Zmuidzinas. Superconducting microresonators: Physics and applications. *Annu. Rev. Condens. Matter Phys.*, 3(1):169–214, 2012.